Quantum sensing with Rydberg Schrödinger cat states

Eva-Katharina Dietsche

Institut de Physique du Collège de France

Laboratoire Kastler Brossel

COLLÈGE DE FRANCE 1530

THÈSE DE DOCTORAT DE L'UNIVERSITÉ PARIS 6

Spécialité : **Physique Quantique**

présentée par

Eva-Katharina DIETSCHE

pour obtenir le grade de

Docteur de l'Université Paris 6

Sujet :

Quantum sensing with Rydberg Schrödinger cat states

Soutenue le 14/09/2017 devant le jury composé de :

Prof.	Agnès Maître	examinateur
Prof.	Pierre Pillet	rapporteur
Prof.	Jean-Michel Raimond	directeur de thèse
Prof.	Ferdinand Schmidt-Kaler	rapporteur
Prof.	Philipp Treutlein	examinateur
Dr.	Sébastien Gleyzes	membre invité

Contents

Introduction **1**

1 Rydberg atoms **11**
1.1 The Hydrogen atom . . . 12
1.1.1 Wave-function of the hydrogen atom . . . 13
1.1.2 The hydrogen atom in the presence of an electric field . . . 16
1.1.3 The hydrogen atom in the presence of a magnetic field . . . 19
1.1.4 The Runge-Lenz vector . . . 20
1.1.5 Stark shift in the Runge-Lenz basis . . . 22
1.1.6 Coupling Hamiltonian . . . 24
1.1.7 Spin coherent states . . . 25
1.2 The rubidium Rydberg atom . . . 32
1.2.1 Energy corrections due to the quantum defect . . . 33
1.2.2 Energy levels in a static electric field . . . 34
1.2.3 Numerical calculation of the coupling Hamiltonian . . . 36
1.3 Discussion . . . 38

2 The Experiment **41**
2.1 The experimental set-up . . . 41
2.2 Preparation and detection of the atoms . . . 43
2.2.1 Laser excitation . . . 44
2.2.2 Adiabatic passage to the circular Rydberg state . . . 45
2.2.3 Detection by ionization . . . 47
2.3 Manipulation of the atomic state . . . 49
2.3.1 Microwave field . . . 50
2.3.2 Radio-frequency field optimization . . . 51
2.4 Electric field gradient compensation . . . 61
2.4.1 Attempt to reduce stray charges . . . 64
2.4.2 Reduction of atomic sample size . . . 64
2.5 Discussion . . . 65

3 Quantum-enabled electrometry **67**
3.1 Measurement precision limits . . . 67
3.1.1 Classical methods . . . 67
3.1.2 The quantum-enabled method . . . 69
3.2 Experimental realization . . . 73

3.2.1 Experimental sequence of the quantum-enabled method 73
3.2.2 The radio-frequency field power 75
3.2.3 Determination of the radio-frequency pulse duration 77
3.2.4 Applying the electric field 78
3.2.5 Calibration of the electric field 79
3.3 Experimental results 80
3.3.1 Experimental results for the classical method 80
3.3.2 Experimental results for the quantum-enabled method 84
3.3.3 Experimental single-atom sensitivity 84
3.3.4 Experimental decoherence 89
3.4 Improved sensitivity with echo-like sequence 91
3.4.1 Experimental realization 92
3.5 Discussion 95

4 Correlation measurements **97**
4.1 Principles of AC electric field variation measurements 98
4.2 Experimental implementation 101
4.2.1 Calibration of the phase sensitivity α^+ 101
4.2.2 Calibration of the phase sensitivity α^- 102
4.3 AC electric field measurement 104
4.3.1 Sensitivity of the AC-electrometer 104
4.3.2 High frequency bandwidth measurement 105
4.3.3 Charge correlation measurement 111
4.4 Noise correlation function measurement 113
4.4.1 Theory of noise measurement 113
4.4.2 Noise measurement 116
4.4.3 Measure the correlation of noise 119
4.5 Characterization of the noise in the experiment 124
4.6 Discussion 126

5 Quantum-enabled magnetometry **129**
5.1 Preparation of the opposite circular superposition 129
5.1.1 General preparation scheme 129
5.1.2 Preparation of the low-m superposition 131
5.1.3 Circularization to opposite circular states 133
5.1.4 The superposition of opposite circular states 137
5.2 Magnetic field measurement 145
5.2.1 The magnetic field coils 145
5.2.2 Calibration of the magnetic field 146
5.2.3 Measurement of the magnetic field 146
5.3 Discussion 149

Conclusions **151**

A The quantum defect constant **155**

B Off-resonant Rabi oscillations - geometrical derivation **157**
B.1 Off-resonant Rabi oscillation - single RF pulse 157
B.2 Ramsey-like off-resonant Rabi oscillations 158
B.3 Resonant Rabi oscillation - single RF pulse 160

C Electric field noise - higher order contrast reduction **161**

D Calibration of the magnetic field using a dark state **163**
D.1 Preparation of the microwave dark state 163
D.2 Calibration of the magnetic field using the dark state 164

Bibliography **179**

Introduction

The endeavour to find a potential application of the counterintuitive aspects of quantum mechanics has intrigued physicists for several decades. Although quantum information, from quantum computers [1, 2] to quantum cryptography [3], seems to be a very promising path, the use of quantum mechanical systems as sensors for various physical properties has emerged in recent years. *Quantum sensors* essentially exploit what could be seen as a weakness of quantum systems: their strong sensitivity to their environment.

Quantum sensing has become a rapidly growing field of quantum technology, using a large variety of experimental platforms, from atoms or ions to superconducting qubits or solid state spins. In the following we give a brief overview of a few quantum mechanical sensors that measure physical quantities from electric and magnetic fields, times and frequencies, to rotations, temperatures and pressures [4].

Examples of quantum sensors

Photons have been the first system where the interest of quantum entanglement [5] to improve the sensitivity of a measurement was demonstrated [6]. Vacuum squeezed states have been employed in a proof-of-principle experiment to improve the sensitivity of gravitational wave detectors [7, 8]. Non-classical states of light are also used to improve imaging [9–12].

Phonons, quantized energy levels of vibration, have recently become accessible in the field of optomechanics [13, 14]. Since the mechanical degrees of freedom couple to various external fields, optomechanical sensors can be used to detect small forces [15], accelerations [16], masses [17], magnetic fields [18], spins [19] and voltages [20].

Neutral atoms are widely used as quantum sensors. A thermal vapour of alkali atoms can serve as a quantum sensor for magnetic fields [21, 22]. Atomic magnetometers with large volumes achieve sensitivities in the range of 100 $\mathrm{aT}/\sqrt{\mathrm{Hz}}$ [23]. Maybe the most advanced application of vapour cells is the detection of cerebral [24, 25] and even neural activity [26, 27]. The advent of laser cooling opened the way to the development of quantum sensors based on ultra-cold atoms. Their reduced velocity enables to obtain longer interaction times, which improved the sensitivity of atomic clocks [28], but also lead to the development of gravimeters [29, 30] and gyrometers [31, 32]. Trapped atoms

are used to detect and image magnetic fields at microscales [33, 34].

Trapped ions can be used as quantum sensors for electric or magnetic fields. The measurement of the electric field based on spectroscopy of the quantized motional levels is predicted to have a sensitivity of 500 nV/m/$\sqrt{\text{Hz}}$ [35]. Ions have also been used to study electric field noise above surfaces [36]. The ground state spin sublevels can be used for magnetometry, with a sensitivity of the order of pT/$\sqrt{\text{Hz}}$ [37, 38]. Single ion atomic clocks are the most advanced atomic clocks today [39].

Rydberg atoms are very sensitive to the electric field due to the strong Stark shift [40, 41]. Rydberg states in vapour cells [42] can be applied to sense weak electric fields in the radio-frequency and microwave frequency range with a sensitivity up to 100 μV/m/$\sqrt{\text{Hz}}$ [43, 44]. In our group, Rydberg atoms have been used to detect single microwave photons stored in a superconducting cavity [45–47].

In the field of *solid state spins*, on the one hand, the nuclear magnetic resonance (NMR) devices were the earliest quantum sensors based on an ensemble of nuclear spins [48, 49] with a sensitivity to the magnetic field of 10 pT/$\sqrt{\text{Hz}}$. Due to their simplicity and robustness they are used in geology, archaeology, and space missions. On the other hand, the nitrogen-vacancy (NV) centres, which are electronic spin defects in diamonds, combine the strong magnetic moment of the spin and the efficient read-out of atomic vapour cells. Their sensitivity to the magnetic field is of 1 nT/$\sqrt{\text{Hz}}$ for single spins [50] and can reach 1 pT/$\sqrt{\text{Hz}}$ for spin ensembles [51], several orders of magnitude above the predicted sensitivity of a few fT/$\sqrt{\text{Hz}}$ [52] due to technical challenges. At the single spin level, NV centres or optically active quantum dots can be used to sense the change of the electric field corresponding to the fluctuation of a charge located tens of nanometres away [53, 54].

Superconducting quantum interference devices (SQUID) are one of the most sensitive types of magnetic sensor [55, 56]. SQUIDs use the Aharonov-Bohm phase which is accumulated by the superconducting wave-function on a closed loop in the presence of a magnetic field and can be read out by a circuit of phase-sensitive Josephson junctions. They are used for example to measure small stray fields (in the order of 100 fT) created by the electric currents in the brain. *Superconducting qubits* [57–61] prepared in superpositions of supercurrents or charge eigenstates have very large magnetic or electric moments, making them of great interest for quantum sensing. Magnetometers based on persistent current qubits can reach a sensitivity of 3.3 pT/$\sqrt{\text{Hz}}$ [62].

Single electron transistors measure the tunnel current across a small conducting island located between source and drain, connected by tunnel junctions. Due to the Coulomb blockade, tunnelling is only allowed if the charge eigenstate of the island lies in a small energy range. Since the energy of this eigenstate is very sensitive to the electric field, the tunnel current is highly field-dependent [63–65] allowing the single electron transistor to reach a very good charge sensitivity of $\sim 10^{-6}e/\sqrt{\text{Hz}}$ [64, 66].

Sensitivity of quantum sensors

As the sensitivity of devices keeps improving, a question arises: What it is the limit to the precision of the measurement? In fact, most experiments today are not limited by classical technical noise, but by the quantum nature of the sensor and the intrinsic quantum fluctuations due to the probabilistic nature of the measurement.

The aim of quantum metrology is to measure a classical quantity A that can be, for instance, a field or a frequency, by using a meter system whose evolution depends on A. The meter system is initially prepared in the state $|\psi_0\rangle$. After the evolution, the final state $|\psi_A\rangle$ of the meter is read out by measuring a certain observable B. The precision on the estimation of A is set by the quantum uncertainty on the measurement of B.

If the meter system is a harmonic oscillator or a large angular momentum [67–75], prepared in a classical state, its quantum fluctuations are directly related to the Heisenberg uncertainty principle [76]. Classical states of a system are described in quantum mechanics by coherent states that are minimum uncertainty states for which the quantum fluctuations are distributed equally between conjugated observables [77]. The minimum sensitivity attainable by measurement strategies involving only classical states is therefore set by the uncertainty principle and is called the *standard quantum limit* [78, 79].

We consider the case where the meter is made up of a large angular momentum J, and the classical quantity A is the angle by which the angular momentum has rotated around the vertical axis. The Heisenberg inequality in this case derives from the non-commutation of the Cartesian spin components [80, 81],

$$\Delta\hat{J}_y \Delta\hat{J}_z \geq \frac{\hbar}{2}\langle\hat{J}_x\rangle.$$

As a minimum uncertainty state, the spin coherent state along the x-direction verifies $\Delta\hat{J}_y = \Delta\hat{J}_z = \hbar\sqrt{J/2}$. These fluctuations correspond to an uncertainty on the direction of the spin $\Delta\phi = 1/\sqrt{2J}$, limiting the precision with which one can determine the rotation angle A and define the standard quantum limit for this measurement.

The standard quantum limit, however, is not the fundamental limit of the achievable measurement precision. By using non-classical states, it is possible to go beyond this limit. It is possible to calculate the lowest achievable uncertainty according to the laws of quantum mechanics, called the *Heisenberg limit* [82], using estimation theory [83]. For a given state $|\psi_A\rangle$ and a given positive operator valued measure (POVM) [84], the *Fisher information* $F(A)$ [85] allows to quantify how much information on A one can extract from the measurement described by the POVM. The uncertainty of the determination of A, as first demonstrated by Cramér [86] and Rao [87], is given by the *Cramér-Rao bound* [88, 89] as

$$\Delta A \geq \frac{1}{\sqrt{F(A)}}.$$

However, this relation depends on the choice of the POVM, which is not necessarily the measure that provides the best possible uncertainty. The lowest uncertainty of the

measurement with a given state is determined with the *quantum* Cramér-Rao bound [88] which is obtained by optimizing the above relation with respect to all possible POVMs [84, 88–91]. Finally, the Heisenberg limit is obtained by further optimizing the quantum Cramér-Rao bound with respect to all available possible initial states.

In the case of the angular momentum, the final state is $|\psi_A\rangle = e^{-i\hat{J}_z A}|\psi_0\rangle$ and the quantum Cramér-Rao bound takes the simple form

$$\Delta A \geq \frac{1}{2\Delta\hat{J}_z}.$$

The smallest uncertainty is obtained for states with the largest value of $\Delta\hat{J}_z$. If we restrict the optimization to spin coherent states, the maximum value of $\Delta\hat{J}_z$ is $\sqrt{J/2}$ and the quantum Cramér-Rao bound gives the standard quantum limit. However, if we consider all possible states, the maximum value of $\Delta\hat{J}_z$ is J, obtained for a quantum superposition of the two eigenstates of $\hat{J}_z$ corresponding to $\pm J$, and we find the Heisenberg limit that scales like $1/2J$.

If the large spin J is an effective spin describing symmetric the states of N two-level systems, the standard quantum limit corresponds to the $1/\sqrt{N}$ shot-noise of N independent measurements. To go beyond the standard quantum limit, it is necessary to entangle the N particles.

Measurements beyond the standard quantum limit have been performed employing non-classical states such as squeezed states [92] prepared via interactions [34, 68, 93–95] or optical non-destructive measurement [67, 69, 96–102], The Heisenberg limit can then be approached and even be reached with Schrödinger cat states [70–73]. The latter are however difficult to prepare [103–106], and so far experiments with cat states have been restricted to $J \approx 5$ (with three ions [71], four photons [72], or ten spins [73]).

Beating the standard quantum limit with Schrödinger cat states in Rydberg atoms

In our experiment, the meter consists of a large spin $J \approx 25$ carried by a single rubidium Rydberg atom, which we use to measure electric or magnetic fields. The Rydberg atom can be described in good approximation by the model of the hydrogen atom. In the absence of external fields, the energy of the eigenstates of the Rydberg atom only depends on the principal quantum number n. In the presence of a static electric field, the degeneracy is partially lifted and the Stark levels of the manifold can be sorted by their magnetic quantum number m and form a triangular structure for $m \geq 0$ (Fig. 1). The energy difference between adjacent levels is proportional to the amplitude of the electric field.

When the atom, initially in the circular state (the state of maximum m, green level in Fig. 1) is coupled to a resonant σ^+ polarized radio-frequency field, the dynamics of the atom is restricted to the ladder made up of the lowest energy level of each m (blue levels in Fig. 1). The atom can be described as an effective angular momentum J evolving on a generalized Bloch sphere (Fig. 2). In this representation, the initial circular state corresponds to a spin coherent state pointing to the north pole (Fig. 2a). The precession

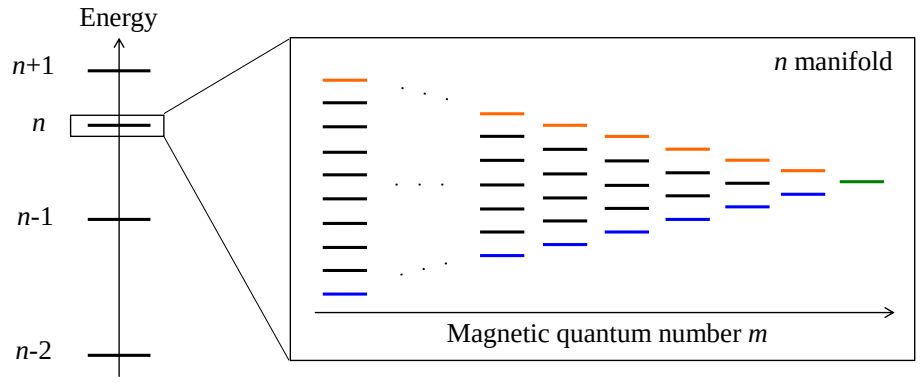

Figure 1: Stark levels of the manifold with principal quantum number n sorted by the magnetic quantum number m. The levels with highest (orange) and lowest (blue) energy for each m are highlighted. The two diagonals overlap in the circular state (green), state with maximum angular momentum.

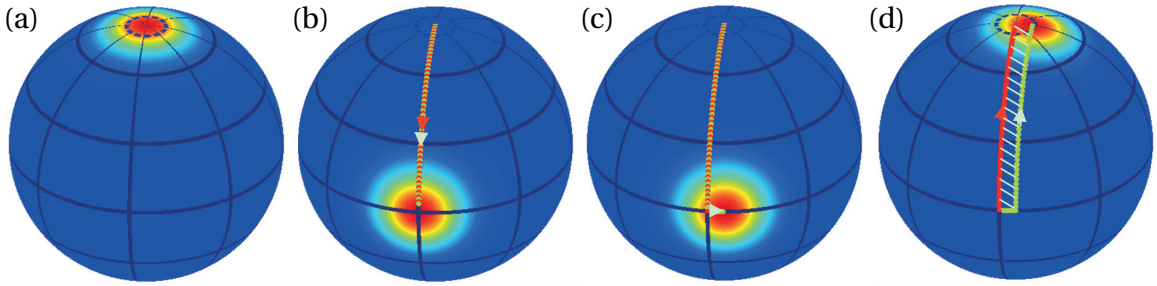

Figure 2: Evolution of the angular momentum state during the measurement sequence. Its quantum state is represented by a phase space distribution that shows the intrinsic quantum fluctuations of the direction of the angular momentum. The classical determination of the angle ϕ is therefore limited by the latter. In the quantum scheme, we deduce the rotation angle from the global phase accumulated by the quantum state as it returns to the north pole.

frequency of the effective angular momentum is proportional to the electric field, and can be used to measure the latter. To that end, a first radio-frequency field pulse prepares a spin coherent state along the direction $(\theta, \phi = 0)$ of the Bloch sphere (Fig. 2b). During a chosen interaction time, the angular momentum follows a precession around the vertical axis in the rotating frame of the radio-frequency and accumulates a classical phase ϕ that depends on the amplitude of the electric field (Fig. 2c). The intrinsic quantum fluctuations in the direction of the angular momentum set a limit on the precision of the determination of ϕ. To overcome this limitation, we can apply a second radio-frequency pulse at the end of the interrogation time that brings the spin coherent state back to the north pole (Fig. 2d). The spin coherent state accumulates a quantum phase Φ during its evolution, which is $J(1-\cos(\theta))$-times larger than ϕ. Measuring this phase provides a much more precise determination of the precession frequency. However, Φ is a global phase, so we need to prepare a quantum superposition of the spin state and a reference state to measure it. This requires the atom to be in a Schrödinger cat state during the interrogation time.

During the first part of my PhD we have implemented this quantum-enabled measurement method. We demonstrated that we are able to reach a sensitivity −7 dB below the standard quantum limit. We reach a single-atom sensitivity of 102 mV/m. At the ~3 kHz repetition rate of our experiment, this corresponds to a sensitivity of 3 mV/m/$\sqrt{\text{Hz}}$. This is two orders of magnitude better than the sensitivity reached by NV-centres [54] or quantum dots [53, 107, 108]. It competes with the best electro-mechanical resonators [109, 110] or single electron transistors [64, 66], which reach sensitivities in the order of $10^{-6}e/\sqrt{\text{Hz}}$ at distances in the μm range, corresponding to 1.4 mV/m/$\sqrt{\text{Hz}}$. The results are published in [111] and described in the PhD thesis of A. Facon [112].

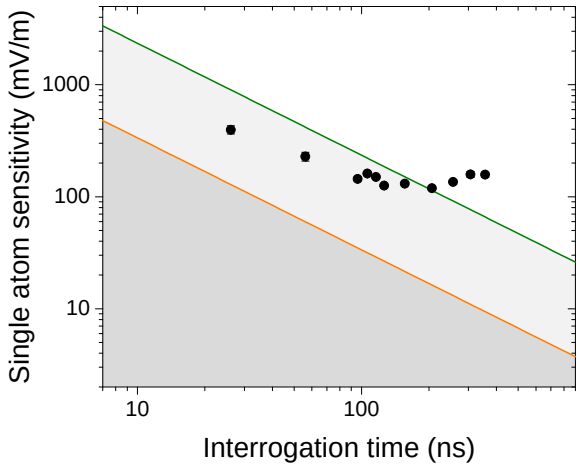

Figure 3: Single atom sensitivity of our electrometer as a function of the interrogation time compared to the standard quantum limit (green) and the Heisenberg limit (orange).

Improving the Schrödinger-cat-electrometer

This first experiment suffered from several limitations. The quantum phase accumulated by the atom and, therefore, the sensitivity depends on the latitude θ that is reached by the spin coherent state after the rotation on the Bloch sphere. Here, the static electric field applied to lift the degeneracy of the Rydberg manifold was very large ~500 V/m in order to limit the effect of stray electric fields perpendicular to the quantisation axis [112]. The amplitude of the radio-frequency drive was not large enough to compensate the effect of the second order Stark shift, which tends to make the energy ladder of the effective angular momentum anharmonic. As a result, the trajectory of the angular momentum barely exceeded the equator. In the experiment θ was limited to 102°. Furthermore, the inhomogeneity of the radio-frequency field caused a reduction of the visibility of the Ramsey interference, which further limited the sensitivity.

The first objective of this work was therefore to improve the performance of the electrometer to obtain a sensitivity as close as possible to the Heisenberg limit. Reducing the electric field gradient in the experiment allowed us to work at a lower electric field, decreasing the effect of the quadratic Stark shift. We also modified the experimental set-up in order improve not only the maximum power that can be applied, but also the homogeneity of the radio-frequency field seen by the Rydberg atom.

These technical upgrades of the experimental set-up lead to the creation of larger and thus more sensitive Schrödinger cat states of the Rydberg atom. We nearly reach an angle of $\theta = \pi$, only limited by the energy structure of the rubidium Rydberg atom. As a result, for small interrogation times, we now reach a sensitivity four times smaller than before, very close to the Heisenberg limit. This demonstrates that the Rydberg atom is a very sensitive, non-invasive microscopic electrometer. Combined with trapping techniques [113–116], it could be used to locally probe very small variations of the electric field or measure the surface charge of a test object [36, 107, 117–122].

Noise spectroscopy with the AC-electrometer

Up to here, we have assumed that the signals are static and deterministic. However, sensing a time-dependent signal is important for many applications, to measure the frequency spectrum of the electric field or to detect charge fluctuations in the vicinity of the atom. As it is, our electrometer acts as a sampling oscilloscope, able to detect variations of the electric field over a very short time interval (~100 ns), but with a very low (~3 kHz) repetition rate. It does not allow us to measure short time variations of a random signal. This is why we developed a method to use our electrometer to measure the correlation function of the electric field with a high bandwidth.

Measuring the correlation function provides a better characterization of the field noise seen by the electrometer, which is essential to implement better protocols to decouple the sensor from its environment. The reconstruction of the frequency spectrum can provide insights into external signals and intrinsic noise of the quantum sensor. Noise spectroscopy experiments usually reconstruct the spectrum of the noise by analysing the coherence decay of the quantum sensor. The contrast of standard Ramsey interferences, for instance, is sensitive to noise from DC to a frequency $1/t$ where t is the duration of the Ramsey sequence. A Hahn-echo sequence [123] has a sensitivity peaked at $f \sim 1/t$ [124] and gives access to the spectral density of the noise at this frequency. Multi-pulse sequences [125–128] allow for an even sharper frequency response and enable to sample noise spectra with a better frequency resolution [129–133].

In our case, we take advantage of the complex structure of the Rydberg manifold to implement a method that directly measures the noise correlation in the time domain. We combine σ^+ and σ^- polarized radio-frequency drives to make the accumulated quantum phase shift Φ sensitive only to the variation of the electric field amplitude at two different times.

Measuring short time correlations also opens the way to detect phenomena that are not synchronized with the experiment. This is especially important if we want to use the electrometer to probe the dynamics of mesoscopic physics devices. Measuring current fluctuations provides information about the dynamics and the interaction of the charge carriers that are complementary to that obtained by the measurement of the average current [134–137]. The development of high-bandwidth charge detectors [65, 138–141] that resolve individual electrons to access the full counting statistics [142–148] of tunnelling charges has thus received a large interest. In these experiments, the typical

dynamics occur on time scales between 0.5 μs and 1 ms and could be resolved by our electrometer.

Magnetometry employing Schrödinger cat states

The manipulation of the atom with a combination of σ^+ and σ^- polarized radio-frequency fields paves the way to the generation of more complex Schrödinger cat states. In particular, we investigate the experimental preparation of a superposition of circular levels with opposite magnetic quantum number m. This states is conceptually interesting as it corresponds to an electron rotating on the same orbit both clockwise and counter-clockwise. Moreover, this state has a high sensitivity to the magnetic field, while, for symmetry reasons, being protected from all electric field fluctuations.

However, its preparation involves an evolution through levels that are highly sensitive to variations of the electric field. The Rydberg electrometer can be used to characterize the electric field noise of the experiment, allowing us to implement basic dynamical decoupling [126, 149, 150] enabling the generation of the superposition of opposite circular states. The final state has a magnetic moment of ~100 μ_B, which is much larger than the magnetic moment of ions, atoms or NV-centres, making this superposition of great interest to measure fast variations of the magnetic field.

Outline of this work

Chapter 1 presents the Rydberg atom and provides the basis on how the state of the atom can be manipulated. The symmetry of the hydrogen atom allows to describe the Rydberg states in terms of two independent angular momenta that couple to orthogonal polarizations of the resonant radio-frequency field. Therefore, in the presence of a purely σ^+ polarized radio-frequency field, the atom can be described by a single effective angular momentum. The state of this angular momentum can be represented on a generalized Bloch sphere. Finally, the difference between the hydrogen model and the rubidium atom, used in our experiment, is discussed. We introduce the quantum defect which allows to describe the energy eigenvalues of the states of low angular momentum in the rubidium atom. We present numerical simulations of the latter which help us to understand the behaviour of the atomic states throughout this work.

Chapter 2 describes the experimental tools necessary to prepare, manipulate and detect the Rydberg atoms. In particular, we discuss the optimization of the well-defined polarization of the radio-frequency fields, as well as the control of the spatial inhomogeneity of the electric field, both crucial in our metrology experiments.

Chapter 3 introduces our electrometer. The metrological signal is obtained by creating a superposition of two very distinct states of the Rydberg atom. Our method relies on the great sensitivity of the relative quantum phase between the two components of the superposition due to their very different polarizabilities. We present that our single atom sensitivity is far beyond the standard quantum limit, close to the fundamental Heisenberg

limit. We discuss the sensitivity of the superposition to the electric field is ultimately limited by the electric field noise in the experiment.

Chapter 4 presents a method to measure the correlation function of the electric field noise by exploiting the richness of the Rydberg manifold structure. This allows us to characterize the correlation function of different applied artificial electric field noises as well as to recover asynchronous signals with a bandwidth of up to 5 MHz. Additionally, an adapted version of the Rydberg electrometer allows to measure the intrinsic electric field noise of the experimental set-up.

Chapter 5 shows the preparation of even larger quantum superpositions, this time of opposite circular states, extremely sensitive to variations in the magnetic field, while unaffected by the electric field noise. We describe the preparation scheme of this state and present its high sensitivity to the magnetic field.

Chapter 1

Rydberg atoms

The Rydberg atom is an atom with a valence electron that is excited in states with very high principal quantum numbers n [151]. These atoms exhibit small binding energies, long decay rates, a large electric dipole, and a high sensitivity to electric and magnetic fields. The electron wave-function is mostly located far from the nucleus. The valence electron therefore feels an hydrogen-like Coulomb potential from the ionic core, consisting of Z protons and $Z-1$ core electrons. The Rydberg atom can thus be described by the hydrogen model, which has the great advantage to be solvable analytically.[1] The effect of the ionic core in the case of alkali atoms, instead of hydrogen atoms, can be described as a correction to the hydrogen model.

In the first part of this chapter (Sec. 1.1) we discuss the description of the eigenstates of the hydrogen atom. A natural choice is the spherical coordinates (Sec. 1.1.1.a). However, in the presence of a static electric field, the spherical symmetry is broken and the parabolic basis becomes more appropriate to describe the atomic states (Sec. 1.1.2). We show that the hydrogen atom can be described in terms of two angular momenta (Sec. 1.1.4), which is convenient to describe the coupling of the atom to a resonant radio-frequency field (Sec. 1.1.6) and provides a description of semi-classical states as a product of spin coherent states (Sec. 1.1.7).

In the second part (Sec. 1.2) we discuss the rubidium atom. Here, the energy eigenvalues of the atom in the presence of a static electric field have to be calculated numerically (Sec 1.2.2) due to the quantum defect, which takes the spatial extension of the ionic core into account (Sec 1.2.1). Finally, the distinctions and similarities between the hydrogen and the rubidium atom are illustrated and explain why we can use the hydrogen-approach for Rydberg atoms for states with wave-functions located far from the nucleus (Sec 1.2.3).

[1] A Rydberg atom can also consist of two (or more) highly excited electrons with similar principal quantum numbers. In this work we restrict the description to alkali atoms. In the case where more than one electron is in an excited state, the hydrogen potential has to be corrected significantly by a term which takes the electron-electron interaction into account.

1.1 The Hydrogen atom

The appearance of Rydberg atoms was first demonstrated in 1885 when Johann Balmer discovered a mathematical description of the spectral line emissions of the hydrogen atom. In 1888, Johannes Rydberg generalized this description in his Rydberg formula [151]

$$\frac{1}{\lambda} = \mathrm{Ry}\left(\frac{1}{n_i^2} - \frac{1}{n_f^2}\right)$$

where λ is the wavelength of the emitted electromagnetic radiation, Ry is the Rydberg constant and n_i and n_f are integers greater or equal to 1.

The empirical Rydberg formula was known long before Niels Bohr's theory [152] in 1913 that describes the Rydberg formula as the energy of transitions, or quantum jumps, between the energy levels of different orbits. Bohr showed that the energy difference can be expressed in terms of the most fundamental constants of nature, including the electron's charge e, the electron mass m_e, Planck's constant h, and the vacuum permittivity ϵ_0, as

$$\Delta E = h\Delta\nu = -\frac{m_e}{2\hbar^2}\left(\frac{e}{4\pi\epsilon_0}\right)^2\left(\frac{1}{n_i^2} - \frac{1}{n_f^2}\right).$$

By comparison we find the Rydberg energy,

$$E_{\mathrm{Ry}} = hc\mathrm{Ry} = \frac{m_e}{2\hbar^2}\left(\frac{e}{4\pi\epsilon_0}\right)^2 \approx 13.6\mathrm{eV}. \tag{1.1}$$

Finally, in 1926, Schrödinger introduced the Schrödinger equation [153] providing a fully quantum mechanical description of the hydrogen atom, which predicts that wave-functions of the electron can form standing waves, or stationary states, also called atomic orbitals, which are a solution of the time-independent Schrödinger equation,

$$\hat{H}\Psi = E\Psi, \tag{1.2}$$

where $\hat{H}$ is the Hamiltonian operator acting on a wave-function Ψ, and E the energy of the state Ψ.

The hydrogen atom consists of a single positively charged proton, the nucleus, and a single negatively charged electron. Electron and proton are bound together by the Coulomb force.

The Hamiltonian of the electron is

$$\hat{H}_0 = \frac{\hat{\boldsymbol{p}}^2}{2m_e} + \hat{V}(\hat{\boldsymbol{r}}), \tag{1.3}$$

with the potential $\hat{V}(\hat{\boldsymbol{r}})$ that describes the Coulomb interaction between electron and

proton, and with $\hat{\boldsymbol{p}}^2/2m_e$ being the kinetic energy, where $\hat{\boldsymbol{p}}$ is the momentum of the electron. The proton is assumed to be motionless due to the mass ratio between electron and proton. In principle, we have to take into account the reduced mass instead of the electron mass, $\mu = (m_e m_p)/(m_e + m_p)$, as well as, the relative momentum operator $\hat{\boldsymbol{p}} = \mu\left(\hat{\boldsymbol{p}}_e/m_e + \hat{\boldsymbol{p}}_p/m_p\right)$. However, due to the mass ratio between electron and proton we neglect the motion of the heavy proton.

The Schrödinger equation (Eq. 1.2) can be solved by choosing a set of coordinates to get the analytical expression of the wave-function.

1.1.1 Wave-function of the hydrogen atom

1.1.1.a Spherical basis

Since the Coulomb potential $\hat{V}(\hat{\boldsymbol{r}}) = \hat{V}(\hat{r})$ is a central potential, depending only on the distance $\hat{r}$ between electron and proton, the angular momentum operator $\hat{\boldsymbol{L}}$ is conserved.

The Schrödinger equation of the hydrogen atom is usually solved by employing the spherical coordinates (r, θ, ϕ). This choice seems natural due to the spherical symmetry of the Coulomb potential. Since $\hat{\boldsymbol{L}}$ commutes with the Hamiltonian, we look for wave-functions written as

$$\psi(\boldsymbol{r}) = R(r)\, Y_l^m(\theta, \phi), \tag{1.4}$$

product of a radial part $R(r)$ and the spherical harmonics $Y_l^m(\theta, \phi)$ with angular quantum number l and magnetic quantum number m. The Schrödinger equation thus becomes a one-dimensional radial differential equation

$$\left(-\frac{\hbar^2}{2m_e r}\frac{\partial^2}{\partial r^2} r + \frac{l(l+1)\hbar^2}{2m_e r^2} - \frac{e^2}{4\pi\epsilon_0 r}\right) R(r) = E R(r), \tag{1.5}$$

where the first term describes the kinetic energy and the two remaining terms act as an effective potential, which contains a centrifugal part $\propto r^{-2}$ and the attractive Coulomb potential $\propto r^{-1}$.

The eigenfunctions $R_{nl}(r)$ of the radial Schrödinger equation in Eq. 1.5 are given by the Laguerre polynomials. The eigenstates of the system can therefore be fully described by the quantum numbers n, l, and m and can be written as $|n, l, m\rangle$ (or $|n, l, m, m_s\rangle$ with $m_s = \pm 1/2$ when considering the electron spin s). The energy eigenvalues follow from the solution of the radial equation and are given by the Bohr formula,

$$E_n = -\frac{E_{\mathrm{Ry}}}{n^2}, \tag{1.6}$$

where E_{Ry} is the Rydberg energy (Eq. 1.1) leading to the ground state energy of the hydrogen atom $E_1 \approx -13.6$ eV. We restrict ourselves to bound states throughout this work. The energy eigenvalues are independent of l and m leading to an n^2-fold degeneracy of

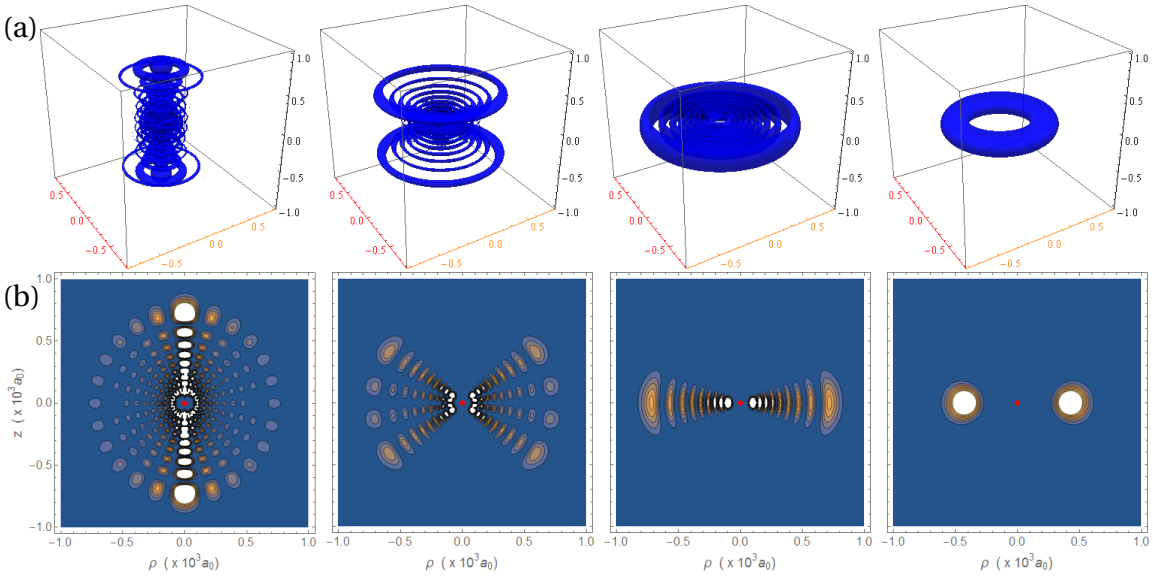

Figure 1.1: Wave functions of some spherical states of the hydrogen atom for $n = 21$: (from left to right) $|n,l,m\rangle = |21,12,0\rangle$, $|n,l,m\rangle = |21,12,9\rangle$, $|n,l,m\rangle = |21,12,12\rangle$, and $|n,l,m\rangle = |21,20,20\rangle$. (a) The wave-functions in three dimensions are represented with the quantization axis (Oz) in the vertical z-direction. The units of the axis are $10^3 a_0$. The represented surface corresponds to a probability density of $1.5 \cdot 10^{-9} a_0^{-3}$. (b) The projection of the wave-function in the ($zO\rho$) plane, where ρ is the radius in cylindrical coordinates (ρ,ϕ,z) in real space. The colors vary from 0 (blue background) to $5 \cdot 10^{-9} a_0^{-3}$ (white). The probability density $|\psi|^2$ does not depend on ϕ, since the latter only shows up in a term $e^{im\phi}$. The pictures are taken from [154].

the levels.

Fig. 1.1 shows the probability density of some of the spherical orbitals. We can clearly observe the symmetry with respect to the $x = 0$, $y = 0$ and $z = 0$ planes. As a result the expectation value of the dipole operator $\hat{\boldsymbol{d}} = q\hat{\boldsymbol{r}}$ for any state $|n,l,m\rangle$ is zero.

1.1.1.b Parabolic basis

In a static electric field the spherical symmetry is broken and it is useful to work in the parabolic basis. The relationship between the parabolic coordinates (ξ,η,ϕ) and the Cartesian coordinates is given by

$$\begin{aligned} x &= \sqrt{\xi\eta}\cos(\phi), \\ y &= \sqrt{\xi\eta}\sin(\phi), \\ z &= \tfrac{1}{2}(\xi-\eta), \end{aligned} \quad \leftrightarrow \quad \begin{aligned} \xi &= r+z = r(1+\cos(\theta)), \\ \eta &= r-z = r(1-\cos(\theta)), \\ \phi &= \tan(y/x). \end{aligned} \tag{1.7}$$

where $r = \frac{1}{2}(\xi+\eta)$ and $r = (x^2+y^2+z^2)^{1/2}$. The azimuthal angle ϕ is defined as in the spherical coordinates, reflecting the cylindrical symmetry, which is not broken by a static electric field in z-direction. Surfaces with a constant value of ξ or η correspond to rotational paraboloids around the z-axis with their focus point at the origin of the

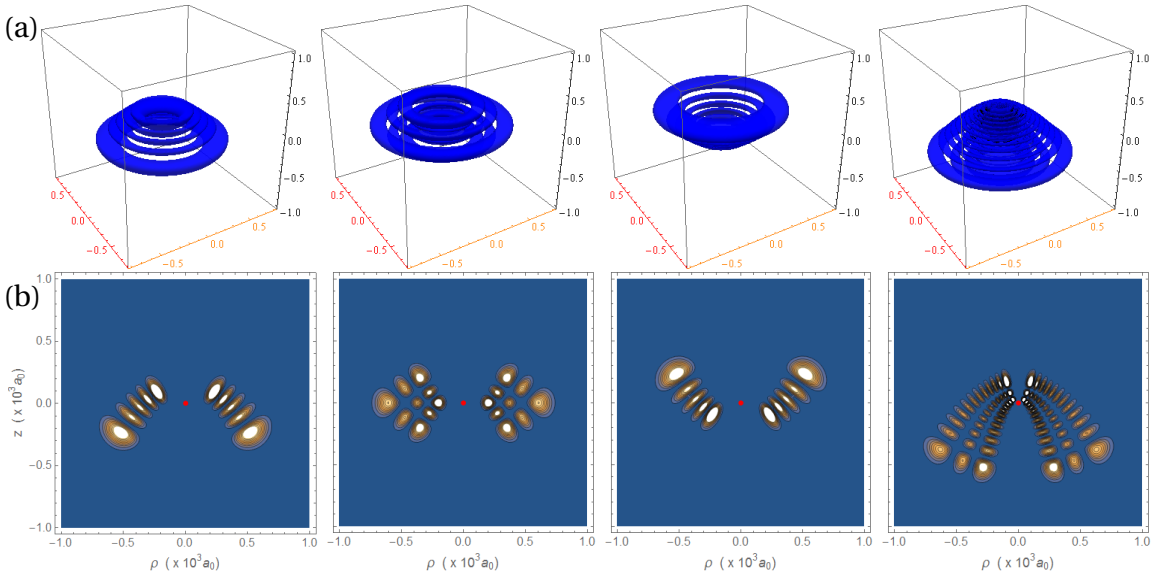

Figure 1.2: Wave functions of some parabolic states of the hydrogen atom for $n = 21$: (from left to right) $|n_1, n_2, m\rangle = |0, 4, 16\rangle$, $|n_1, n_2, m\rangle = |2, 2, 16\rangle$, $|n_1, n_2, m\rangle = |4, 0, 16\rangle$ and $|n_1, n_2, m\rangle = |2, 10, 7\rangle$. The wave-functions are represented with the same characteristics as in Fig. 1.1. The first three examples show the influence of the parabolic quantum number n_1 at a constant magnetic quantum number m. The last example shows the influence of m. The pictures are taken from [154].

Cartesian coordinate system.

The Schrödinger equation can also be separated in parabolic coordinates. Because of the cylindrical symmetry, $\hat{L}_z$ commutes with the Hamiltonian and we look for solutions which are also eigenstates of $\hat{L}_z$, of the form,

$$\psi(\boldsymbol{r}) = u_1(\xi)\, u_2(\eta)\, e^{im\phi}. \tag{1.8}$$

As a result we obtain two differential equations for ξ and η that can be solved by introducing two new quantum numbers, the parabolic quantum numbers n_1 and n_2 which are non-negative integers and fulfil

$$n = n_1 + n_2 + |m| + 1.$$

From this condition we infer that n_1 and n_2 take values between 0 and $n - |m| - 1$.

The two parts in the wave-function (Eq. 1.8) correspond to the respective parabolic quantum numbers, $u_1(\xi) = u_{n_1,m}(\xi)$ and $u_2(\eta) = u_{n_2,m}(\eta)$. The parabolic states are fully described by $|n_1, n_2, m\rangle$ (or $|n_1, n_2, m, m_s\rangle$ when considering the spin[2]). In some situations it might be more convenient to use the notation $|n, n_1, m\rangle$, $|n, n_2, m\rangle$ or $|n, n_1, n_2, m\rangle$.

In Fig. 1.2 the probability density of some of the parabolic orbitals are shown. In contrast to the spherical wave-functions, the parabolic ones are asymmetric with respect

[2]We omit the spin most of the time, since the electromagnetic radiation we consider throughout this work does not change the spin, and the spin state does not change the transition frequency.

to the $z = 0$-plane, leading to a non-zero expectation value of the dipole operator. For a given m, the dipole moment of the orbital varies by changing the parabolic quantum number n_1 (and by consequent n_2). Exchanging the values of n_1 and n_2 corresponds to a symmetry with respect to the horizontal plane.

The parabolic quantum numbers determine the degree of the Laguerre polynomial and the shape of the orbital. The parabolic eigenstates are linear superpositions of spherical eigenstates and vice versa. There are only two states that are identical in both bases, $|n_1 = 0, n_2 = 0, m = \pm m_{\max}\rangle = |n, l = n-1, m = \pm m_{\max}\rangle$. Due to their torus-like wave-function these states are called *circular* Rydberg states. The wave-function of these states is shown in the fourth column in Fig. 1.1. Theses states correspond to semi-classical states for which the wave-function is localized around classical Bohr orbits.

1.1.2 The hydrogen atom in the presence of an electric field

In the presence of an external static electric field $\boldsymbol{F} = F\boldsymbol{u}_z$, the Hamiltonian can be written as

$$\hat{H} = \hat{H}_0 + \hat{V}_{\mathrm{DC}},$$

where the first term represents the free hydrogen Hamiltonian (Eq. 1.3) and the second term the additional potential due to the static electric field,

$$\hat{V}_{\mathrm{DC}} = -\hat{\boldsymbol{d}} \cdot \boldsymbol{F}_{\mathrm{DC}} = -q\hat{\boldsymbol{r}} \cdot \boldsymbol{F}_{\mathrm{DC}} = e\hat{z}F, \tag{1.9}$$

breaking the spherical symmetry. The cylindrical symmetry around the field axis, however, remains and the magnetic quantum number m is still a good quantum number.

The potential $\hat{V}_{\mathrm{DC}}$ leads to a shift in the energy eigenvalues which is called the **Stark shift**. An analytical solution to this problem has not been found a yet, but it is possible to calculate the energy eigenvalues with very high precision using perturbation theory [155–157].

The first order energy correction, or the **first order Stark shift**, can be calculated by diagonalizing $\hat{z}$ in the restriction of a given manifold of principal quantum number n [158]. In principle we can use any of the bases presented before, but since we can express $z = \frac{1}{2}(\xi - \eta)$, the Schrödinger equation remains separable in parabolic coordinates in the presence of the electric field, making the parabolic basis the appropriate choice. Knowing the analytical expressions of $u_{n_2,m}(\eta)$ and $u_{n_1,m}(\xi)$, one can compute

$$\langle n_1, n_2, m|\hat{z}|n_1', n_2', m'\rangle = \int u^*_{n_1,m}(\xi)\, u^*_{n_2,m}(\eta) \left[\frac{1}{2}(\xi - \eta)\right] u_{n_1',m'}(\xi)\, u_{n_2',m'}(\eta)\, e^{i(m\phi - m'\phi)}\, d^3r.$$

We find that $\hat{z}$ is diagonal in the $|n_1, n_2, m\rangle$-basis with the matrix elements

$$\langle n_1, n_2, m|\hat{z}|n_1', n_2', m'\rangle = \frac{3}{2} a_0 n(n_1 - n_2)\delta_{n_1 n_1'}\delta_{n_2 n_2'}\delta_{mm'}, \tag{1.10}$$

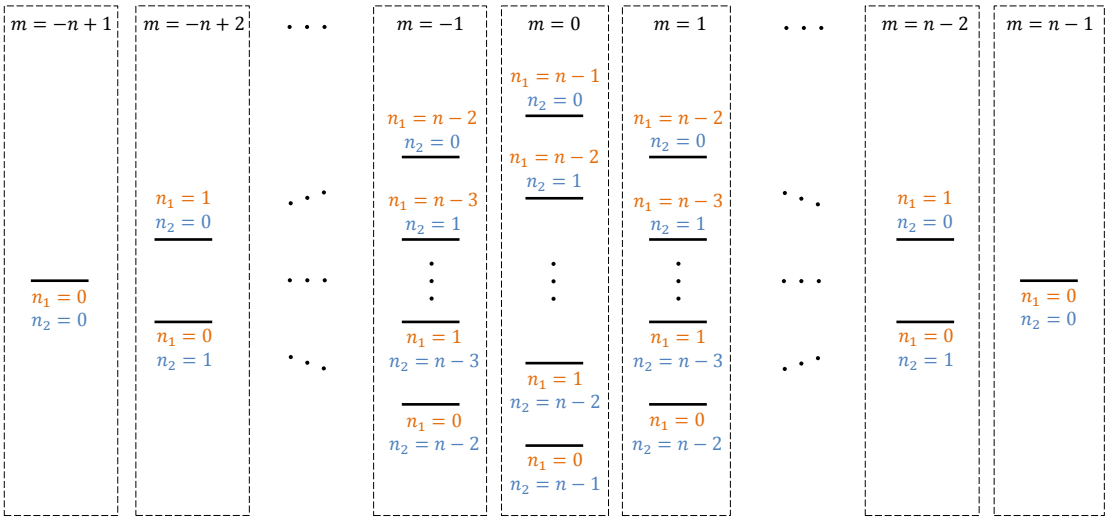

Figure 1.3: Energy levels of the hydrogen atom in a static electric field F are shifted from their zero-field energy E_n. For each value of the magnetic quantum number m, the respective $n-|m|$ levels split into equidistant vertical ladders, called m-ladders. In this sketch, the levels are sorted by their energy for each value of m and are labelled with the parabolic quantum numbers n_1 (orange) and n_2 (blue).

where a_0 is the Bohr radius. The new eigenstates remain the parabolic states and the new energy eigenvalues can be written as

$$E = E_n + E_n^{(1)}, \quad \text{with} \quad E_n^{(1)} = \frac{3}{2} e a_0 n (n_1 - n_2) F, \tag{1.11}$$

where E_n are the unperturbed energy eigenvalues given by Bohr's formula (Eq. 1.6), and $E_n^{(1)}$ the first order Stark shift. The linear Stark shift, proportional to n and to the applied electric field strength F, partially lifts the degeneracy of the n^2 levels of the n-manifold. However, the degeneracy of levels with same $(n_1 - n_2)$ value remains. For each value of m, the states split into equidistant ladders of $n-|m|$ states, also called m-ladders, which are distributed symmetrically with respect to the unperturbed energy E_n. In Fig. 1.3, the energy eigenvalues of the eigenstates $|n_1, n_2, m\rangle$ are sketched over the respective magnetic quantum number m.

The second order energy correction, or **second order Stark shift**, is given by [159]

$$E_n^{(2)} = \sum_{n' \neq n, n_1', m'} \frac{|\langle n', n_1', m'| \hat{V}_{\mathrm{DC}} |n, n_1, m\rangle|^2}{E_n - E_{n'}}. \tag{1.12}$$

Note that the $\hat{z}$ commutes with $\hat{L}_z$ so we can restrict this sum to $m' = m$. Once no longer restricted to a given manifold, the operator $\hat{z}$ is no longer diagonal in the parabolic basis. The parabolic states are therefore no longer the eigenstates. However, we continue to use the parabolic quantum numbers to label the states, keeping in mind that their wave-functions are no longer fully described by Eq. 1.8.

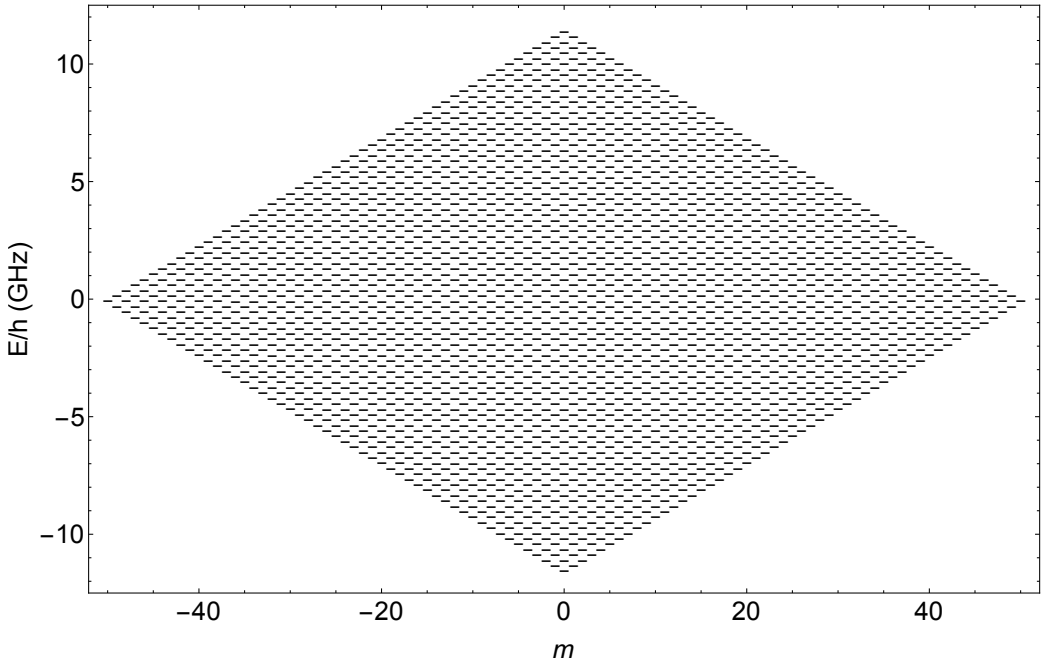

Figure 1.4: Analytical calculation of the energy levels of the hydrogen atom with $n = 51$ in an electric field $F = 234.5$ V/m taking into account the first and second order Stark effect. The chosen reference energy is E_n for $n = 51$ (Eq.1.6)

The second order Stark effect can be interpreted as a polarisation of the atom by the electric field leading to an induced dipole $\delta \boldsymbol{d}$ whose amplitude is proportional to the electric field amplitude F. The interaction of this dipole with the electric field $-\delta \boldsymbol{d} \cdot \boldsymbol{F}$ results in an energy shift proportional to F^2.

The quadratic Stark shift is given by [159, 160]

$$E_n^{(2)} = -\frac{1}{32}\frac{(ea_0F)^2}{E_{\mathrm{Ry}}} n^4 (17n^2 - 3(n_1 - n_2)^2 - 9m^2 + 19), \tag{1.13}$$

with E_{Ry} the ground state energy of the hydrogen atom (Eq. 1.1). The second order correction depends on the magnetic quantum number m (which is not the case for the first order correction) but is independent of its sign. The term $(n_1 - n_2)^2$ leads to a shift independent of the orientation of the orbital. Only levels with identical quantum numbers n_1 and n_2 and opposite values of m remain degenerate.

In Fig. 1.4 the energy eigenvalues with $n = 51$ of the hydrogen atom are shown in a static electric field of $F = 234.5$ V/m, sorted by their magnetic quantum number m. The energy eigenvalues are calculated analytically taking into account the linear and quadratic Stark shift. The chosen reference energy is E_n for $n = 51$ (Eq.1.6). The predominant linear Stark effect leads to an almost equidistant energy difference for each vertical m-ladder. However, we notice that even states with $n_1 - n_2 = 0$, for example the two circular states at the extreme right and left of the level structure, are slightly shifted away from the reference energy E_n.

In a static electric field of $F = 234.5$ V/m, used in Fig. 1.4, the linear Stark shift in the $n = 51$ manifold is of about $\omega_{at}/2\pi$ =230 MHz between all adjacent levels. Higher order Stark shifts remain small energy corrections as compared to the linear Stark shift. In the same static electric field, the quadratic Stark shift of the transition between the circular state $|51c\rangle = |n = 51, n_1 = n_2 = 0, m = 50\rangle$ and its two elliptical neighbours, $|51e1\rangle = |n = 51, n_1 = 0, n_2 = 1, m = 49\rangle$ and $|51e1'\rangle = |n = 51, n_1 = 1, n_2 = 0, m = 49\rangle$, are no longer degenerate since they are shifted by ±0.5 MHz away from the linear Stark shift of 230 MHz.

The notation $|51c\rangle$ for the circular state (with $m > 0$) and $|51ex\rangle$, $x = n_2$ for the elliptical states on the lowest diagonal with $n_1 = 0$, or $m_2 = j_2$, is used throughout this thesis. The first elliptical state $|n = 51, n_1 = 0, n_2 = 1, m = 49\rangle$ is called $|51e1\rangle$, the second one $|n = 51, n_1 = 0, n_2 = 2, m = 48\rangle$ is called $|51e2\rangle$, and so forth.

1.1.3 The hydrogen atom in the presence of a magnetic field

The presence of a magnetic field $\boldsymbol{B}$ shifts the energy of the atomic states due to the interaction between the applied magnetic field and the magnetic moment of the atom. The total Hamiltonian of the atom in a magnetic field is

$$\hat{H_M} = \hat{H}_0 + \hat{V}_M$$

where $\hat{V}_M$ is the perturbation due to the B-field. The latter can be expressed as

$$\hat{V}_M = -\hat{\boldsymbol{\mu}} \cdot \boldsymbol{B}, \quad \text{with} \quad \hat{\boldsymbol{\mu}} = -\frac{\mu_B}{\hbar}\left(g_L \hat{\boldsymbol{L}} + g_S \hat{\boldsymbol{S}}\right),$$

with $\hat{\boldsymbol{\mu}}$ being the magnetic moment of the atom which contains the Bohr magneton $\mu_B = \frac{e\hbar}{2m_e}$, the orbit angular momentum $\hat{\boldsymbol{L}}$ and the spin angular momentum $\hat{\boldsymbol{S}}$, each multiplied by the appropriate gyromagnetic ratio, $g_L = 1$ and $g_S \approx 2$. The expression of $\hat{V}_M$ can be simplified by taking into account that the applied magnetic field $\boldsymbol{B} = B\boldsymbol{u}_z$ is along the z-direction:

$$\hat{V}_M = \frac{\mu_B B}{\hbar}\left(g_L \hat{L}_z + g_S \hat{S}_z\right).$$

In the case of an unperturbed Hamiltonian $\hat{H}_0$, the magnetic quantum number m and the spin quantum number m_s are good quantum numbers and the eigenstates are the $|n_1, n_2, m, m_s = \pm 1/2\rangle$ states.

In the presence of the magnetic field, the energy of the state $|n, n_1, m, m_s\rangle$ are shifted

by[3]

$$E_M = \langle n_1, n_2, m, m_s | \hat{V}_M | n_1, n_2, m, m_s \rangle = \mu_B B(g_L m + g_S m_s),$$

with, in particular, the relative energy shift of two levels with m and m' and same spin quantum number m_s as

$$\Delta E_M = \mu_B B g_L (m - m').$$

For a transition with Δm the shift in frequency is

$$\Delta \nu_M = \frac{g_L \mu_B B}{h} \Delta m \tag{1.14}$$

with $g_L \mu_B / h \approx 1.4$ MHz/G.

1.1.4 The Runge-Lenz vector

It is also possible to solve the Schrödinger equation inside a given manifold using only algebraic arguments based on the symmetry of the Coulomb problem [161]. This is an alternative method to find the parabolic basis, but it provides a more insightful description of the parabolic states.

In classical mechanics, the Runge-Lenz vector is a constant of motion and was initially defined for planetary orbits. In the case of a $1/r$ potential, the Runge-Lenz vector $\boldsymbol{A}$ lies in the plane of motion and points from the focus to the perihelion (the nearest point of the orbit to its focus).

In quantum mechanics, the Runge-Lenz vector is associated to an operator $\hat{\boldsymbol{A}}$ defined by

$$\hat{\boldsymbol{A}} = \frac{1}{2}\left(\hat{\boldsymbol{p}} \times \hat{\boldsymbol{L}} - \hat{\boldsymbol{L}} \times \hat{\boldsymbol{p}}\right) - m_e \kappa \frac{\boldsymbol{r}}{r},$$

with $\kappa = e^2/4\pi\epsilon_0$ for the Coulomb force. Already in 1926, Pauli obtained the energy of the bound states of the hydrogen atom algebraically by making use of the Lie algebra generated by the conserved quantities of the orbital angular momentum operator $\hat{\boldsymbol{L}}$ and the Runge-Lenz operator $\hat{\boldsymbol{A}}$ [153].

Inside a given manifold with principal quantum number n and energy eigenvalue $E_n <$

[3] In principle, for small electric fields, where states with $|n_1, n_2, m, m_s = +1/2\rangle$ and $|n_1, n_2, m+1, m_s = -1/2\rangle$ are degenerate, we also have to take into account the spin orbit coupling, expressed as an additional term $\hat{V}_{LS} \propto \hat{\boldsymbol{L}} \cdot \hat{\boldsymbol{S}}$ in the Hamiltonian. This leads to the fact that m and m_s are no longer good quantum numbers and the above mentioned eigenstates are not eigenstates of the Hamiltonian $\hat{H}_0 + \hat{V}_M + \hat{V}_{LS}$, but rather the states $|n, l, j, m_j\rangle$ where $\hat{\boldsymbol{J}} = \hat{\boldsymbol{L}} + \hat{\boldsymbol{S}}$. However, in practice, we always work in a large enough electric field so that the states mentioned before are not degenerate. In this case, m and m_s remain good quantum numbers and the term $\hat{V}_{LS}$ introduces at most a slight shift of the energy levels. The eigenstates $|n, n_1, m, m_s\rangle$ therefore remain the eigenstates of the Hamiltonian $\hat{H}_0 + \hat{V}_M + \hat{V}_{LS} + \hat{V}_{\mathrm{DC}}$ and the simplified description in the main text holds.

0, the Runge-Lenz operator can be normalized. The normalized Runge-Lenz operator $\hat{\boldsymbol{a}} = \hat{\boldsymbol{A}}/\sqrt{-2m_eE_n}$ has the same dimension as $\hat{\boldsymbol{L}}$. We can introduce two new angular momentum operators [158],[4]

$$\hat{\boldsymbol{J}}_1 = \frac{1}{2}\left(\hat{\boldsymbol{L}} - \hat{\boldsymbol{a}}\right) \quad \text{and} \quad \hat{\boldsymbol{J}}_2 = \frac{1}{2}\left(\hat{\boldsymbol{L}} + \hat{\boldsymbol{a}}\right). \tag{1.15}$$

The eigenvalues of $\hat{\boldsymbol{J}}_1^2$ and $\hat{\boldsymbol{J}}_2^2$ are of the form $j_1(j_1+1)\hbar^2$ and $j_2(j_2+1)\hbar^2$, with $j_1 = j_2 = (n-1)/2 \equiv j$ being integers or half-integers.

The new angular momentum operators $\hat{\boldsymbol{J}}_1$ and $\hat{\boldsymbol{J}}_2$ commute and are therefore two independent angular momenta. Inside a given n-manifold $\hat{\boldsymbol{J}}_1^2$, $\hat{J}_{1z}$, $\hat{\boldsymbol{J}}_2^2$, and $\hat{J}_{2z}$ form a complete set of commuting observables where $\hat{\boldsymbol{J}}_1^2$ and $\hat{\boldsymbol{J}}_2^2$ are constant. The hydrogen levels can be represented as the states $|j_1, m_1, j_2, m_2\rangle$ where $m_1\hbar$ are the eigenvalues of $\hat{J}_{1z}$ and $m_2\hbar$ the eigenvalues of $\hat{J}_{2z}$.[5] We can formally write

$$|j_1, m_1, j_2, m_2\rangle = |j_1, m_1\rangle \otimes |j_2, m_2\rangle .$$

1.1.4.a Connection of the Runge-Lenz basis to the parabolic basis

From the definition of the two new angular momenta $\hat{\boldsymbol{J}}_1$ and $\hat{\boldsymbol{J}}_2$ (Eq. 1.15) we find that

$$\hat{L}_z = \hat{J}_{1z} + \hat{J}_{2z} \quad \text{and} \quad \hat{a}_z = \hat{J}_{2z} - \hat{J}_{1z}.$$

Therefore,

$$\hat{L}_z |j_1, m_1, j_2, m_2\rangle = \hbar(m_1 + m_2) |j_1, m_1, j_2, m_2\rangle$$
$$\hat{a}_z |j_1, m_1, j_2, m_2\rangle = \hbar(m_2 - m_1) |j_1, m_1, j_2, m_2\rangle .$$

The action of $\hat{L}_z$ in the parabolic basis is already known,

$$\hat{L}_z |n_1, n_2, m\rangle = \hbar m |n_1, n_2, m\rangle .$$

To calculate the action of $\hat{a}_z$ on the parabolic basis, we use the Pauli replacement, a link introduced by Pauli [161] between the position operator $\hat{\boldsymbol{r}}$ and the Runge-Lenz operator $\hat{\boldsymbol{a}}$ [158, 160],

$$\hat{\boldsymbol{r}} = -\frac{3}{2}\frac{a_0 n}{\hbar}\hat{\boldsymbol{a}}. \tag{1.16}$$

Then Eq. 1.10 becomes

$$\hat{a}_z |n_1, n_2, m\rangle = \hbar(n_2 - n_1) |n_1, n_2, m\rangle .$$

Since $\hat{L}_z$ and $\hat{a}_z$ are linear combinations of $\hat{J}_{1z}$ and $\hat{J}_{2z}$, they also form a complete set

[4] Please note that the definitions of $\hat{\boldsymbol{J}}_1$ and $\hat{\boldsymbol{J}}_2$ are slightly different in Englefield [158].

[5] Since $j_1 = j_2 = (n-1)/2 \equiv j$, the eigenstates can also be expressed as $|j, m_1, j, m_2\rangle$. Both notations are used throughout this work.

of commuting observables inside a given manifold. We can thus identify $|n_1, n_2, m\rangle = |j_1, m_1, j_2, m_2\rangle$ with $n_1 = j - m_2$ and $n_2 = j - m_1$ for $m \geq 0$, and $n_1 = j - m_1$ and $n_1 = j - m_2$ for $m \leq 0$ where $j = j_1 = j_2 = (n-1)/2$.[6]

1.1.4.b Connection of the Runge-Lenz basis to the spherical basis

This description also provides an easy way to connect the spherical basis and the parabolic basis. To express the eigenstates of the spherical basis $|n, l, m\rangle$ as a function of the eigenstates of the Runge-Lenz basis $|j_1, m_1, j_2, m_2\rangle$, we use that inside a given manifold with principal quantum number n, the two new angular momenta operators $\hat{\boldsymbol{J}}_1$ and $\hat{\boldsymbol{J}}_2$ can be composed to the orbital angular momentum $\hat{\boldsymbol{L}} = \hat{\boldsymbol{J}}_1 + \hat{\boldsymbol{J}}_2$. In the spherical basis, $|n, l, m\rangle$ can formally be written as $|j_1, j_2, l, m\rangle$. Using the rules for addition of angular momenta, the eigenstates $|n, l, m\rangle$ and the eigenstates $|j_1, m_1, j_2, m_2\rangle$ are connected through the Clebsch-Gordan coefficients $\langle j_1, m_1, j_2, m_2 | j_1, j_2, l, m\rangle$ by

$$|n, l, m\rangle = \sum_{m_1, m_2} |j_1, m_1, j_2, m_2\rangle \langle j_1, m_1, j_2, m_2 | j_1, j_2, l, m\rangle . \tag{1.17}$$

1.1.5 Stark shift in the Runge-Lenz basis

The Stark shift due to the presence of a static electric field can also be expressed in terms of the operators $\hat{\boldsymbol{J}}_1$ and $\hat{\boldsymbol{J}}_2$ since we have identified $|n_1, n_2, m\rangle$ and $|j_1, m_1, j_2, m_2\rangle$. The first order Stark shift (Eq. 1.11) is found by diagonalizing $\hat{V}_{\mathrm{DC}}$, proportional to the position operator $\hat{z}$, in the parabolic basis. We can just as well diagonalize $\hat{V}_{\mathrm{DC}}$ in the Runge-Lenz basis using the Pauli replacement.

The perturbation $\hat{V}_{\mathrm{DC}}$ restricted to the n-manifold, can be expressed as

$$\hat{V}^{(1)}_{\mathrm{DC}} = \hbar \omega_{\mathrm{at}} (\hat{J}_{1z} - \hat{J}_{2z}), \tag{1.18}$$

with the frequency

$$\omega_{\mathrm{at}}(F) = \frac{3}{2} \frac{e a_0 n}{\hbar} F. \tag{1.19}$$

This Hamiltonian describes the energy of two angular momenta of frequencies $+\omega_{\mathrm{at}}$ and $-\omega_{\mathrm{at}}$. Even in the presence of an electric field, the system can be described as two independent angular momenta. The Stark energy shift can be separated as

$$E^{(1)}(|j_1, m_1, j_2, m_2\rangle) = E(|j_1, m_1\rangle) + E(|j_2, m_2\rangle).$$

In Fig. 1.5, the energy eigenvalues of the eigenstates $|j_1, m_1, j_2, m_2\rangle$ (with $j_1 = j_2 = j$)

[6] By comparing the eigenvalues of the orbital angular momentum $\hat{L}_z$ and the eigenvalues of the normalized Runge-Lenz operator $\hat{a}_z$, we find $m = m_1 + m_2$ and $n_2 - n_1 = m_2 - m_1$. Together with the relation of the parabolic quantum numbers with the principal quantum number, $n = n_1 + n_2 + |m| + 1$, we can calculated the above equivalences.

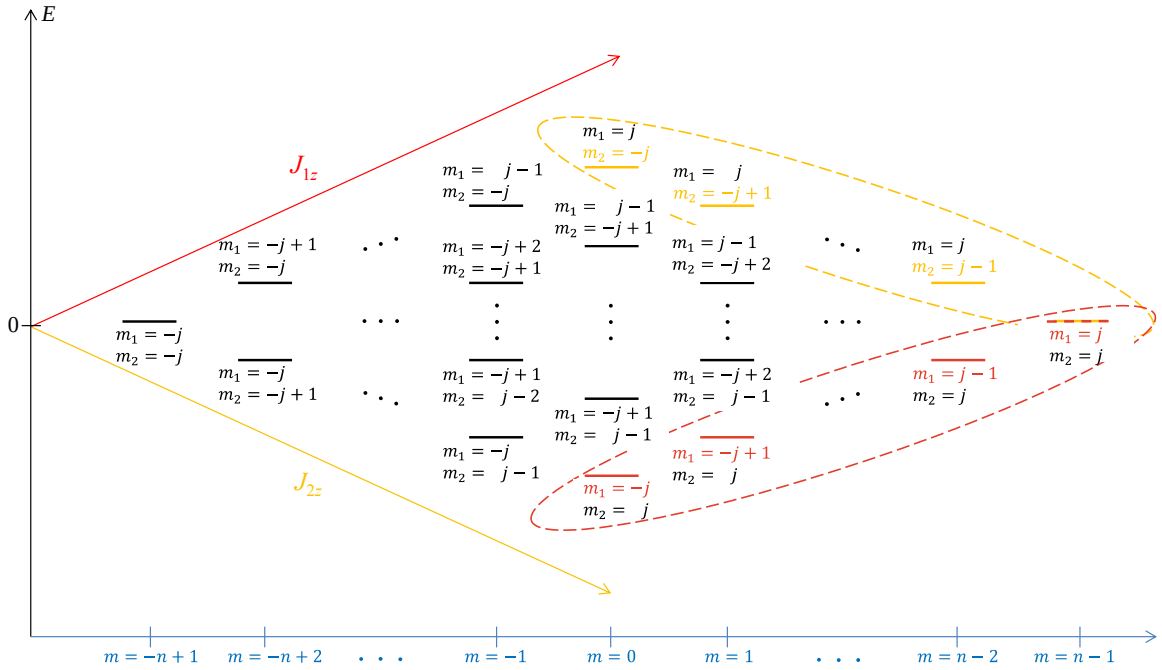

Figure 1.5: Energy levels of the hydrogen atom in a static electric field F are shifted from their zero-field energy E_n. For each value of the magnetic quantum number m, the respective $n-|m|$ levels split into equidistant vertical ladders, as in Fig. 1.3. In this sketch, the levels are labelled with the eigenvalues of $\hat{J}_{1z}$ (in red) and $\hat{J}_{2z}$ (in yellow) being m_1 and m_2.

are sketched over the respective magnetic quantum number m. The states are labelled by the quantum numbers m_1 and m_2. Levels of same m_1 form diagonal ladders along the direction of $\hat{J}_{2z}$, levels of same m_2 form diagonal ladders along the direction of $\hat{J}_{1z}$. The two diagonal ladders that intercept at the circular state with $|j_1, m_1 = j_1, j_2, m_2 = j_2\rangle$ at $m = m_{\max} = n-1$ are highlighted. The only difference between Figs. 1.5 and 1.3 is the labelling of the levels.

To calculate the second order Stark shift in terms of $\hat{\boldsymbol{J}}_1$ and $\hat{\boldsymbol{J}}_2$, one can replace $n_1 - n_2$ by $m_1 - m_2$ and m by $m_1 + m_2$ in Eq. 1.13 to find

$$E^{(2)}(|j_1, m_1, j_2, m_2\rangle) = -\frac{1}{72}\frac{(\hbar\omega_{\text{at}})^2}{E_{Ry}} n^2 \left(19 + 17n^2 - 12(m_1^2 + m_2^2 + m_1 m_2)\right),$$

Due to coupling to states of manifolds with $n' \neq n$, the two angular momenta $\hat{\boldsymbol{J}}_1$ and $\hat{\boldsymbol{J}}_2$ are not independent any more and the energy eigenvalue of the state $|j_1, m_1, j_2, m_2\rangle$ cannot be written as the sum $E(|j_1, m_1\rangle) + E(|j_2, m_2\rangle)$. The second order perturbation term in the Hamiltonian can be written as

$$\hat{V}_{\text{DC}}^{(2)} = -\frac{1}{72}\frac{\omega_{\text{at}}^2}{E_{Ry}} n^2 \left((19 + 17n^2)\mathbb{1} - 12(\hat{J}_{1z}^2 + \hat{J}_{2z}^2 + \hat{J}_{1z}\hat{J}_{2z})\right), \tag{1.20}$$

where the terms proportional to $\hat{J}_{1z}^2$ and $\hat{J}_{2z}^2$ can be interpreted as self-Kerr effects and the term proportional to $\hat{J}_{1z}\hat{J}_{2z}$ as a cross-Kerr effect.

In a qualitative description of the hydrogen atom in the following sections, we restrict the Stark shift to a purely linear one.

1.1.6 Coupling Hamiltonian

The eigenstates of the manifold of principal quantum number n of the hydrogen atom in the presence of a static electric F can be described as a product states of the eigenstates $|j_1, m_1\rangle$ and $|j_2, m_2\rangle$ of two angular momenta $\hat{\boldsymbol{J}}_1$ and $\hat{\boldsymbol{J}}_2$ (Sec. 1.1.4). The energy of the eigenstates plotted as a function of the magnetic quantum number m (see Fig. 1.4) form sets of parallel diagonal ladders separated by $\hbar\omega_{\mathrm{at}}$ (Eq. 1.19). The typical frequency difference between adjacent levels, ω_{at}, is, for the static electric fields we apply in our experiments, in the radio-frequency domain. By applying a radio-frequency field with ω_{rf}, at resonant with the atomic frequency ω_{at}, we can drive transitions between adjacent levels on the diagonal ladders

We consider the interaction of the hydrogen atom with a radio-frequency field in the horizontal xy-plane. The coupling Hamiltonian can be written as

$$\hat{V}_{\mathrm{rf}} = -q\boldsymbol{F}_{\mathrm{rf}}(t)\cdot\hat{\boldsymbol{r}},$$

where $\boldsymbol{F}_{\mathrm{rf}}(t)$ is the time dependent radio-frequency electric field, which can be decomposed into

$$\boldsymbol{F}_{\mathrm{rf}}(t) = \boldsymbol{F}^{+}_{\mathrm{rf}}(t) + \boldsymbol{F}^{-}_{\mathrm{rf}}(t),$$

with $\boldsymbol{F}^{+}_{\mathrm{rf}}(t)$ corresponding to the σ^+ polarized component of the radio-frequency field, and $\boldsymbol{F}^{-}_{\mathrm{rf}}(t)$ to the σ^- polarized component. The $\sigma^\pm$ polarized radio-frequency field can be written as

$$\begin{aligned}\boldsymbol{F}^{\pm}_{\mathrm{rf}}(t) &= F^{\pm}_{\mathrm{rf}}\left(\cos(\omega_{\mathrm{rf}}t)\,\boldsymbol{u}_x \pm \sin(\omega_{\mathrm{rf}}t)\,\boldsymbol{u}_y\right)\\ &= \frac{1}{2}F^{\pm}_{\mathrm{rf}}\left((\boldsymbol{u}_x \mp i\,\boldsymbol{u}_y)e^{i\omega_{\mathrm{rf}}t} + (\boldsymbol{u}_x \pm i\,\boldsymbol{u}_y)e^{-i\omega_{\mathrm{rf}}t}\right),\end{aligned}$$

leading to coupling Hamiltonians for the σ^+ and σ^- polarized radio-frequency field of the form

$$\hat{V}^{\pm}_{\mathrm{rf}}(t) = \frac{1}{2}eF^{\pm}_{\mathrm{rf}}\left((\hat{x} \mp i\,\hat{y})e^{i\omega_{\mathrm{rf}}t} + (\hat{x} \pm i\,\hat{y})e^{-i\omega_{\mathrm{rf}}t}\right). \tag{1.21}$$

We can use the Pauli replacement (Eq. 1.16) to rewrite

$$\hat{x} \pm i\,\hat{y} = \frac{3}{2}\frac{a_0 n}{\hbar}\left(\hat{J}^{\pm}_1 - \hat{J}^{\pm}_2\right), \tag{1.22}$$

introducing the ladder operators[7] $\hat{J}_1^{\pm}$ and $\hat{J}_2^{\pm}$

$$\hat{J}_1^{\pm} = \left(\hat{J}_{1x} \pm i\hat{J}_{1y}\right) \quad \text{and} \quad \hat{J}_2^{\pm} = \left(\hat{J}_{2x} \pm i\hat{J}_{2y}\right). \tag{1.23}$$

The $\hat{x} \pm i\hat{y}$ operators only couple states with $\Delta m_1 = 0$ and $\Delta m_2 = \pm 1$ or states with $\Delta m_2 = 0$ and $\Delta m_1 = \pm 1$. We find [158]

$$\langle j_1, m_1 \pm 1, j_2, m_2 | \hat{x} \pm i\hat{y} | j_1, m_1, j_2, m_2 \rangle = \frac{3}{4} a_0 n \sqrt{n^2 - 4m_1^2 \pm 4m_1 - 1} \quad \text{and} \tag{1.24}$$

$$\langle j_1, m_1, j_2, m_2 \pm 1 | \hat{x} \pm i\hat{y} | j_1, m_1, j_2, m_2 \rangle = \frac{3}{4} a_0 n \sqrt{n^2 - 4m_2^2 \pm 4m_2 - 1}. \tag{1.25}$$

Using Eq. 1.22, we can rewrite Eq. 1.21 as

$$\hat{V}_{\mathrm{rf}}^{\pm}(t) = \frac{1}{2}\Omega_{\mathrm{rf}}^{\pm}\left(\left(\hat{J}_1^- - \hat{J}_2^-\right) e^{\pm i\omega_{\mathrm{rf}} t} + \left(\hat{J}_1^+ - \hat{J}_2^+\right) e^{\mp i\omega_{\mathrm{rf}} t}\right), \quad \text{with} \quad \Omega_{\mathrm{rf}}^{\pm} = \frac{3}{2}\frac{e a_0}{\hbar} n F_{\mathrm{rf}}^{\pm}, \tag{1.26}$$

where $\Omega_{\mathrm{rf}}^{\pm}$ is the Rabi frequency of the radio-frequency field. The operator $\hat{J}_1^+$, for example, corresponds to a transition $\Delta m_1 = +1$ towards a level with higher energy. The term $\hat{J}_1^+ e^{+i\omega_{\mathrm{rf}} t}$ is thus non-resonant. This is also the case for the term $\hat{J}_2^- e^{+i\omega_{\mathrm{rf}} t}$ (due to the negative value of the frequency of $\hat{\boldsymbol{J}}_2$, a decrease of the value of m_2 corresponds to a gain in energy). If $\omega_{\mathrm{rf}} \approx \omega_{\mathrm{at}}$, those terms and their hermitian conjugate can be neglected. The expression in Eq. 1.26 can therefore be simplified using the rotating frame approximation. We find

$$\hat{V}_{\mathrm{rf}}^{+}(t) = \frac{1}{2}\Omega_{\mathrm{rf}}^{+}\left(\hat{J}_1^+ e^{-i\omega_{\mathrm{rf}} t} + \hat{J}_1^- e^{i\omega_{\mathrm{rf}} t}\right) \quad \text{and} \tag{1.27}$$

$$\hat{V}_{\mathrm{rf}}^{-}(t) = \frac{1}{2}\Omega_{\mathrm{rf}}^{-}\left(\hat{J}_2^+ e^{i\omega_{\mathrm{rf}} t} + \hat{J}_2^- e^{-i\omega_{\mathrm{rf}} t}\right). \tag{1.28}$$

A σ^+ polarized radio-frequency field induces transitions on the $\hat{\boldsymbol{J}}_1$ spin ladder, whereas a σ^- polarized radio-frequency field induces transitions on the $\hat{\boldsymbol{J}}_2$ spin ladder, each leaving the other spin unaltered.

1.1.7 Spin coherent states

The total Hamiltonian $\hat{H} = \hat{H}_0 + \hat{V}_{\mathrm{DC}} + \hat{V}_{\mathrm{rf}}^+ + \hat{V}_{\mathrm{rf}}^-$ is a sum of the unperturbed Hamiltonian $\hat{H}_0$, of the perturbation due to the static electric field $\hat{V}_{\mathrm{DC}}$ and of the coupling to the σ^+ and σ^- polarized radio-frequency fields, $\hat{V}_{\mathrm{rf}}^+$ and $\hat{V}_{\mathrm{rf}}^-$. Inside a given manifold, neglecting the second order Stark effect, the terms $\hat{V}_{\mathrm{DC}}$, $\hat{V}_{\mathrm{rf}}^+$, and $\hat{V}_{\mathrm{rf}}^-$ can all be expressed in terms of

[7] The action of a ladder operators are defined by

$$\hat{J}^{\pm}|j,m\rangle = \hbar\sqrt{j(j+1) - m(m\pm 1)}\,|j, m\pm 1\rangle = \hbar\sqrt{(j\mp m)(j\pm m+1)}\,|j, m\pm 1\rangle.$$

the angular momentum operators $\hat{\boldsymbol{J}}_1$ and $\hat{\boldsymbol{J}}_2$ (Eqs. 1.18, 1.27, 1.28):

$$\hat{V}_{\mathrm{DC}} = \hbar\omega_{\mathrm{at}}(\hat{J}_{1z} - \hat{J}_{2z}),$$
$$\hat{V}^{+}_{\mathrm{rf}} = \frac{1}{2}\Omega^{+}_{\mathrm{rf}}\left(\hat{J}^{+}_1 e^{-i\omega_{\mathrm{rf}}t} + \hat{J}^{-}_1 e^{i\omega_{\mathrm{rf}}t}\right),$$
$$\hat{V}^{-}_{\mathrm{rf}} = \frac{1}{2}\Omega^{-}_{\mathrm{rf}}\left(\hat{J}^{+}_2 e^{i\omega_{\mathrm{rf}}t} + \hat{J}^{-}_2 e^{-i\omega_{\mathrm{rf}}t}\right).$$

Inside a given manifold, the total Hamiltonian can therefore be rewritten as $\hat{H} = \hat{H}_0 + \hat{H}_1 + \hat{H}_2$, with

$$\hat{H}_1 = \hbar\omega_{\mathrm{at}}\hat{J}_{1z} + \frac{1}{2}\Omega^{+}_{\mathrm{rf}}\left(\hat{J}^{+}_1 e^{-i\omega_{\mathrm{rf}}t} + \hat{J}^{-}_1 e^{i\omega_{\mathrm{rf}}t}\right),$$
$$\hat{H}_2 = -\hbar\omega_{\mathrm{at}}\hat{J}_{2z} + \frac{1}{2}\Omega^{-}_{\mathrm{rf}}\left(\hat{J}^{+}_2 e^{i\omega_{\mathrm{rf}}t} + \hat{J}^{-}_2 e^{-i\omega_{\mathrm{rf}}t}\right),$$

and $\hat{H}_0$ is constant inside a given manifold. The Hamiltonian $\hat{H}_1$ acts only on $|j_1, m_1\rangle$, whereas $\hat{H}_2$ acts only on $|j_2, m_2\rangle$. If initially the atom is prepared in a product state, the state of the hydrogen atom remains in a product state,

$$|\Psi(t)\rangle = |\Psi_1(t)\rangle \otimes |\Psi_2(t)\rangle\,, \tag{1.29}$$

where $|\Psi_1(t)\rangle$ is the state of $\hat{\boldsymbol{J}}_1$ and $|\Psi_2(t)\rangle$ the state of $\hat{\boldsymbol{J}}_2$. To study $|\Psi_1(t)\rangle$ and $|\Psi_2(t)\rangle$, it is convenient to represent the state of the spin in the rotating frame at the radio-frequency ω_{rf}. The evolution is then given by the time-independent Hamiltonian,

$$\tilde{H}_i = \hbar\delta\hat{J}_{iz} + \frac{1}{2}\Omega^{\pm}_{\mathrm{rf}}\left(i\hat{J}^{+}_i e^{+i\phi} - i\hat{J}^{-}_i e^{-i\phi}\right), \tag{1.30}$$

where we introduce the phase ϕ of the radio-frequency drive.

Starting with the circular state $|j_1, j_1\rangle \otimes |j_2, j_2\rangle$ and applying a radio-frequency pulse creates the state

$$|\Psi(t)\rangle = \left(e^{-i\tilde{H}_1 t/\hbar}|j_1, j_1\rangle\right) \otimes \left(e^{-i\tilde{H}_2 t/\hbar}|j_2, j_2\rangle\right). \tag{1.31}$$

1.1.7.a Spin coherent states on the generalized Bloch sphere

In case the radio-frequency is resonant with the frequency between adjacent levels, $\omega_{\mathrm{rf}} = \omega_{\mathrm{at}}$, the detuning vanishes, $\delta = 0$, and Eq.1.30 becomes

$$\tilde{H}_i = \Omega^{\pm}_{\mathrm{rf}}\left(-\sin(\phi_i)\hat{J}_x + \cos(\phi_i)\hat{J}_y\right).$$

We restrict the following description to the $\hat{\boldsymbol{J}}_1$ operator. The exponent of the time-evolution operator $e^{-i\tilde{H}_1 t/\hbar}$ can be replaced by $\tilde{H}_1 t = \theta_1 \hat{\boldsymbol{J}}_1 \cdot \boldsymbol{n}_1$, product of rotation angle θ_1, the angular momentum operator $\hat{\boldsymbol{J}}_1$ and the rotation axis $\boldsymbol{n}_1 = (-\sin(\phi_1), \cos(\phi_1), 0)$.

We introduce the rotation operator for a σ^+ polarized radio-frequency field as

$$\hat{R}_1(\theta_1,\phi_1) = e^{\frac{i}{\hbar}\theta_1 \hat{\boldsymbol{J}}_1\cdot\boldsymbol{n}_1} = e^{-\frac{i\theta_1}{\hbar}(-\sin(\phi_i)\hat{J}_x+\cos(\phi_i)\hat{J}_y)}. \tag{1.32}$$

If applied on the state $|j_1, j_1\rangle$, the rotation operator generates the state $|\theta_1,\phi_1\rangle$,

$$|\theta_1,\phi_1\rangle = \hat{R}_1(\theta_1,\phi_1)\,|j_1, j_1\rangle\,,$$

which is called a spin coherent state (SCS) or Bloch state. The spin coherent state can be expressed in the basis of the states $\{|j_1, m_1\rangle\}$ as [80, 162]

$$|\theta_1,\phi_1\rangle = \sum_{m_1=-j_1}^{j_1} c_{m_1}\,|j_1, m_1\rangle \tag{1.33}$$

with the coefficients

$$c_{m_1} = \begin{pmatrix} 2j_1 \\ j_1+m_1 \end{pmatrix}^{1/2} \cos\left(\frac{\theta_1}{2}\right)^{j_1+m_1} \sin\left(\frac{\theta_1}{2}\right)^{j_1-m_1} e^{i(j_1-m_1)\phi_1}.$$

The state $|j_1, j_1\rangle = |\theta_1 = 0, \phi_1\rangle$ consists of a single state of the $\{|j_1, m_1\rangle\}$ basis. After a rotation of the initial circular state, the spin coherent state is centred around the coordinates (θ_1,ϕ_1). For rotation angles $\theta_1 > 0$, the spin coherent state is a superposition of an increasing number of states of the $\{|j_1, m_1\rangle\}$ basis, reaching its maximum at $\theta_1 = \pi/2$. For further increasing rotation angles, the number of states involved in the superposition decreases until the rotation angle $\theta_1 = \pi$ for which the spin coherent state consists again in the single state $|j_1, -j_1\rangle = |\theta_1 = \pi, \phi_1\rangle$. The projections of the spin are

$$\langle\hat{J}_{1x}\rangle = J\sin(\theta_1)\cos(\phi_1)$$
$$\langle\hat{J}_{1y}\rangle = J\sin(\theta_1)\sin(\phi_1)$$
$$\langle\hat{J}_{1z}\rangle = J\cos(\theta_1).$$

The overlap of two spin coherent states $|\theta_1,\phi_1\rangle$ and $|\theta_1',\phi_1'\rangle$ can be expressed as [80]

$$|\,\langle\theta_1,\phi_1|\theta_1',\phi_1'\rangle\,|^2 = \cos^{4j_1}\left(\frac{\Theta}{2}\right), \tag{1.34}$$

where Θ is the angle between the two vectors of directions (θ_1,ϕ_1) and (θ_1',ϕ_1') of the two spin coherent states and is given by

$$\cos(\Theta) = \cos(\theta_1)\cos(\theta_1') + \sin(\theta_1)\sin(\theta_1')\cos(\phi_1-\phi_1').$$

The representation of a large spin with $j_1 = (n-1)/2$ is closely related to representation of a spin 1/2 on a Bloch sphere. In the Hilbert space of a spin 1/2, the state of the system can be represented by a vector (x, y, z) evolving on the surface of a three-dimensional sphere, called Bloch sphere. If $j = 1/2$, a given point of the Bloch sphere (θ,ϕ) fully characterizes the state of the spin.

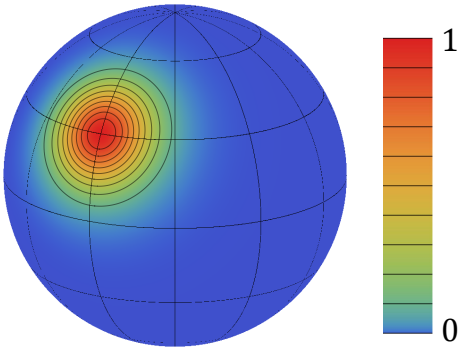

Figure 1.6: The Q-function of a spin coherent state in the direction (θ_1, ϕ_1) *with* $\theta_1 = 60°$ *and* $\phi_1 = 0°$*. The color scale is linear from 0 to 1 and the contour lines are every 0.1.*

If $j > 1/2$, the representation of the state of spin on a Bloch sphere is more complex. The states $|j_1, m_1\rangle$, for example, have a well-defined projection of $\hat{J}_{1z}$. However, since they are eigenstates of the operator $\hat{J}_{1z}$ they are invariant under the action of this operator and therefore are invariant under rotations around the Z-axis. Consistently, the values of $\hat{J}_{1x}$ and $\hat{J}_{1y}$ are completely undetermined ($\langle \hat{J}_{1x} \rangle = \langle \hat{J}_{1y} \rangle = 0$).

The state of a spin with $j > 1/2$ must be represented as a quasi-probability distribution on a generalized Bloch sphere of radius $\langle \hat{\boldsymbol{J}}^2 \rangle^{1/2} = \hbar\sqrt{j_1(j_1+1)}$. In the case of a spin coherent state, this distribution is localized around the direction (θ, ϕ). For a $|j_1, m_1\rangle$ state this distribution is around a circle at the intersection of the generalized Bloch sphere and the horizontal plane $Z = m_1\hbar$.

In order to describe the state of the spin $\hat{\boldsymbol{J}}_1$ quantitatively we introduce two quasi-probability functions defined on the whole sphere: the Q-function and the Wigner-function. The Q-function for an angular momentum $\hat{\boldsymbol{J}}_1$ is defined by [163–165]

$$Q(\theta_1, \phi_1) = \frac{2j_1 + 1}{4\pi} \langle j_1, j_1 | R_1^\dagger(\theta_1, \phi_1) \rho_1 R_1(\theta_1, \phi_1) | j_1, j_1 \rangle, \tag{1.35}$$

where ρ_1 is the density matrix of the angular momentum. The Q-function can be interpreted as the overlap of the state $|j_1, m_1 = j_1\rangle$ and the spin coherent state $|\theta_1, \phi_1\rangle$. As a result $Q(\theta_1, \phi_1)$ is positive and ≤ 1.

If j is an integer, we can also generalize the Wigner-function, useful to characterize the quantum nature of a state, for an angular momentum $\hat{\boldsymbol{J}}_1$, [165, 166]

$$W(\theta_1, \phi_1) = \sum_{p=0}^{2j_1} \sum_{q=-p}^{p} \rho_{pq} Y_p^q(\theta_1, \phi_1), \tag{1.36}$$

where Y_p^q are the spherical harmonics and ρ_{pq} the matrix elements that can be expressed as $\rho_{pq} = \mathrm{Tr}[\hat{\rho}\, \hat{T}_{pq}^\dagger]$, with the multipole operator $\hat{T}_{pq}^\dagger$ defined in [166]. The Wigner-function $W(\theta_1, \phi_1)$ can have positive and negative values.

The quasi-probability distribution associated to $\hat{R}(\theta, \phi)|\Psi\rangle$ is obtained by a rotation $\hat{R}(\theta, \phi)$ applied on the quasi-probability distribution associated to $|\Psi\rangle$.

Fig. 1.6 presents the Q-function of the spin coherent state $|\theta_1, \phi_1\rangle$. The width of the Gaussian-shaped quasi-probability distribution is related to the quantum fluctuations. If we define $(\hat{J}_{n_1}, \hat{J}_{\theta_1}, \hat{J}_{\phi_1})$ as a set of orthogonal components of $\hat{\boldsymbol{J}}_1$, where $\hat{J}_n$ is along the direction (θ_1, ϕ_1), the spin coherent states fulfil the uncertainty relation of Heisenberg,

$$\left\langle \Delta \hat{J}^2_{\theta_1} \right\rangle \left\langle \Delta \hat{J}^2_{\phi_1} \right\rangle = \frac{\hbar^2}{4} \left\langle \hat{J}_{n_1} \right\rangle^2,$$

with the minimum uncertainty equally distributed in the directions perpendicular to (θ_1, ϕ_1) of the Bloch sphere. The uncertainty in the direction of the spin coherent state is given by

$$\Delta\theta_1 = \frac{\Delta \hat{J}_{\theta_1}}{\left\langle \hat{J}_{n_1} \right\rangle} = \frac{1}{\sqrt{2J}}. \tag{1.37}$$

1.1.7.b Spin coherent states with off-resonant radio-frequency drive

In case the radio-frequency is not resonant with the frequency between adjacent levels, $\omega_{\mathrm{rf}} \neq \omega_{\mathrm{at}}$, the detuning becomes non-zero $\delta \neq 0$ and the Hamiltonian in the rotating frame approximation becomes $\tilde{H} = \boldsymbol{\Omega} \cdot \hat{\boldsymbol{J}}_n$. The state $|\Psi_1(t)\rangle$ is a spin coherent state along the direction given by of the vector $\boldsymbol{J}_1(t)$ that rotates with frequency $|\boldsymbol{\Omega}|$ around $\hat{\boldsymbol{J}}_n$. However, due to its global phase this state is only proportional to $|\theta_1, \phi_1\rangle$,

$$e^{-i\tilde{H}_1 t/\hbar} |j_1, j_1\rangle \propto |\boldsymbol{J}_1(t)\rangle = |\theta_1, \phi_1\rangle .$$

1.1.7.c Spin coherent states in the n-manifold

Up to here, we only consider the operator $\hat{\boldsymbol{J}}_1$. If, however, the state $|\Psi(t)\rangle$ in Eq. 1.31 is a product state of the spins $\hat{\boldsymbol{J}}_1$ and $\hat{\boldsymbol{J}}_2$, the state can be decomposed as

$$|\Psi(t)\rangle = R_1(\theta_1, \phi_1) \otimes R_2(\theta_2, \phi_2) \, |j_1, j_1, j_2, j_2\rangle = R_1(\theta_1, \phi_1) \, |j_1, j_1\rangle \otimes R_2(\theta_2, \phi_2) \, |j_2, j_2\rangle .$$

The state of the atom is therefore described as a product of two spin coherent states (Eq. 1.33),

$$|\Psi(t)\rangle = |\theta_1, \phi_1\rangle \otimes |\theta_2, \phi_2\rangle = \sum_{m_1} \sum_{m_2} c_{m_1} c_{m_2} \, |m_1, m_2\rangle .$$

The probability to be in the state $|j_1, m_1, j_2, m_2\rangle$ is given by $P(|m_1, m_2\rangle) = |c_{m_1}|^2 |c_{m_2}|^2$ and is depicted in Fig. 1.7.

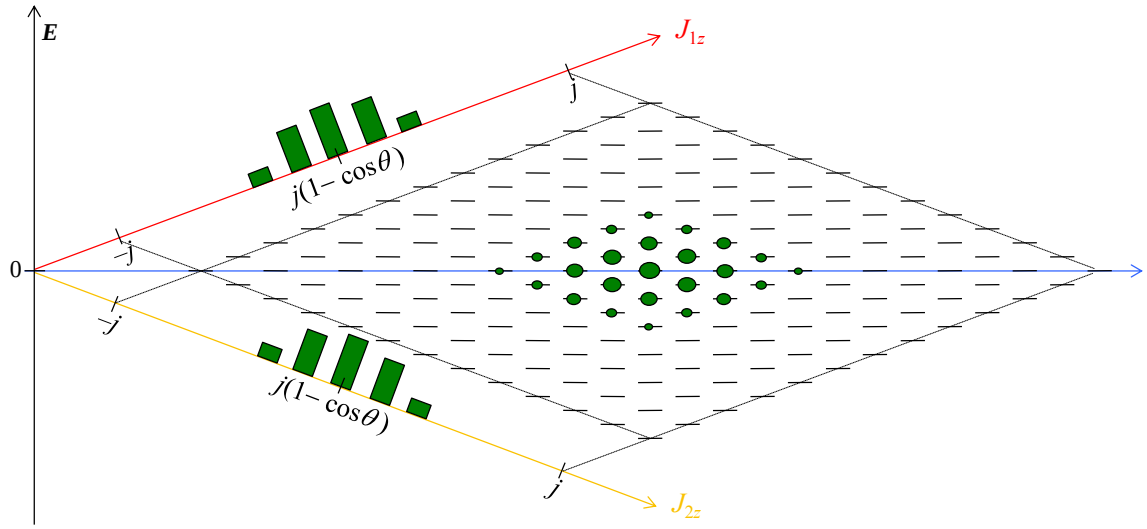

Figure 1.7: Sketched population of Stark levels after rotation from the circular state.

1.1.7.d Semi-classical states

The spin coherent states are states for which the direction of the spin is defined as precisely as allowed by quantum mechanics. They are the closest state to a classical angular momentum $\boldsymbol{J}_0$ such that $\langle\hat{\boldsymbol{J}}\rangle = \boldsymbol{J}_0$.

The product states of two spin coherent states of $\hat{\boldsymbol{J}}_1$ and $\hat{\boldsymbol{J}}_2$ are the closest states to a classical localization of the electron. They correspond to a wave-function that is localized around the Kepler orbit defined by the angular momentum $\boldsymbol{L} = \langle\hat{\boldsymbol{J}}_1\rangle + \langle\hat{\boldsymbol{J}}_2\rangle$ and ellipticity $\boldsymbol{a} = \langle\hat{\boldsymbol{J}}_2\rangle - \langle\hat{\boldsymbol{J}}_1\rangle$. They are therefore semi-classical states, justifying the name of "coherent states" [167–169].

Fig. 1.8 shows the wave-functions of some spin coherent states $|\theta_1,\phi_1\rangle \otimes |j_2,j_2\rangle$, the latter being superpositions of states with $|j_1,m_1\rangle \otimes |j_2,j_2\rangle$, shown in Fig. 1.9. Some of the properties of the orbits of these elliptical states, like their dimension or their polarizability, can be deduced from the classical orbit parameters.

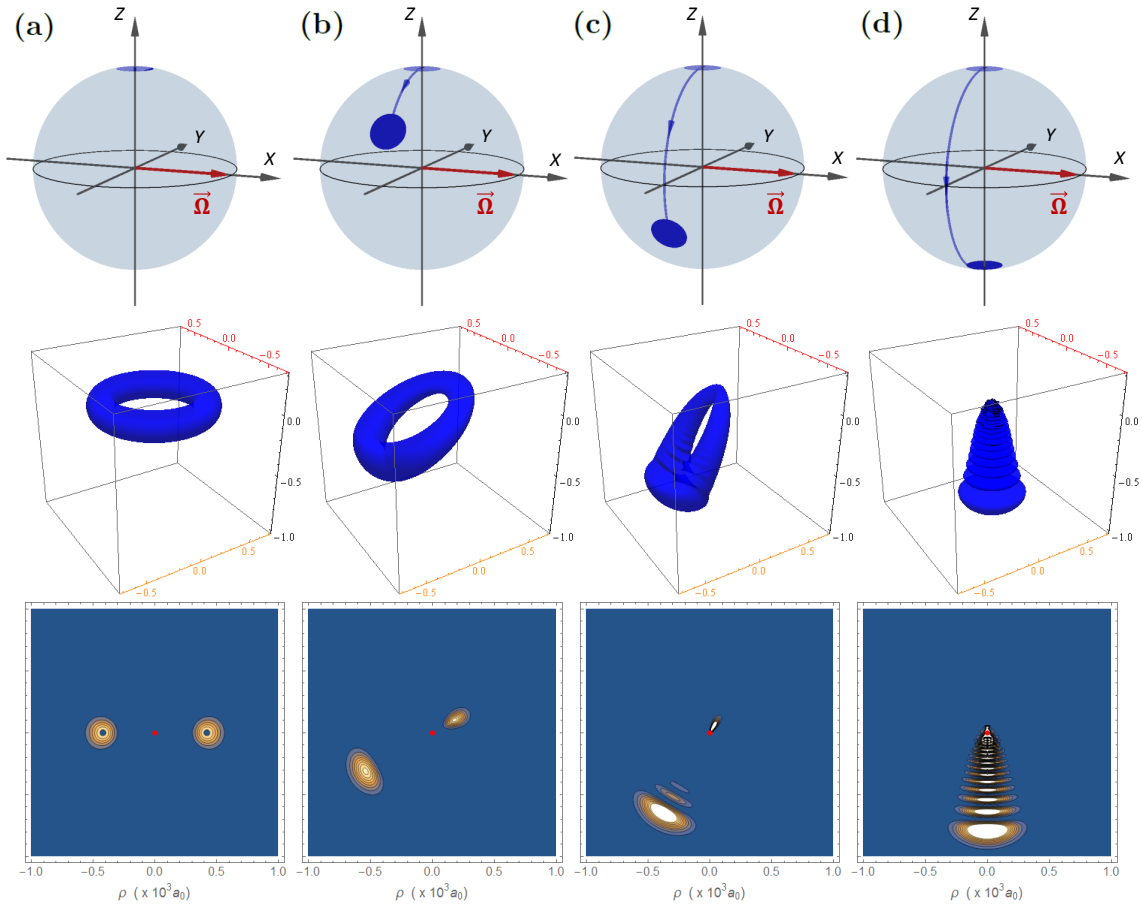

Figure 1.8: Wave functions of some coherent spin states (SCS) of the hydrogen atom for $n = 21$ with $m_2 = j_2$: (from right to left) $|\theta,\phi\rangle = |0,0\rangle = |j_1, m_1 = j_1\rangle$, $|\theta,\phi\rangle = |\pi/3,0\rangle$, $|\theta,\phi\rangle = |2\pi/3,0\rangle$ and $|\theta,\phi\rangle = |\pi,0\rangle = |j_1, m_1 = -j_1\rangle$. In the first row, the Q-function of the SCS is sketched. The wave-functions in rows two and three are represented with the same characteristics as in Fig. 1.1. Example (a) and (d) correspond to the same wave-function as example 4 and 1, respectively, in Fig. 1.9. These two states are the extema in the spin ladder with $m_2 = j_2$ and occupy therefore the south (a) and north pole (d) of the generalized Bloch sphere. The pictures are taken from [154].

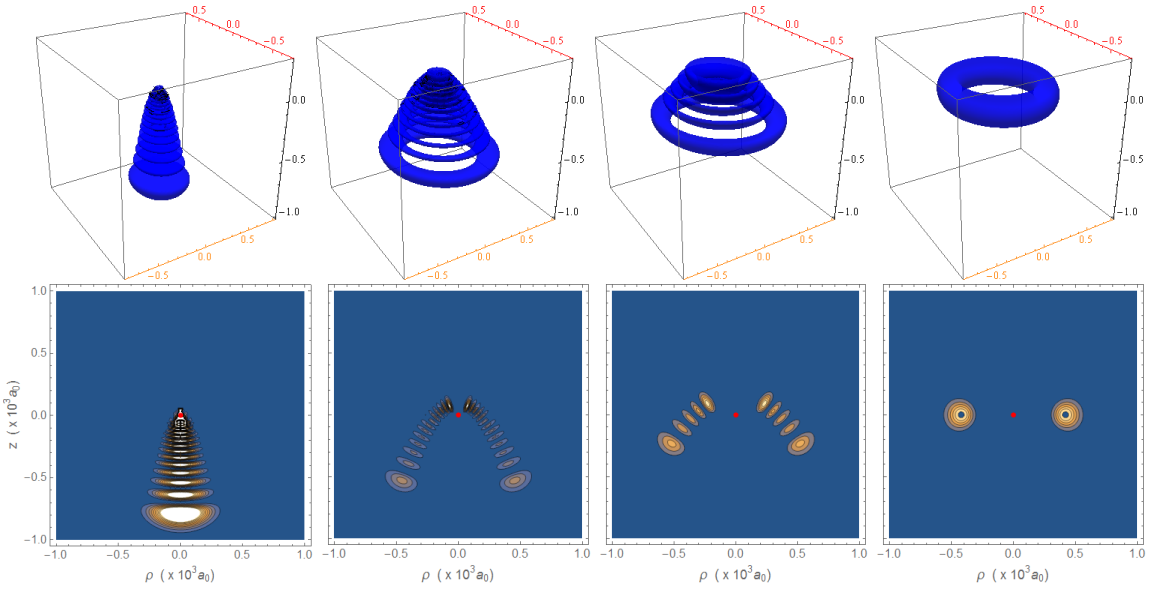

Figure 1.9: Wave functions of some states in the Runge-Lenz basis of the hydrogen atom for $n = 21$ with fixed $m_2 = j_2$: (from left to right) $|j_1, m_1, j_2, m_2\rangle = |10, -10, 10, 10\rangle$, $|j_1, m_1, j_2, m_2\rangle = |10, -2, 10, 10\rangle$, $|j_1, m_1, j_2, m_2\rangle = |10, 6, 10, 10\rangle$ and $|j_1, m_1, j_2, m_2\rangle = |10, 10, 10, 10\rangle$. The wave-functions are represented with the same characteristics as in Fig. 1.1. In the first wave-function, with $m_1 = 10$, the orbital is very elliptical and localized along the Oz-axis. In the fourth example, with $m_1 = j_1 = 10$, we find the circular state being the only one which is also an eigenstate in the spherical basis with $|n, l_{max}, m_{max}\rangle$. The pictures are taken from [154].

1.2 The rubidium Rydberg atom

The rubidium atom is an alkali atom with a single valence electron with principal quantum number $n = 5$ for the ground state. This electron can be excited to a Rydberg state, a state with high principal quantum number $n \gg 5$ close to the ionisation limit. The higher the electron is excited the smaller the energy difference gets between manifolds of adjacent principal quantum numbers. In our experiments we use Rydberg states of manifolds of principal quantum number around $n \sim 50$. In this regime the energy difference between adjacent manifolds is around 50 GHz and therefore in the microwave range.

In this section, the difference between the hydrogen and the rubidium atom is discussed. Unlike the Hamiltonian for the hydrogen atom, the one for the rubidium atom cannot be solved analytically even in zero field. It is nevertheless possible to calculate the energy eigenvalues of the rubidium atom by introducing a correction that takes into account the non-negligible spatial extension of the ionic core. This correction is called the quantum defect and is discussed in Sec. 1.2.1. We discuss the numerical calculation of the energy eigenvalues of the rubidium atom in the presence of a static electric field (Sec. 1.2.2) and of the dipole matrix elements for transitions driven in the presence of a resonant radio-frequency field (Sec. 1.2.3).

1.2.1 Energy corrections due to the quantum defect

The main difference between the hydrogen and the rubidium atom is the point-like nucleus of the hydrogen, made up of a single proton, in contrast to the ionic core of the rubidium, made up of 36 electrons, 37 protons and 48 neutrons.[8] In Rydberg states with principal quantum number $n \sim 50$, the valence electron is most of the time located at a great distance from the ionic core with respect to the core's dimension. For electron orbitals located far away from the nucleus, the protons' charge is completely screened by the inner electrons' charge and the ionic core can be considered as a point-like positive charge $+e$. However, for electron orbitals with low l quantum number and therefore high ellipticity, the valence electron penetrates the charge cloud of the ionic core. The assumption of a point-like core is therefore no longer valid, as the positive charge of the core's protons is no longer perfectly screened by the core electrons. The attraction of the core on the valence electron becomes stronger, which leads to a tighter binding and therefore energetically lower lying states compared to the respective levels in a hydrogen atom.

The ionic core made up of an electron cloud interacting with the nucleus is also susceptible to be polarized when interacting electrostatically with the valence electron. This effect modifies the potential seen by the valence electron and provokes a change in the energy eigenvalues and eigenstates. The effect of the polarizability of the ionic core also decreases with a higher angular momentum quantum number l [151].

As a result, the e^2/r-potential of a single point-like charge (of the screened ionic core or of the hydrogen atom) tends to become a deeper Ze^2/r-potential when the electron comes close to the nucleus. The Runge-Lenz operator $\hat{\boldsymbol{A}}$ based on the pure $1/r$-symmetry of the potential is no longer conserved, leading to the fact that the parabolic basis is not the most natural one to treat the correction of core polarizability and core penetration. The spherical symmetry, however, is still conserved. The angular momentum operator $\hat{\boldsymbol{L}}$ commutes with the Hamiltonian making the spherical basis naturally more adapted to describe these energy corrections [159].

The effect of the finite size of the ionic core is taken into account by introducing an effective principal quantum number n_{eff} for low angular momentum states. The energy of the states becomes

$$E_{nlj} = -\frac{E_{Ry}}{n_{\text{eff}}^2}, \quad \text{with} \quad n_{\text{eff}} = n - \delta_{nlj}, \tag{1.38}$$

where δ_{nlj} is called the quantum defect constant

$$\delta_{nlj} = \delta_0 + \frac{\delta_2}{(n-\delta_0)^2} + \frac{\delta_4}{(n-\delta_0)^4} + \ldots \tag{1.39}$$

This phenomenological constant does not only depend on l, but also slightly on the principal quantum number n and the total angular momentum quantum number j associated to the total angular momentum $\hat{\boldsymbol{J}} = \hat{\boldsymbol{L}} + \hat{\boldsymbol{S}}$ with orbital momentum operator $\hat{\boldsymbol{L}}$

[8] We consider ^{85}Rb throughout this thesis.

and electron spin operator $\hat{\boldsymbol{S}}$. The fine structure has to be taken into account for low l states since the rubidium atom, due to its higher atomic number Z, is more sensitive to relativistic effects than the hydrogen atom.

For high principal quantum numbers n, the first two terms in Eq. 1.39 are sufficient to yield the quantum defect to a good approximation. The explicit values for δ_0 and δ_2 are given by [170–172] and are summed up in Appendix A.1. For the f state, with $l = 3$, the quantum defect constant is $\delta_{nlj} \approx 0.016$. However, for $l \leq 2$, the quantum defect constant δ_{nlj} can be greater than 1. States with $l > 3$ have very small quantum defect constants and can therefore be assumed to be hydrogen-like. The quantum defect of high-l states is important to describe the structure at very low electric field.[9] At larger electric fields ($F \approx 200$ V/m), however, the energy shift due to the quantum defect of the levels with $l > 4$ is very small compared to the Stark shift and can therefore be neglected.

1.2.2 Energy levels in a static electric field

In the absence of external fields, the energy eigenvalues of the hydrogen atom of manifold n are all degenerate (Sec. 1.1.1.b). In the rubidium atom, however, due to the quantum defect, the energy eigenvalues of some states with low angular momentum quantum number l are shifted away from the manifold.

1.2.2.a Numerical calculation of the energy levels

The Hamiltonian of the rubidium atom in the presence of a static electric field is given by

$$\hat{H}_{\mathrm{Rb}} = \hat{H}_{0,\mathrm{Rb}} - eF\hat{z}, \tag{1.40}$$

with the dipole matrix element $\hat{d} = e\hat{z}$. To calculate the energy diagram in a non-zero electric field, we need to numerically diagonalize this Hamiltonian. The energy eigenvalues of the rubidium atom depend through the quantum defect on the quantum numbers n, l and j. We therefore choose to use the $\{|n,l,j,m_j\rangle\}$-basis for the calculation.

The matrix describing $\hat{H}_{0,\mathrm{Rb}}$ in the $\{|n,l,j,m_j\rangle\}$-basis is a diagonal matrix with the elements E_{nlj} (Eq. 1.38). The values of E_{nlj} are calculated from the hydrogen model corrected by the quantum defect for $l \leq 4$ states. We used the first two terms of Eq. 1.39 for $l \leq 3$ and only the first term for $l = 4$.

In order to calculate the matrix elements of the second term $eF\hat{z}$ in the Hamiltonian $\hat{H}_{\mathrm{Rb}}$ (Eq. 1.40), we separate the wave-function in its angular and radial part (Eq. 1.4),

$$\langle n,l,j,m_j|\,\hat{\boldsymbol{r}}\,|n',l',j',m_j'\rangle = \langle l,j,m_j|\,\hat{\boldsymbol{r}}/r\,|l',j',m_j'\rangle \int R_{\mathrm{Rb},nl}(r)\, r\, R'^{*}_{\mathrm{Rb},n'l'}(r)(r^2 dr). \tag{1.41}$$

The angular part $\langle l,j,m_j|\,\hat{\boldsymbol{r}}/r\,|l',j',m_j'\rangle$ can be calculated with the Clebsch-Gordan coef-

[9] In [173] show that for low static electric fields strengths F we also have to take the quantum defect up to $l = 4$ into account in order to describe the energy levels properly.

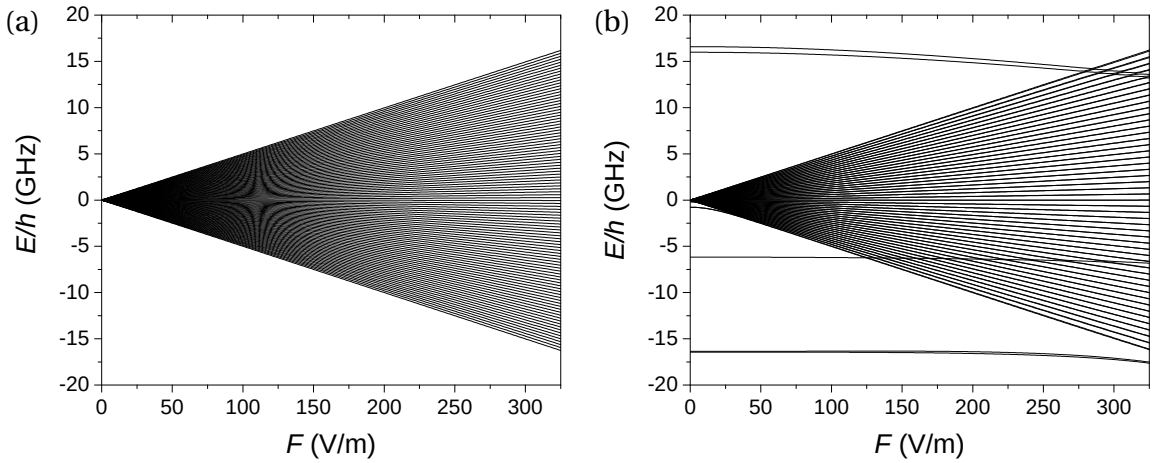

Figure 1.10: (a) Analytical calculation of the energy levels of the hydrogen atom for $m = 0$ and $m = 1$ as a function of the electric field F. (b) Numerical calculation of the energy levels with $m_j = 1/2$ of the rubidium atom as a function of the electric field F. In both cases, the chosen reference energy is the energy of the $|52c\rangle$ states at zero electric field.

ficients (Eq. 1.17). A lot of those terms are zero due to the selection rules. The radial integral $\int R_{nl}(r) r R'^{*}_{n'l'}(r)(r^2 dr)$ is calculated numerically using the *Numerov method* [174], a numerical algorithm to solve ordinary second-order differential equations which are independent of the first order derivative. The algorithm integrates the Schrödinger equation at the energy that is the one corrected by the quantum defect. Applications of the Numerov method to Rydberg atoms can be found in [151] and [159].

The influence of manifolds with $n' \neq n$ on the manifold of interest n, decreases with increasing difference between n' and n. We therefore restrict the numerical calculation to a window of $E_n \pm h\nu$ with $\nu = 200$ GHz if not stated otherwise. Finally, since $\hat{J}_z$ commutes with z, we can diagonalize separately states with different m_j.

In the hydrogen atom, the Stark effect lifts the degeneracy between states of same values of magnetic quantum number m and the states split linearly into equidistant ladders of $n - |m|$ states which are distributed symmetrically with respect to the unperturbed energy E_n, shown in Fig. 1.10a.

Fig. 1.10b shows the numerically calculated energy eigenvalues for the rubidium atom plotted for $m_j = 1/2$ as a function of the electric field amplitude F. The levels of the manifold are shifted linearly with increasing electric field amplitude, whereas the states which are shifted to lower energies due to the quantum defect show a quadratic Stark shift until they join the manifold. Mathematically this corresponds to the moment where the matrix element of $eF\hat{z}$ becomes larger than the energy shift due to the quantum defect. This is the electric field where the levels becomes "hydrogen-like". As soon as the Stark shift is larger than the fine structure, m_j is not longer a good quantum number and the m_j states become $|m = m_j - 1/2, m_s = +1/2\rangle$ and $|m = m_j + 1/2, m_s = -1/2\rangle$ states.

In Fig. 1.11, the energy levels of the rubidium atom with principal quantum number $n = 51$ are shown. The energy eigenvalues are calculated for an electric field $F = 234.5$ V/m. We recognize the irregularities in the level structure caused by the missing states in the

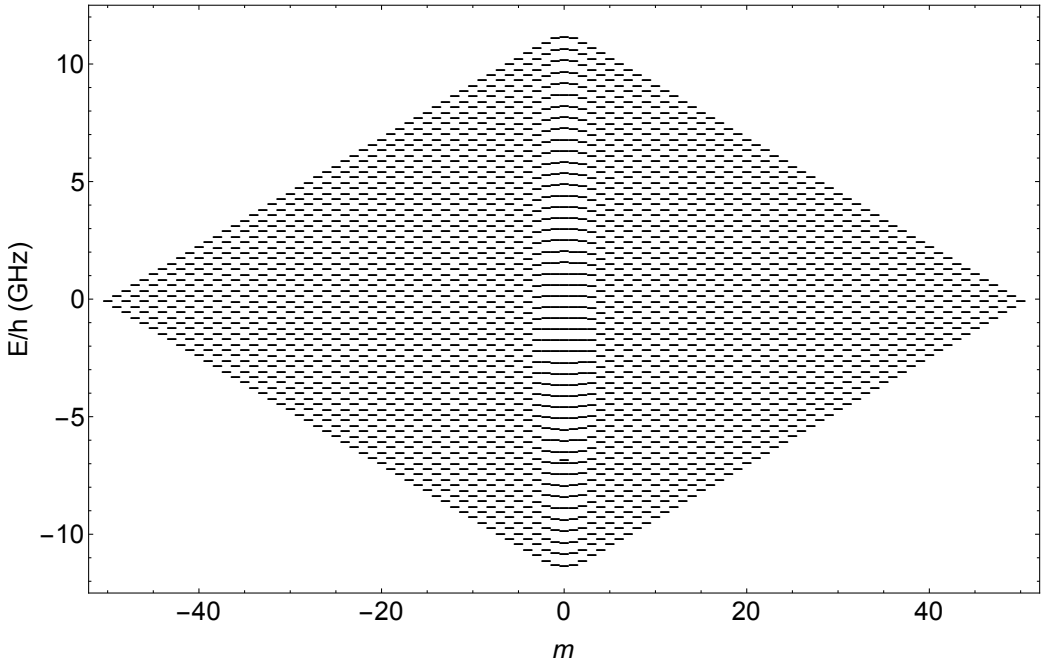

Figure 1.11: Numerical calculation of the energy levels of the rubidium atom with $n = 51$ in an electric field $F = 2.345$ V/cm. For states with $|m| < 4$ we recognize the missing levels in the horizontal m-ladders resulting from the quantum defect for low l states. The reference energy is the $|51c\rangle$ states at zero electric field.

horizontal m-ladders with $|m| \leq 3$ with respect to the hydrogen atom (see Fig. 1.4). In the hydrogen atom, the number of levels in each m-ladder decreases for each time m increases by one for $\Delta m = 1$ (for $m \geq 0$). In the rubidium atom, since the $l = 0$, $l = 1$ and $l = 2$ levels have not joined the manifold (see Fig. 1.10b) some m levels are missing. This means that the $m = 0$, $|m| = 1$ and $|m| = 2$ ladders have the same number of levels as $|m| = 3$.

1.2.3 Numerical calculation of the coupling Hamiltonian

The coupling Hamiltonian induced by the radio-frequency fields $\hat{V}_{\mathrm{rf}}^{+}$ and $\hat{V}_{\mathrm{rf}}^{-}$ (Eqs. 1.27 and 1.28) is found by numerically calculating the dipole matrix elements $\langle n, n_1, n_2, m|\ \hat{x} \pm i\,\hat{y}\ |n', n_1', n_2', m'\rangle$[10] depending on the polarization of the radio-frequency field.[11]

We focus on the lowest diagonal σ^+ spin ladder (see Fig. 1.5). We numerically calculate the dipole matrix elements $d_{m-1,m}$ of this diagonal ladder between adjacent m-states with $m-1$ and m. In Fig. 1.12, the matrix elements are plotted in units of ea_0 as a function of the magnetic quantum number m together with the analytically calculated elements for the hydrogen atom. For the latter the dipole matrix elements have the form

[10] We keep the same notation $|n, n_1, n_2, m\rangle$ for the Stark levels in the rubidium atom.

[11] We no longer restrict the calculation to a single value of m_j but two adjacent values, m_j and $m_j + 1$.

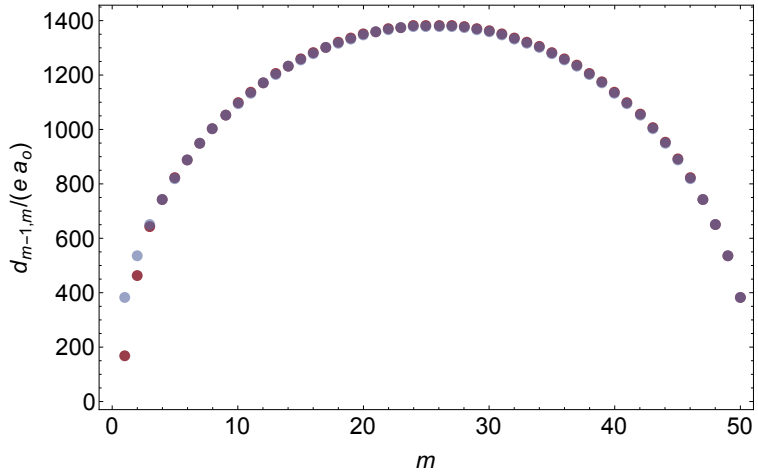

Figure 1.12: Dipole matrix elements of the rubidium atom (red) and hydrogen (blue) between the levels of magnetic quantum number $m-1$ and m of the lowest σ^+ diagonal ladder.

(Eqs. 1.24, 1.25)[12]

$$d_{m-1,m} = \langle n_1 = 0, n_2, m-1 | \hat{x} - i\hat{y} | n_1 = 0, n_2, m \rangle = \frac{3}{2} a_0 n \sqrt{m(n-m)}.$$

The dipole matrix elements for hydrogen and rubidium overlap very well for values of $m > 3$ meaning that the rubidium atom is "hydrogen-like" as expected. The values of $d_{0,1}$ and $d_{1,2}$ differ significantly for hydrogen and rubidium due to the quantum defect which shifts the low-l levels away from the manifold.

To compare the energy calculated for the rubidium atom and for the hydrogen atom, we compute the energy of the bare states $|n, n_1 = 0, n_2, m\rangle \otimes |N_{\mathrm{rf}}\rangle$, the energy in the rotating frame of the atomic states of the lowest σ^+ diagonal. Fig. 1.13 shows the energy of the bare states of the lowest σ^+ diagonal where the energy of $N_{\mathrm{rf}} = 50 - m$ radio-frequency photons polarized σ^+ are added to the energy eigenvalues. The bare energy eigenvalues are calculated in an electric field of $F = 234.5$ V/m and are then added to radio-frequency photons with $\omega_{\mathrm{rf}} = 2\pi \cdot 230$ MHz.

The bare energy eigenvalues of the rubidium atom is compared to the bare energy eigenvalues calculated for the hydrogen atom by taking into account the first and second order Stark effect. In Fig. 1.13a we see that the bare energy eigenvalues for the rubidium and the hydrogen atom are very close for levels between the circular state and the state with $m = 3$. The difference between rubidium and hydrogen increases for decreasing m below $m = 3$. The state with $m = 0$ is more than $h \cdot 200$ MHz above the corresponding state in the hydrogen atom.

In the close up in Fig. 1.13b, we see the signature of the quadratic Stark shift in the parabolic curvature of the bare levels. For levels close to the circular state we see a very good agreement between numerical calculations for the rubidium atom and the analytical

[12] Here we use the relations $m_1 = j_1 - n_1$ and $n = n_1 + n_2 + |m| + 1$, with $n_2 = 0$, and $j_1 = (n-1)/2$.

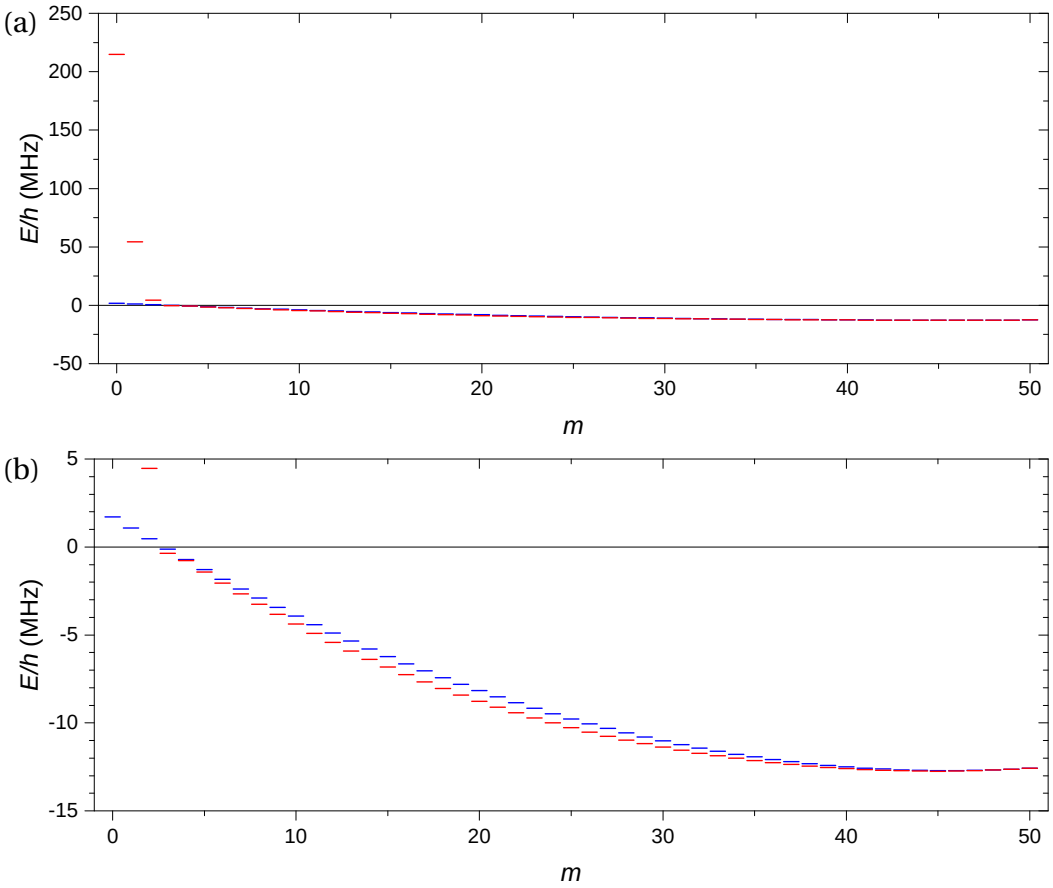

Figure 1.13: Bare states of the lowest σ^+ diagonal ladder for hydrogen and rubidium in an energy range of $\Delta E = h\cdot$ 300 MHz (a) and a close up in an energy range of $\Delta E = h\cdot$ 30 MHz (b).

one for the hydrogen atom. We see a small, increasing discrepancy in the energy levels between $m > 4$ and $m \lesssim 40$, where the numerical simulations for the rubidium atom should give the same behaviour as for the hydrogen atom. This mismatch cannot be explained by higher order Stark shifts not taken into account for the hydrogen energies. It rather gives the limit of the precision of our numerical simulation, in particular the program that calculates the radial overlap.

1.3 Discussion

In this chapter we discussed that the Rydberg state of the hydrogen atom in the presence of a static electric field can be described as two independent angular momenta $\hat{\boldsymbol{j}}_1$ and $\hat{\boldsymbol{j}}_2$. They can be addressed independently using two orthogonal polarizations of the radio-frequency field. The circular state corresponds to the state $|j_1, j_1\rangle \otimes |j_2, j_2\rangle$.

When the atom, initially in the circular state, is driven by a purely σ^+ polarized radio-frequency field, it behaves like an angular momentum and its state can be represented on a generalized Bloch sphere. If driven by a radio-frequency field with arbitrary polarization,

the state of the atom evolves as a product state of two spin coherent states associated to the angular momenta $\hat{\boldsymbol{J}}_1$ and $\hat{\boldsymbol{J}}_2$.

In the case of an alkali atom, in our case rubidium, the Rydberg state can still be described by the model of the hydrogen atom. The size of the ionic core is taken into account in this model by introducing the quantum defect that modifies the energy of states with a low angular momentum quantum number. As a result, in the presence of a static electric field, the energy structure of the rubidium atom is only hydrogen like for a magnetic quantum number $m \geq 3$. The energy and dipole moment involving states with $m \leq 2$ have thus to be calculated numerically.

In the next chapter we describe the preparation of the circular state and how we can manipulate the spin coherent state of the atom.

Chapter 2

The Experiment

The manipulation of the state of the Rydberg atom inside a Stark manifold by circular polarized radio-frequency fields is performed in an experimental set-up consisting of three parts: the oven that creates the atomic beam, the experimental zone in which the Rydberg atom is prepared and manipulated, and the detection zone in which the state of the atom is read out.

In this chapter we begin with the description of the mechanical part of the experimental set-up, the electrode structure in which the atomic state is prepared and manipulated (Sec. 2.1). We show how we transfer the atom from its ground state to the circular Rydberg state (Sec. 2.2), the initial state for our metrology sequences. We discuss how we generate the radio-frequency pulses that allow us to coherently manipulate the atom inside the Rydberg manifold (Sec. 2.3). Finally, we present techniques to optimize the spatial homogeneity of the electric field which improves the coherence time of the atoms (Sec. 2.4).

2.1 The experimental set-up

The atomic beam consists of fast atoms effusing from an oven in which rubidium metal is heated to about 200 °C. The beam, collimated by several diaphragms to a diameter of about 0.7 mm, crosses the experimental set-up and the detector with a thermal velocity distribution with average speed of about 300 m/s.[1]

Once the atomic beam is collimated it enters the electrode structure, schematically depicted in Fig. 2.1a. Two electrodes with flat horizontal surfaces create the static electric field whose amplitude defines the frequency ω_{at}. The ring electrodes surrounding them are used to apply the radio-frequency field with well defined polarization. The holes in the ring electrodes provide optical access for the laser beams to excite the atom into the

[1] The oven of our experiment has been described in several PhD theses. During this thesis no significant changes were made, we therefore invite the interested reader to consult [112, 154] for details.

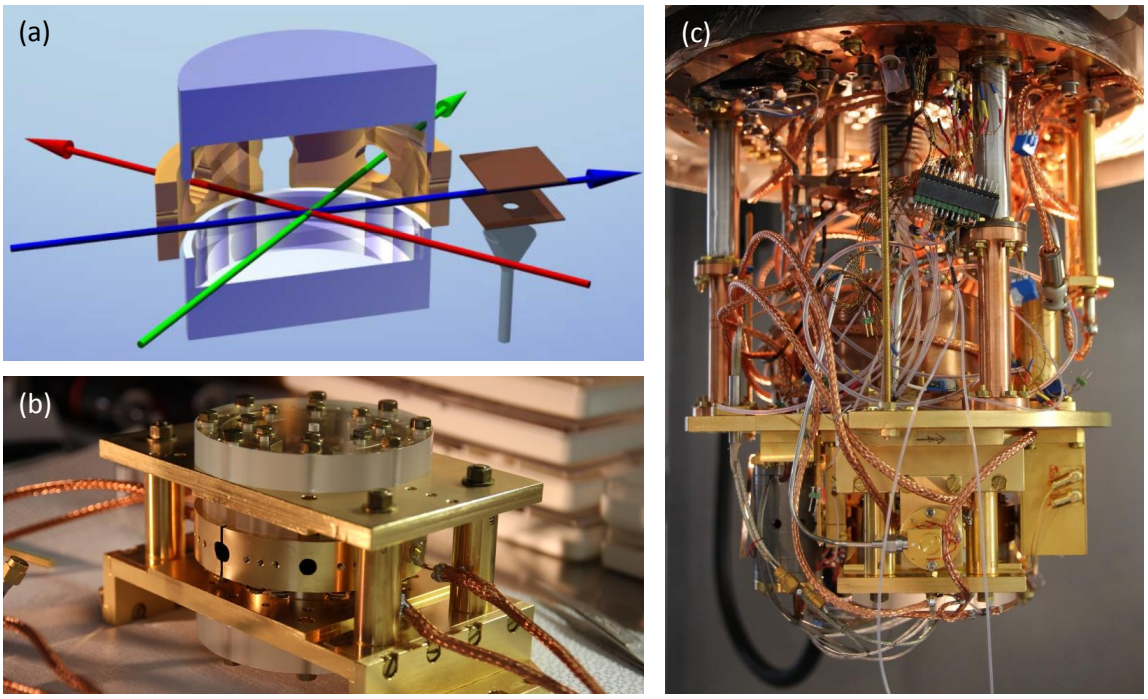

Figure 2.1: Experimental set-up. (a) The sketch of the electrode structure shows the atomic beam (blue) that intersects with the laser beams (green and red) in the center of the experimental zone made up of two round plane electrodes (blue) and four ring electrodes (yellow, only two shown in the sketch) before it enters the detector (brown) where the state of the atom is read out by ionisation. (b) A picture of the electrode structure shows the ring electrodes as well as the plane electrodes holders made of sapphire (transparent). (c) The whole set-up is placed in a cryogenic environment at 4 K.

Rydberg state. All electrodes are made of copper and coated by a thin layer of gold (see Fig. 2.1b).

The ring electrodes are separated by a gap of 1 mm to limit capacitive coupling between the electrodes and to reduce cross-talk. They are mounted on insulating blocks made of Araldite and are held in place by brass screws and springs. The springs ensure that the ring electrodes do not become loose when the insulating blocks contract slightly more than the brass screws in the cryogenic environment.

Finally, the plane capacitor electrodes are mounted on sapphire discs, insulated electrically from the ground plates. The choice of sapphire is due to the material's hardness and good thermal conductance.

During this work we implemented several modifications to the experimental set-up. In the initial version of the experimental set-up [112, 154], the radio-frequency field was generated by eight ring electrodes that were connected to pairs by short copper wires. In this work, we replaced the pairs of electrodes with four ring electrodes in order to limit electrical resonances in the radio-frequency circuit. Also, initially, all electrodes were made of gold coated copper to avoid the patch effect due to the copper oxidation. However, covering the electrodes with graphite is known to reduce stray

electric fields [175]. We have thus covered all surfaces in direct "view" of the atom with Aquadag, a colloidal graphite suspended in a solution. However, the gain in coherence time was limited if not non-existent, leading to the conclusion that the graphite is either not working or that the coherence time is limited by noise instead of the stray charges.

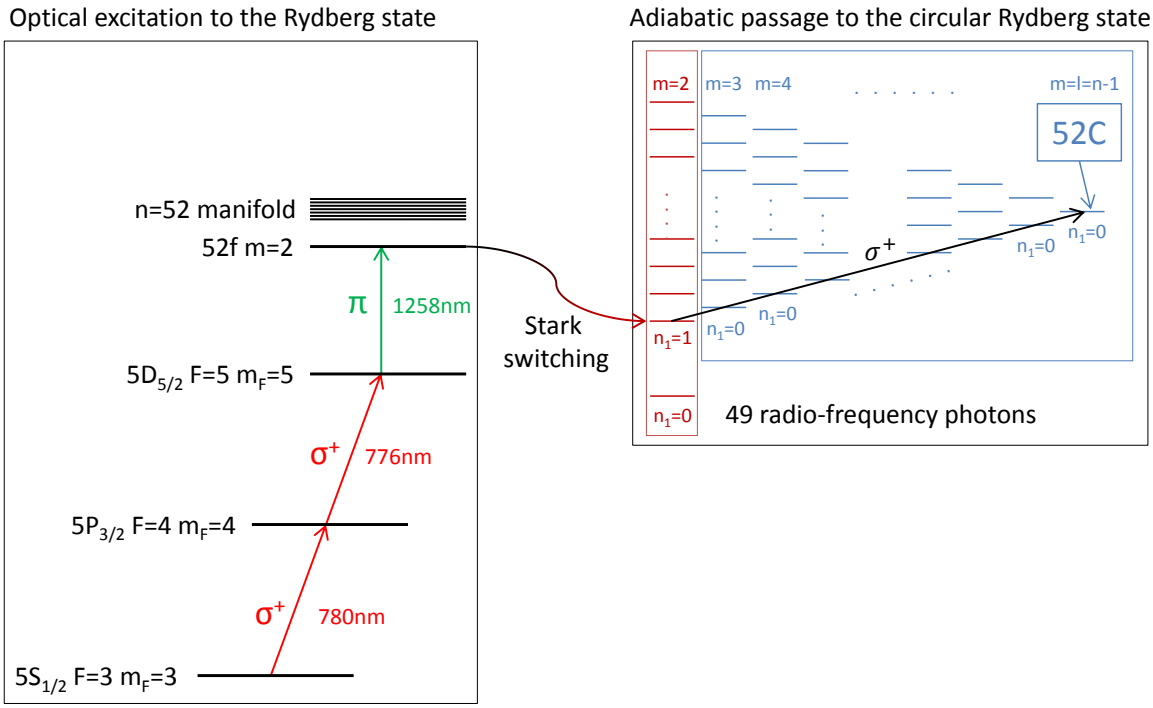

Figure 2.2: Preparation scheme of the circular Rydberg state. The atom is first excited in the $52f$ *Rydberg state by three optical photons (red and green, the colors correspond to the laser beams in Fig 2.1) in the presence of a small electric field: The* ^{85}*Rb atom is excited from the hyperfine level* $|5S_{1/2}, F = 3, m_F = 3\rangle$ *of the ground state to the* $|5P_{3/2}, F = 4, m_F = 4\rangle$ *state by a first* σ^+ *photon with a wavelength of 780 nm. A second* σ^+ *photon with a wavelength of 776 nm brings the atom in the* $|5D_{5/2}, F = 5, m_F = 5\rangle$ *state. A* π *photon with a wavelength of 1258 nm excites the atom to the final optical excited state* $|52, l = 3, m = 2\rangle$*. In the second step, after increasing the electric field so that the laser accessible* $52f$ *state can join the* $n = 52$ *manifold, the state of the atom is adiabatically transferred to the* $|52c\rangle$ *by 49 radio-frequency photons.*

2.2 Preparation and detection of the atoms

For most of the experiments presented in this work the atom is initially prepared in the circular Rydberg state $|52c\rangle$. In order to prepare this state, the atom needs to be provided with both energy and angular momentum. To this end, the atom in the ground state has to absorb three optical photons with well chosen polarizations and 49 σ^+ polarized radio-frequency photons in an adiabatic passage. The excitation scheme is shown in Fig. 2.2. The two essential steps, the optical excitation and the radio-frequency adiabatic passage are described in the following sections. We then describe the detection of the atomic state by ionization.

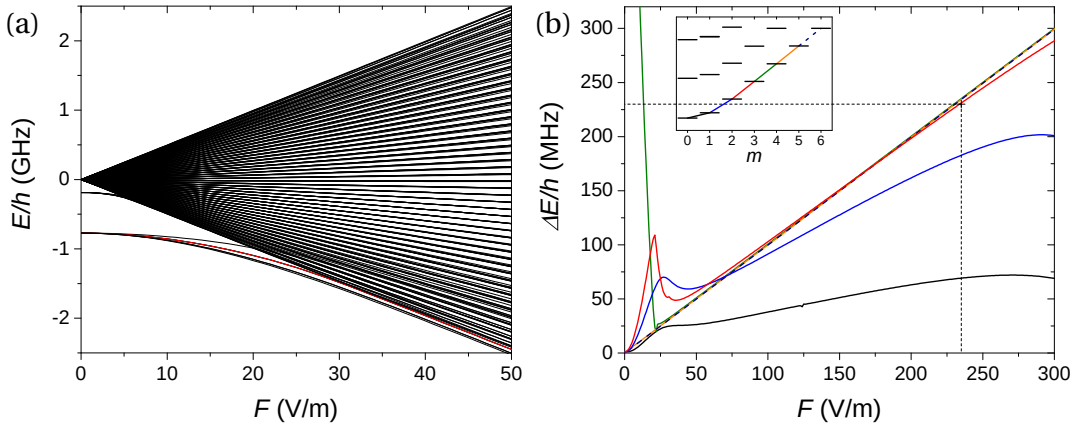

Figure 2.3: (a) Numerical calculation of the energy levels of the lowest σ^+ diagonal with $m = 0,1,2,3$ of the rubidium atom with $n = 52$ as a function of the electric field F, where the $|52f, m = 2\rangle$ state is highlighted (red). (b) The energy difference for selected $\Delta m = +1$ transitions (see inset for color code): $m = 0 \leftrightarrow 1$ (black) and $m = 1 \leftrightarrow 2$ (blue) are very different from the hydrogen-like transitions (green, yellow, dashed); $m = 2 \leftrightarrow 3$ (red) becomes resonant with the hydrogen-like transitions for an electric field ~200 V/m.

2.2.1 Laser excitation

The first step of the preparation is the laser excitation to the Rydberg state. The choice of the level that are prepared is due to two conditions. First, we need to excite a level whose energy is close to the manifold. Due to the quantum defect, the s, p and d states have energy eigenvalues far from the manifold. The f state, however, is relatively close to the manifold (only $E/h = 773$ MHz below the energy of the degenerated $n = 52$ manifold) so that this state adiabatically connects to the nearly hydrogen-like states when the electric field is increased, shown in Fig. 2.3a.

Second, we need to prepare a state that can be easily transferred into the circular state. As we have seen, states with $m < 3$ of the rubidium atom are not hydrogen-like. However, as shown in Fig. 2.3b, at $F \approx 230$ V/m, the transition frequency of the lowest $m = 2$ state to the lowest $m = 3$ state of the manifold is very similar to the frequency of the hydrogen like transition of the manifold (level structure in inset of Fig. 2.3b). This is why we initially prepare the $|52, l = 3, m = 2\rangle$ state, noted as "$52f$". Each photon can add one unit of orbital angular momentum $|\Delta l| = 1$. Since the atom is initially in an s ground state, we can reach a p state with one, a d state with two and an f state with three photons.

To prepare the 52f state the polarization of the laser photons plays an important role. We need a σ^+ polarized photon with a wavelength of $\lambda = 780.24$ nm, a σ^+ polarized photon with $\lambda = 775.97$ nm and a π polarized photon with $\lambda = 1258.38$ nm (see Fig. 2.2).

In order to have a pure σ^+ polarization, the quantization axis has to be along the direction of the laser beam of the σ^+ polarized photons. Therefore, the optical excitation is performed in a small electric field applied on the ring electrodes along the axis of the 780 nm & 776 nm laser beam direction, shown in Fig. 2.4a. The electric field is small enough so that the $52f$ state is still far away from the manifold, but large enough to lift

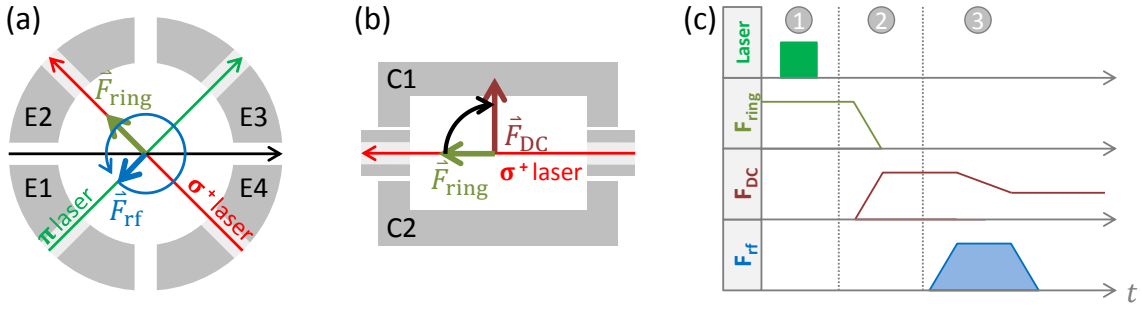

Figure 2.4: Top view (a) and side view (b) of the electrode structure and chronological sequence (c) of the preparation process. The laser beams, σ^+ (red) and π (green) intersect with the atomic beam (black) in the center of the electrode structure in a small electric field F_{ring} applied between electrodes E2 and E4 (step (1) in (c)). The quantization axis is then turned from the horizontal to the vertical direction with the plane capacitor electrodes C1 and C2 (step (2) in (c)). The adiabatic passage transfers the state of the atom in the circular state by applying an σ^+ polarized radio-frequency field (blue) with electrodes E1 and E2 while slowly reducing the static electric field F (step (3) in (c)).

the degeneracy between the states with different values of $|m|$ (see Fig. 2.3a). We typically use an electric field of ~23 V/m. This ensures that we excite only the $m = +2$ or $m = -2$ state, making it more fault tolerant to imperfections in the laser polarization.

The applied static electric field defines the quantization axis of the Rydberg state. Therefore, the directing electric field must not be changed too quickly, otherwise the initially well-defined Rydberg state mixes up with other states. However, when the electric field is changed slowly enough, the atomic state adiabatically follows the direction of the electric field and remains in its well-defined Rydberg state with respect to the new quantization axis. During the "Stark switching", we not only increase the electric field to typically ~200 V/m but also change its direction by reducing the electric field amplitude applied on the ring electrodes and increasing the one applied between the plane electrodes during 1 μs. As a result the atom goes from the $|52f, m = 2\rangle$ state with respect to the horizontal axis to the $|52, n_1 = 1, m = 2\rangle$ state with respect to the vertical axis.

To conclude the description of the laser excitation of the Rydberg atom, the lasers of wavelength 780 nm and 776 nm are continuous, whereas the laser of wavelength 1258 nm is pulsed with a duration of 1 μs. The angle between the laser beams and the atomic beam allow us to select the velocity of the atoms due to the Doppler effect. The typical speed of the atoms is ~ (2502 ± 7) m/s. A detailed description of the optical set-up can be found in [173].

2.2.2 Adiabatic passage to the circular Rydberg state

The circular Rydberg state $|51c\rangle$ is reached through an adiabatic passage in which the atom absorbs 49 radio-frequency photons of $\omega_{rf} = 2\pi \cdot 230$ MHz, each adding $\Delta m = +1$ to the magnetic quantum number. In order to only drive $\Delta m = +1$ transitions the radio-frequency field has to be polarized purely σ^+. In the case of an applied radio-frequency

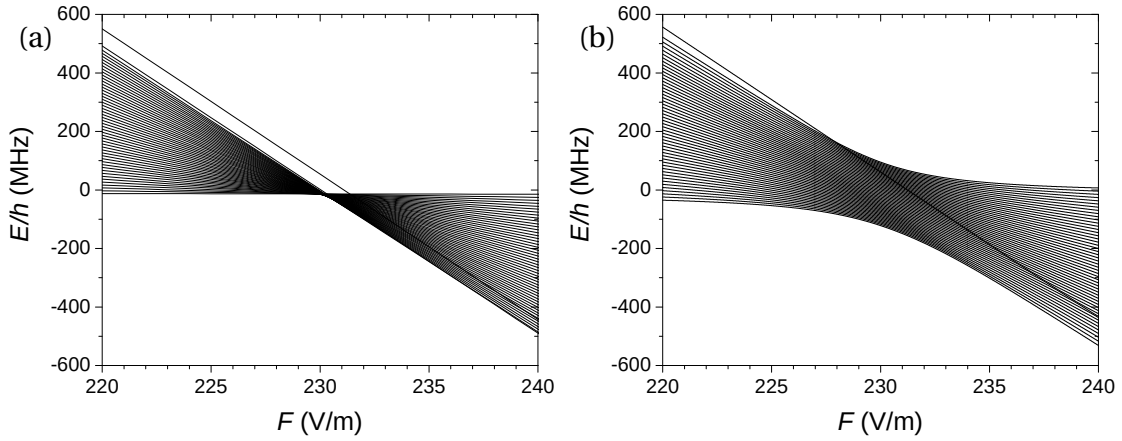

Figure 2.5: Numerically calculated rubidium levels dressed by the radio-frequency photons without (a) and with applied radio-frequency field (b). The horizontal level is the $|52c\rangle$ *state. The levels with the highest Stark shift, and therefore largest slope, are the* $|52, n_1 = 1, m = 2\rangle$ *state and the* $|52, n_1 = 2, m = 1\rangle$ *state. The latter is separated from the manifold and not involved in the adiabatic passage. The bare states in (a) cross at* ~ 230 *V/m. The dressed states in (b) show a large anti-crossing where the* $m = 2$ *state at high electric field connects to the circular state at low electric field.*

field with σ^+ and σ^- polarized components, we would also drive $\Delta m = -1$ transitions and would not reach the circular state (see Fig. 2.2).

In an electric field ~200 V/m, the transitions to the $m = 1$ and $m = 0$ states can be neglected, since this electric field amplitude the transitions $m = 1 \leftrightarrow 2$ and $m = 0 \leftrightarrow 1$ are far from the resonant transitions $m = 2 \leftrightarrow 3$, $m = 3 \leftrightarrow 4$, etc. (see Fig. 2.3b). The lowest level in the adiabatic passage is therefore the initial $|52, n_1 = 1, m = 2\rangle$ state.

The energy eigenvalues of the involved levels can now be represented using the dressed state picture. The bare states are $|52, n_1, m, N_{\mathrm{rf}} + 51 - m\rangle$, where $N_{\mathrm{rf}} + 51 - m$ is the number of radio-frequency photons. Fig. 2.5a shows the bare states of the lowest σ^+ diagonal where the energy of N_{rf} radio-frequency photons of $\omega_{\mathrm{rf}} = 2\pi \cdot 230$ MHz is added to the atomic energy. When the radio-frequency field is applied the dressed states form a huge anti-crossing in which the two extremal levels, the initial $|52, n_1 = 1, m = 2\rangle$ and the final $|52c\rangle$ state, are connected, shown in Fig. 2.5b.

In order to drive the adiabatic passage we set the electric field to $F = 240$ V/m so that $\delta = \omega_{\mathrm{at}} - \omega_{\mathrm{rf}} = 2\pi \cdot 10$ MHz. The radio-frequency field power is increased in 0.5 μs. The electric field F is then ramped down linearly in 1.5 μs to 220 V/m so that $\delta = -2\pi \cdot 10$ MHz. During this frequency ramp, the atomic frequency ω_{at} crosses the resonance. Finally, the radio-frequency is switched off in 0.5 μs (see Fig. 2.4c). The ramping of the radio-frequency field in 0.5 μs allows, first, that the $|52, n_1 = 1, m = 2\rangle$ state at $\delta = 2\pi \cdot 10$ MHz from the anti-crossing to connect to the radio-frequency dressed state

$$|52, n_1 = 1, m = 2, N_{\mathrm{rf}} + 49\rangle + \epsilon\,|52, n_1 = 0, m = 3, N_{\mathrm{rf}} + 48\rangle + \ldots$$

with $\epsilon \ll 1$. Second, after the adiabatic passage, this allows to connect the radio-frequency

dressed state

$$|52, n_1 = 0, m = 51, N_{\text{rf}} + 0\rangle + \epsilon\,|52, n_1 = 0, m = 50, N_{\text{rf}} + 1\rangle + \ldots$$

to the final state $|52, n_1 = 0, m = 51\rangle = |52c\rangle$. The typical Rabi frequency of the radio-frequency field is of $\Omega_{\text{rf}} \approx 2\pi \cdot 3$ MHz. With this method we can reach a transfer efficiency larger than 98% [176].

Finally, a microwave π pulse ("purification") transfers the population of the $|52c\rangle$ state in the $|51c\rangle$ state.

2.2.3 Detection by ionization

Due to the proximity of the energy of the states to the continuum, the atoms can be ionized in a relatively small electric field.

The detection zone itself consists up of two conducting plates on which the ionization voltage is applied. The plate on which the positive voltage is applied has a small hole. The plate on which the negative voltage is applied has a small ramp facing the hole. This creates an electric field gradient that ensures that only the states for which the ionization threshold corresponds to the electric field at the position of the hole ionize in front of the hole (states with ionization thresholds smaller or larger ionize before or after). The free electron is then accelerated through the hole towards the channeltron, where it is detected. To obtain the ionization signal, the experiment is repeated while scanning the voltage applied on the detector. Then, we set the voltage to the value corresponding to the state we want to detect. The width of the hole and the slope of the ramp determine the resolution of our detector.

The electric field required to separate the electron from the ionic core depends on the state of the atom [177]. For states with similar wave-functions, for instance circular states with different principal quantum numbers n, the states with higher n get ionized at smaller electric fields, since they have a smaller binding energies, as shown in Fig 2.6a. However, the ionization threshold does not only depend on n. For instance, the circular state $|52c\rangle$ ionizes at a much higher ionization field than the lower energy state $52f$, or more accurately the state $|52, n_1 = 1, m = 2\rangle$, shown in Fig 2.6b.

We can understand this semi-classically by looking at the potential seen by the electron in the presence of an electric field, which adds a eFz term to the e^2/r Coulomb potential, as shown in Fig. 2.7. This creates a saddle point in the potential, opening a way for the electron to leave the attraction of the core. When the electric field is ramped up, the $52f$ state evolves adiabatically into the state $|52, n_1 = 1, m = 2\rangle$ whose wave-function is mostly localized in the $z < 0$ region (see Fig. 1.9 for wave functions). Since this is the region where the saddle point is, this makes it easier for the electron to ionize. The circular wave-function, on the other hand, is localized in the $z = 0$ plane and does not explore the region of the saddle point where the electron can escape, making it harder to ionize this state with respect to the $52f$ state. The ionization threshold of the $52f$ states is therefore lower than that of the circular state.

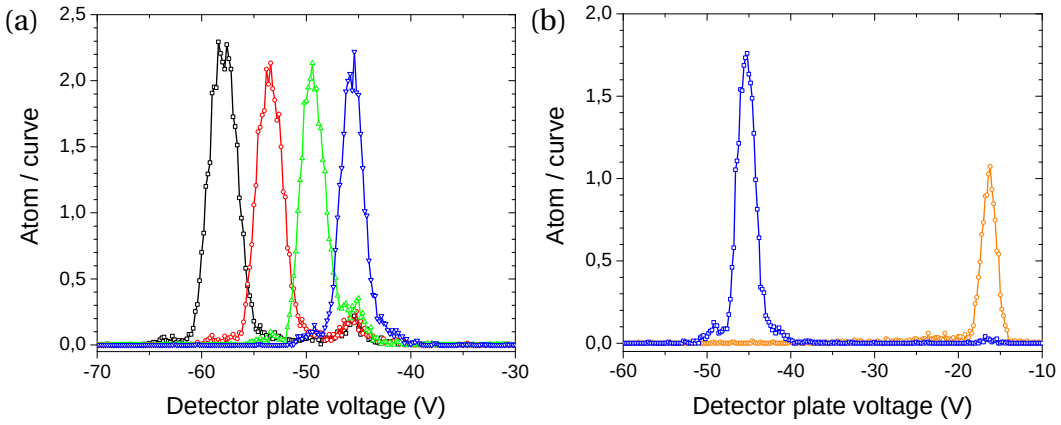

Figure 2.6: (a) The ionization signals of different circular Rydberg states are shown as a function of the voltage applied on the detector plate with the ramp. Since the detector plate with a hole is at 0 V, the ionization field is proportional to the applied voltage. The circular states shown are $|49c\rangle$ *(black),* $|50c\rangle$ *(red),* $|51c\rangle$ *(green) and* $|52c\rangle$ *(blue). (b) The ionization signal of the circular Rydberg state* $|52c\rangle$ *(blue) and the elliptic state* $52f$ *(orange). The difference in height is due to the lifetime of the state and the detection parameters which are optimized for the circular states.*

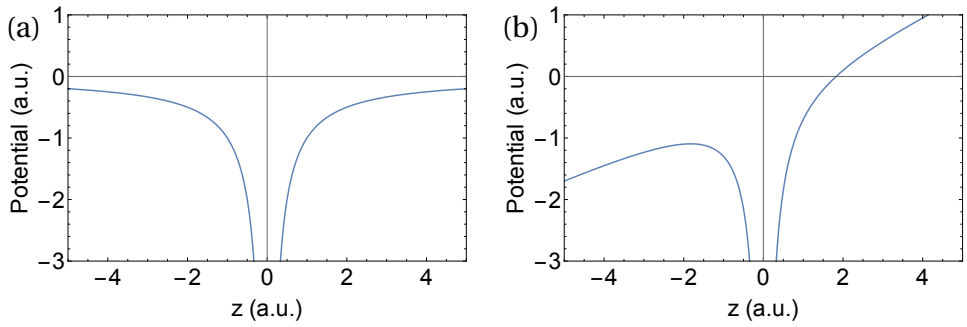

Figure 2.7: (a) The Coulomb potential e^2/r *plotted as a function of the vertical direction* z*. (b) The applied electric field adds a* eFz *term which tilts the potential.*

The $52f$ state lies on the σ^+ diagonal connected to the $|52c\rangle$ state. Levels on this diagonal are more localized in the $z<0$ region when m decreases (see Fig. 1.9). Therefore, the necessary electric field to let the electron escape from the core potential gradually decreases from the circular to the $m=2$ state.

The effect is reversed for the levels on the σ^- diagonal connected to the $|52c\rangle$ state. The levels above the circular state have wave-functions which are localized in the $z>0$ region, leading to an ionization threshold higher than that of the circular state.

The ionization thresholds for states with similar energy eigenvalues are close and cannot be resolved properly by our detector, as shown in Fig. 2.8 for $|49c\rangle$, $|49e1\rangle$ and $|49e1'\rangle$. Therefore, we employ microwave probe pulses which selectively transfer the population of a given state into another manifold, which can then be resolved by ionization. The selectivity of the microwave probes comes from the differential Stark shift between two manifolds, shown in Fig. 2.9. The differential Stark shift between adjacent transitions

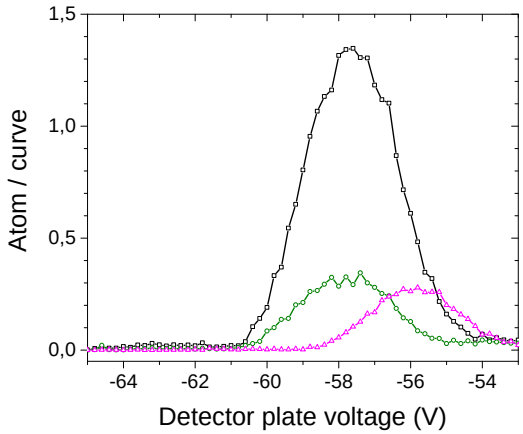

Figure 2.8: (a) The ionization signal of Rydberg states close to the circular state is shown as a function of the voltage applied on the detector plate with the ramp. Since the detector plate with a hole is at 0 V, the applied voltage is proportional to the ionization field. The Rydberg states shown are $|49c\rangle$ *(black),* $|49e1\rangle$ *(pink) and* $|49e1'\rangle$ *(dark green). The difference in height is due to the different preparation methods.*

between manifold n and n' is given in first order by (Eq. 1.11)

$$\Delta\omega_{\text{at}} = \frac{3}{2}\frac{ea_0}{\hbar}(n-n')F.$$

The difference in differential Stark shift for $n = 52$ and $n' = 51$ in an electric field of $F \approx 235$ V/m is $\Delta\omega_{\text{at}} \approx 2\pi\cdot 4.5$ MHz. This frequency difference can easily be resolved by the microwave pulses we apply usually, which have a spectral width of ~ 500 kHz for a $\sim 2\mu$s pulse duration.

It is in principle possible to resolve states with the same linear Stark shift, due to the second order Stark shift using longer microwave probe pulses and an increased electric field amplitude [176]. This technique, however, is not used in this manuscript.

2.3 Manipulation of the atomic state

There are different tools available to manipulate the state of the atom. Microwave pulses allow us to transfer the population from one state of manifold n to another state of manifold $n' \neq n$ (Sec. 2.3.1). Radio-frequency pulses allow us to drive transitions between levels of a given manifold. By controlling the polarization of the radio-frequency field we can selectively drive $\Delta m = +1$ or $\Delta m = -1$ transitions. The optimization process of the σ^+ polarized radio-frequency will be described in Sec. 2.3.2.

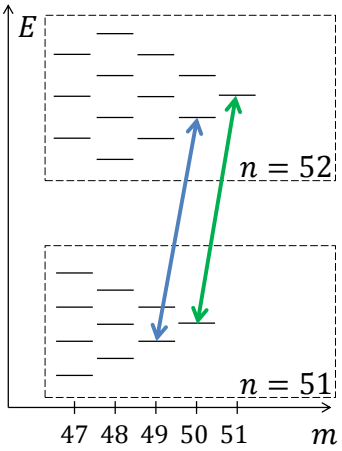

Figure 2.9: Due to the differential Stark shift, the blue and green transitions have different frequencies, which allows to selectively transfer the population from a given state to a different manifold.

2.3.1 Microwave field

Frequency sources in the microwave range, offering a sub-Hz precision, are infinitely narrow compared to the atomic transitions. The microwave field therefore offers a powerful tool to manipulate and analyse the state of the atom.

In order to generate frequencies around 50 GHz, the typical transition frequency between adjacent manifolds for $n \approx 50$, we use a synthesizer Anritsu-MG3692 which produces a signal of about 12.5 GHz. A non-linear element, called a mixer, then generates higher order harmonics of the microwave radiation. The frequency of the initial signal is adjusted so that the fourth order harmonics corresponds to the frequency resonant with the targeted transition of the atom.

We then have two options to bring the microwave radiation inside the cryostat:

With a first source, installed in [154], the microwave radiation is coupled into a coaxial cable by an adapter that is single mode for frequencies between 50 GHz and 75 GHz. The microwave field is brought inside the cryostat by coaxial cables, with a cut-off frequency of 60 GHz. Finally, it is coupled to an antenna that radiates into a circular wave-guide which ends far from the experimental zone. From there on, the microwave field gets reflected from all copper surfaces and creates stationary modes with a random polarization. This leads to stationary microwave modes polarized π, σ^+ and σ^-. The amplitude of each polarization seen by the atom varies with the applied frequency but also with the position along the atom trajectory.

With a second source, installed in this work, the microwave radiation is coupled in a second coaxial cable by an adapter that is single mode for frequencies between 40 GHz and 60 GHz. Once inside the cryostat, the microwave radiation is coupled out of the coaxial cable with a second adapter (40 GHz to 60 GHz) close to one of the free entry holes between the ring electrodes, much closer to the experimental zone. The coax-to-

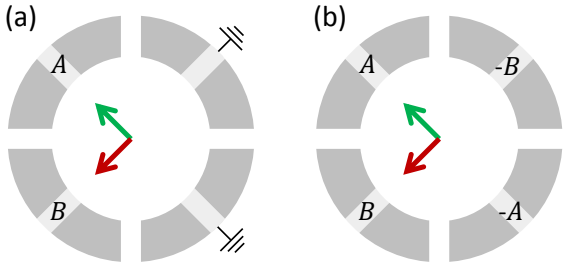

Figure 2.10: (a) The radio-frequency signals A and B is applied on two ring electrodes. (b) To improve the homogeneity of the radio-frequency field the Rf signal A and −A, and B and −B are applied on opposite electrodes.

waveguide adapter generates a microwave field with a well defined linear polarization. We hoped that placing the adapter closer to the experimental set-up would allow us to have a microwave field with a more controlled polarization. The anticipated better homogeneity of the microwave field was unfortunately not observed. However, having two different sources provides us with two different stationary wave structures along the trajectory of the atoms at a given frequency, which can be useful when optimizing the microwave pulses, since we have no control over the stationary mode structures.

Additionally, the lower frequency in the second source allows, in principle, transitions to higher Rydberg manifolds.[2] We currently work in a frequency range between 47 GHz and 54 GHz which corresponds to transitions between the $n = 49$ and $n = 52$ manifolds.

2.3.2 Radio-frequency field optimization

To control which transition we drive with the radio-frequency field, we need to apply a well-defined polarization. The radio-frequency field is created by connecting radio-frequency synthesizer outputs to the ring electrodes. In principle, each electrode, when driven by an radio-frequency signal, creates a radio-frequency field with linear polarization. By applying radio-frequency signals of same amplitude shifted in phase by $\pm\pi/2$ on two neighbouring electrodes, we can generate a $\sigma^{\pm}$ polarized radio-frequency field, see Fig. 2.10a.

However, the situation is more complex in practice. On the one hand, due to the difference in the transmission of the line that brings the radio-frequency signal down to the electrodes inside the cryostat, we need to optimize the relative phase and amplitude of the drive of the electrodes by using the atoms as microscopic probes of the polarization. On the other hand, a single electrode creates a radio-frequency field with a gradient in its amplitude along the trajectory of the atoms. In order to create a homogeneous radio-frequency field, it is better to apply a radio-frequency signal with opposite phase on opposite electrodes, see Fig. 2.10b.

In order to be able to apply radio-frequency fields with different frequency or different

[2] The transitions to higher Rydberg manifolds were not a success so far.

phases on the atoms, each electrode is connected to two or three different radio-frequency synthesizer outputs. The full radio-frequency circuit is shown in Fig. 2.11. The σ^+ radio-frequency field used for the adiabatic passage to circularize the Rydberg atoms is generated by a PCI RF card with two outputs, shown in Fig. 2.11a, which are connected to two ring electrodes. The amplitude of the radio-frequency field is controlled by mixers. A first DC power supply allows us to vary the relative amplitude between the two signals. Then a pair of mixers controlled by the same arbitrary waveform generator (AWG) allows us to vary the pulse shape of both radio-frequency signals.

The radio-frequency field used for the metrology experiments are generated by two radio-frequency synthesizer "H" and "N" with four outputs each, shown in Fig. 2.11b, connected to the four ring electrodes. Here, the amplitude is controlled by the experiment control software and the shape of the radio-frequency pulses is created by a high-resolution AWG which allows us to create very short radio-frequency pulses. The signal of the AWG is applied on three mixers, which are used as switches.

The power and phase of each radio-frequency signal has to be optimized on the atomic signal. However, the optimization procedure itself depends on the final purpose of the radio-frequency field.

During this work we implemented several improvements: We added a second synthesizer to have two independent radio-frequency outputs per electrode for the metrology experiments. We installed a new arbitrary waveform generator (Tektronix AWG5012B) with a time resolution of down to 0.8 ns,[3] compared to 10 ns in the previous version. We developed a program to integrate this device in our experiment control software which was not the case with the former AWG.

2.3.2.a Optimization of the radio-frequency for the adiabatic passage

The radio-frequency field generated by the PCI RF cards is directly optimized on the adiabatic passage. We first roughly equalize the amplitudes created by each PCI RF card output by balancing the Rabi frequency induced by a radio-frequency field on a two-level system of two low-m states. The full method can be found in [176]. We then scan the relative phase of the signal applied on the two electrodes until we see a peak at the ionization threshold of the $|52c\rangle$ circular state. Once we have a significant amount of atoms near the circular state, we apply a microwave π pulse that selectively transfers the $|52c\rangle$ to the $|51c\rangle$ state. We optimize the relative phase and amplitude of the two PCI RF card outputs to maximize the number of atoms transferred to the $|51c\rangle$ state. This transfer is at its maximum when the adiabatic passage from the $52f$ to the $|52c\rangle$ state is the most effective and only the $|52c\rangle$ state is populated. We then have a pure σ^+ polarized radio-frequency field.

[3] Tektronix AWG5012B with 1.2 GS/s, two independent analogue outputs, four independent digital "marker" outputs, bandwidth up to 370 MHz.

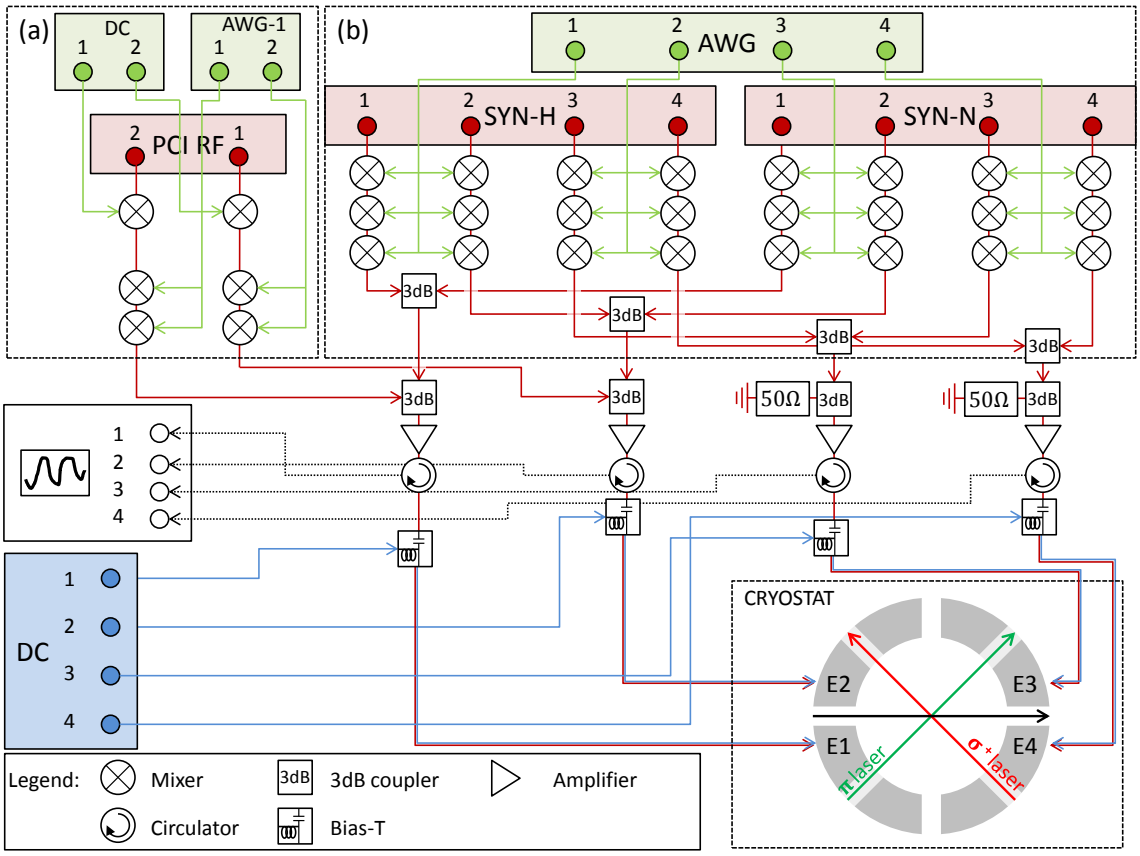

Figure 2.11: Cabling of the radio-frequency circuit for the adiabatic passage (a) and for the metrology sequence (b): (a) The radio-frequency signal is generated by a PCI RF card. The pulses are shaped by an arbitrary waveform generator. (b) The radio-frequency signal is generated by two synthesizers with four outputs each. The pulses are shaped by a high-resolution arbitrary waveform generator. All signals applied on the same electrode are combined through 3 dB couplers before they are amplified and passed through a circulator. We add the DC field via Bias-T. The signal is then applied to the electrodes by coaxial cables.

2.3.2.b Optimization of the radio-frequency for the metrology sequence

The polarization of the signal generated by the PCI RF cards is optimized on a 2.2 μs long radio-frequency pulse. In the metrology experiment we use much shorter radio-frequency pulses and need a more homogeneous radio-frequency field. We therefore implemented a different method to optimize the polarization of the radio-frequency field for the metrology sequences. We developed a technique that allows us to optimize the polarization using much shorter radio-frequency pulses with the power that is used in the experiment.[4]

We optimize the polarization of the radio-frequency field at a given frequency, $\omega_{\mathrm{rf}} = 2\pi \cdot 230$ MHz resonant in the $n = 51$ manifold in a static electric field of $F = 234.5$ V/m.

[4] It is possible to globally change the radio-frequency power by changing the amplitude of the signal of the AWG applied on the mixers. However, the non-linearity of the mixers might degrade the polarization. This is why we optimize the polarization at the final power that is used in the experiment.

If the atom is initially in the $|51c\rangle$ circular state, the state of the Rydberg atom after a radio-frequency field pulse of duration $t_{\rm rf}$ is (Eq. 1.29)

$$|\Psi(t_{\rm rf})\rangle \propto |\theta_1,\phi_1\rangle \otimes |\theta_2,\phi_2\rangle = |\boldsymbol{J}_1(t_{\rm rf})\rangle \otimes |\boldsymbol{J}_2(t_{\rm rf})\rangle\,,$$

where $|\theta_1,\phi_1\rangle$ and $|\theta_2,\phi_2\rangle$ are the spin coherent states due to the rotation induced by the σ^+ and σ^- polarized radio-frequency field respectively and where $\boldsymbol{J}_1(t_{\rm rf})$ and $\boldsymbol{J}_2(t_{\rm rf})$ correspond to the vectors pointing at the (θ_1,ϕ_1) and (θ_2,ϕ_2) direction of the Bloch sphere.

In principle, in the presence of both σ^+ and σ^- polarizations, the dynamics of the atom explores the full manifold. As a result we would have to measure the population of a lot of levels to characterize the relative amplitude of σ^+ and σ^-. However, it is possible to narrow down the number of levels whose population we need to measure by using an off-resonant drive. If the radio-frequency is detuned with respect to the atomic frequency, the dynamics is that of off-resonant Rabi oscillations.

Since the radio-frequency field has a fixed frequency, we prepare the atom in the $n = 50$ manifold instead of the $n = 51$ manifold, so that the atomic frequency is detuned with respect to the radio-frequency. The time-independent Hamiltonian inside a the $n = 50$ manifold is given by (see Sec. 1.1.7)

$$\tilde{H} = \hbar\delta_+ \hat{J}_{1z} - \hbar\delta_- \hat{J}_{2z} + \Omega_{\rm rf}^+ \hat{J}_{1x} + \Omega_{\rm rf}^- \hat{J}_{2x} \tag{2.1}$$

where $\Omega_{\rm rf}^+$ and $\Omega_{\rm rf}^-$ are the Rabi frequencies of the σ^+ and σ^- polarized components of the radio-frequency field (Eq. 1.26). The detuning δ_+ and δ_- are calculated from the difference of the radio-frequency to the transition frequency between the $|50c\rangle$ circular state and its two nearest neighbours. The transition frequency between the states $|50c\rangle$ and $|50e1\rangle = |50, n_1 = 0, n_2 = 1, m = 48\rangle$ ($|50e'1\rangle = |50, n_1 = 1, n_2 = 0, m = 48\rangle$ respectively) is 225.49 MHz (224.56 MHz) for an electric field of $F = 234.5$ V/m. The difference is due to the quadratic Stark effect. This leads to two different detunings $\delta_+ = 2\pi \cdot 4.51$ MHz and $\delta_- = 2\pi \cdot 5.44$ MHz for a radio-frequency of $\omega_{\rm rf} = 2\pi \cdot 230$ MHz.

The detuning between atomic frequency and radio-frequency leads to an off-resonant dynamics where the vectors $\boldsymbol{J}_1(t_{\rm rf})$ and $\boldsymbol{J}_2(t_{\rm rf})$ rotate around an axis $(\Omega_\pm, 0, \delta_\pm)$ close to the vertical direction, with rotation frequency $(\Omega_\pm^2 + \delta_\pm^2)^{1/2}$. The vectors therefore return periodically to the north pole of the Bloch sphere. The probability to find the atom in the circular state $|50c\rangle = |j_1, m_1 = j_1\rangle \otimes |j_2, m_2 = j_2\rangle$, after a radio-frequency pulse applied for time $t_{\rm rf}$, is given by

$$P_{|50c\rangle}(t_{\rm rf}) = |\langle 50c|\Psi(t_{\rm rf})\rangle|^2 = |\langle j_1, j_1|\boldsymbol{J}_1(t_{\rm rf})\rangle|^2 \cdot |\langle j_2, j_2|\boldsymbol{J}_2(t_{\rm rf})\rangle|^2, \tag{2.2}$$

consisting in two independent terms for $|\boldsymbol{J}_1(t_{\rm rf})\rangle$ and $|\boldsymbol{J}_2(t_{\rm rf})\rangle$. The analytical expression is given in Appendix B.1.

The left column of Fig. 2.12 shows the trajectory of the vectors $\boldsymbol{J}_1(t_{\rm rf})$ and $\boldsymbol{J}_2(t_{\rm rf})$ on the Bloch sphere. The right column Fig. 2.12 presents the probability to return to the north pole for the $\boldsymbol{J}_1(t_{\rm rf})$ and $\boldsymbol{J}_2(t_{\rm rf})$ vectors, given by the overlaps $P_1(t_{\rm rf}) = |\langle j_1, j_1|\boldsymbol{J}_1(t_{\rm rf})\rangle|^2$ and $P_2(t_{\rm rf}) = |\langle j_2, j_2|\boldsymbol{J}_2(t_{\rm rf})\rangle|^2$, as a function of the radio-frequency duration $t_{\rm rf}$. Due to the quadratic Stark shift, δ_+ and δ_- are different and therefore $\boldsymbol{J}_1(t_{\rm rf})$ and $\boldsymbol{J}_2(t_{\rm rf})$ do not have

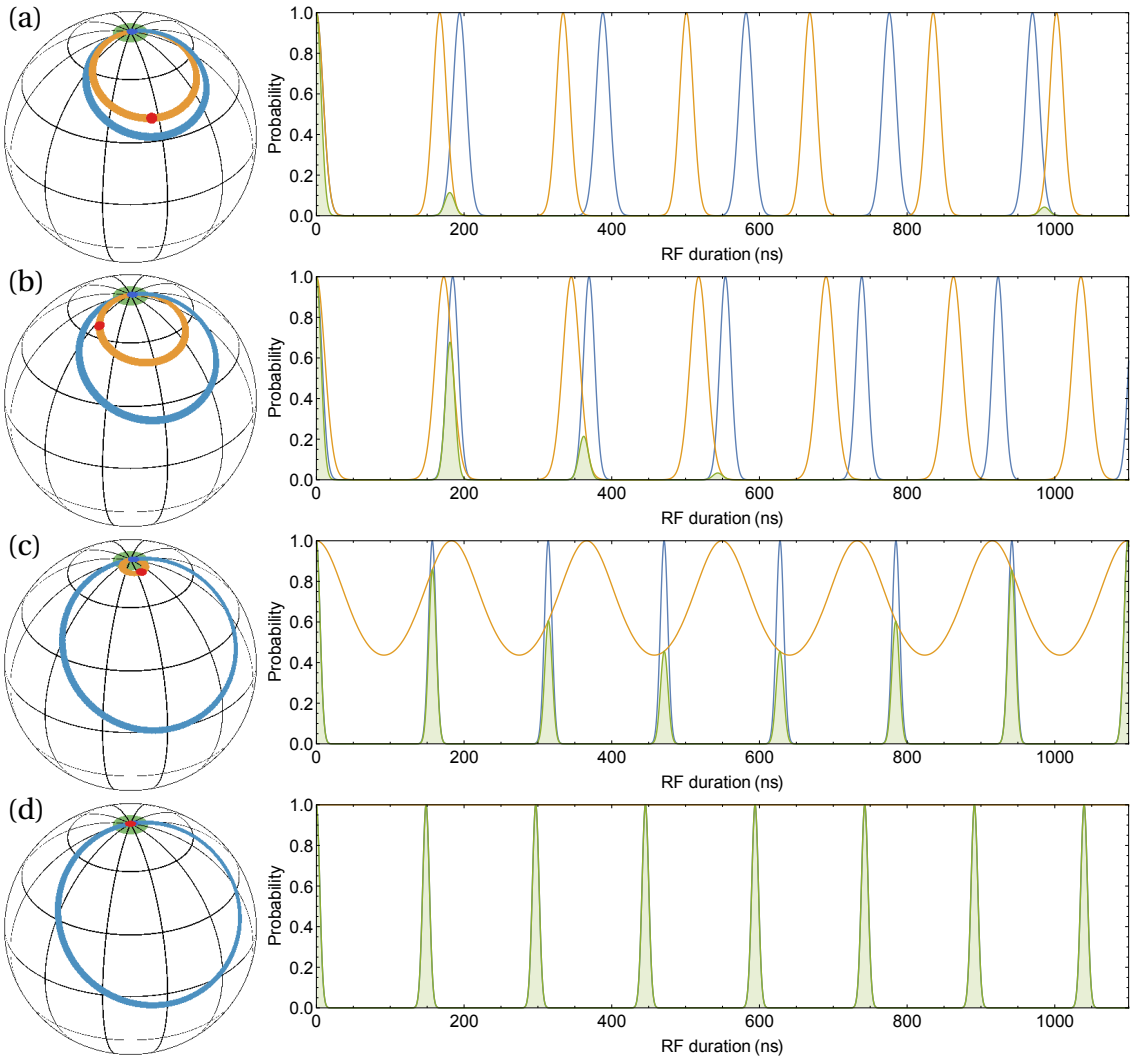

Figure 2.12: Left column: Trajectory of the vectors $\boldsymbol{J}_1(t_{rf})$ (blue) and $\boldsymbol{J}_2(t_{rf})$ (orange) on the Bloch sphere. The red dot indicates the position of the vector $\boldsymbol{J}_2(t_{rf})$ at the radio-frequency pulse duration corresponding to the third time that the $\boldsymbol{J}_1(t_{rf})$ vector returns to the circular state (green circle at the north pole of Bloch sphere). Right column: Analytical calculations of the probabilities $P_1(t_{rf})$ (blue) and $P_2(t_{rf})$ (orange), as well as the probability to find the state in the circular state $P_{|50c\rangle}(t_{rf}) = P_1(t_{rf})P_2(t_{rf})$ (green, shaded), plotted as a function of the radio-frequency pulse duration t_{rf}. Each line corresponds to a different ratio $R = (\Omega_+ - \Omega_-)/(\Omega_+ + \Omega_-)$ with $\Omega_+ + \Omega_- = 2\pi \cdot 5$ MHz between the Rabi frequencies for the σ^- and the σ^+ component of the field. For $R = 0$ (a), the two components are equally balanced between ($\Omega_+ = \Omega_-$), for $R = 0.2$ (b) and $R = 0.8$ (c) the σ^+ component becomes dominant $\Omega_+ > \Omega_-$ until $R = 1$ (d), the σ^- vanishes completely ($\Omega_- = 0$). The analytic expressions used in this graph are given in Appendix B.1.

the same rotation frequencies. Therefore $\boldsymbol{J}_1(t_{\mathrm{rf}})$ and $\boldsymbol{J}_2(t_{\mathrm{rf}})$ do not return to the north pole at the same time. Every time $\boldsymbol{J}_1(t_{\mathrm{rf}})$ returns to the north pole, the probability to find the atom in the circular state depends on the direction of $\boldsymbol{J}_2(t_{\mathrm{rf}})$. To find the atom in the circular state, both vectors have to point to the north pole. Since the two vectors do not rotate with the same frequency, this is only the case if the vector $\boldsymbol{J}_2(t_{\mathrm{rf}})$ remains at the north pole all the time. This implies that the σ^- component of the radio-frequency field can be minimized by maximizing the probability to return to the circular state at a well chosen radio-frequency duration.

The principle of the optimization can be understand from Fig. 2.12. We first generate an arbitrary radio-frequency field by driving to neighbouring electrodes with two independent output of a synthesizer and generate a pulse of duration t_{rf} that correspond to a the third blue peak of Fig. 2.12. We then vary the relative phase and relative amplitude between the two radio-frequency driving signals in order to maximize the the probability to find the atom in the $|50c\rangle$ state (green line). We can see on the figure that the smaller the σ^- polarized component is, the higher the probability to find the atom in $|50c\rangle$ becomes. This gives us a quantitative criteria for the optimization process. In the limit where $\Omega_\pm \ll \delta_\pm$, the oscillation frequency only depends on $\delta_\pm$ and $\boldsymbol{J}_1(t_{\mathrm{rf}})$ or $\boldsymbol{J}_2(t_{\mathrm{rf}})$ return to the north pole every $1/\delta_+$ or $1/\delta_-$ respectively, see Fig. 2.12a. However, the Rabi frequencies of the $\sigma^\pm$ components, Ω_+ and Ω_-, are related. When we minimize Ω_-, we increase Ω_+. With the typical radio-frequency power used in the experiment, we then reach a regime where Ω_+ is no longer negligible with respect to δ_+. The position of the peak of the probability $P_1(t_{\mathrm{rf}}) = |\langle j_1, j_1|\boldsymbol{J}_1(t_{\mathrm{rf}})\rangle|^2$ to return to the north pole (blue line in Fig. 2.12b,c,d) is no longer independent of Ω_+. Maximizing the probability of return to the $|50c\rangle$ circular state for a given radio-frequency duration t_{rf} is dangerous, since we end up optimizing the power of the σ^+ component to have the peak of the $P_1(t_{\mathrm{rf}})$ probability at the chosen duration t_{rf} instead of minimizing the σ^- component. In other words, with this method we have to optimize on a "moving peak". We therefore have to develop a more efficient method.

2.3.2.c New method to optimize of the radio-frequency for the metrology sequence

Our optimization method is based on a Ramsey-like experiment, shown in Fig. 2.13a. We first apply a short radio-frequency pulse (~40 μs) that rotates the $\boldsymbol{J}_1$ and $\boldsymbol{J}_2$ vectors away from the north pole. We then wait for a time t_{delay}. We finally apply a second short radio-frequency pulse with the same duration and phase. During the waiting time the angular momenta $\boldsymbol{J}_1$ and $\boldsymbol{J}_2$ precess around the z axis at the frequencies δ_+ and δ_- respectively in the rotating frame. Periodically, the angular momentum vectors $\boldsymbol{J}_1$ and $\boldsymbol{J}_2$ pass through the position where the second radio-frequency pulse brings the state back to the north pole, as shown in Fig. 2.13bc.

The probabilities $P_1(t_{\mathrm{delay}}) = |\langle j_1, j_1|\boldsymbol{J}_1(t_{\mathrm{delay}})\rangle|$ and $P_2(t_{\mathrm{delay}}) = |\langle j_2, j_2|\boldsymbol{J}_2(t_{\mathrm{delay}})\rangle|$ to return to the north pole for the vectors $\boldsymbol{J}_1(t_{\mathrm{delay}})$ and $\boldsymbol{J}_2(t_{\mathrm{delay}})$ as a function of the delay t_{delay} between the two radio-frequency pulses are shown in Fig. 2.14. We see that the probabilities have peaks which are regularly spaced in time as a function of t_{delay}. The position of the peaks is roughly half integer of $(\delta_\pm)^{-1}$. This position depends a lot less on

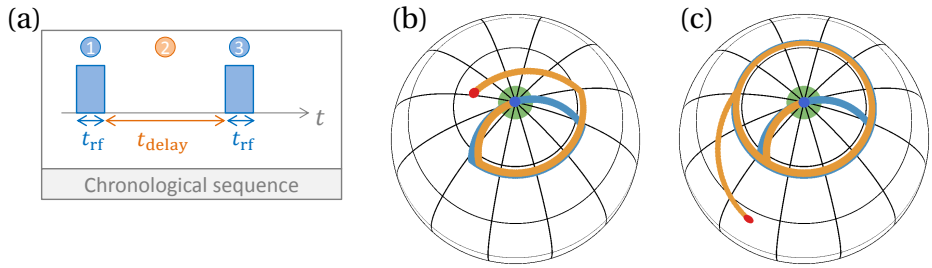

Figure 2.13: (a) Chronological sequence of the optimization method as a function of the time. The two radio-frequency pulses (blue) are applied with a variable delay t_{delay} (orange). (b,c) The trajectory of the vectors $\boldsymbol{J}_1$ (blue) and $\boldsymbol{J}_2$ (orange) on the Bloch sphere is shown for two values of t_{delay}. A first radio-frequency pulse brings $\boldsymbol{J}_1$ and $\boldsymbol{J}_2$ away from the north pole. During a time $_{delay}$, they rotate around the vertical axis at the frequencies δ_+ and δ_-. Then we apply the second radio-frequency pulse. By carefully choosing t_{delay}, we can make sure that the second radio-frequency pulse brings $\boldsymbol{J}_1$ back to the north pole. However, since $\delta_+ \neq \delta_-$, the second radio-frequency pulse does not bring back $\boldsymbol{J}_2$ to the north pole (b). By choosing $t_{delay} \sim \frac{1}{2}(\delta_+ - \delta_-)^{-1}$, we can ensure that the second radio-frequency pulse brings $\boldsymbol{J}_2$ even further away from the north pole (c).

the Rabi frequency $\Omega_\pm$ as can be seen in Fig. 2.14.

To optimize the polarization of the radio-frequency field, the duration of delay is fixed on a peak of the probability $P_1(t_{\text{delay}})$ (blue line in Fig. 2.14) close to $t_{\text{opt}} = \frac{1}{2}(\delta_- - \delta_+)^{-1} =$ 538 ns. This corresponds to the third peak at $t_3 = 504$ ns. After this waiting time, the vectors $\boldsymbol{J}_1$ and $\boldsymbol{J}_2$ are in phase opposition, since $\boldsymbol{J}_2$ has accumulated half a turn more with respect to $\boldsymbol{J}_1$ (see Fig. 2.13c). The probability to find the atom in the circular state (green line in Fig. 2.14) after a delay corresponding to the third peak, is thus extremely sensitive to the presence of a small σ^- component.

Finally, to optimize the polarization experimentally, we measure not only the probability to find the atom in the circular state $|50c\rangle$, but also in the elliptical state $|50e1'\rangle$. Fig. 2.15 demonstrates analytically the robustness of this method to experimental imperfections. Fig. 2.15a presents the expected probability $P_{|50c\rangle}(t_3)$ as we simulate optimizing the relative phase between the two electrodes, both creating σ^+ and σ^- of the same amplitude, $\Omega_+ = \Omega_-$ ($R = 0$). Fig. 2.15c presents the expected probability $P_{|50c\rangle}(t_3)$ at optimized relative phase ($\varphi = \varphi_{\text{opt}}$), but varying the ratio $R = (\Omega_+ - \Omega_-)/(\Omega_+ + \Omega_-)$ between Ω_+ and Ω_-, by scanning the amplitude of the signal applied on one of the electrodes. In each case the maximum of the probability $P_{|50c\rangle}(t_3)$ corresponds to the optimal setting for the driving signal. If the delay t_3 is chosen incorrectly (see Figs. 2.15b and 2.15d), the maximum of $P_{|50c\rangle}(t_3)$ as a function of the relative amplitude does not coincide exactly with the setting that provides a pure σ^+ radio-frequency field. However, the minimum of the probability of $P_{|50e1'\rangle}(t_3)$ always coincides with the optimum of the polarization.

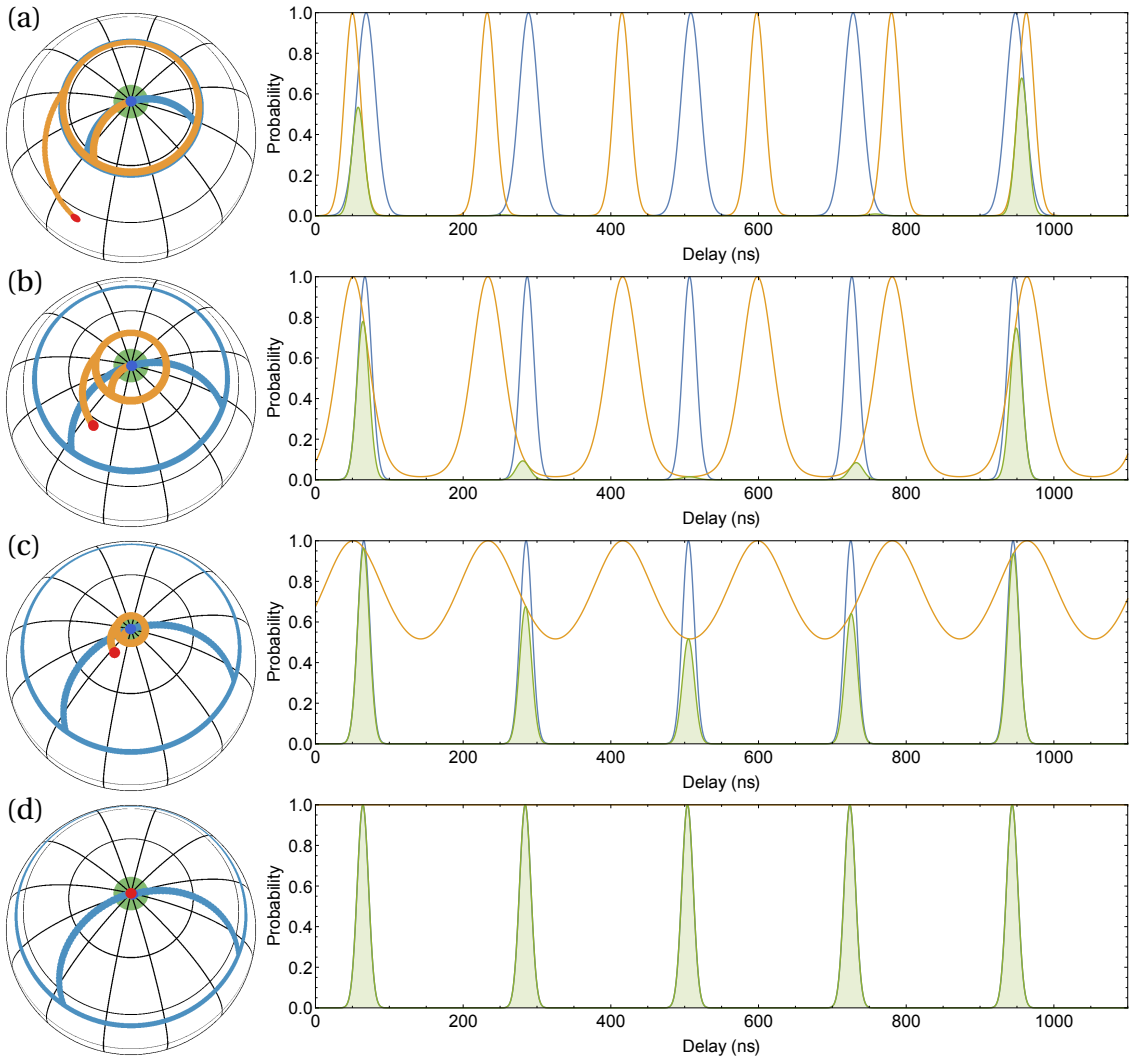

Figure 2.14: Left column: Trajectory of the vectors $\boldsymbol{J}_1$ (blue) and $\boldsymbol{J}_2$ (orange) on the Bloch sphere for a delay t_{delay} such that $P_1(t_{delay}) = 1$ (third blue peak in right column). Right column: Analytical calculations of the probabilities $P_1(t_{delay})$ (blue) and $P_2(t_{delay})$ (orange), as well as the probability $P_{|50c\rangle}(t_{delay})$ (green shaded) to find the atom in the circular state $|50c\rangle = |j_1, j_1\rangle \otimes |j_2, j_2\rangle$, are shown as a function of the delay t_{delay} between the two radio-frequency pulses for different ratios between σ^+ and σ^-: equally balanced $R = 0$ (a), σ^+ component increasingly dominates $R = 0.5$ (b) and $R = 0.8$ (c) until σ^- has completely vanished $R = 1$ (d). R is defined as in Fig. 2.12. The analytic expressions used in this graph are given in Appendix B.2.

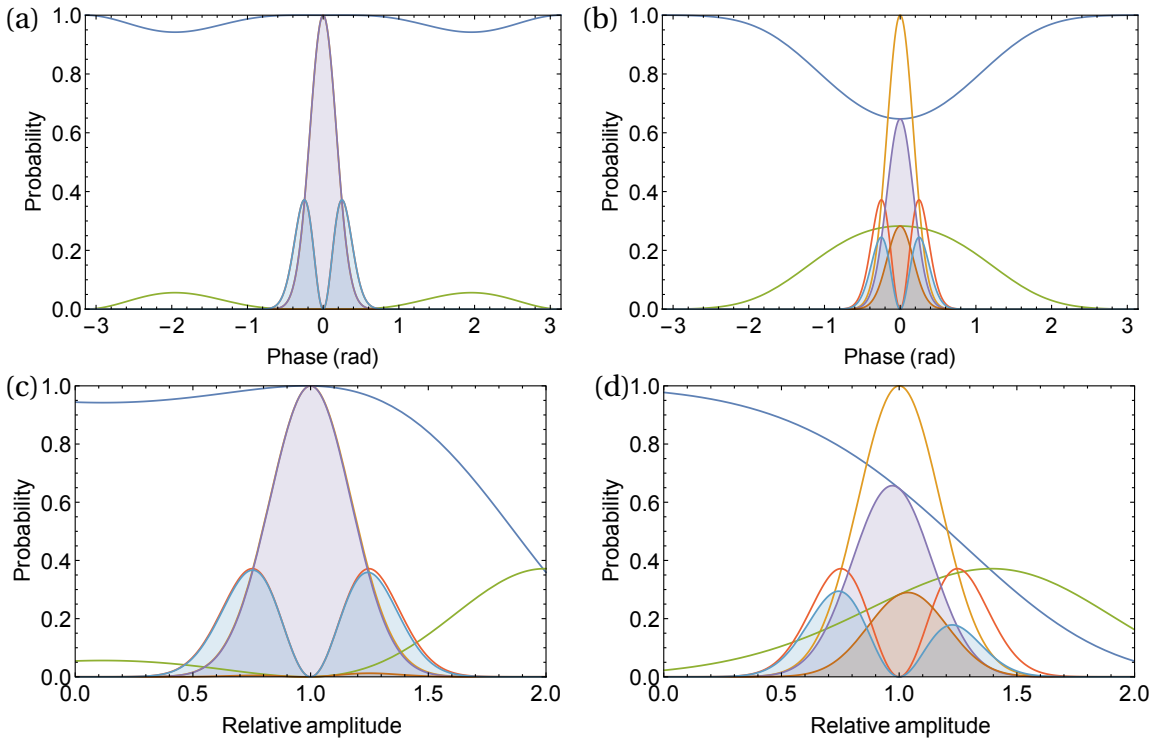

Figure 2.15: The probabilities $P_1(t_{delay} = t_3)$ (blue), $P_2(t_3)$ (yellow), $P_{1,e1}(t_3)$ (green), $P_{2,e1'}(t_3)$ (red) and the probabilities $P_{|50c\rangle}(t_3)$ (violet shaded), $P_{|50e1\rangle}(t_3)$ (orange shaded) and $P_{|50e1'\rangle}(t_3)$ (turquoise shaded) to find the atom in the states $|50c\rangle$, $|50e1\rangle$ and $|50e1\rangle$ respectively, plotted as a function the difference from the optimal radio-frequency phase $\Delta\varphi = \varphi - \varphi_{opt}$ (a) and value of R (c) for the optimum $t_{delay} = t_3 = 504$ ns and over the phase difference $\Delta\varphi$ (b) and value of R (d) for a slightly longer $t_{delay} = t_3' = 511$ ns. We consider two electrodes A and B on which two radio-frequency signals with tunable phase and amplitude are applied. The pure σ^+ polarized field is created when the amplitudes are the same ($R = 1$) and the phase is $\varphi_{opt} = \pi/2$. The analytic expressions used in this graph are given in Appendix B.2.

2.3.2.d Experimental optimization of the radio-frequency

The radio-frequency is generated by two synthesizer labelled "H" and "N". Both synthesizer have four outputs with independent phase and amplitude. The four outputs of each synthesizer are each connected to one ring electrode as shown in Fig 2.11. Output H1 and N1 are connected to electrode E1, outputs H2 and N2 to electrode E2, etc. In a first step, we tune the relative phase and amplitude between the two outputs of each pair H1&H2, N1&N2, H3&H4 and N3&N4, so that each of them, independetly, creates a purely σ^+ polarized radio-frequency field when they drive the respective electrodes. We choose to pair together electrodes E1&E2 and electrodes E3&E4 because of their position with respect to the atomic beam. The second step consists of equalizing the relative radio-frequency power of the four σ^+ polarized radio-frequency fields created by the four pairs of output signals, so that the radio-frequency field created when H1&H2&H3&H4 (respectively N1&N2&N3&N4) are simultaneously driving the electrodes is the most homogeneous.

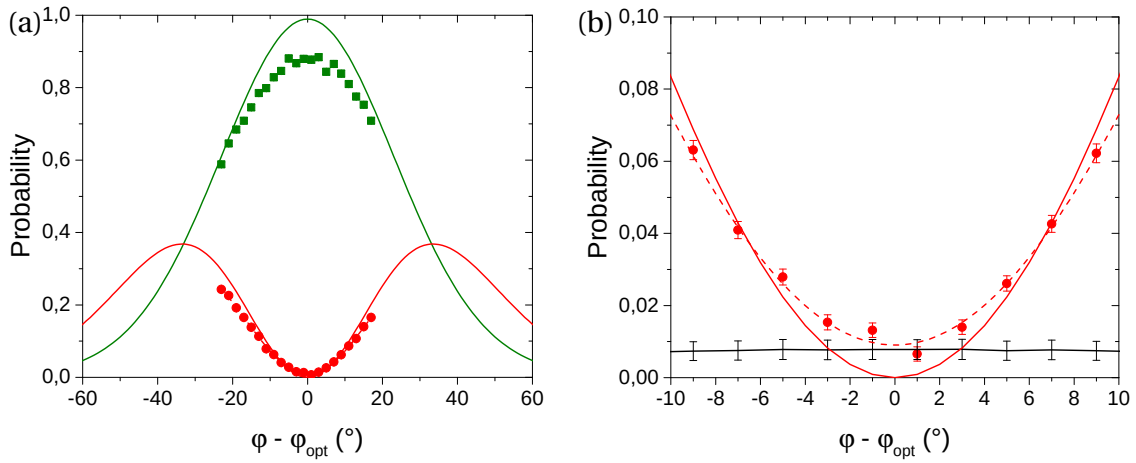

Figure 2.16: Optimization of the radio-frequency polarization of the H3&H4 outputs. (a) The probability to find the atom in the states $|50c\rangle$ *(green) and* $|50e1'\rangle$ *(red) as a function of the relative phase between the two signals that generate the* σ^+ *polarized radio-frequency field. The analytical calculations of the probability (full lines) fit qualitatively. The discrepancy is probably due to the efficiency of the microwave probe. (b) Local zoom of (a) shows the probability to find the atom in the* $|50e1'\rangle$ *(red) fitted by a Gaussian (red dashed), together with the analytical calculations (full red line). The black line shows estimated number of* $|50c\rangle$ *atoms that are wrongly transferred in the* $n = 49$ *manifold by the* $|50e1'\rangle \rightarrow |49e1'\rangle$ *probe and therefore counted as* $|50e1'\rangle$ *atoms.*

Fig. 2.16a shows the probability to find the atom in the $|50c\rangle$ and $|50e1'\rangle$ state as a function of the relative phase between the two signals applied on electrodes E3&E4 as a final step of the optimization process. The probability to return to the elliptic state $e1'$ is minimum at the optimum phase, while the probability to return to the circular state reaches a maximum. The population of each state is measured by selectively transferring the population from the $|50c\rangle$ or $|50e1'\rangle$ state to the $|49c\rangle$ or $|49e1'\rangle$ state respectively and detecting the population in the $n = 49$ manifold. Fig. 2.16b is a local zoom allowing us to estimate in principle, the purity of the σ^+ polarization purity from the minimum value of the probability $P_{|50e1\rangle}$. This is, however, limited by the selectivity of the microwave

probes. The probability to find the atom in the $|50e1'\rangle$ state does not vanish completely at the optimum phase $\varphi = \varphi_{\text{opt}}$. This is due to the false detection caused by the off-resonant transfer of the population of the $|50c\rangle$ state in the $n = 49$ manifold when we apply the microwave pulse for the $|50e1'\rangle \rightarrow |49e1'\rangle$ transfer. As a result, the minimum value of the probability $P_{|50e1\rangle}$ only provides a very pessimistic estimation of the ratio $\Omega_-/(\Omega_+^2 + \Omega_-^2)^{1/2} \approx 2.75\%$ limited by the background of the measurement.

Fig. 2.17a shows off-resonant Rabi oscillations for an optimized σ^+ polarized radio-frequency field, and for a slightly degraded σ^+ polarization in Fig. 2.17b. We also recorded the Ramsey-like sequence with two short off-resonant radio-frequency pulses as a function of the delay t_{delay} between the radio-frequency pulses for an optimized σ^+ polarized radio-frequency field, shown in Fig. 2.17c, and for a slightly degraded σ^+ polarization in Fig. 2.17d. In the optimized case we see small peaks of the probability $|50e1'\rangle$ at the position of the peaks of the probability $|50c\rangle$. If the probability $|50e1'\rangle$ was due to the residual σ^- component of the radio-frequency field, we would expect a modulation of the height of these peak as a function of the different peaks. Instead, they all have the same height. This confirms that the peaks in the probability to find the atom in the $|50e1'\rangle$ state are certainly atoms in the $|50c\rangle$ state wrongly detected as $|50e1'\rangle$ state.

The second step is the optimization of the homogeneity of the radio-frequency field. After the σ^+ polarization of the radio-frequency field generated by each of the output pairs H1&H2, H3&H4, N1&N2 and N3&N4 is optimized, the power of the σ^+ field created by the different pairs has to be equalized in order to assure a homogeneous radio-frequency field. This is done by no longer preparing the atom in the $|50c\rangle$ state but in the $|51c\rangle$ state. Once in the $n = 51$ manifold, the atom undergoes resonant Rabi oscillations in the presence of the resonant radio-frequency field. We apply a σ^+ polarized radio-frequency field created by two pairs, for example H1&H2 and H3&H4, for a long duration (~200 ns). We scan the phases φ_3 and φ_4 of the H3&H4 pair, while keeping the relative phase between φ_3 and φ_4 constant, to maximize the probability $P_{|51c\rangle}(t_{\text{rf}} = 200\text{ ns})$ to measure the atom in the $|51c\rangle$ state. The analytical expression is given in Appendix B.3. We iterate between scanning the relative phase and power of the pair H3&H4 until the atom does not leave $|51c\rangle$ any more. This is when we reach the point where the σ^+ field created by H1&H2 and H3&H4 have exactly the same amplitude and interfere destructively. We then shift the phases φ_3 and φ_4 by 180° to have the field created by the H1&H2 and H3&H4 interfere constructively. This technique is then repeated to adapt the power of N1&N2 and N3&N4.[5]

2.4 Electric field gradient compensation

The static electric field allows to Stark shift the levels and to control the detuning between the atomic frequency and the radio-frequency. Since the atoms are excited in an atomic packet of non-zero volume, we are sensitive to spatial inhomogeneities of the electric field at the position in the experimental zone where we apply the radio-frequency pulses. However, it is possible to locally compensate the electric field gradient.

[5] In fact, we equalize two by two the power of all pairs.

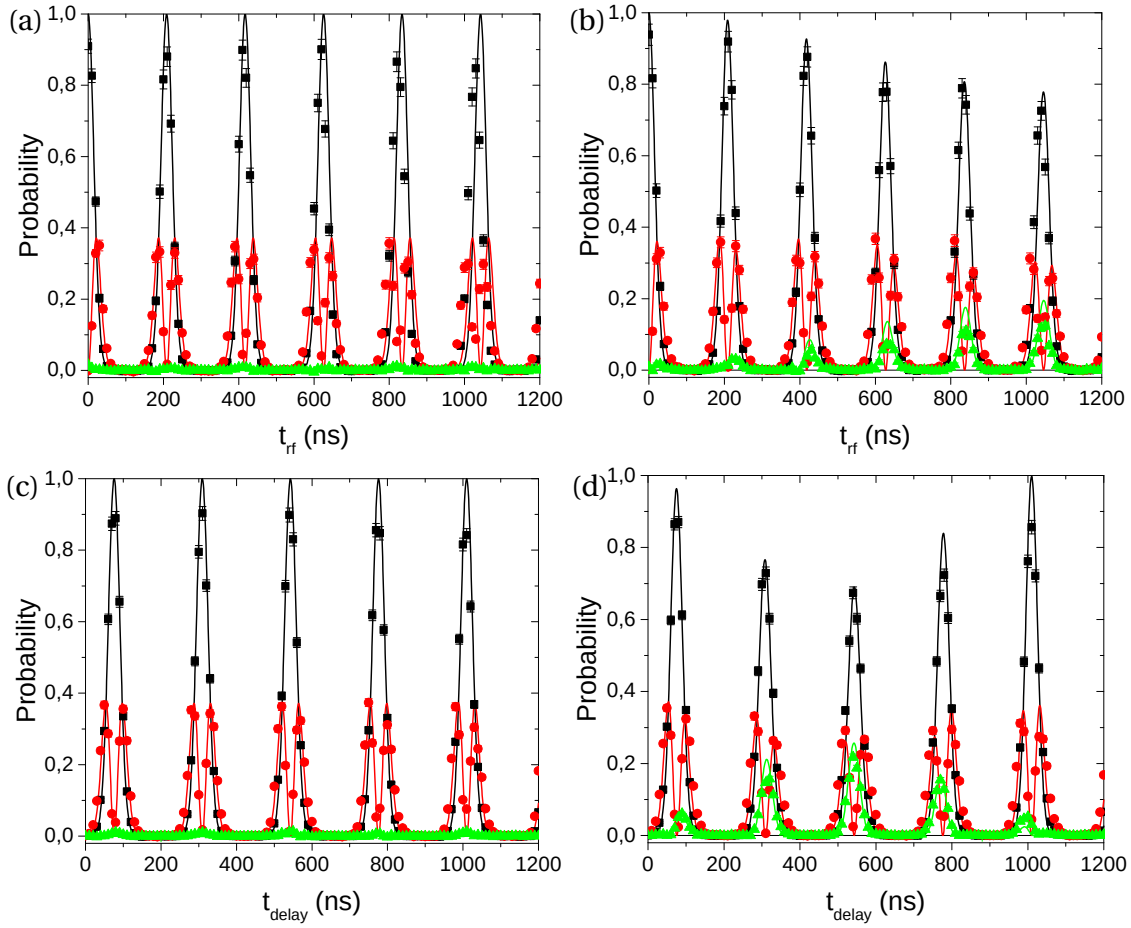

Figure 2.17: (a,b) Off-resonant Rabi oscillations as a function of the radio-frequency duration t_{rf}. The probabilities to find the atom in the circular state $|50c\rangle$ (black) or in the elliptical states $|50e1\rangle$ (red) or $|50e1'\rangle$ (green) are shown in the case of an optimized σ^+ polarized radio-frequency field with Rabi frequency $\Omega^+_{rf} = 2\pi \cdot 2.16$ MHz in the optimized case (a) and in the degraded case (the relative RF phase is detuned by 20°) (b). (c,d) Probability of the Ramsey-like sequence with two short RF pulses as a function of the delay t_{delay} between the RF pulses in the optimized case (c) and in the degraded case (the relative RF phase is detuned by 20°) (d). The analytic expressions used in this graph are given in Appendices B.1 and B.2. The parameters are chosen from the fits of the black line in (a) and (b).

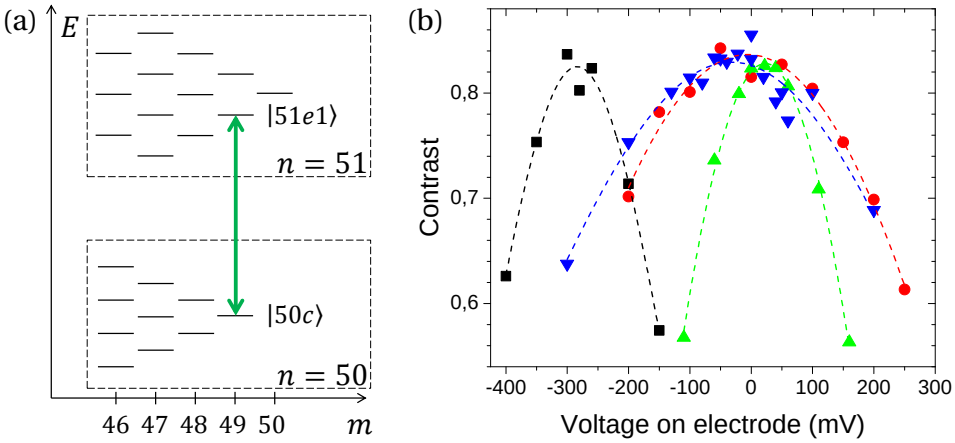

Figure 2.18: (a) The differential Stark shift between the levels $|50c\rangle$ *and* $|51e1\rangle$ *(green) is in first order the same as the atomic frequency* ω_{at} *in the* $n = 51$ *manifold. (b) The contrast of the microwave Ramsey fringes between* $|50c\rangle$ *and* $|51e1\rangle$ *is shown as a function of the gradient compensation voltage applied on the four electrodes during the process of compensating the gradient in the following order: E4 (black), E2 (red), E1 (green), E3 (blue) (see Fig. 2.11 for the electrode structure).*

Throughout this work we find that the electric field gradients are a source of decoherence in the contrast of the Ramsey interference signals. To compensate for electric field gradients we can apply static offset voltages on the ring electrodes.

The optimization of the compensation of the electric field gradients is done by performing microwave Ramsey fringes between the $|50c\rangle$ and the $|51e1\rangle$ states, see Fig. 2.18a. The choice of the states $|50c\rangle$ and $|51e1\rangle$ is due to their differential Stark shift which is in first order $\omega_{\mathrm{at}} = \frac{3}{2} e a_0 F/\hbar$. This transition experiences the same Stark inhomogeneous broadening as the angular momenta $\hat{\boldsymbol{J}}_1$ and $\hat{\boldsymbol{J}}_2$ precession frequency. We apply a first $\pi/2$-pulse to create a superposition between the two states and recombine them after a time t_{mw} by a second $\pi/2$-pulse. When varying the phase between the two pulses we get the typical sine-shaped Ramsey interference signal. In our set-up it is convenient to vary the frequency ν_{mw} in order to vary the phase $\varphi_{\mathrm{mw}} = 2\pi\nu_{\mathrm{mw}} t_{\mathrm{mw}}$.

The contrast of the Ramsey fringes depends on the homogeneity of the electric field in the volume of the atomic packet. By compensating the electric field gradients the homogeneity can be improved and the contrast of the fringes be increased.

Fig. 2.18b shows the contrast of the microwave Ramsey fringes with a delay of $t_{\mathrm{mw}} = 10\ \mu$s between the two $\pi/2$ Ramsey pulses as a function of the voltage applied on the four ring electrodes. We see that the contrast depends on the electric field created by the ring electrodes. The maximum contrast is reached when the electric field gradient is compensated in all four directions. In order to optimize the electric field gradient we also vary the voltage applied in opposite electrodes symmetrically and asymmetrically. This, however, has only a small impact on the measured contrast.

In order to further reduce the sensitivity to spatial inhomogeneities on the size of the atomic packet, we implemented several improvements, which we discuss briefly in

the following.

2.4.1 Attempt to reduce stray charges

In the past we saw a drastic change in the value of stray electric fields over time. We find a drift of ~10 mV/m per day measured over 2 months [112]. We suspect a deposition of stray charges on the electrodes or other parts in the vicinity of the experimental zone which might originate from hotter parts of the experiment. Since the thermal shield at 4 K helium temperature has holes for the optical access of the laser excitation, we decided to cover the holes with coated SF56 windows in order to prevent potential stray charges from entering the experimental zone.

We had the impression that the zero electric field was more stable than before. Unfortunately, we observed a slow deposition on the windows which diffused the laser light until the transmitted laser power dropped to only 10%. We therefore decided to remove the windows.

2.4.2 Reduction of atomic sample size

The size of the atomic packet is defined by the focus of the laser beams which intersect the atomic beam in the center of the experimental zone and is estimated to be in the order of ~0.5 mm^3. By reducing the diameter of the laser beams by a factor 10 the size of the atomic packet can be reduced by about a factor of 100, potentially making the atomic packet less susceptible to electric field gradients.

We can reduce the diameter of the laser beam by a tighter focus, which is achieved by first enlarging the diameter of the beam and then focussing it by a lens with focus at the position of the intersection between laser and atomic beam. In order to widen the diameter, we change the lens of the fibre output coupler which brings the laser beam near the optical access of the cryostat. This allows us to broaden the beam to a diameter of about 1 cm. At the same time, we install lenses with 300 mm focus at the optical accesses of the cryostat.

Fig. 2.19 shows the contrast of the $50c-51e1$ microwave fringes as a function of the delay between two $\pi/2$ Ramsey pulses. We see that the coherence time, defined by the width of the Gaussian fit of the contrast, is higher when the electric field gradient is compensated, ~36 μs for the initial ~0.5 mm^3 atomic packet size. After a few days, the coherence time gets reduced to ~31 μs, but can be compensated by again optimizing the electric field gradient compensation.

We estimate that we reduced the diameter of the 1258 nm beam from ~530 μm to ~88 μm. This only leads to an increased coherence time of ~43 μs, corresponding to an improvement factor of ~43 μs/31 μs $\approx$ 1.4 in the coherence time.

We proceeded to reduce the diameter of the 780/776 nm beams to ~65 μm and to

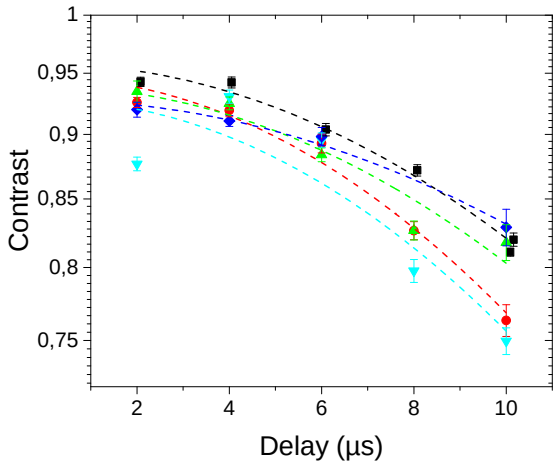

Figure 2.19: The contrast of the $50c - 51e1$ *microwave Ramsey fringes are shown as a function of the delay between the* $\pi/2$ *pulses for different conditions: electric field gradient compensated on day A, measured on day A (black) and day B (red); electric field compensated on day B, measured on day B (green), day C (cyan) and day D with tighter focus of the 1258 nm beam (blue). The days A, B, C, and D lie within a window of about two weeks. The width of the Gaussian fits gives the coherence times ~36 µs (black and green), ~31 µs (red and cyan) and ~43 µs (blue).*

optimize the power of the laser beams to be sure that the effective excitation volume was limited by the size of the beams. However, we did not see a significant improvement. This could be a first indication that the inhomogeneous broadening is rather due to the electric field noise than to the electric field gradient.

Besides, the reduced size of the laser beams leads to a reduced number of atoms that are excited per pulse by a factor of 3. So finally we decided that the small gain in the coherence time was not enough to overcome the loss in the atom number and we returned to the previous optical elements for all laser beams.[6]

2.5 Discussion

In this chapter we described how to prepare and detect the circular Rydberg states. We described the radio-frequency circuit that allows us to generate the well polarized radio-frequency field to manipulate that atoms and the methods we use to tune the phase and amplitude of the ten independent radio-frequency synthesizer. A first pair is dedicated to the radio-frequency field that we need to adiabatically transfer the atom from the low-l laser-accessible Rydberg state to the circular state at the beginning of each sequence. The other eight channels, all phase coherent, are connected to the four ring electrodes around the center of the experimental set-up and allow us to manipulate the state of the atom inside a given manifold once the atom is prepared in the circular state. This provides us

[6]The moment when we returned to the large laser beams, we prepared Schrödinger cat states of the metrology sequence and observed that the contrast of the fringes as a function of the delay between the radio-frequency pulses was of the same order of magnitude with small or large beams.

with the essentials to perform very sensitive measurements of the electric and magnetic fields.

Chapter 3

Quantum-enabled electrometry

The Rydberg atom driven by a σ^+ polarized radio-frequency field can be described as a large $\boldsymbol{J}$-spin system, whose free precession frequency is directly proportional to the amplitude of the electric field F. The aim of this experiment is to measure the amplitude F of the electric field.

We consider the lowest spin ladder of $\hat{\boldsymbol{J}}_1$, corresponding to $m_2 = +j_2$. This means that we do not have to consider m_2 and we call $j_1 = J$ and $m_1 = M$ throughout this chapter. The initial state $|J, M = +J\rangle$ is the circular state $|51c\rangle$ at the north pole of the generalized Bloch sphere on which the spin evolves.

We begin this chapter with the introduction of the precision limits of the classical and quantum-enabled strategies in the case of a perfect spin J (Sec. 3.1). We describe the experimental realization in the case of the rubidium atom (Sec. 3.2). The experimental results show that the sensitivity of the single-atom electrometer reaches the Heisenberg limit when the spin undergoes a non-classical evolution through Schrödinger cat states (Sec. 3.3). Finally, the sensitivity of this method can be improved by a echo-like sequence (Sec. 3.4).

3.1 Measurement precision limits

The atom is described by a spin whose free precession frequency is proportional to the electric field amplitude F. Measuring this precession frequency allows to measure F.

3.1.1 Classical methods

Classically, to measure the precession frequency one measures the angle by which the system has rotated during a time τ. Starting from an angular momentum aligned in the vertical direction, we apply a first radio-frequency pulse to induce a rotation $\hat{R}(\theta, 0)$,

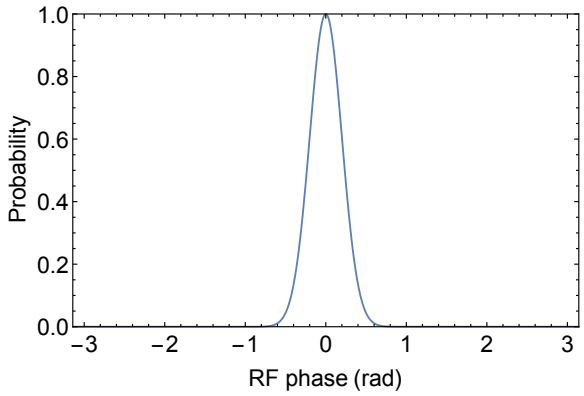

Figure 3.1: The analytically calculated probability to find the atom in the $|J,J\rangle$ state after the full sequence in the case of the classical method for $\theta = \pi/2$ as a function of the radio-frequency phase φ_{rf} for $\phi = 0$.

bringing the system to the spin coherent state $|\theta,0\rangle$ centred around the direction $(\theta,0)$. We then let the system evolve freely for a time τ, during which it precesses (in the rotating frame of the radio-frequency) at the frequency $\delta\omega = \omega_{\text{at}} - \omega_{\text{rf}}$, ending in the state $|\theta,\phi\rangle$, where $\phi = (\omega_{\text{at}} - \omega_{\text{rf}})\tau$. One way to detect a variation of ϕ is to rotate the spin with a second radio-frequency pulse, with an adjustable phase φ_{rf}, and measure the probability to find the final state of the spin $|\psi_f\rangle$ in the $|J,J\rangle$ state.

However, the intrinsic quantum fluctuations of $|\psi_f\rangle$ limit the precision with which one can determine the angle ϕ. The probability $P_c(\varphi_{\text{rf}})$ to detect the system in the state $|J,J\rangle$ at the end of the sequence as a function of the phase difference $\phi - \varphi_{\text{rf}}$ is given by,[1]

$$P_c(\varphi_{\text{rf}}) = |\langle J,J|\psi_f\rangle|^2 = |\langle\theta,\varphi_{\text{rf}}|\theta,\phi\rangle|^2 \approx \exp(-J\sin^2(\theta)(\phi-\varphi_{\text{rf}})^2/2), \tag{3.1}$$

where we use that

$$\langle J,J|\psi_f\rangle = \langle J,J|\,\hat{R}(\theta,\pi+\varphi_{\text{rf}})\,|\theta,\phi\rangle = \langle\theta,\varphi_{\text{rf}}|\theta,\phi\rangle\,.$$

It is a Gaussian centred around $\varphi_{\text{rf}} = \phi$, with a width $1/\sqrt{J}$ for $\theta = \pi/2$ that corresponds to the quantum fluctuations in the direction of the spin that limit the precision with which one can determine the value of ϕ.

Fig. 3.1 presents the probability $P_c(\varphi_{\text{rf}})$ for $\phi = 0$. The best strategy to measure ϕ is to set the phase φ_{rf} at the point of maximum slope at $\varphi'_{\text{rf}} = \pm 1/\sqrt{J}$ and measure the probability $P_c(\varphi'_{\text{rf}})$. If $\phi \neq 0$, the center of the Gaussian is shifted and the probability $P_c(\varphi_{\text{rf}})$ changes by an amount

$$\delta P_c = \frac{\partial P_c}{\partial\phi}\phi.$$

[1] $|\langle\theta,\varphi_{\text{rf}}|\theta,\phi\rangle|^2 = \cos^{4J}(\Theta/2) \approx \exp(-4J(\Theta/2)^2/2)$ with $\Theta \approx \sin(\theta)(\varphi_{\text{rf}}-\phi)$ for $\varphi_{\text{rf}} - \phi \approx 0$.

Since $P_c(\varphi_{\mathrm{rf}})$ is a Gaussian of width $1/\sqrt{J}$, the maximum slope is given by

$$\frac{\partial P_c}{\partial \phi} = \sqrt{\frac{J}{e}}.$$

If the experiment is repeated k times, we can estimate the value of P_c with an uncertainty given by the standard deviation of the binomial distribution of [178]

$$\sigma_P^{(k)} = \frac{\sqrt{P_c(1-P_c)}}{\sqrt{k}} = \frac{\sigma_P^{(1)}}{\sqrt{k}},$$

and the uncertainty in the direction of the spin coherent state is given by

$$\sigma_\phi^{(k)} = \frac{\sigma_P^{(1)}}{\sqrt{k}} \left(\frac{\partial P_c}{\partial \phi}\right)^{-1} = \frac{\sigma_\phi^{(1)}}{\sqrt{k}}.$$

The precision with which the electric field can be measured with this method is

$$\sigma_F^{(1)} = \sigma_\phi^{(1)} \left(\frac{\partial \phi}{\partial F}\right)^{-1} = \sigma_P^{(1)} \left(\frac{\partial P_c}{\partial \phi}\right)^{-1} \left(\frac{\partial \phi}{\partial F}\right)^{-1} = \sigma_P^{(1)} \left(\frac{\partial P_c}{\partial \phi}\right)^{-1} \left(\frac{\partial \phi}{\partial \omega_{\mathrm{at}}}\right)^{-1} \left(\frac{\partial \omega_{\mathrm{at}}}{\partial F}\right)^{-1}.$$

Since $\sigma_P \approx 1/2$ and $\partial P_c/\partial \phi = (J/e)^{1/2}$ and $\partial \phi/\partial \omega_{\mathrm{at}} = \tau$, we find

$$\sigma_F^{(1)} = \sqrt{\frac{e}{2}} \frac{1}{\sqrt{2J}} \frac{1}{\tau} \left(\frac{\partial \omega_{\mathrm{at}}}{\partial F}\right)^{-1}.$$

This method is not the optimal method to determine the electric field F. Nevertheless, the intrinsic quantum fluctuations of the direction of the spin coherent state $\sigma_\phi = (2J)^{1/2}$ (Eq. 1.37) means that any method using a spin coherent state is not able to determine the electric field F with a uncertainty better than

$$\sigma_F^{(1)} = \sigma_\phi^{(1)} \left(\frac{\partial \phi}{\partial F}\right)^{-1} = \sigma_\phi^{(1)} \left(\frac{\partial \omega_{\mathrm{at}}}{\partial F}\right)^{-1} \left(\frac{\partial \phi}{\partial \omega_{\mathrm{at}}}\right)^{-1} = \frac{1}{\sqrt{2J}} \frac{1}{\tau} \left(\frac{\partial \omega_{\mathrm{at}}}{\partial F}\right)^{-1} = \sigma_{F,\mathrm{SQL}}^{(1)}. \tag{3.2}$$

This sets a bound to the achievable sensitivity using a classical method (based on a spin coherent state) called the **standard quantum limit** (SQL).

This limit only holds if the method uses spin-coherent states. To go beyond, one needs to prepare the system in a non-classical state. In this case, the sensitivity is bounded by the Heisenberg limit which gives, for a given resource, the lowest sensitivity that can be reached by the measurement according to the laws of quantum mechanics [83].

3.1.2 The quantum-enabled method

In order to beat the SQL, we measure, instead of ϕ, the global quantum phase Φ which is accumulated by the spin J during its evolution on the Bloch sphere, when it comes back

to the $|J,J\rangle$ state.

3.1.2.a The global quantum phase

The global quantum phase Φ is defined from the overlap between the initial state $|J,J\rangle$ and the final state $|\psi_f\rangle$,

$$\langle J,J|\psi_f\rangle = |\langle J,J|\psi_f\rangle|e^{-i\Phi},$$

where $\langle J,J|\psi_f\rangle = \langle\theta,\varphi_{\mathrm{rf}}|\theta,\phi\rangle$ and where Φ is the argument of $\langle\theta,\varphi_{\mathrm{rf}}|\theta,\phi\rangle$. With the expression of the scalar product of two spin coherent states [80] we find[2]

$$\Phi = J[\phi-\varphi_{\mathrm{rf}}+2\mathrm{Atan}[\cos(\theta)\tan((\phi-\varphi_{\mathrm{rf}})/2)]], \tag{3.3}$$

function of ϕ and φ_{rf}, but depending only on the difference $(\phi-\varphi_{\mathrm{rf}})$.

To measure this global phase Φ, we need a reference state $|R\rangle$ with the same sensitivity to the electric field as the state $|J,J\rangle$ while being unaffected by the applied radio-frequency pulses. The atom is initially prepared in the superposition of the circular state $|J,J\rangle$ and the reference state $|R\rangle$,

$$\frac{1}{\sqrt{2}}(|J,J\rangle+|R\rangle),$$

by a first $\pi/2$ pulse. The $|J,J\rangle$ state then undergoes successive transformations of the spin J. Finally, after a second $\pi/2$ pulse with an adjustable phase φ_{mw} [179],

$$|J,J\rangle \rightarrow \frac{1}{\sqrt{2}}(|R\rangle+e^{i\varphi_{\mathrm{mw}}}|J,J\rangle) \quad \text{and}$$
$$|R\rangle \rightarrow \frac{1}{\sqrt{2}}(-e^{-i\varphi_{\mathrm{mw}}}|R\rangle+|J,J\rangle),$$

the probability to find the atom in the $|J,J\rangle$ state is given by

$$P_q(\varphi_{\mathrm{rf}},\varphi_{\mathrm{mw}}) = \frac{1}{4}+\frac{1}{4}P_c(\varphi_{\mathrm{rf}})+\frac{1}{2}\sqrt{P_c(\varphi_{\mathrm{rf}})}\cos(\Phi-\varphi_{\mathrm{mw}}), \tag{3.4}$$

with Φ given by Eq. 3.3. The probability to find the atom in $|J,J\rangle$ therefore oscillates with the global quantum phase Φ, which is a function of θ and $\phi-\varphi_{\mathrm{rf}}$, with an amplitude proportional to $\sqrt{P_c(\varphi_{\mathrm{rf}})}$.

The probability $P_q(\varphi_{\mathrm{rf}},\varphi_{\mathrm{mw}})$ is shown in the right column of Fig. 3.2 as a function of the relative radio-frequency phase φ_{rf} for different values of θ and fixed $\phi\approx 0$. The probability in the case of the quantum-enabled method presents much steeper features than the classical method with spin coherent states, shown in comparison in the plotted probability $P_c(\varphi_{\mathrm{rf}})$ in left column of Fig. 3.2. To assess the sensitivity to a small variation of ϕ, each time the probability is plotted for two slightly different values of the classical

[2] $\langle\theta,\varphi_{\mathrm{rf}}|\theta,\phi\rangle = \exp(iJ(\varphi_{\mathrm{rf}}-\phi))\left[\cos((\varphi_{\mathrm{rf}}-\phi)/2)-i\cos(\theta)\sin((\varphi_{\mathrm{rf}}-\phi)/2)\right]^{2J}$.

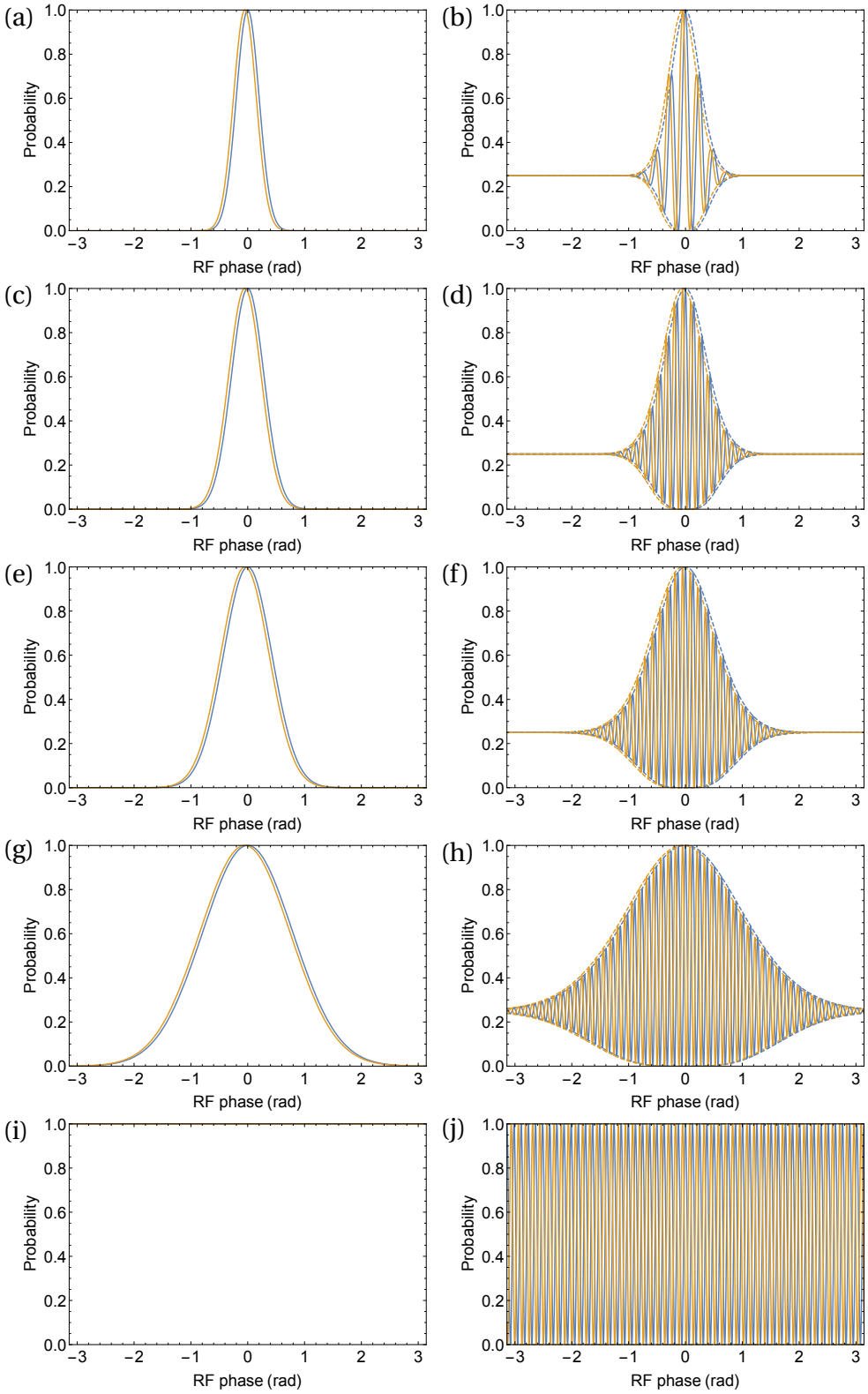

Figure 3.2: The analytically calculated probability to find the atom in the $|J,J\rangle$ state after the full sequence in the case of the classical (left) and the quantum-enabled method (right) as a function of the radio-frequency phase φ_{rf} for two slightly different accumulated classical phases $\phi = 0$ (blue) and $\phi = 0.05$ rad (yellow), for $\theta = \pi/2$ (a,b), $\theta = 138.4°$ (c,d), $\theta = 148.2°$ (e,f), $\theta = 162.4°$ (g,h) and $\theta = 2\pi$ (i,j). The relative microwave phase is $\varphi_{mw} = 0°$.

phases ϕ, corresponding to two different precession frequencies during the interrogation time τ.

The optimum for the classical strategy is for the angle $\theta = \pi/2$, for which the width of the Gaussian is $1/\sqrt{J}$ (Eq. 3.1), shown in Fig. 3.2a. As θ increases above $\pi/2$, the Gaussian gets broader leading to a worse sensitivity of the classical strategy. On the contrary, the sensitivity of the quantum strategy becomes better, as the oscillations in probability become more and more narrow.

3.1.2.b Single-atom sensitivity

The single-atom sensitivity of the quantum-enabled method is given by

$$\sigma_F^{(1)} = \sigma_P \left(\frac{\partial P_q}{\partial F} \right)^{-1} = \sigma_P \left| \frac{\partial P_q}{\partial \Phi} \right|^{-1} \left| \frac{\partial \Phi}{\partial F} \right|^{-1} \tag{3.5}$$

with $P_q = P_q(\varphi_{\mathrm{rf}}, \varphi_{\mathrm{mw}})$ given in Eq. 3.4 and σ_P being the standard deviation of a single atomic state detection.

The best sensitivity is obtained when we set the phase $\varphi_{\mathrm{rf}} = \varphi_{\mathrm{rf},0}$ that maximizes the contrast of the fringes. We assume here that the electric field F is close to the reference field F_0, for which $\omega_{\mathrm{at}}(F_0) = \omega_{\mathrm{rf}}$, and therefore $\varphi_{\mathrm{rf},0} = 0$. For small variations of the electric field $\mathrm{d}F = F - F_0$, the classical probability is maximum, $P_c(\varphi_{\mathrm{rf},0}) = 1$, and the probability $P_q(\varphi_{\mathrm{rf},0}, \varphi_{\mathrm{mw}})$ becomes (Eq. 3.4)

$$P_q(\varphi_{\mathrm{rf},0}, \varphi_{\mathrm{mw}}) = \frac{1}{2}\left(1 + \cos(\Phi - \varphi_{\mathrm{mw}})\right).$$

By varying the relative microwave phase φ_{mw} between the two $\pi/2$ pulses, we can record Ramsey fringes whose phase depends on the quantum phase Φ. In order to have the maximum sensitivity to variations of Φ induced by variations of the electric field F, we set the microwave phase φ_{mw} at a point of maximum slope so that $P_q(\varphi_{\mathrm{rf},0}, \varphi_{\mathrm{mw}}) = 1/2$. Therefore, $\sigma_P = \sqrt{P_q(1-P_q)} = 1/2$ is maximum and $\partial P_q/\partial\Phi = 1/2$.

The quantum phase Φ can be expanded to first order in a small electric field variation $\mathrm{d}F = F - F_0$ as

$$\Phi(F) \approx J(1-\cos(\theta))(F-F_0)\tau\frac{\partial\omega_{\mathrm{at}}}{\partial F} = \eta\phi(F), \tag{3.6}$$

where we introduce the **enhancement factor** $\eta = J(1-\cos(\theta))$. The quantum phase $\Phi(F)$ is η times larger than the classical phase $\phi(F)$. The enhancement factor can be written as $\eta = J - \langle M \rangle$ indicating the difference in latitude between the projection of the spin coherent state and the initial $|J, J\rangle$ state.

We introduce the **phase sensitivity**

$$\alpha = \frac{\partial\Phi}{\partial F} = J(1-\cos(\theta))\tau\frac{\partial\omega_{\mathrm{at}}}{\partial F}, \tag{3.7}$$

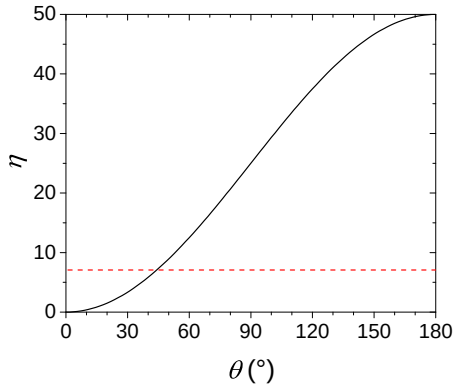

Figure 3.3: The enhancement factor $\eta = J(1-\cos(\theta))$ (black) in comparison with the $\sqrt{2J}$ (red) as a function of the angle θ. The quantum strategy becomes more sensitive than the SQL for $\theta > 44.2°$, where η exceeds $\sqrt{2J}$.

which leads to a theoretical single-atom measurement sensitivity of (Eq. 3.5)

$$\sigma_F^{(1),\mathrm{th}} = \frac{1}{J(1-\cos(\theta))\tau}\left|\frac{\partial\omega_{\mathrm{at}}}{\partial F}\right|^{-1}, \tag{3.8}$$

which scales as $1/J$. The quantum-enabled sensitivity becomes smaller than the SQL (Eq. 3.2), $\sigma_F^{(1),\mathrm{th}} < \sigma_{F,\mathrm{SQL}}^{(1)}$, when the enhancement factor $\eta = J(1-\cos(\theta))$ becomes larger than $\sqrt{2J}$. This is the case for $\theta > 44.2°$, as shown in Fig. 3.3.

The single-atom sensitivity is at its optimum for $\theta = \pi$,

$$\sigma_{F,\mathrm{HL}}^{(1)} = \frac{1}{2J\tau}\left|\frac{\partial\omega_{\mathrm{at}}}{\partial F}\right|^{-1} = \frac{1}{\sqrt{2J}}\sigma_{F,\mathrm{SQL}}^{(1)}, \tag{3.9}$$

where it reaches the **Heisenberg limit** (HL) which is the best achievable sensitivity achieve due to the laws of quantum mechanics for a given resource [83].

3.2 Experimental realization

3.2.1 Experimental sequence of the quantum-enabled method

To measure the quantum phase Φ, we need a reference state $|R\rangle$. We use the $|49c\rangle$ state, which, like the $|51c\rangle$ state, has no linear Stark shift. Since the $|49c\rangle$ state belongs to a different manifold, it is not resonantly coupled to the applied radio-frequency field. The detuning is $\delta_{49} = \omega_{\mathrm{at},49} - \omega_{\mathrm{rf}} \approx 2\pi \cdot 9$ MHz. However, due to the off-resonant drive, it is slightly affected by the radio-frequency field, but as seen in Sec. 2.3.2, if we choose the duration of the radio-frequency pulse correctly, the part of the wave-function in the $n = 49$ manifold has returned to the $|49c\rangle$ state at the end of each radio-frequency pulse.

The quantum-enabled method can also be described by a Ramsey interferometer,

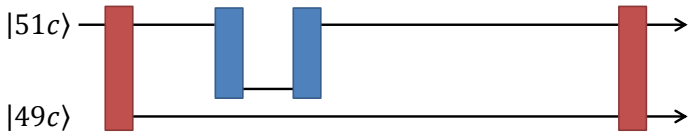

Figure 3.4: The quantum-enabled method represented as a Ramsey interferometer. The Ramsey $\pi/2$ pulses (red) create a superposition of the $|51c\rangle$ and $|49c\rangle$ states. The radio-frequency pulses (blue) transfer the $|51c\rangle$ component of the superposition into a state with very different polarizability between the radio-frequency pulses.

shown in Fig. 3.4, where one branch accumulates a phase with respect to the other due to the different polarizabilities of the two states between the applied radio-frequency pulses.

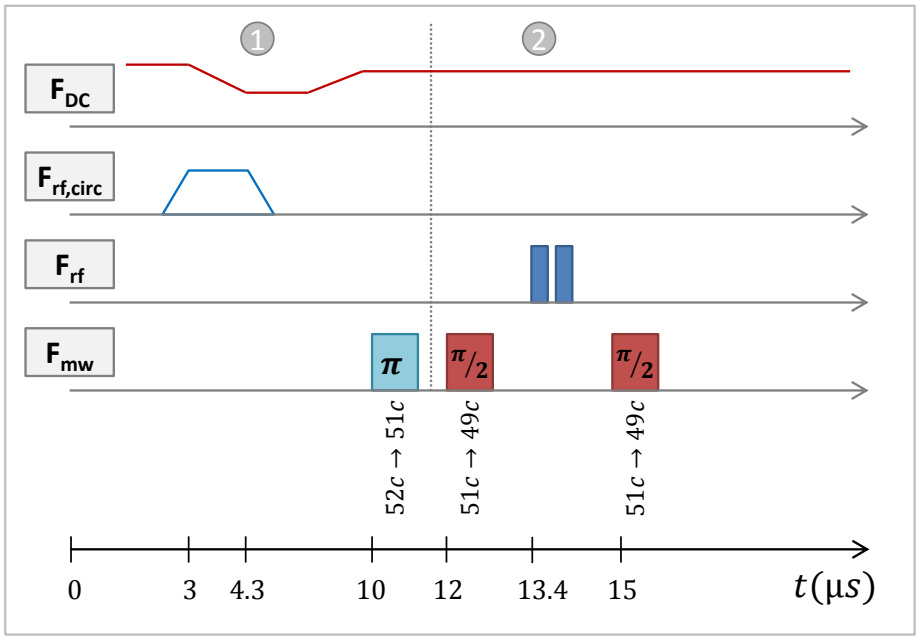

Figure 3.5: Experimental sequence of the quantum-enabled strategy. The initial state $|51c\rangle$ is prepared in step (1) by an adiabatic passage and a microwave π pulse (turquoise). The main experiment (2) consist in a first microwave $\pi/2$ pulse (red), a double radio-frequency pulse (blue) and a second microwave $\pi/2$ pulse. The final population of the state $|51c\rangle$ is read out either directly by ionization or by a first selective transfer of the population of the $|51c\rangle$ state to the $n = 49$ manifold followed by ionization. The time $t = 0$ is defined by the laser pulse.

The experimental sequence of the quantum-enabled strategy is shown in Fig. 3.5. The moment of the laser pulse defines the time zero of the experimental sequence. The electric field of 234.5 V/m is reached at 7 μs after the atom is prepared in the $|52c\rangle$ state by the adiabatic passage between 4.3 μs and 5.8 μs. The first microwave π pulse, also called "purification" pulse, to prepare the $|51c\rangle$ state is applied at 10 μs and has a duration of 1.25 μs. A first two-photon Ramsey microwave $\pi/2$ pulse at 12 μs prepares the superposition $\frac{1}{\sqrt{2}}(|51c\rangle + |49c\rangle)$. The first radio-frequency pulse is applied at 13.4 μs with a duration t_{rf}. Due to the off-resonant drive, the part of the wave-function in the

$n = 49$ manifold is slightly affected by the radio-frequency field. Therefore, we choose a radio-frequency pulse duration of $t_{rf} \approx \delta_{49}^{-1}$ to ensure that the $n = 49$ part of the wavefunction returns to the $|49c\rangle$ state after t_{rf}. After an interrogation time τ between 10 ns and 600 ns, we apply a second radio-frequency pulse. The second microwave pulse at 15 μs recombines the two parts of the superposition. The two microwave $\pi/2$ pulses have a duration in the order of 0.46 μs and 0.49 μs. The difference is due to the stationary modes of the microwave field in the experimental zone. We regularly optimize the duration to compensate for long time drifts of the microwave power seen by the atoms.

For the quantum-enabled measurement, we detect the atoms in $|51c\rangle$ and $|49c\rangle$ states directly at their ionization threshold. To record the measurement data, we play the sequence twice, once measuring the number of atoms in the $|51c\rangle$ state, $N(51c)$, once of those in the $|49c\rangle$ state, $N(49c)$. We also measure the number of atoms initially prepared in the $|51c\rangle$ state, $N(51n)$, by only playing a sequence with the preparation part (see (1) in Fig. 3.5). The main drawback of the determination of the probability to find the atom in the $|51c\rangle$ state, $P(51c) = N(51c)/N(51n)$, is that it is possible to count as $|51c\rangle$ atoms which are in states different than the $|51c\rangle$ state but with similar ionization thresholds. In principle, it is also possible to deduce the contrast of the interference of the states $|51c\rangle$ and $|49c\rangle$ from the measurement of the probability to find the atom in the $|49c\rangle$ state, $P(49c) = N(49c)/N(51n)$. Here, the background due to non-$|49c\rangle$ states should be lower, since the $n = 49$ manifold is less affected by the applied radio-frequency field. However, $P(49c)$ suffers from the difference in detection efficiency between the state $|51c\rangle$ for the normalization and the state $|49c\rangle$ for the signal. The uncertainty on the ratio of the detection efficiency directly affects the estimation of the sensitivity. We therefore prefer to use the probability $P(51c)$.

Finally, we repeat the three sequences twice for two different electric fields $F_{up} = F_0 + \Delta F/2$ and $F_{down} = F_0 - \Delta F/2$ in order to measure the effect of a change ΔF of the electric field.

In the next section, we describe how we calibrate the radio-frequency power, how we precisely determine the duration t_{rf} of the radio-frequency pulses, and how we calibrate the variation of the electric field ΔF.

3.2.2 The radio-frequency field power

The sensitivity of the measurement depends on the maximum angle θ reached by the spin coherent state. In the spin approximation, where we neglect that not all levels are hydrogen-like, the angle θ is the Rabi angle

$$\theta_{rf} = \Omega_{rf} t_{rf},$$

with the Rabi frequency Ω_{rf} and the pulse duration t_{rf}. We thus need to calibrate Ω_{rf}.

The Rabi frequencies of the radio-frequency applied in the experiments can be obtained from a fit of the depopulation of the $|51c\rangle$ state as a function of the programmed pulse width, shown in Fig. 3.6a. Since the $|51c\rangle$ state couples resonantly to the applied

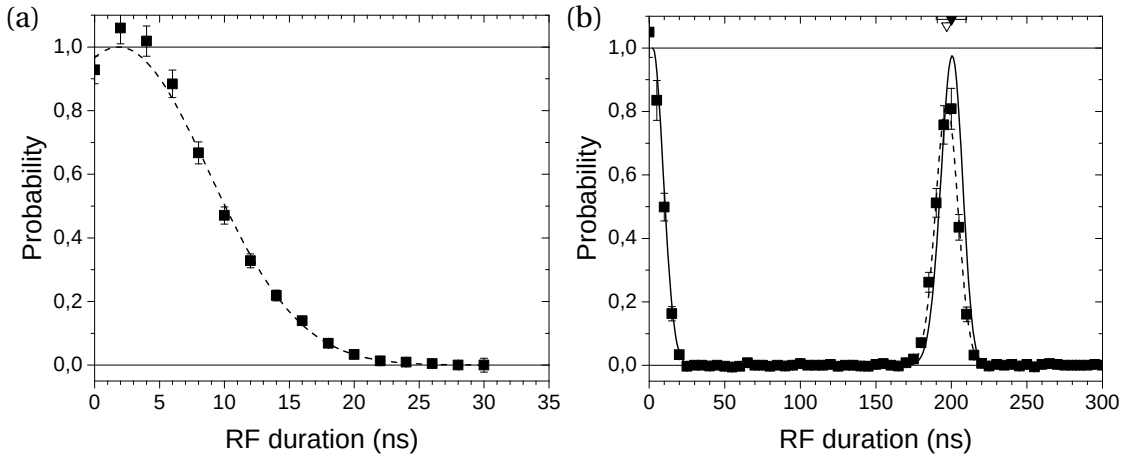

Figure 3.6: Resonant Rabi oscillations in the $n = 51$ manifold. The population of the $|51c\rangle$ state is plotted as a function of the radio-frequency duration. The probability is measured using a selective probe between the levels $|51c\rangle$ and $|49c\rangle$ to ensure that we only measure the population in the circular state. (a) The Rabi frequency Ω^{+}_{rf} is fitted with Eq. 3.10 (dashed line) from the depopulation of the initial state. (b) The full Rabi oscillations with numerical simulations for the rubidium atom (full line) and the Gaussian-fitted maximum of return (dashed line).

radio-frequency field, the oscillation frequency is directly given by the Rabi frequency Ω_{rf}. The probability to find the atom in the $|51c\rangle$ state is given by (Eq. B.6)

$$P_{|51c\rangle}(t_{\mathrm{rf}}) = \cos^{2(n-1)}\left(\frac{\Omega^{+}_{\mathrm{rf}}(t_{\mathrm{rf}} - t_0)}{2}\right), \tag{3.10}$$

where $n = 51$ and t_0 is the offset radio-frequency duration to take into account the rise and fall time of the radio-frequency. From the fit in Fig. 3.6a, we find the Rabi frequency $\Omega_{\mathrm{rf}} = (4.55 \pm 0.11)$ MHz for the radio-frequency field we apply, together with the offset $t_0 = (1.83 \pm 0.30)$ ns. We choose this method to calibrate the Rabi frequency, since at the beginning of the Rabi oscillation the atom only populates high-m states which are hydrogen-like. Our fit-function thus does not depend on the correct description of the rubidium atom. Even the differential quadratic Stark effect, in the order of tens of kHz for neighbouring m-levels, can be neglected at this time scale.

It is also possible to record the full Rabi oscillation. In Fig. 3.6b we see that after a radio-frequency pulse duration of $t_{\mathrm{rf}} \approx 200$ ns the atom returns to the $|51c\rangle$ state. We then use the fitted Rabi frequency Ω_{rf} to numerically simulate the evolution of the Rabi oscillation in the $n = 51$ manifold taking into account the energy eigenvalues of the Stark levels of the rubidium atom. In fact, due to the quantum defect, we have a truncated Bloch sphere where the southernmost levels cannot be reached by a radio-frequency Rabi-π pulse from the north pole. When consulting Fig. 1.13, we see that the levels $m = 0$ and $m = 1$ are shifted far away from the radio-frequency ω_{rf}. As a result, the duration t_{rf} for which the atom returns to the $|51c\rangle$ state is not exactly $2\pi \cdot \Omega^{-1}_{\mathrm{rf}}$ and the return probability does not reach 100%. The simulations are in good agreement with the data shown in Fig. 3.6b. This confirms the value of the fit in Fig. 3.6a. However, these simulations rely on the numerical

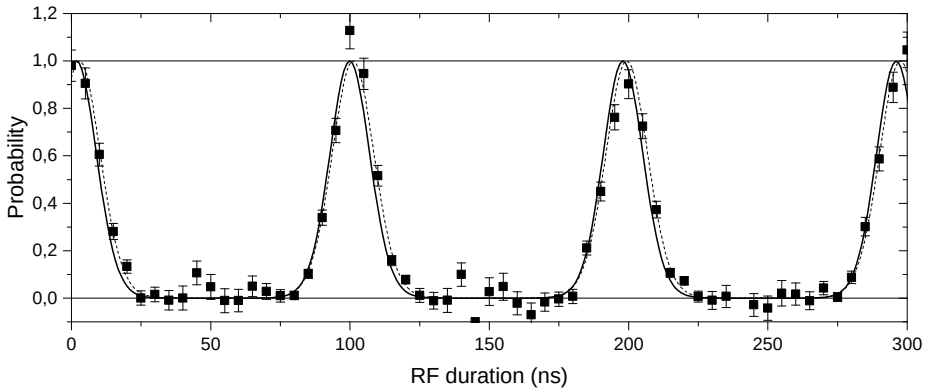

Figure 3.7: Off-resonant Rabi oscillations in the $n = 49$ manifold. The population of the $|49c\rangle$ state is plotted as a function of the radio-frequency duration. The probability is measured using a selective probe from the level $|49c\rangle$ to $|51c\rangle$ to ensure that we only measure the population in the circular state $|49c\rangle$. The duration of the final radio-frequency pulse t_{rf} is fitted from the first peak. The dashed line corresponds to the analytical formula for off-resonant Rabi oscillations (Eq. B.2 adapted for $n = 49$) with the detuning and the Rabi frequency as free fit parameters. The numerical simulation of the experiment (full line) with the Rabi frequency fitted from Fig. 3.6a is plotted in comparison.

simulation of the energy eigenvalues and the precise determination of the value of the electric field. For this reason we do not use them to calibrate the Rabi frequency but as a verification of the fit. The horizontal error bar indicates the error in the position of the maximum of $P_{|51c\rangle}(t_{\mathrm{rf}})$ due to the uncertainty on the fitted value of Ω_{rf}.

3.2.3 Determination of the radio-frequency pulse duration

The Rabi frequency is typically $\Omega_{\mathrm{rf}} \approx 2\pi \cdot 4$ MHz. In the electric field $F = 234.5$ V/m, the detuning between the radio-frequency and the atomic frequency in the $n = 49$ manifold is $\delta_{49} = 2\pi \cdot 9.06$ MHz. In the $n = 49$ manifold the radio-frequency field still induces off-resonant Rabi oscillations between the Stark levels. The part of the wave-function in the $n = 49$ manifold can be represented as a spin coherent state of another effective spin $\hat{\boldsymbol{J}}'$ that rotates at a frequency of $\tilde{\Omega}_{\mathrm{rf}} = (\Omega_{\mathrm{rf}}^2 + \delta_{49}^2)^{1/2} \approx 2\pi \cdot 9.9$ MHz. This means that the oscillation frequency in the $n = 49$ manifold depends much less on the radio-frequency power than the oscillation frequency in the $n = 51$ manifold. The pulse duration is therefore basically given by $t_{\mathrm{rf}} \approx \delta_{49}^{-1}$.

Fig. 3.7 presents the probability to return to the state $|49c\rangle$ for an atom initially prepared in the $|49c\rangle$ state as a function of the programmed radio-frequency pulse duration t_{rf}. We choose the duration of the radio-frequency pulse so that the effective spin $\hat{\boldsymbol{J}}'$ performs exactly one rotation and the atom is back in the $|49c\rangle$ state at the end of the radio-frequency pulse.

The optimum phase sensitivity is reached for $\theta = \pi$. However, for angles θ close to π, we reach the south pole where the atom does not behave like a perfect spin any more. To test the sensitivity of the method for different Rabi angles, we choose three different Rabi

frequencies Ω_{rf}.

Table 3.1 summarizes the values of the Rabi frequencies Ω_{rf}, the offset t_0, the pulse duration t_{rf} and the estimated latitude $\Omega_{\mathrm{rf}}(t_{\mathrm{rf}} - t_0)$ reached by the spin coherent state in the $n = 51$ manifold. The offset is consistently $t_0 \approx 2$ ns. The estimated latitude ranges from 138.4° to 162.4°. Note that the angle 162.4° is below the latitude corresponding to $m = 2$.

Label	Ω_{rf}	t_0	t_{rf}	$\Omega_{\mathrm{rf}}(t_{\mathrm{rf}} - t_0)$
a	$2\pi \cdot (3.74 \pm 0.10)$ MHz	(2.35 ± 0.41) ns	105 ns	$(138.4 \pm 3.7)°$
b	$2\pi \cdot (4.01 \pm 0.14)$ MHz	(1.45 ± 0.49) ns	104 ns	$(148.2 \pm 5.2)°$
c	$2\pi \cdot (4.55 \pm 0.11)$ MHz	(1.83 ± 0.30) ns	101 ns	$(162.4 \pm 4.0)°$

Table 3.1: The Rabi frequency Ω_{rf} and the offset t_0 are fitted from the resonant Rabi oscillations in the $n = 51$ manifold. The applied radio-frequency duration t_{rf} is fitted from off-resonant Rabi oscillations in the $n = 49$ manifold. The Rabi angle is estimated as $\Omega_{rf}(t_{rf} - t_0)$. The mean radio-frequency offset duration is $t_0 = 1.88$ ns. The curves in Figs. 3.6 and 3.7 corresponds to setting a. The value of t_{rf} has no error bar since it is the pulse duration we program in the sequence.

3.2.4 Applying the electric field

The aim of this experiment is to measure a change in the electric field amplitude F with a sensitivity close to the Heisenberg limit. To measure the sensitivity of our measurement to variations of the electric field, we alternate between the two amplitudes $F_{\mathrm{up}} = F_0 + \Delta F/2$ and $F_{\mathrm{down}} = F_0 - \Delta F/2$.

The electric field F_0 is applied with an arbitrary waveform generator (AWG) with two outputs connected to the two plane electrodes. The voltage is ramped up and down during the preparation of the atoms, but is maintained at a constant value of ±3.258 V during part (2) of the sequence in Fig. 3.5. The value is chosen so that the atomic frequency between the levels $|51c\rangle$ and $|51e1\rangle$ is $\omega_{\mathrm{at}} = 2\pi \cdot 230$ MHz. Experimentally, we measure an atomic frequency of $\omega_{\mathrm{at}} = 2\pi \cdot (230.06 \pm 0.01)$ MHz which is the long-time average of the measured transition frequency in the weeks around the day when the data was taken. This corresponds to an electric field of $F = 234.5$ V/m.

In order to apply a small change in amplitude ΔF of the electric field without being limited by the voltage resolution of the arbitrary waveform generator with which we apply the voltage on the plane capacitor electrodes,[3] we connect an additional AWG through a $R_1 = 100$ kΩ resistor to one of the plane electrodes, as shown in Fig. 3.8. This resistor, together with the output resistor $R_2 = 50$ Ω of the (green) AWG acts as a voltage divider. The voltage applied on the plane electrode ΔV_{out} is proportional to the voltage output

[3] The voltage resolution of the arbitrary waveform generator was a limitation in the previous experiment and is described in [112].

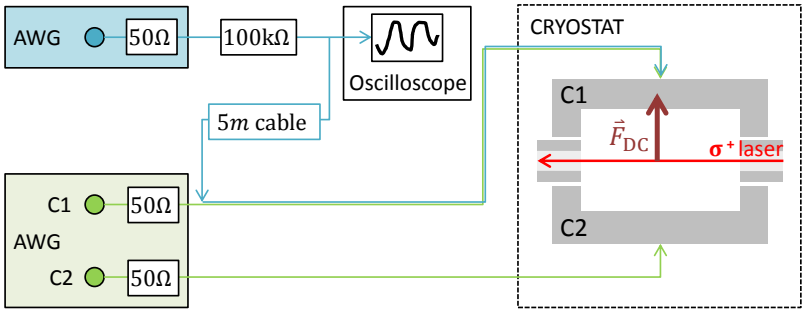

Figure 3.8: The cabling for the DC voltage applied on the capacitor plates C1 and C2. The auxiliary arbitrary waveform generator (blue AWG) is used for small resolution electric field variations. It is connected to the principal DC voltage by a voltage divider and a 5 m long cable.

ΔV_{in} of the additional (blue) AWG,

$$\Delta V_{\text{out}} = \frac{R_2}{R_1 + R_2} \Delta V_{\text{in}} \approx 5 \cdot 10^{-4} \Delta V_{\text{in}}.$$

Experimentally, we find

$$\Delta V_{\text{out}} = 5.1 \cdot 10^{-4} \Delta V_{\text{in}}.$$

As a result, applying $\Delta V_{\text{in}} = 1$ V with the additional AWG corresponds to a voltage change of $\Delta V_{\text{out}} = 0.51$ mV. We expect that applying $\Delta V_{\text{in}} = 1$ V leads to a change in the electric field amplitude in the order of

$$\Delta F = \frac{0.51 \text{ mV}}{2 \cdot 3.258 \text{ V}} \cdot 234.5 \text{ V/m} = 18.35 \text{ mV/m}.$$

3.2.5 Calibration of the electric field

The above calculation gives a rough estimate[4] of the calibration of the electric field. We verify this calibration by measuring the frequency shift induced by the electric field variation ΔF on the $|50c\rangle - |51e1\rangle$ transition using Ramsey spectroscopy, shown in Fig. 3.9.

The Ramsey fringes are recorded as a function of the microwave frequency for two different electric fields corresponding to a given difference of applied voltage of ΔV_{out}, shown in Fig. 3.9b. We perform the experiment for a change of $\Delta V_{\text{out}} = 0.51$ mV on electrode C1 leading to a frequency shift $\Delta\nu_{\text{mw}} = (18.1 \pm 0.8)$ kHz of the $|50c\rangle - |51e1\rangle$ transition.

We use the hydrogen model with linear and quadratic Stark shift to calculate to which variation in the electric field corresponds the change $\Delta\nu_{\text{mw}} = 18$ kHz of the $|50c\rangle - |51e1\rangle$ transition at an electric field around $F_0 = 234.5$ V/m. We find $\Delta F = 18.31$ mV/m in good

[4] In particular, it does not take into account stray electric fields.

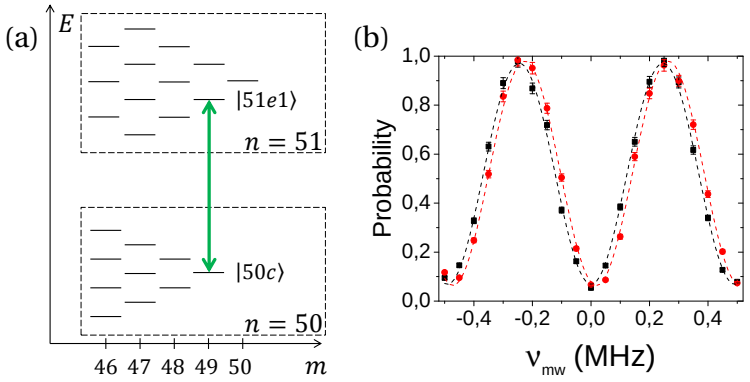

Figure 3.9: (a) The transition between the levels $|50c\rangle$ *and* $|51e1\rangle$ *(green) involved in the Ramsey fringes. (b) Recorded Ramsey fringes for two electric fields corresponding to a difference* $\Delta V_{out} = 0.51$ *mV. The measured difference between the fringes at* $F_{up} = F_0 + \Delta F/2$ *(black) and* $F_{down} = F_0 + \Delta F/2$ *(red) is* $\Delta\nu_{mw} = (18.1 \pm 0.8)$ *kHz.*

agreement with the previous estimation.

3.3 Experimental results

3.3.1 Experimental results for the classical method

We first record the probability $P_c(\varphi_{\mathrm{rf}})$ to find the atom in the $|J, J\rangle$ state after the classical sequence is recorded as a function of the radio-frequency phase φ_{rf}. The classical sequence, is very similar to the one for the quantum-enabled strategy shown in Fig. 3.5. The main difference is that there is no $\pi/2$ microwave pulse. The state therefore only populates the $n = 51$ manifold. After the two radio-frequency pulses, a microwave π pulse transfers the population of the $|51c\rangle$ in the $|49c\rangle$ state to ensure that we only measure the population that returns to the circular state $|51c\rangle$.

Fig. 3.10 shows the probability $P_c(\varphi_{\mathrm{rf}})$ for different interrogation times τ and different settings *a*, *b*, *c* from Table 3.1. The probability is measured for two different electric fields, $F_{\mathrm{up}} = F_0 + \Delta F/2$ and $F_{\mathrm{down}} = F_0 - \Delta F/2$, with a difference in amplitude of $\Delta F = 73.2$ mV/m.

For the smallest Rabi frequency $\Omega_{\mathrm{rf}} = \Omega_a$ the atom behaves nearly as expected for a spin (see Fig. 3.10, first column). The distance between the center of the signals corresponding to the two different electric fields increases with increasing interrogation time τ. The absolute position also slightly moves due to the quadratic Stark effect. The effective frequency of the spin is different when the spin coherent state is in a lower latitude, which leads to a smaller detuning between the atomic frequency and the radio-frequency. The fact that the width increases and the height decreases with increasing interrogation time τ (see Fig. 3.10, first column, from top to bottom), can also be due to this anharmonicity.

We numerically calculated the level structure and dipole matrix elements of the rubidium atom as introduced in chapter 1 (Sec. 1.2.2). The numerical simulations (solid

lines in Fig. 3.10) confirm the increase of the width and the reduction of the height of the signals and globally agree with the measured signal. However, the absolute position of the numerically simulated peaks is shifted. This is either due to a numerical error in the value of the energy eigenvalues, indicated by the discrepancy between hydrogen and rubidium for high-m states discussed in Sec. 1.2.3, or due to an error in the determination of the electric field F_0. Nevertheless, within a small correction, in the case of $\Omega_{\mathrm{rf}} = \Omega_a$, the rubidium atom behaves like a spin.

Fig. 3.11 shows the Q-functions centred around the south pole of the Bloch sphere corresponding to Fig. 3.10 for the settings a, b, c of Table 3.1 and for the different interrogations times τ. In the case of setting a (see Fig. 3.11, first column), the Q-function of the spin is slightly deformed but still has a population distribution of a spin coherent state, shown in Fig. 3.12a.

For the intermediate Rabi frequency $\Omega_{\mathrm{rf}} = \Omega_b$, setting b of Table 3.1 (see Fig. 3.10, second column), we see a peak for short interrogation times τ. But since the spin starts to populate the $m = 2$ level, see Fig. 3.12b, we observe a beat between the population of the hydrogen-like and the non-hydrogen-like levels that leads to the appearance of a second peak. This behaviour is qualitatively reproduced by the numerical simulations, especially at short interrogation times. At longer interrogation times, there seems to be a discrepancy in the beat frequency which could be due to the already mentioned error in the simulation of the energy eigenvalues.

For the largest Rabi frequency $\Omega_{\mathrm{rf}} = \Omega_c$, setting c of Table 3.1 (see Fig. 3.10, third column), the signal gets very broad. Due to the quantum defect leading to a truncated Bloch sphere, the southernmost levels, with $m = 0$ and $m = 1$, cannot be reached by a radio-frequency π-pulse from the north pole, since they are shifted out of resonance. The first radio-frequency pulse thus transfers the atom into a state where most of the population is found in the level $m = 2$, see Fig. 3.12c. Since the $|J, M\rangle$ state has phase, the state is spread around the latitude corresponding to $m = 2$ and a pulse with any relative radio-frequency phase φ_{rf} brings back the state close to the north pole. The probability $P_c(\varphi_{\mathrm{rf}})$ therefore varies very slowly. However, unlike the state $m = 0$, the $m = 2$ state cannot be brought back to the north pole with an efficiency of 100%, and the probability $P_c(\varphi_{\mathrm{rf}})$ is limited to $\sim 70\%$.

To determine the radio-frequency phase $\varphi_{\mathrm{rf}} = \varphi_{\mathrm{rf},0}$ for which the probability $P_c(\varphi_{\mathrm{rf}})$ is maximum, we record the curves of Fig. 3.10 for $F = F_0$. For $\Omega_{\mathrm{rf}} = \Omega_a$, the radio-frequency is fitted by a simple Gaussian function. For $\Omega_{\mathrm{rf}} = \Omega_b$, we follow the left peak for consistency. For $\Omega_{\mathrm{rf}} = \Omega_c$, we fit the signal with two Gaussian peaks in order to phenomenologically reproduce the shape of the signal and determine the position of the maximum probability.

Note that the experiment for $\Omega_{\mathrm{rf}} = \Omega_a$ can be used as a first method to measure the electric field F. The sensitivity in this case is given by

$$\sigma_F^{(1)} = \frac{1}{2}\sqrt{e}\frac{w}{H}\frac{\Delta F}{\Delta\phi},$$

where w is the Gaussian width of the probability $P_c(\varphi_{\mathrm{rf}})$ (as defined in Eq. 3.1) and H is

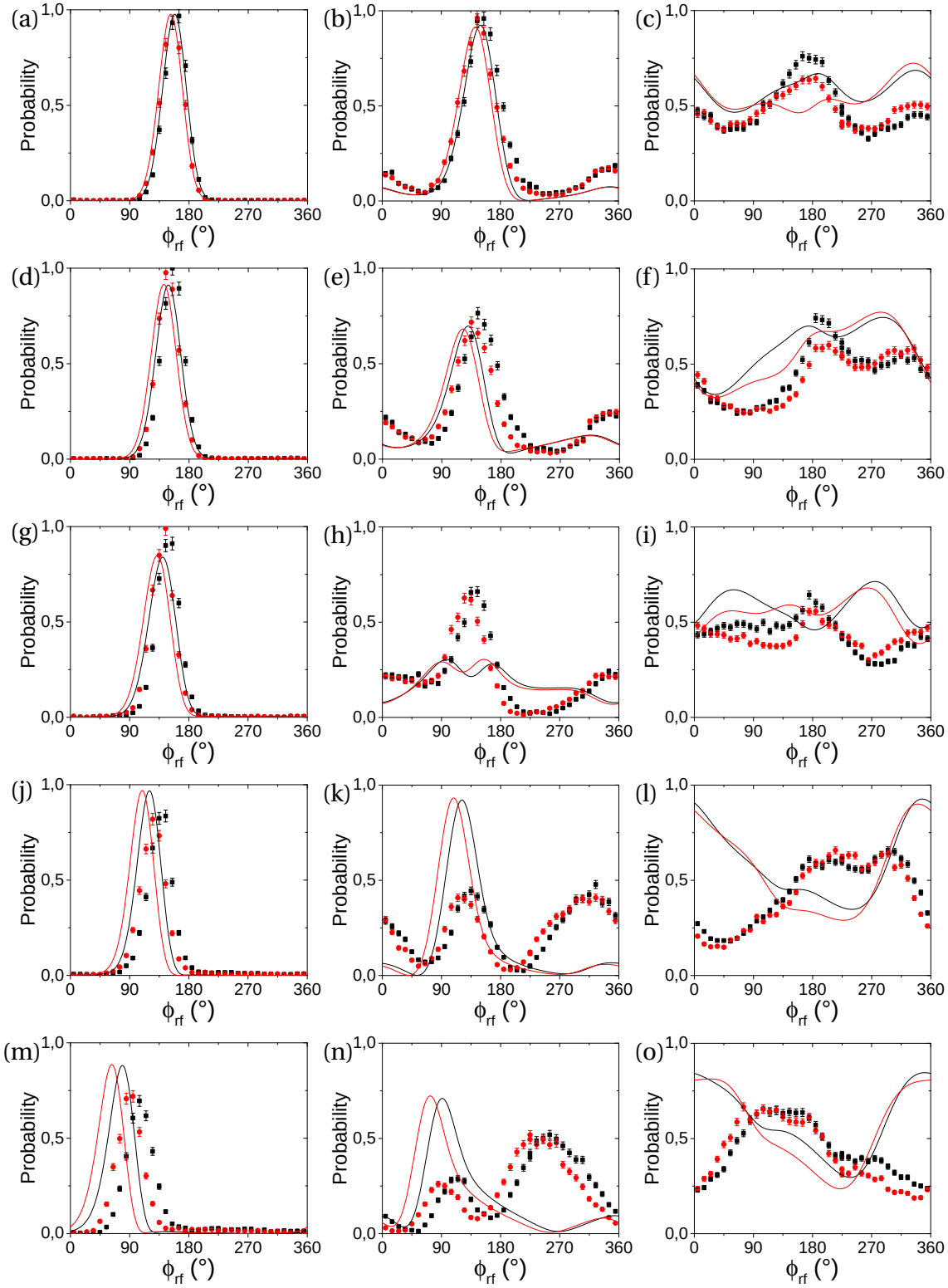

Figure 3.10: The measured classical probabilities for two electric fields F_{up} (black) and F_{down} (red) separated by $\Delta F = 73.2$ mV/m for the settings a (first column), b (second column) and c (third column) of Table 3.1 and for increasing interrogation times from top to bottom, i.e. $\tau = 10$ ns (first row), $\tau = 50$ ns (second row), $\tau = 100$ ns (third row), $\tau = 200$ ns (fourth row), $\tau = 400$ ns (fifth row) as a function of the relative radio-frequency phase $\varphi_{rf} + \pi$.

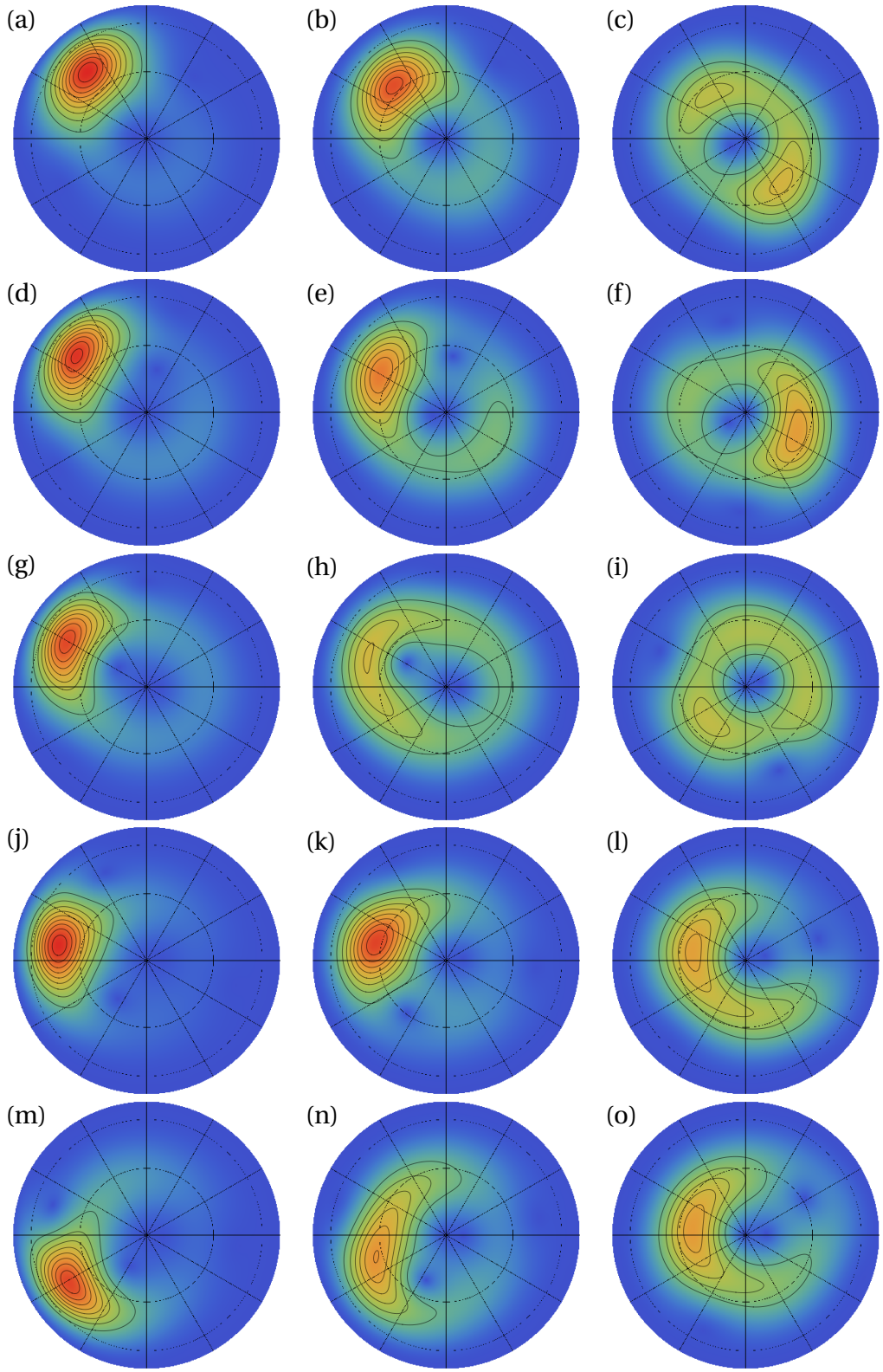

Figure 3.11: Numerical simulations for the Q-function of the state just before the second radio-frequency pulse centred around the south pole of the Bloch sphere for the settings a (first column), b (second column) and c (third column) of Table 3.1 and for increasing interrogation times from top to bottom, i.e. τ =10 ns (first row), τ =50 ns (second row), τ =100 ns (third row), τ =200 ns (fourth row), τ =400 ns (fifth row). The color scale is linear from 0 to 1 and the contour lines are every 0.1 (see Fig. 1.6 for the color scale).

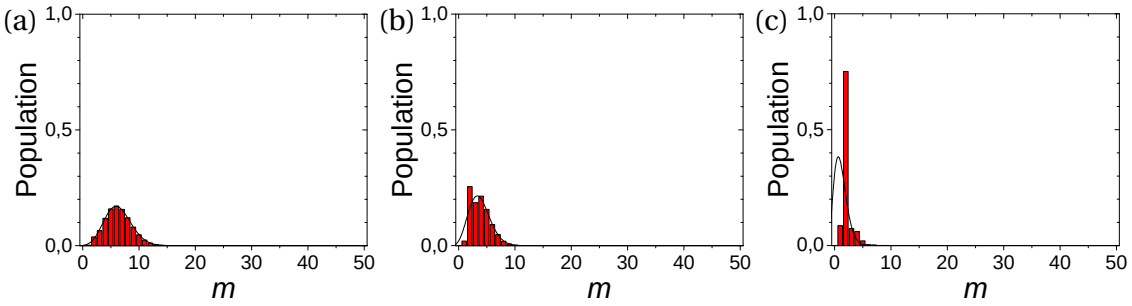

Figure 3.12: Numerical simulation of the population distribution of the states after the first radio-frequency pulse for the Rabi frequencies $\Omega_{rf} = \Omega_a$ (a), $\Omega_{rf} = \Omega_b$ (b), $\Omega_{rf} = \Omega_c$ (c), corresponding to settings a,b,c in Table 3.1 as a function of the level m. The theoretical distribution (Eq. 1.33) expected for a spin coherent state corresponding to the estimated Rabi angle in Table 3.1 is shown as the full black lines.

the height of the peak.

3.3.2 Experimental results for the quantum-enabled method

We then repeat the same sequence after adding the two Ramsey $\pi/2$ microwave pulses. Fig. 3.13 shows the measured probability $P_q(\varphi_{\mathrm{rf}}, \varphi_{\mathrm{mw}})$ to find the atom in the $|51c\rangle$ state after the quantum-enabled method for an interrogation time of $\tau = 10$ ns. In comparison we plot the results of the corresponding numerical simulations.

In the quantum-enabled method, the probability to return to the $|J, J\rangle$ state shows fast oscillations inside an envelope $\sqrt{P_c(\varphi_{\mathrm{rf}})}$ defined by the classical probability. This can be observed for the numerical simulations and for the measured data. In principle, the envelope can be calculated directly from the classical probability as $\left(1/2 \pm 1/2\sqrt{P_c(\varphi_{\mathrm{rf}})}\right)^2$ (Eq. 3.4). We see that the experimental data does not reach the lower envelope. This is due to imperfections of the Ramsey $\pi/2$ pulses in the quantum-enabled method which transfer a little less the 50% from the $|51c\rangle$ to the $|49c\rangle$ state.

By increasing the Rabi frequency from $\Omega_{\mathrm{rf}} = \Omega_a$ to $\Omega_{\mathrm{rf}} = \Omega_c$, the oscillation frequency increases. However, at the same time the contrast decreases since the amplitude is ultimately determined by $P_c(\varphi_{\mathrm{rf}})$. In order to assess this trade-off we calculate the sensitivity of this method in the following section.

3.3.3 Experimental single-atom sensitivity

The optimum radio-frequency phase $\varphi_{\mathrm{rf}} = \varphi_{\mathrm{rf},0}$ differs for each Rabi frequency Ω_{rf} and interrogation time τ. We record the probability $P_q(\varphi_{\mathrm{rf},0}, \varphi_{\mathrm{mw}})$ as a function of the microwave phase φ_{mw} of the Ramsey $\pi/2$ pulses.

Fig. 3.14a shows Ramsey fringes without applied radio-frequency pulses for the two different electric fields separated by $\Delta F = 18.3$ mV/m. The two fringes overlap to the

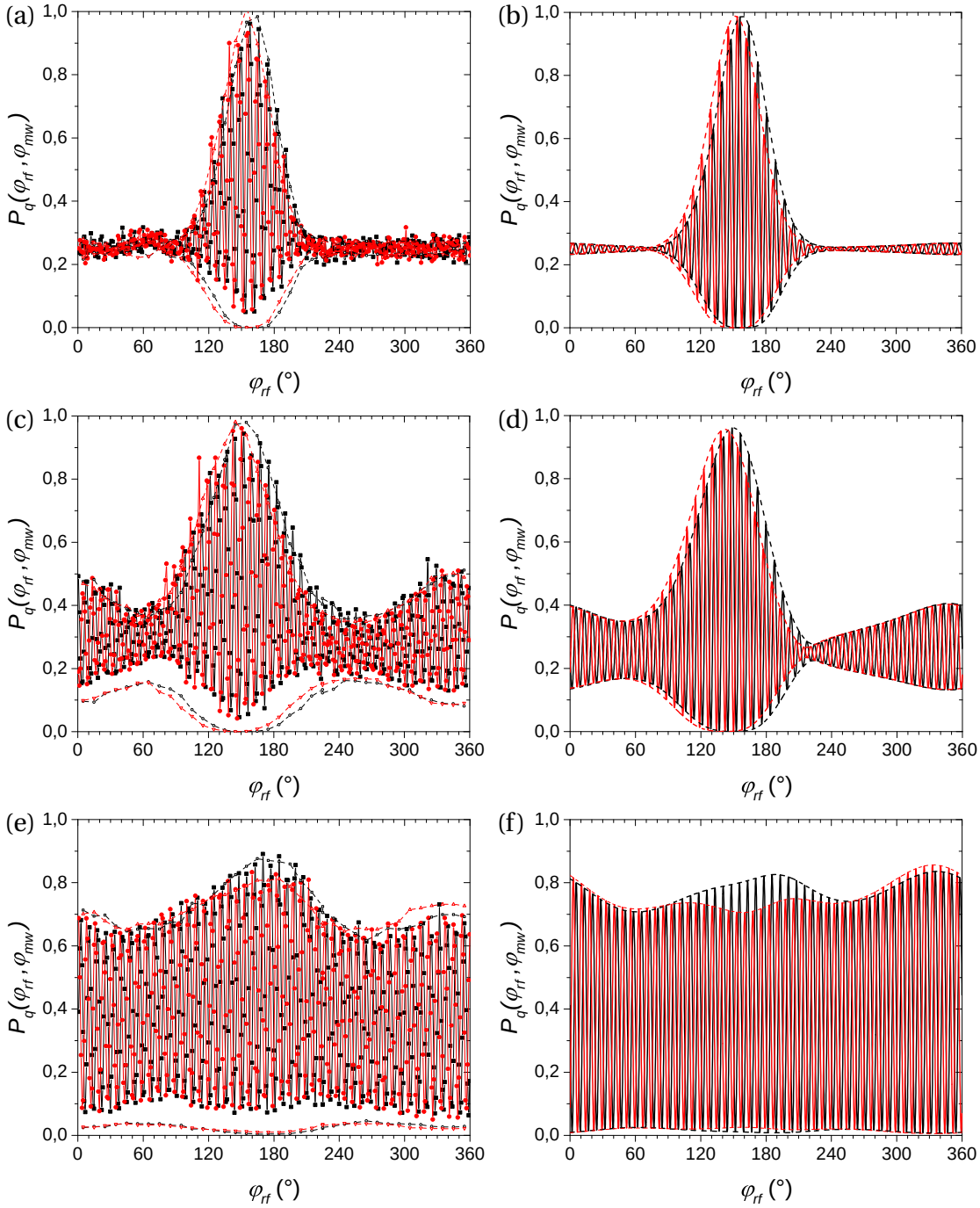

Figure 3.13: The probability $P_q(\varphi_{rf},\varphi_{mw})$ is shown as a function of the radio-frequency phase φ_{rf} for the three Rabi frequencies $\Omega_{rf}=\Omega_a$ (a,b), Ω_b (c,d) and Ω_c (e,f) for an interrogation time $\tau = 10$ ns and an electric field variation of $\Delta F = 73.2$ mV/m between F_{up} (black) and F_{down} (red). In the left column are shown the experimental data (full) together with the envelope (hollow points, dashed line) calculated from the measured probability $P_c(\varphi_{rf})$ as $\left(1/2 \pm 1/2\sqrt{P_c(\varphi_{rf})}\right)^2$ (Eq. 3.4). In the right column are shown the numerical simulations of a rubidium atom for $P_q(\varphi_{rf},\varphi_{mw})$ (full lines) and the envelope from $P_c(\varphi_{rf})$ (dashed lines).

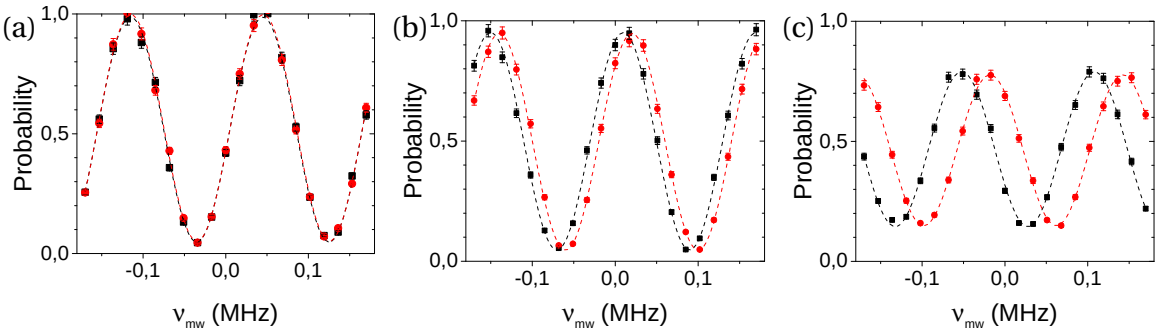

Figure 3.14: (a) The Ramsey fringes between the levels $|51c\rangle - |49c\rangle$ with no applied radio-frequency pulse. (b) The measured quantum-enabled probability $P_q(\varphi_{rf,0},\varphi_{mw})$ as a function of $\nu_{mw} \propto \varphi_{mw}$ for two electric fields F_{up} (black) and F_{down} (red) separated by $\Delta F = 18.3$ mV/m for $\Omega_{rf} = \Omega_a$ for an interrogation time $\tau = 10$ ns. (c) Same for an interrogation time $\tau = 200$ ns.

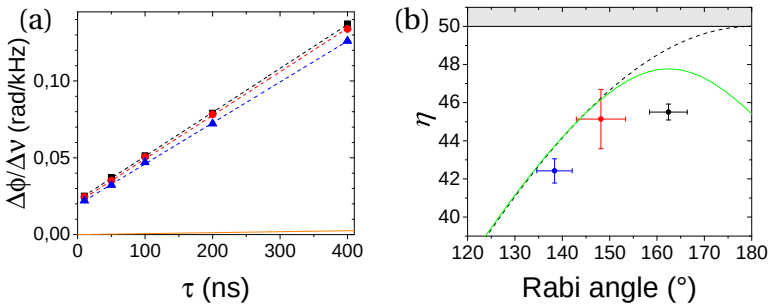

Figure 3.15: (a) Experimental results of the ratio $\Delta\Phi_\tau/\Delta\nu$, together with the respective linear fit, for the Rabi frequencies Ω_a (blue), Ω_b (red) and Ω_c (black). The orange line is the accumulated classical phase $\Delta\phi/\Delta\nu = 2\pi\tau$. (b) Enhancement factor $\eta = J - \langle M\rangle$ (slope plotted in (a) divided by 2π) as a function of the Rabi angle, together with the numerical simulation (green) of the rubidium atom of $J - \langle M\rangle$ for a radio-frequency duration of $t_{rf} = 103.33$ ns and the ideal enhancement factor (dashed) given by $J(1-\cos(\theta))$. The grey area corresponds to an unattainable enhancement factor $> 2J$ beyond the Heisenberg limit.

precision of our measurement.[5] The contrast C is almost 100%. The reduction is due to imperfections in the $\pi/2$ pulses.

Fig. 3.14b shows Ramsey fringes with applied radio-frequency pulses for $\Omega_{\mathrm{rf}} = \Omega_a$ and an interrogation time of $\tau = 10$ ns. The shift between the two fringes gives the variation of the global quantum phase $\Delta\Phi$ induced by the change of the electric field of $\Delta F = 18.3$ mV/m. The contrast of the fringes is still almost 100%. For a larger interrogation time, i.e. $\tau = 200$ ns in Fig. 3.14c, the phase global quantum phase $\Delta\Phi$ is larger and the two fringes are shifted farther. During the longer interrogation time, however, the superposition between two states of very different polarizabilities is exposed to electric field fluctuations over a longer time leading to a blurring of the fringes and therefore a reduced contrast.

[5]The superposition of the states $|51c\rangle$ and $|49c\rangle$ still has a differential quadratic Stark shift. For $F_0 = 234.5$ V/m and $\Delta F = 18.3$ mV/m, the differential quadratic Stark shift corresponds to 0.85 kHz. The two Ramsey pulses are separated by 3 μs, the accumulated phase shift is therefore $\Delta\varphi_{\mathrm{mw}} = 0.016$ rad.

We fit the quantum phase shift $\Delta\Phi$ and the contrast C for the recorded Ramsey fringes with a sine-function. The results are shown in Fig. 3.15a. Since we expect the global quantum phase shift to be proportional to the electric field variation ΔF, we plot $\Delta\Phi/\Delta\nu$ as a function of τ, where $\Delta\nu = \frac{1}{2\pi}\frac{\partial\omega}{\partial F}\Delta F$ is the variation of the spin frequency due to ΔF. The experimental points form a line which can be fitted by

$$\frac{\Delta\Phi}{\Delta\nu} = 2\pi\eta\tau + \frac{\Delta\Phi_0}{\Delta\nu}$$

The offset phase $\Delta\Phi_0/\Delta\nu$ at $\tau = 0$ ns is due to the global phase accumulated during the finite duration of the radio-frequency pulses. The expected slope has the form $2\pi\eta$, where $\eta = J - \langle M\rangle$ is the dimensionless enhancement factor.

Fig. 3.15b shows the fitted enhancement factor η as a function of the estimated Rabi angle $\Omega_{\mathrm{rf}}(t_{\mathrm{rf}} - t_0)$. For an ideal spin, η should follow $J(1-\cos(\theta))$ (dashed line in Fig. 3.15b). For $\theta = \pi$ the enhancement factor would be maximum, $2J$, which corresponds to the Heisenberg limit. The points corresponding to $\Omega_{\mathrm{rf}} = \Omega_a$ (blue) and $\Omega_{\mathrm{rf}} = \Omega_b$ (red) are slighty below the theoretical curve and we observe a saturation effect for $\Omega_{\mathrm{rf}} = \Omega_c$ (black in Fig. 3.15b). This saturation can be explained by the energy structure of the rubidium atom. The numerical simulation of the latter (green line in Fig. 3.15b) leads to the value of $J - \langle M\rangle$ in the case of the rubidium atom as a function of the Rabi angle $\Omega_{\mathrm{rf}} t_{\mathrm{rf}}$. In the simulation, we fix the radio-frequency pulse duration to $t_{\mathrm{rf}} = 103.33$ ns, mean value of the settings a, b, c in Table 3.1, and vary the Rabi frequency Ω_{rf}. We observe the saturation also in the numerical simulation. However, there is a discrepancy between the measured points and the numerically simulated curve. This can be due to experimental imperfections, for example a residual σ^- component in the radio-frequency field, or to a more fundamental reason: as we start to populate the non-hydrogen-like levels, the model of the rotation of a spin is no longer valid and the enhancement factor is not simply given by $J - \langle M\rangle$.

The experimental single-atom sensitivity corresponding to the interrogation time τ is calculated from Eq. 3.5 assuming that $\partial\Phi/\partial F \approx \Delta\Phi/\Delta F$. We also have to take into account that the term $\partial P/\partial\Phi = C/2$ is reduced by the finite contrast C of the interference fringes. Therefore, the single-atom sensitivity becomes (Eq. 3.5)

$$\sigma_F^{(1),\mathrm{exp}} = \frac{1}{C}\frac{\Delta F}{\Delta\Phi}. \tag{3.11}$$

In order to asses the sensitivity of the method during the interrogation time τ, we calculate

$$\sigma_{F,\tau}^{(1),\mathrm{exp}} = \frac{1}{C}\frac{\Delta F}{\Delta\Phi_\tau}, \tag{3.12}$$

with the reduced global quantum phase shift $\Delta\Phi_\tau = \Delta\Phi - \Delta\Phi_0$.

Fig. 3.16a presents the single-atom sensitivity during the interrogation time as a function of τ. The setting with a Rabi frequency of $\Omega_{\mathrm{rf}} = \Omega_a$ shows the overall lowest sensitivity. Naively, we would expect that the setting with the largest estimated Rabi angle leads to the lowest sensitivity. However, the enhancement factor η (see Fig. 3.15b)

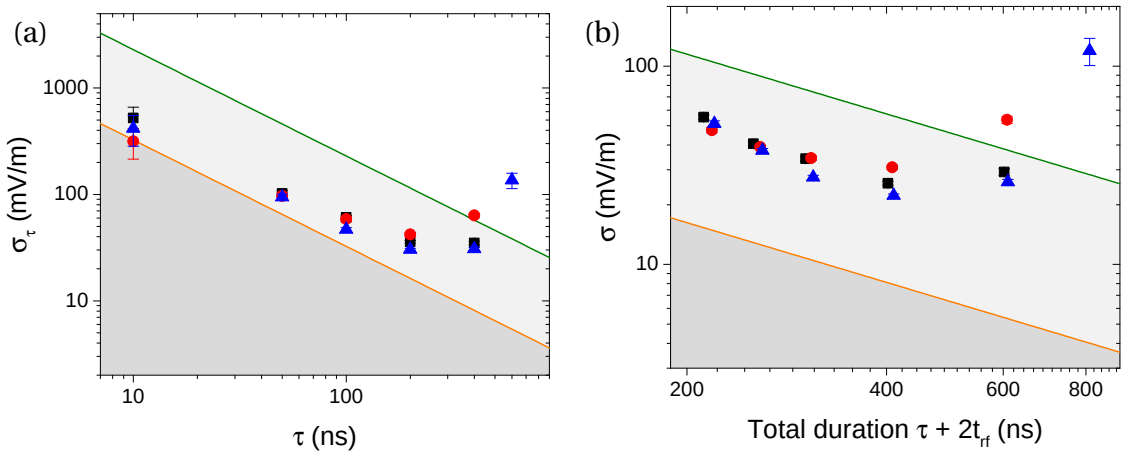

Figure 3.16: (a) Sensitivity as a function of the interrogation time τ, the delay between the two radio-frequency pulses in comparison with the standard quantum limit (green) and the Heisenberg limit (orange), for Ω_a (blue), Ω_b (red) and Ω_c (black). (b) Total sensitivity as a function of the total duration or the double radio-frequency pulses $t_{rf}+\tau+t_{rf}$.

in the case of $\Omega_{\mathrm{rf}}=\Omega_c$ is not much larger than for Ω_a. Additionally, the contrast of the fringes in the case of Ω_c is reduced because a smaller fraction of the population returns to the north pole. This is even worse in the case of $\Omega_{\mathrm{rf}}=\Omega_b$, although the enhancement factor η is larger than for Ω_a. Here, due the anharmonicity in the low-m states, the probability to return to the $|51c\rangle$ state drops drastically when we increase the interrogation time. In all cases, the sensitivity that we measure is eventually limited by electric field inhomogeneities when increasing the interrogation time. For small interrogation times $\tau<200$ ns, the sensitivity, inversely proportional to the product $C\Delta\Phi_\tau$, scales like τ^{-1}. For interrogation times $\tau>200$ ns the contrast reduction becomes too large and the sensitivity saturates.

The sensitivity $\sigma^{(1),\mathrm{exp}}_{F,\tau}$ can now be compared to the standard quantum limit (SQL, Eq. 3.2) and the Heisenberg limit (HL, Eq. 3.9). For a very short interrogation time of $\tau=10$ ns, the sensitivity we measure for $\Omega_{\mathrm{rf}}=\Omega_a$ is $\sigma^{(1),\mathrm{exp}}_{F,\tau}=(418\pm133)$ mV/m. When comparing with the HL at $\tau=10$ ns, $\sigma^{(1)}_{F,\mathrm{HL}}=325$ mV/m, and the SQL $\sigma^{(1)}_{F,\mathrm{SQL}}=2297$ mV/m, we find that the measured sensitivity lies by a factor of ~5.5 (or by -14.8 dB) below the SQL.[6] We reach the lowest sensitivity at $\tau=200$ ns interrogation time with $\sigma^{(1),\mathrm{exp}}_{F,\tau}=(30.4\pm0.8)$ mV/m for Ω_a. With our repetition rate of $f_{\mathrm{rep}}=1/311\mu s$ this yields a integrated sensitivity of

$$\sigma^{\mathrm{exp}}_{F,\tau,\mathrm{int}}=\frac{\sigma^{(1),\mathrm{exp}}_{F,\tau}}{\sqrt{f_{\mathrm{rep}}/2}}=\sqrt{2\cdot311\mu\mathrm{s}}\,(30.4\pm0.8)\ \mathrm{mV/m}=(0.76\pm0.02)\ \mathrm{mV/m}/\sqrt{\mathrm{Hz}}.$$

In comparison we also calculate the total sensitivity over the full duration of the double

[6] The ratio in dB is calculated by $G_{\mathrm{dB}}=20\cdot\log\left(\frac{\sigma^{(1),\mathrm{exp}}_{F}}{\sigma^{(1)}_{F,\mathrm{SQL}}}\right)=-14.80$ dB. The ratio between the HL and the SQL in dB is $G_{\mathrm{dB}}=20\cdot\log\left(\frac{\sigma^{(1)}_{F,\mathrm{HL}}}{\sigma^{(1)}_{F,\mathrm{SQL}}}\right)=20\cdot\log\left(\frac{1}{\sqrt{2J}}\right)=-16.99$ dB.

radio-frequency pulses $t_{\mathrm{rf}} + \tau + t_{\mathrm{rf}}$. In this case the experimental single-atom sensitivity is calculated with the full global quantum phase shift $\Delta\Phi$ without subtracting the phase accumulated during the radio-frequency pulses. The single-atom sensitivity given by Eq. 3.11 is therefore smaller than the single-atom sensitivity when taking into account only the accumulated phase shift during the interrogation time τ (Eq. 3.12). The total sensitivity is shown in comparison in Fig. 3.16b. The lowest sensitivity for $\Omega_{\mathrm{rf}} = \Omega_a$ at $\tau = 200$ ns interrogation time is now $\sigma_F^{(1),\mathrm{exp}} = (22.2 \pm 0.4)$ mV/m for an overall duration of $t_{\mathrm{rf}} + \tau + t_{\mathrm{rf}} = 410$ ns, where $t_{\mathrm{rf}} = 105$ ns. The integrated sensitivity becomes

$$\sigma_{F,\mathrm{int}}^{(1),\mathrm{exp}} = \frac{\sigma_F^{(1),\mathrm{exp}}}{\sqrt{f_{\mathrm{rep}}/2}} = \sqrt{2 \cdot 311\mu\mathrm{s}}\ (22.2 \pm 0.4)\ \mathrm{mV/m} = (0.55 \pm 0.01)\ \mathrm{mV/m}/\sqrt{\mathrm{Hz}}.$$

The results presented here show a significant improvement with respect to the previous version of this experiment [111, 112] developed and performed during the first part of my PhD thesis where we measured a best overall sensitivity of 120 mV/m, compared to the recent experiments with 30.4 mV/m, both during interrogation time of 200 ns. Thanks to a smaller quadratic Stark effect, a higher radio-frequency field power and a better homogeneity of the radio-frequency field, we are now able to reach an angle of $\theta \approx \pi$, limited now by the energy structure of the rubidium atom. Nevertheless, for small interrogation times, we now reach a sensitivity very close to the Heisenberg limit, which represents the maximum achievable performance allowed by quantum mechanics for this system. The sensitivity we reach is ~14.8 dB below the standard quantum limit comparable to what is reached in the state-of-the-art squeezing experiments (~20 dB in [69]). The integrated sensitivity, when considering the total duration of the radio-frequency pulses, of 0.55 mV/m/$\sqrt{\mathrm{Hz}}$ is comparable to the state-of-the-art electrometry experiments [64, 66, 124].

3.3.4 Experimental decoherence

The contrast C of the fringes is, in theory, given by the classical probability as $\sqrt{P_c(\varphi_{\mathrm{rf}})}$. However, due to the electric field noise and inhomogeneity, the atoms see a slightly different electric field in each realization of the experiment. We can write the electric field as $F + \delta F$ where F is the mean electric field averaged over all repetitions of the experiment and δF is the difference between the electric field in the i-th repetition and the average electric field, $\delta F_i = F_i - F$. Since we average over several repetitions to measure the interference fringes, the electric field fluctuations lead to a reduction of the contrast of the fringes. When assuming a Gaussian noise, this reduction of the contrast is a function of the phase sensitivity α and the standard deviation σ_F of the electric field noise. We therefore expect the normalized contrast $C/\sqrt{P_c(\varphi_{\mathrm{rf}})}$ to scale like

$$\frac{C}{\sqrt{P_c(\varphi_{\mathrm{rf}})}} \propto e^{-\frac{1}{2}\alpha^2\sigma_F^2}. \tag{3.13}$$

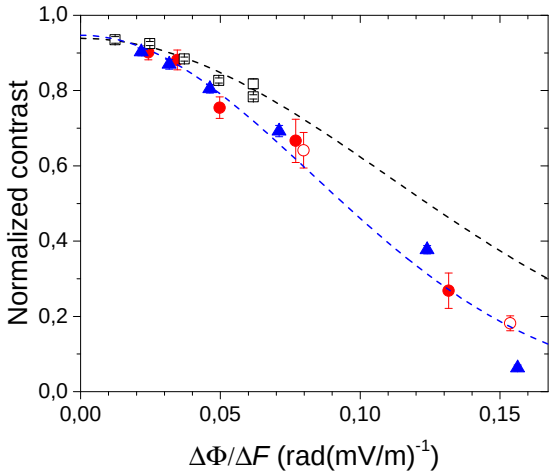

Figure 3.17: The normalized contrast ($C/\sqrt{P_c(\varphi_{rf,0})}$) of the Ramsey fringes of the quantum-enabled sequence with radio-frequency pulses with Ω_a (blue) and Ω_b (red) as a function of the phase sensitivity $\alpha = \Delta\Phi/\Delta F$. In comparison we add the contrast of the microwave Ramsey fringes between the states $|50c\rangle - |51e1\rangle$ (see Fig. 2.19) as a function of $\Delta\phi_{mw}/\Delta F = 2\pi t \frac{\Delta\nu}{\Delta F}$, where t is the delay between the Ramsey pulses (black, hollow). The black line corresponds to the Gaussian fit of the microwave data with a standard deviation of $\sigma_F =$ 9.0 mV/m, the blue line to the Gaussian fit of the two radio-frequency Ramsey fringes with a standard deviation of $\sigma_F = 12.0$ mV/m.

In Fig. 3.17, we plot $C/\sqrt{P_c(\varphi_{\mathrm{rf}})}$ as a function of α and can thus deduce the standard deviation $\sigma_F = (12.0 \pm 0.9)$ mV/m of the electric field noise from the Gaussian fit of the normalized contrast.

We can compare $C/\sqrt{P_c(\varphi_{\mathrm{rf}})}$ to the contrast reduction observed for the Ramsey fringes of the $|50c\rangle$ to $|51e1\rangle$ transition. In this case, the phase sensitivity is given by

$$\alpha_{\mathrm{mw}} = \tau \frac{\partial \omega_{\mathrm{at}}}{\partial F}.$$

This allows us to convert the coherence time of (35.8 ± 2.9) μs (see Fig. 2.19) into the standard deviation of the electric field noise of $\sigma_F = (9.0 \pm 0.7)$ mV/m.

The discrepancy between the two values of σ_F can be explained by the bandwidth of each measurement. For the Ramsey fringes of the $|50c\rangle$ to $|51e1\rangle$ transition, the delay between the two pulses is of the order of a few μs filtering out the high frequency noise. The quantum-enabled method probes the electric field with a much higher bandwidth since the delay between the two radio-frequency pulses is much shorter and is therefore sensitive to electric field noise with higher frequency, leading to a larger standard deviation σ_F.

3.4 Improved sensitivity with echo-like sequence

It seems that the contrast of the fringes is due to inhomogeneous broadening due to the electric field noise. This causes the sensitivity to increase for large interrogation times. The dispersion can be a result of spatial inhomogeneity or of temporal noise. The low-frequency part of the temporal electric field noise can be suppressed by using spin-echo techniques [123], allowing us to get an even lower sensitivity.

We thus implement an echo-like sequence, represented as an Ramsey interferometer in Fig. 3.18. We first apply a microwave $\pi/2$ pulse to prepare the superposition $\frac{1}{\sqrt{2}}(|51c\rangle + |49c\rangle)$. At time t, we apply a first radio-frequency pulse, followed after an interrogation time τ by a second radio-frequency pulse, the phase of which is chosen to bring back the part of the wave-function in the $n = 51$ manifold to the circular state $|51c\rangle$, as described in the previous part of this chapter. Here, however, instead of directly applying the second $\pi/2$ microwave pulse, we change the amplitude of the electric field, so that the radio-frequency is now resonant with the Stark transitions in the $n = 49$ manifold. At time t', we apply a third radio-frequency pulse, of duration t'_{rf}, that rotates the angular momentum $\hat{\boldsymbol{J}}_1$ associated to the $n = 49$ manifold. After an interrogation time τ, we apply the fourth radio-frequency field pulse that brings back the part of the wave-function in the $n = 49$ manifold in the corresponding circular state $|49c\rangle$. This echo-sequence can be written as

$$\begin{aligned} |51c\rangle + |49c\rangle &\xrightarrow{t} e^{-i\Phi_{51}(F+\delta F)}|51c\rangle + |49c\rangle \\ &\xrightarrow{t'} e^{-i\Phi_{51}(F+\delta F)}|51c\rangle + e^{-i\Phi_{49}(F'+\delta F')}|49c\rangle\,. \end{aligned} \tag{3.14}$$

After the first pair of radio-frequency pulses, the spin associated to the $n = 51$ manifold has accumulated a phase (Eq. 3.6)

$$\Phi_{51}(F+\delta F) = \alpha_{51}\cdot(F+\delta F) = \Phi_{51}(F) + \alpha_{51}\delta F$$

where F is the average value of the electric field, δF the value of the electric field noise at time t, and α_{51} the phase sensitivity associated to the $n = 51$ manifold which depends on the Rabi frequency Ω_{rf}, the duration of the radio-frequency pulses t_{rf} and the interrogation time τ. The phase Φ_{49} is expressed similarly by $\Phi_{49}(F'+\delta F') = \Phi_{49}(F') + \alpha_{49}\delta F'$ where α_{49} is the phase sensitivity associated to the $n = 49$ manifold.

We assume that the electric field noise is correlated over a time scale of at least $\Delta t = t' - t$ which is the minimum time we need to perform the echo sequence. The electric field noise at times t and t' is therefore the same, $\delta F = \delta F'$. In this case, the final state of the echo-sequence in Eq. 3.14 can be written as

$$e^{-i[\Phi_{49}(F')+\alpha_{49}\delta F]}\left[e^{-i[\Phi_{51}(F)-\Phi_{49}(F')+(\alpha_{51}-\alpha_{49})\delta F]}|51c\rangle + |49c\rangle\right],$$

where the phase $e^{-i[\Phi_{49}(F')+\alpha_{49}\delta F]}$ can be omitted since it is a global phase. We are only interested in the relative phase between $|51\rangle$ and $|49\rangle$, called the total accumulated

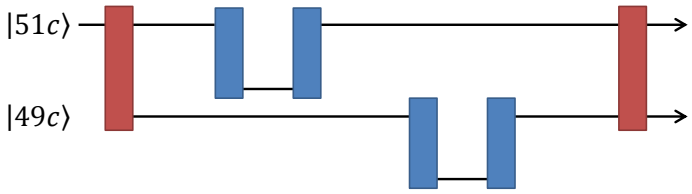

Figure 3.18: The Echo-like sequence of the quantum-enabled method represented as a Ramsey interferometer. The Ramsey $\pi/2$ pulses (red) create a superposition of the $|51c\rangle$ and $|49c\rangle$ states. During the first pair of radio-frequency pulses (blue), the $n = 51$ component of the superposition accumulates a global quantum phase, during the second pair of radio-frequency pulses, the $n = 49$ component accumulates ideally the same global quantum phase.

quantum phase,

$$\Phi = \Phi_{51}(F) - \Phi_{49}(F') + (\alpha_{51} - \alpha_{49})\delta F.$$

Since the radio-frequency acts similarly on the spin associated to $n = 51$ and $n = 49$, the phase sensitivities are approximately the same, $\alpha_{51} \approx \alpha_{49}$,[7] and the total quantum phase, $\Phi \approx \Phi_{51}(F) - \Phi_{49}(F')$, is insensitive to the electric field noise δF, while having the same sensitivity to the electric field F as the fringes without echo for a variation that occurs on a time scale that is short compared to $t' - t$. Like all echo techniques, this method is only sensitive to variations of the electric field and actually measures the difference $F - F'$ of the electric field at times t and t'. The echo fringes therefore have the same sensitivity to a change ΔF in the electric field at time t as the fringes without echo, as long as the electric field at t' is constant. However, the reduction of contrast of the Ramsey fringes due to the electric field noise is

$$C \propto e^{-\frac{1}{2}(\alpha_{51}-\alpha_{49})^2\sigma_F^2} \approx 1,$$

if $\alpha_{51} \approx \alpha_{49}$, which is much smaller than in the case without echo, where $C \propto e^{-\frac{1}{2}\alpha^2\sigma_F^2}$.

3.4.1 Experimental realization

The experimental sequence is similar to the case of the quantum-enabled method presented in the last section. The main difference is that we add a second radio-frequency pulse pair and an electric field step in order to be resonant with the $n = 49$ manifold during this second radio-frequency pulse pair. The experimental sequence is shown in Fig. 3.19.

The Ramsey pulses in this experiment are at 12 μs (as before) and 35 μs (much later than before), from the initial laser pulse at 0 μs, and have a duration of 0.48 μs and 0.65 μs.[8]

[7] In principle, the phase sensitivities can be adapted by changing the interrogation time τ between the $n = 49$ radio-frequency pulses. However, this is not done in this experiment.

[8] The duration of the Ramsey pulses differ from the duration of the previous section. The duration is

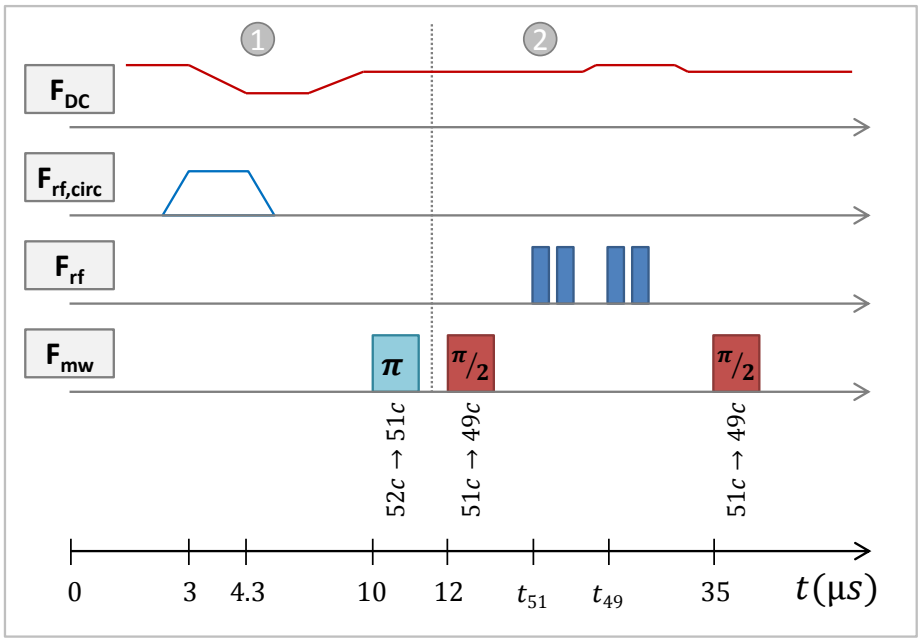

Figure 3.19: The experimental sequence for the echo method. The first radio-frequency pulse pair, applied at t_{51}, is resonant in the $n = 51$ manifold, whereas the second radio-frequency pulse pair, applied at t_{49} during a slightly increased electric field amplitude, is resonant in the $n = 49$ manifold. The time $t = 0$ is defined by the laser pulse.

The first radio-frequency pair is applied in an electric field $F_{51} \approx 234.5$ V/m making the radio-frequency field ($\omega_{\mathrm{rf}} = 2\pi \cdot 230$ MHz) resonant with the atomic frequency $\omega_{\mathrm{at},51} = 2\pi \cdot 230.06$ MHz. We use a radio-frequency field with the Rabi frequency $\Omega_{\mathrm{rf},51} = \Omega_a = 2\pi \cdot (3.74 \pm 0.10)$ MHz and a radio-frequency duration $t_{\mathrm{rf},51} = 105$ ns corresponding to a complete period of oscillation of the off-resonant Rabi oscillations in the $n = 49$ manifold. This corresponds to setting a in Table 3.1.

The second radio-frequency pair is applied in the electric field $F_{49} \approx 244.1$ V/m where the atomic frequency in the $n = 49$, measured to be $\omega_{\mathrm{at},49} = 2\pi \cdot 229.99$ MHz, becomes resonant with the radio-frequency field. The Rabi frequency can be fitted on the depopulation of the $|49c\rangle$ state. The measured value of $\Omega^{+}_{\mathrm{rf},49} = 2\pi \cdot (3.67 \pm 0.23)$ MHz is in good agreement with the expected value of $49/51 \cdot \Omega^{+}_{\mathrm{rf},51} \approx 2\pi \cdot 3.59$ MHz.[9] The radio-frequency duration is chosen from the period of the off-resonant Rabi oscillations in the $n = 51$ manifold. We measure $t_{\mathrm{rf},49} = 101$ ns.

The interrogation time $\tau = 400$ ns ($\tau = 600$ ns) is the same for both pairs of radio-frequency pulses. The electric field is switched from F_{51} to F_{49} at 14.1 μs (14.3 μs) during 100 ns, reaching the new value at 14.2 μs (14.4 μs). The first radio-frequency pulse starts at 13.4 μs, the third radio-frequency pulse at 14.3 μs (14.5 μs depending on the interrogation time τ).

regularly adjusted due to the long-term drift of the microwave power seen by the atom.

[9] For a given amplitude of the radio-frequency field, the Rabi frequency in different manifold scales with principal quantum number n.

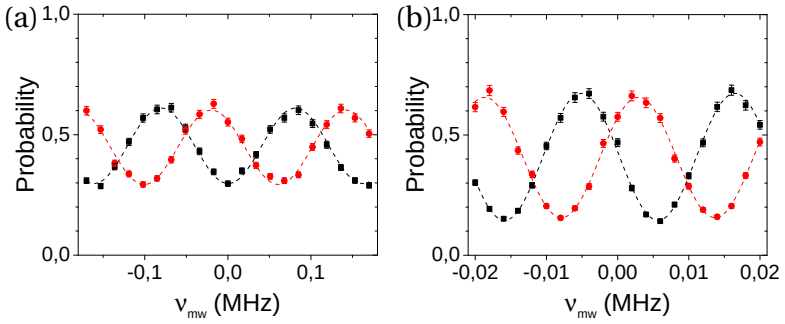

Figure 3.20: The measured quantum-enabled probability as a function of the MW frequency φ_{mw} for two electric fields F_{up} (black) and F_{down} (red) separated by $\Delta F = 183\mu V/cm$ for Ω_a for an interrogation time τ =400 ns with (a) a single radio-frequency pulse pair and (b) two radio-frequency pulse pairs. The echo-sequence (b) shows an increased contrast and the same phase shift $\Delta\Phi$.

We choose the relative radio-frequency phase between the two pulses of the first radio-frequency pair $\varphi_{\mathrm{rf},51} = \varphi_{\mathrm{rf},0}$ so that the probability $P_c(\varphi_{\mathrm{rf},51})$ to return to the $|51c\rangle$ state after the second radio-frequency pulse is maximum.

In principle, we would tune the relative radio-frequency phase between the two pulses of the second radio-frequency pair in the same manner to optimize the probability of the part of the wave-function in the $n = 49$ manifold to return to the $|49c\rangle$ state after the last radio-frequency pulse. Unfortunately, we do not have enough radio-frequency sources to have three radio-frequency fields with independent phases. To circumvent this problem, the electric field F_{49} is fine-tuned to ensure that the same relative phase φ_{rf} optimizes the return probability for both parts of the wave-function, in $n = 49$ and $n = 51$. Changing the electric field by 1 mV/m allows us to tune $\varphi_{\mathrm{rf},49}$ by $(0.19 \pm 0.02)^\circ$, allowing us to get $\varphi_{\mathrm{rf},49} \approx \varphi_{\mathrm{rf},51} \approx \varphi_{\mathrm{rf},0}$.

To measure the phase sensitivity of the echo-fringes we apply an electric field pulse with amplitude ΔF only during the first radio-frequency pulse pair, since the fringes would otherwise be insensitive to the DC change of the electric field. In the experimental sequence the electric field pulse alternates between amplitude ΔF ("F_{up}") and amplitude zero ("F_{down}").

Fig. 3.20 shows the measured Ramsey fringes for the sequence with a single radio-frequency pulse pair and the echo-sequence with two radio-frequency pulse pairs for an interrogation time of $\tau = 400$ ns. The quantum phase shift $\Delta\Phi$ is the same for both fringes. However, the contrast of the echo-fringes is increased due to the reduced sensitivity to the electric field noise.

The single-atom sensitivity for the echo-sequence is calculated as before from the contrast C and the accumulated quantum phase $\Delta\Phi_\tau$ (during τ) and plotted in Fig. 3.21 as a function of the interrogation time τ. The sensitivity is shown in comparison with the sensitivity measured with a single radio-frequency pair with $\Omega_{\mathrm{rf}} = \Omega_a$. We added the

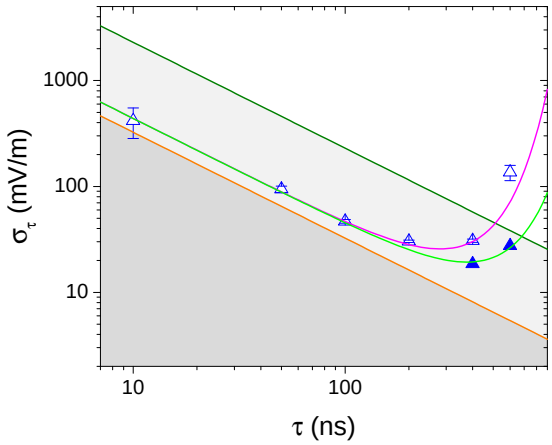

Figure 3.21: Single-atom sensitivity as a function of the interrogation time τ for $\Omega_{rf} = \Omega_a$ in the case of the echo-like sequence (full points) and in the case without echo (hollow points, see Fig. 3.16a) in comparison with the standard quantum limit (green) and the Heisenberg limit (orange). The analytical model of the sensitivity is plotted for $\sigma_F = 12$ mV/m (pink) and $\sigma_F = 9$ mV/m (bright green).

analytical model to describe the behaviour of the sensitivity calculated as (Eq. 3.12)

$$\sigma_{F,\tau}^{(1),\mathrm{exp}} = \frac{1}{C}\frac{\Delta F}{\Delta \Phi_\tau}$$

with $C = C_0 e^{-\frac{1}{2}\alpha^2\sigma_F^2}$ (Eq. 3.13) and $\Delta\Phi_\tau/\Delta F = \alpha = \eta\tau(\Delta\omega_{\mathrm{at}}/\Delta F)$ (Eq. 3.7). The only free parameters are the contrast C_0 and the standard deviation of the electric field noise σ_F. With this model we can fit the sensitivity in the case without echo for $\sigma_F = 12$ mV/m and $C_0 \approx 0.77$. In the case of the echo sequence, the model fits best for $\sigma_F = 9$ mV/m.

We see that we can further reduce the sensitivity by performing the echo-sequence. The lowest sensitivity is now reached for $\tau = 400$ ns with $\sigma_{F,\tau}^{(1),\mathrm{exp}} = (18.6 \pm 0.3)$ mV/m, leading to an integrated sensitivity of $\sigma_{F,\mathrm{int}}^{(1),\mathrm{exp}} = (0.46 \pm 0.01)$ mV/m/$\sqrt{\mathrm{Hz}}$. However, we also have to assert that, especially for longer interrogation times $\tau = 600$ ns, we cannot fully compensate the reduction of contrast due to the electric field noise. We assume that this is mainly due to electric field noise which varies faster then the time delay between the first and the second pair of radio-frequency pulses.

3.5 Discussion

In this chapter we presented the sensitivity of the single-atom electrometer. By measuring the accumulated quantum phase, we are able to reach a sensitivity very close to the fundamental Heisenberg limit. For short interrogation times of 10 ns, the sensitivity is by a factor of 5.5 below the standard quantum limit, which corresponds to -14.8 dB, comparable to the state-of-the-art of -20 dB obtained by employing squeezed states [69]. The single-atom sensitivity of 30.4 mV/m for an interrogation time of 200 ns corresponds

to the electric field of a single charge located at 218 μm making this method interesting to measure condensed matter devices.

We explored the limitations of the electrometer to electric field noise and inhomogeneities and showed that by using an echo technique, the effect of the electric field noise is reduced leading to an even lower overall sensitivity of 18.6 mV/m for an interrogation time of 400 ns.

Our system provides an unprecedented single-atom sensitivity. Its limitation is the repetition rate of the experimental sequence which only allows to probe the electric field every 311 μs. This drastically limits the bandwidth and impairs our integrated sensitivity.

To be able to use our electrometer to explore physics of mesoscopic devices, we need to find a way to measure faster phenomena. In the next chapter we present a method derived from this measurement which allows us to measure variations of the electric field on a time scale that is only limited by the duration of the radio-frequency pulses themselves and not by the repetition rate of the experiment. This opens the way to much faster dynamics with potential applications in condensed matter physics.

Chapter 4

Correlation measurements

At the end of the previous chapter we discussed that the use of spin-echo techniques in the metrology measurement sequence makes our electric field measurement less sensitive to slowly varying electric field fluctuations. The phase we measure is now sensitive to the difference of the electric field at two different moments in time. This paves the way to correlation measurements. However, the techniques used in chapter 3 involve a switching of the electric field during the Ramsey pulse sequence in order to use the radio-frequency pulses first resonant in the $n = 51$ manifold and thereafter in the $n = 49$ manifold. In this chapter we discuss a technique in which we make use of both angular momenta, $\hat{\boldsymbol{J}}_1$ and $\hat{\boldsymbol{J}}_2$, coupled to σ^+ and σ^- radio-frequency pulses respectively, to alternately generate states inside a given manifold that have opposite polarizabilities. This allows us to accumulate a quantum phase that depends on the difference of the amplitude of the electric field between the times when the σ^+ and σ^- polarized radio-frequency fields are applied. As this method does not require to switch the amplitude of the electric field between the radio-frequency pulses, it enables the measurement of electric field correlations for very short time delays only limited by the duration of the radio-frequency pulses. To reduce this time to the minimum, we make use of the quantum phase accumulated during the radio-frequency pulses themselves reducing the delay to nearly zero.

In this chapter, we introduce the AC-electrometer (Sec. 4.1) and describe the experimental implementation with σ^+ and σ^- polarized radio-frequency pulses (Sec. 4.2). We assess the bandwidth of the AC-electrometer and discuss the linear regime of the measurement of the AC electric field (Sec. 4.3). We discuss how to measure the correlation function of an electric field noise by using the quadratic regime of the AC-electrometer (Sec. 4.4), before concluding with the measurement of the intrinsic noise of the experiment (Sec. 4.5).

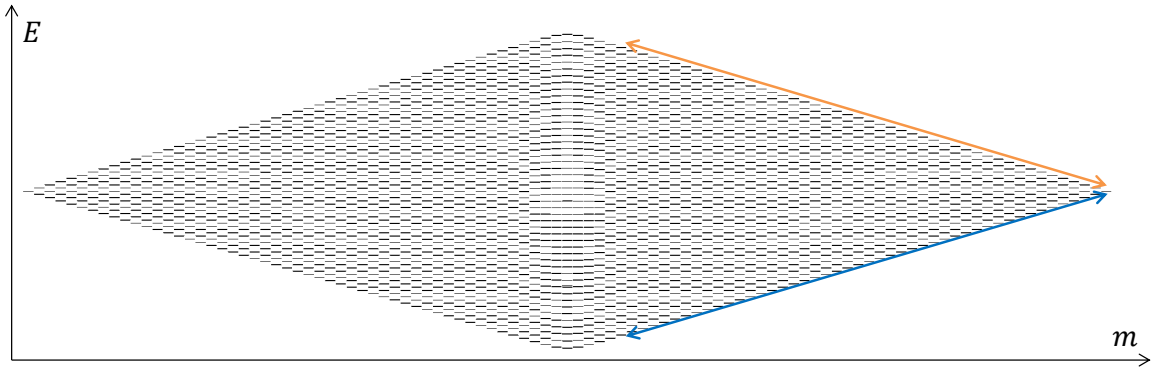

Figure 4.1: The energy eigenvalues of the rubidium atom. In the presence of a σ^+ polarized radio-frequency field, the population, initially in the $|51c\rangle$ state will evolve along the blue arrow. In the case of a σ^- polarized radio-frequency field, the population evolves along the orange arrow.

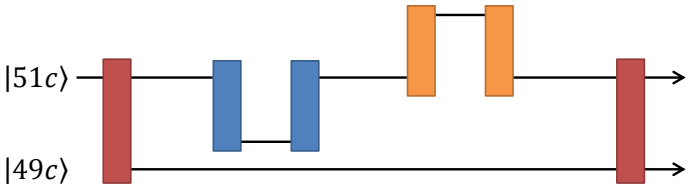

Figure 4.2: The fast correlation sequence of the quantum-enabled method represented as a Ramsey interferometer. The Ramsey $\pi/2$ pulses (red) create a superposition of the $|51c\rangle$ and $|49c\rangle$ states. During the first pair of radio-frequency pulses (blue) the $n = 51$ component of the superposition accumulates a global quantum phase Φ^+, during the second pair of radio-frequency pulses (orange) the $n = 51$ component accumulates a global quantum phase Φ^-, with opposite sign with respect to Φ^+.

4.1 Principles of AC electric field variation measurements

In the previous chapter we show how the preparation of a superposition of the reference state $|49c\rangle$ and a spin coherent state of $\hat{\boldsymbol{J}}_1$ in the manifold $n = 51$ along the lowest σ^+ diagonal (blue diagonal in Fig. 4.1) allows us to get a very good sensitivity to the electric field. Due to the large difference in polarizability between the $|49c\rangle$ reference state and the spin coherent state, the superposition acquires a relative phase Φ^+ that is extremely sensitive to variations of the electric field.

If, instead of using σ^+, we use σ^- polarized radio-frequency pulses, the spin coherent state we prepare is a spin coherent state of $\hat{\boldsymbol{J}}_2$ in the manifold $n = 51$, quantum superposition of states along the highest σ^- diagonal (orange diagonal in Fig. 4.1). The difference of polarizability between this state and the $|49c\rangle$ reference state is still very large, but this time the relative phase Φ^- has the opposite sign with respect to Φ^+, as represented as a Ramsey interferometer in Fig. 4.2.

We can then use a combination of σ^+ and σ^- radio-frequency pulses to perform a measurement that is sensitive to the difference of the electric field between the times t^+

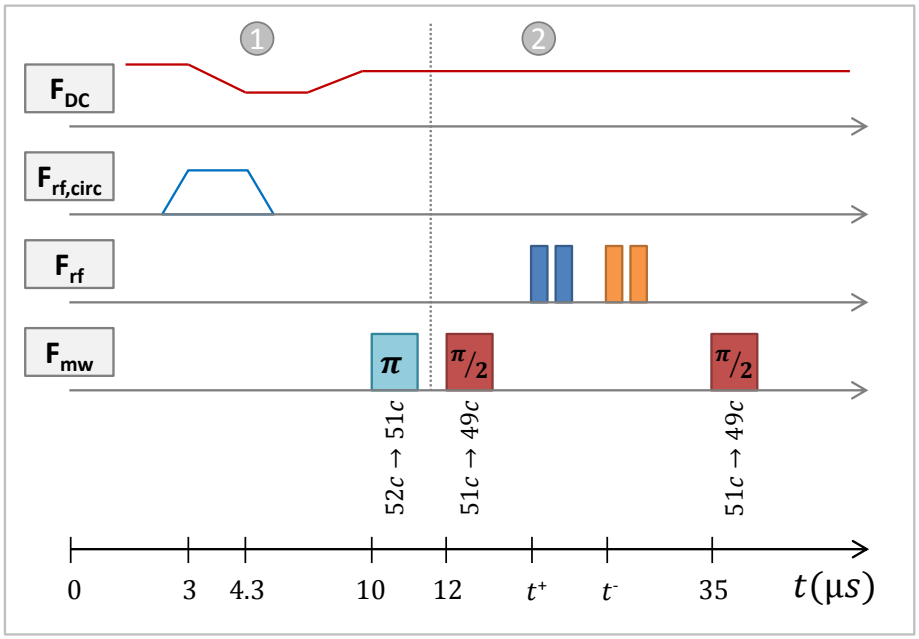

Figure 4.3: Experimental sequence of the AC-electrometer. We use two pulses of σ^+ and two σ^- polarized radio-frequency fields. The first (σ^+ polarized) radio-frequency pair is applied at $t^+ = 13.4$ μs. The second (σ^- polarized) radio-frequency pair is applied at $t^- = 22.4$ μs, or 9 μs after the first pair. The two microwave $\pi/2$ pulses are applied at 9 μs and 35 μs. The time $t = 0$ is defined by the laser pulse.

and t^-. The experimental sequence is described in Fig. 4.3. The atom is initially prepared in the $|51c\rangle$ state. First, a microwave $\pi/2$ pulse prepares a superposition of the states $|49c\rangle$ and $|51c\rangle$. At time t^+, a σ^+ polarized radio-frequency pulse prepares the $n = 51$ part of the wave-function in a spin coherent state of the lowest σ^+ diagonal. A subsequent σ^+ radio-frequency pulse, whose phase is chosen to maximize the probability $P_c^+(\varphi_{\mathrm{rf}}^+)$ for the atom to return to the $|51c\rangle$ state is applied. Under the effect of these two radio-frequency pulses the atom accumulates a relative phase

$$\Phi^+ = \alpha^+(F(t^+) - F_0).$$

Here, instead of applying the second microwave $\pi/2$ pulse to read out the phase Φ^+, like in chapter 3, we apply two σ^- polarized radio-frequency pulses (with a relative phase φ_{rf}^- chosen to maximize the probability $P_c^-(\varphi_{\mathrm{rf}}^-)$ to return to the $|51c\rangle$ state) at time t^-, which imprints the second phase accumulated during the σ^- polarized radio-frequency pulse pairs

$$\Phi^- = \alpha^-(F(t^-) - F_0),$$

leading to the total quantum phase

$$\Phi = \Phi^+ + \Phi^-.$$

By carefully choosing the power and delay between the radio-frequency pulses, we can

ensure that $\alpha^+ = -\alpha^- \equiv \alpha$ and

$$\Phi = \alpha(F(t^+) - F(t^-)).$$

Finally, we apply a second $\pi/2$ pulse resonant with the $|49c\rangle - |51c\rangle$ transition that recombines the two parts of the interferometer (see Fig. 4.2). The probability to find the atom in the $|51c\rangle$ state after this sequence can be calculated by (Eq. 3.4)

$$P_q(\varphi_{\mathrm{rf}}^+, \varphi_{\mathrm{rf}}^-, \varphi_{\mathrm{mw}}) = \frac{1}{4} + \frac{1}{4}P_c^+(\varphi_{\mathrm{rf}}^+)P_c^-(\varphi_{\mathrm{rf}}^-) + \frac{1}{2}\sqrt{P_c^+(\varphi_{\mathrm{rf}}^+)P_c^-(\varphi_{\mathrm{rf}}^-)}\cos(\Phi - \varphi_{\mathrm{mw}}), \qquad (4.1)$$

which is a function of the total accumulated quantum phase Φ, the relative radio-frequency $\varphi_{\mathrm{rf}}^{\pm}$ phase between the $\sigma^{\pm}$ polarized radio-frequency pulse pairs, the relative phase of the microwave $\pi/2$ pulses φ_{mw}, and the probability $P_c^{\pm}(\varphi_{\mathrm{rf}}^{\pm})$ to return to the $|51c\rangle$ state when only the σ^+ (only σ^- respectively) pulses are applied.

In this experiment, we choose to detect the atom in the $|49c\rangle$ state at the end of the sequence. As we have seen in the previous chapter, the probability $P_c(\varphi_{\mathrm{rf}})$ to return to the $|J,J\rangle$ state of the angular momentum after the radio-frequency pulses is limited by experimental imperfections (examples are the quadratic Stark effect and the anharmonicity due to the quantum defect) and is less than 100%. We thus expect that at the end of the sequence a non-negligible population in the elliptical states close to the $|51c\rangle$ state. Since the $|51e'1\rangle$ elliptic state[1] has nearly the same ionization threshold as the $|51c\rangle$, we want to avoid that the detection signal of the $|51c\rangle$ state is contaminated by a residual population of atoms in states other than $|51c\rangle$ that are detected as $|51c\rangle$. Even if the $|49c\rangle$ state is also affected by the radio-frequency pulses, its dynamics is an off-resonant Rabi oscillation and it remains closer to the north pole. It is therefore less affected by the imperfections mentioned before and we expect the ionization signal at the threshold of the $|49c\rangle$ state to be less contaminated by non-$|49c\rangle$ states. We thus record the number of atoms $N(49c)$ in the $|49c\rangle$ and normalize by the number of atoms $N(51c)$ in the $|51c\rangle$ that we initially prepare. To calculate the probability $P(49c)$, however, we have to take into account the ratio of detection efficiency η between $|51c\rangle$ and $|49c\rangle$,

$$P(49c) = \eta\frac{N(49c)}{N(51c)}.$$

The $|49c\rangle$ state is the second output of the Ramsey interferometer in Fig. 4.2. The probability to find the atom in the $|49c\rangle$ state after the full sequence is very similar to P_q (Eq. 4.1) and is given by

$$P'_q(\varphi_{\mathrm{rf}}^+, \varphi_{\mathrm{rf}}^-, \varphi_{\mathrm{mw}}) = \frac{1}{4} + \frac{1}{4}P_c^+(\varphi_{\mathrm{rf}}^+)P_c^-(\varphi_{\mathrm{rf}}^-) - \frac{1}{2}\sqrt{P_c^+(\varphi_{\mathrm{rf}}^+)P_c^-(\varphi_{\mathrm{rf}}^-)}\cos(\Phi - \varphi_{\mathrm{mw}}). \qquad (4.2)$$

We see that the contrast of the Ramsey fringes is the same whether we measure the probability to find the atom in the $|51c\rangle$ state or in the $|49c\rangle$ state.

[1] The $|51e'1\rangle$ level is the level closest to the $|51c\rangle$ level on the highest σ^- diagonal spin-ladder.

4.2 Experimental implementation

4.2.1 Calibration of the phase sensitivity α^+

In this section we present how the σ^+ radio-frequency pulses are generated and how the phase sensitivity α^+ is calculated.

In this experiment we use two electrodes to generate each radio-frequency pulse. To optimize the polarization of the σ^+ polarized radio-frequency pulses, we use the procedure as described in details in Sec. 2.3.2, where the radio-frequency field is optimized for the signals applied on two electrodes at a time. We choose electrodes E1&E2, connected to outputs H1&H2 and N1&N2 (see Fig. 2.11 for the radio-frequency circuit), to generate the σ^+ polarized radio-frequency field.

The duration of the radio-frequency pulses is determined by the period of the off-resonant Rabi oscillations in the $n = 49$ manifold. The part of the population stored in the $n = 49$ manifold needs to return to the circular state $|49c\rangle$ before being recombined with the population in the $n = 51$ manifold (Sec. 3.2.2).

The best sensitivity is reached for the maximum angle θ between the north pole of the Bloch sphere and the direction of the spin coherent state after the first radio-frequency pulse. At the same time, the spin coherent state should not enter the part of the spin-ladder where the low-m states are shifted by the quantum defect. In the previous chapter we find that the trade-off lies at an angle θ of the order of 140°. This is the angle that we aim to reach in this experiment. We measure a Rabi frequency of the σ^+ polarized radio-frequency field of $\Omega^+_{\mathrm{rf}} = 2\pi \cdot (3.97 \pm 0.07)$ MHz. The duration of the radio-frequency pulses is determined by the off-resonant Rabi oscillations in the $n = 49$ manifold. We find $t^+_{\mathrm{rf}} = (102.0 \pm 0.2)$ ns. This corresponds to a Rabi angle $\theta^+ = \Omega^+_{\mathrm{rf}}(t^+_{\mathrm{rf}} - t_0) \approx 143.8°$ where $t_0 = (1.37 \pm 0.23)$ ns takes into account the finite rise time of the radio-frequency pulses.

We determine the optimum radio-frequency phase φ^+_{rf} to maximize the probability $P^+_c(\varphi^+_{\mathrm{rf}})$ to return to the $|51c\rangle$ state by recording P^+_c as a function of the relative radio-frequency phase when we only applying the two σ^+ polarized radio-frequency pulses, shown in Fig. 4.4. Here, the two pulses are applied consecutively without any delay ($\tau^+ = 0$ ns). The maximum probability which can be reached is $P^+_c(\varphi^+_{\mathrm{rf}}) \approx 95\%$.

In order to calibrate the phase sensitivity α^+, we record Ramsey fringes at two different electric field amplitudes F_{up} and F_{down} separated by ΔF =73.2 mV/m as a function of the relative microwave frequency. They are shown in Fig. 4.5a. The sequence includes the first $\pi/2$ microwave pulse, the two σ^+ polarized radio-frequency pulses with relative phase φ^+_{rf}, and a second $\pi/2$ microwave pulse. However, since the two $\pi/2$ pulses are separated by ~24 μs, the contribution of the differential Stark effect of the $|51c\rangle - |49c\rangle$ transition is no longer negligible. The phase shift in Fig. 4.5a is thus the sum of the variation of the quantum phase $\Delta\Phi^+$, accumulated during the radio-frequency pulses, and a phase shift $\Delta\varphi_{\mathrm{mw}}$ due to the differential Stark shift between the levels $|49c\rangle$ and $|51c\rangle$. The contribution $\Delta\varphi_{\mathrm{mw}}$ can be independently be measured by recording the same Ramsey fringes

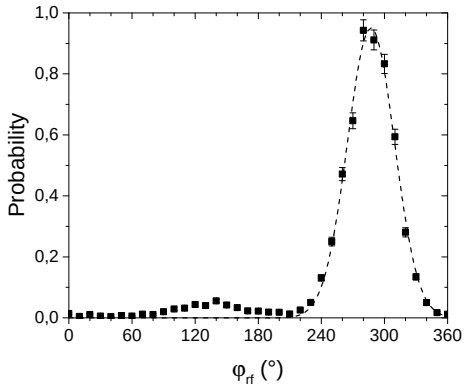

Figure 4.4: The probability to return to the $|51c\rangle$ state after the σ^+ polarized radio-frequency pulses are applied as a function of the absolute phase of the N1&N2 synthesizer output. The appearance of a small peak on the left shows that the spin coherent state nearly reaches the anharmonic region of the Stark levels. The Gaussian fit of the right peak to find the maximum return is shown (dashed).

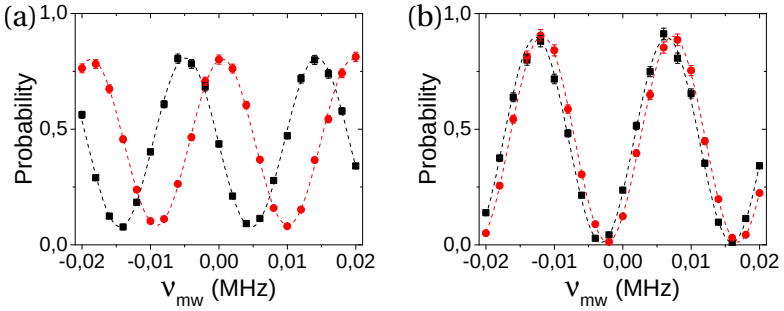

Figure 4.5: (a) Ramsey microwave fringes between $|51c\rangle$ and $|49c\rangle$ in two different electric fields, F_{up} (black) and F_{down} (red) separated by $\Delta F = 73.2$ mV/m with the σ^+ polarized radio-frequency pulses, lead to a phase shift of $\Delta\varphi_{mw} + \Delta\Phi^+$. (b) The phase shift between the fringes for F_{up} and F_{down} without applied radio-frequency pulses is $\Delta\varphi_{mw}$.

in the same conditions but without applying the radio-frequency pulses (see Fig. 4.5b). From the two measurements we find $\alpha^+ = \Delta\Phi^+/\Delta F = (0.0198 \pm 0.0001)$ rad(mV/m)$^{-1}$. The value is the average of several identical measurements performed over several days.

4.2.2 Calibration of the phase sensitivity α^-

We generate the σ^- polarized radio-frequency field with the electrodes E3&E4, connected to the synthesizer outputs H3&H4 and N3&N4. So far, the phases and amplitudes of all the synthesizer outputs are optimized to generate σ^+ polarized radio-frequency fields. To optimize the σ^- polarized radio-frequency pulses, we use the same optimization method (see Sec. 2.3.2.c), but we initially prepare the atom in the $|-50c\rangle$ state, the circular state with $m = -(n-1)$. To that end, we first invert the direction of the electric field that we apply during the laser excitation, so that the polarization of the 780 nm and 776 nm laser are now σ^- with respect to the new quantization axis. As a result we prepare

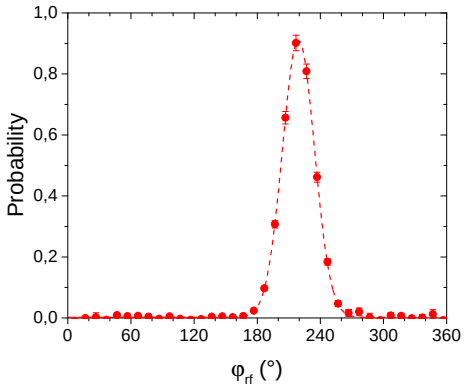

Figure 4.6: The probability to return to the $|51c\rangle$ state after the σ^- polarized radio-frequency pulses are applied with an interrogation time of $\tau^- = 12$ ns.

the $|52f, m = -2\rangle$ state. We then optimize the relative phase of the PCI RF card (see Sec. 2.3.2.a) used for the adiabatic passage, in order to create a radio-frequency field with σ^- polarization that transfers the state of the atom into the $|-52c\rangle$ state. We can then use the same transition frequencies and techniques, as for the σ^+ optimization, to tune the phase and amplitude of the outputs H3&H4 and N3&N4 to generate a pure σ^- polarized radio-frequency field.[2] Since we generate the radio-frequency field using only two electrodes, the field amplitude is very inhomogeneous. During the optimization process, we apply the radio-frequency pulses at $t^- = 22.4$ μs, which is the time at which the radio-frequency pulses occurs in the final sequence.

We choose the power of the σ^- polarized radio-frequency field to have a Rabi frequency similar to the one of the σ^+ polarized radio-frequency field, $\Omega^-_{\mathrm{rf}} \approx \Omega^+_{\mathrm{rf}}$. To measure the Rabi frequency Ω^-_{rf}, we measure the depopulation of the $|+51c\rangle$ state as a function of the duration of the radio-frequency pulse that we apply on the atom. We measure $\Omega^+_{\mathrm{rf}} = 2\pi \cdot (3.90 \pm 0.07)$ MHz with a radio-frequency duration offset $t_0 = (1.61 \pm 0.23)$ ns. We choose t^-_{rf} to ensure that it corresponds to exactly one period of the off-resonant Rabi oscillation in the $n = 49$ manifold. We find $t^-_{\mathrm{rf}} = (96.8 \pm 0.2)$ ns. The Rabi angle can be estimated as $\theta^- = \Omega^-_{\mathrm{rf}}(t^-_{\mathrm{rf}} - t_0) \approx 136.8°$ which is slightly smaller than θ^+. The smaller Rabi angle leads to a smaller sensitivity. This can, however, be counterbalanced by increasing the delay τ^- between the two σ^- polarized radio-frequency pulses.

To adjust the phase sensitivities $\alpha^+ \approx \alpha^-$, we measure the sensitivity α^- as a function of the delay τ^-. For each value of τ^-, we record the probability P^-_c to return to the $|51c\rangle$ state after the two σ^- radio-frequency pulses as a function of the relative phase between the two pulses, shown for $\tau^- = 12$ ns in Fig. 4.6, in order to find the optimum phase φ^-_{rf}. The maximum probability which can be reached is $P^-_c(\varphi^-_{\mathrm{rf}}) \approx 91\%$. We then record the Ramsey fringes where we apply a first $\pi/2$ microwave pulse, the two σ^- polarized radio-frequency pulses and the second $\pi/2$ microwave pulse for two different values of the static electric field in order to measure the accumulated quantum phase $\Delta\Phi^-$ (here again, we take into account the phase shift $\Delta\varphi_{\mathrm{mw}}$), shown for $\tau^- = 12$ ns in Fig. 4.7a. Fig. 4.7b shows the

[2] We can use exactly the same experimental sequences except for the microwave pulses. Since the microwave transitions now have polarizations of σ^- instead of σ^+, we have to adjust the duration of the pulses to account for the polarization dependent standing wave structure.

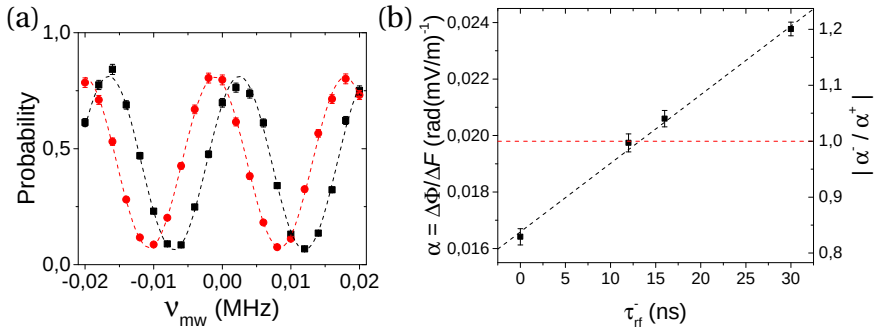

Figure 4.7: (a) Ramsey microwave fringes between $|51c\rangle$ *and* $|49c\rangle$ *in two different electric fields,* F_{up} *(black) and* F_{down} *(red) separated by* $\Delta F = 73.2$ *mV/m. The* σ^- *polarized radio-frequency pulse pair lead to a phase shift of* $\Delta\Phi = \Delta\varphi_{mw} + \Delta\Phi^-$*. (b) The phase sensitivity* $\alpha^- = \Delta\Phi^-/\Delta F$ *as a function of the interrogation time* τ^- *(black) follows the linear fit (black dashed). The same absolute value of the phase sensitivity of the* σ^+ *polarized radio-frequency pulses* $\alpha^+ = \Delta\Phi^+/\Delta F$ *for an interrogation time of* $\tau^+ = 0$ *ns (red dashed) is attained for* $\tau^- = 12$ *ns.*

phase sensitivity $\alpha^- = \Delta\Phi^-/\Delta F$ as a function of the interrogation time τ^-. The phase sensitivity $\alpha^+ = \Delta\Phi^+/\Delta F$ is met for $\tau^- = 12$ ns. We find a phase sensitivity for the σ^- polarized radio-frequency pulse pair of $\alpha^- = \Delta\Phi^-/\Delta F = (0.0198 \pm 0.0002)$ rad(mV/m)$^{-1}$. The value is the average of several measurements performed over a few days.

4.3 AC electric field measurement

4.3.1 Sensitivity of the AC-electrometer

We finally record the Ramsey fringes corresponding to the full sequence, as depicted in Fig 4.3, including the first $\pi/2$ microwave pulse, the σ^+ followed by the σ^- polarized radio-frequency pulse pairs, and the second $\pi/2$ microwave pulse. The result is shown in Fig. 4.8. The contrast of the fringes is $C = (64.1 \pm 0.3)\%$. The phase of the fringes is proportional to the difference in the electric field $F(t^+) - F(t^-)$ applied at times t^+ and t^-. By setting the phase of the interferometer at the point of maximum slope, the variation of the probability is

$$\delta P_q = \frac{C}{2}\alpha(F(t^+) - F(t^-))$$

and the sensitivity of the AC-electrometer is determined by (Eq. 3.11),

$$\sigma_F^{\exp} = \frac{1}{C\alpha}.$$

We find a single-shot sensitivity of $\sigma_F^{\exp} = (79.4 \pm 0.9)$ mV/m. This sensitivity is -2.9 dB below the standard quantum limit $\sigma_{F,\mathrm{SQL}}^{(1)} = 111.5$ mV/m calculated for the whole duration

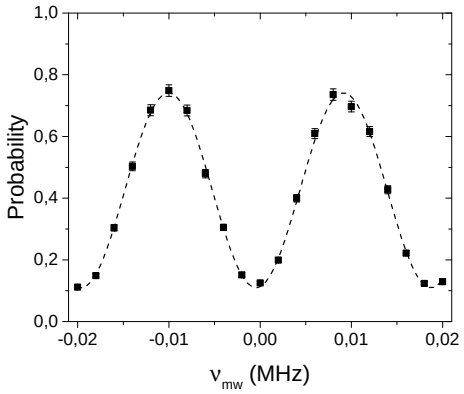

Figure 4.8: Ramsey fringes with the $\sigma+$ and $\sigma-$ radio-frequency pulse pairs at $t^+ = 13.4$ μs and $t^- = 22.4$ μs respectively, with interrogations times of $\tau^+ = 0$ ns and $\tau^- = 12$ ns.

of the pulse pair of $t = 2t^-_{\mathrm{rf}} + \tau^- = 206$ ns. The Heisenberg limit is $\sigma^{(1)}_{F,\mathrm{HL}} = 15.8$ mV/m. The atom acts as an electrometer that is sensitive to AC variations of the electric field beyond the standard quantum limit.

4.3.2 High frequency bandwidth measurement

In addition to the sensitivity, it is important to assess the bandwidth of our AC-electrometer as this determines the spectrum of the noise that the electrometer is sensitive to. The electrometer is by construction insensitive to low-frequency variations of the electric field. However, the value of the low cut-off frequency can be reduced by increasing the time delay $T = t^- - t^+$ between the two pairs of radio-frequency pulses (until the atom exits the electrode structure). This limitation is purely technical and could be avoided using stationary atoms [113–116]. The high frequency bandwidth is determined by the duration of the pair of radio-frequency pulses, which in our case is 204 ns for the first radio-frequency pair or 206 ns for the second radio-frequency pair. We thus expect to be able to measure frequencies up to a few MHz.

4.3.2.a Time response of the AC-electrometer

To characterize the bandwidth, we measure the response of the AC-electrometer to a step of electric field, as sketched in Fig. 4.9.

First, we record Ramsey fringes as a function of the microwave frequency at a constant electric field, shown in Fig. 4.10a. We set the frequency of the microwave generator to be at the point of maximum slope and use the auxiliary AWG to generate a small additional time varying electric field $\Delta F(t)$. We choose for $\Delta F(t)$ a pair of electric field pulses with a duration of 1 μs, edge times of 100 ns, starting times separated by 8.5 μs, and an electric field amplitude step of $\Delta F = 36.6$ mV/m. The signal is triggered by an independent digital pulse. By varying the time at which the trigger pulse is sent, we can vary the time at which the pulses occur, and the radio-frequency pulses can sample the time varying electric

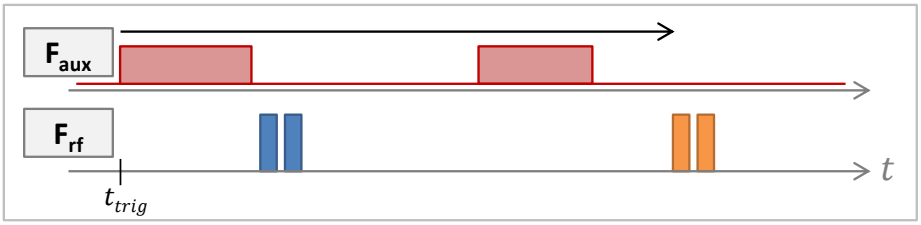

Figure 4.9: The experimental sequence of the bandwidth assessment with the first (σ^+ polarized) radio-frequency pulse pair (blue) and the second (σ^- polarized) radio-frequency pulse pair (orange). The electric field waveform (red) consists in two pulses of 1 µs pulse width whose starting time is separated by 8.5 µs. This waveform is scanned through the radio-frequency pulse pairs separated by 9 µs.

field at different times, as shown in Fig. 4.9. The trigger of the AWG is scanned over 3 µs. The corresponding measured probability as a function of the trigger delay is shown in Fig. 4.10b.

Since the microwave is chosen to be at the point of maximum slope of the interference signal, shown in Fig. 4.10a, the probability, given by

$$P'_q = P_0 + \frac{C}{2}\sin(\Delta\Phi^+ + \Delta\Phi^-),$$

becomes, in the limit of small total accumulated phases $(\Delta\Phi^+ + \Delta\Phi^-) \approx 0$,

$$P'_q = P_0 + \frac{C}{2}\Delta\Phi^+ + \frac{C}{2}\Delta\Phi^-,$$

where $\Delta\Phi^\pm$ are the additional accumulated quantum phases during the $\sigma^\pm$ pulses due to the electric field steps.

Far from the transitory regimes, the probability is given by

$$P'_q = P_0 + \frac{C}{2}\alpha(F(t^+) - F(t^-)) = P_0 + G_0(F(t^+) - F(t^-)),$$

where $G_0 = C/(2\alpha)$ is the "DC" response of the electrometer.

We observe different regimes in Fig. 4.10b, depicted in Fig. 4.11:

- Both radio-frequency pulse pairs happen when the electric field is F_{down} (DD in Fig. 4.11).[3] The probability P'_q remains at the inflection point of the Ramsey fringes, up to 12.3 µs trigger delay in Fig. 4.10b.
- The first radio-frequency pulse pair happens during the first electric field pulse with F_{up} (UD). The probability P'_q increases proportional to $\Delta\Phi^+ = \alpha^+\Delta F$ between 12.4 µs and 12.8 µs.

[3] DD stands for F_{down} for the first radio-frequency pulse pair and F_{down} for the second radio-frequency pulse pair, DU for F_{down} for the first radio-frequency pulse pair and F_{up} for the second radio-frequency pulse pair, etc.

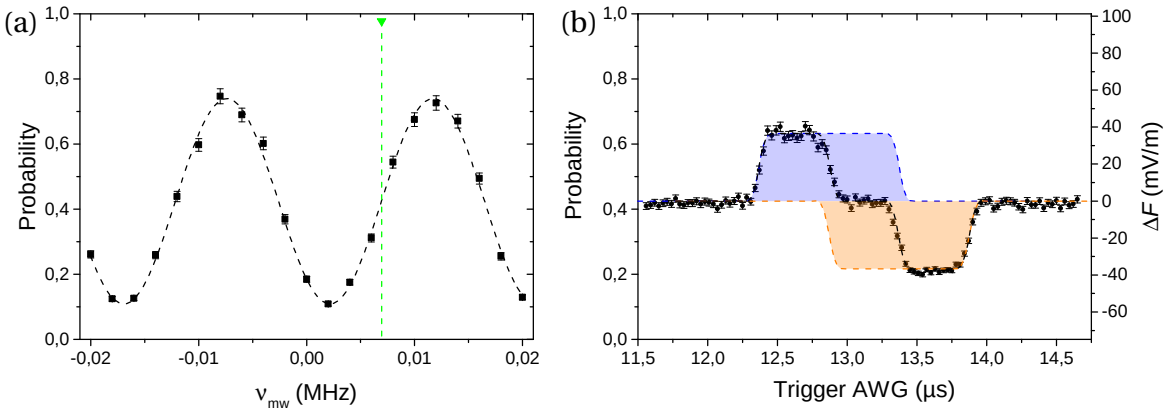

Figure 4.10: (a) Ramsey fringes in the electric field F_{down} (DD). The green dashed line indicates the phase chosen to record the bandwidth measurement. (b) The probability P'_q to find the atom in the $|49c\rangle$ state is plotted as a function of the trigger delay of the AWG. The dashed line correspond to the numerical simulation of the bandwidth experiment for a pair of perfect square electric field pulses (blue: only σ^+ polarized radio-frequency pulse pair, orange: only σ^- polarized radio-frequency pulse pair, black: both). While for the first pair of radio-frequency pulses with phase sensitivity $\alpha^+ > 0$ the measured probability is increased in a higher electric field (blue shaded area), for the second pair of radio-frequency pulses with phase sensitivity $\alpha^- < 0$, the probability is decreased (orange shaded area). The axis on the right corresponds to the electric field deduced from the probability P'_q using $\Delta F = (P'_q - P_0)/(|\alpha|C/2)$.

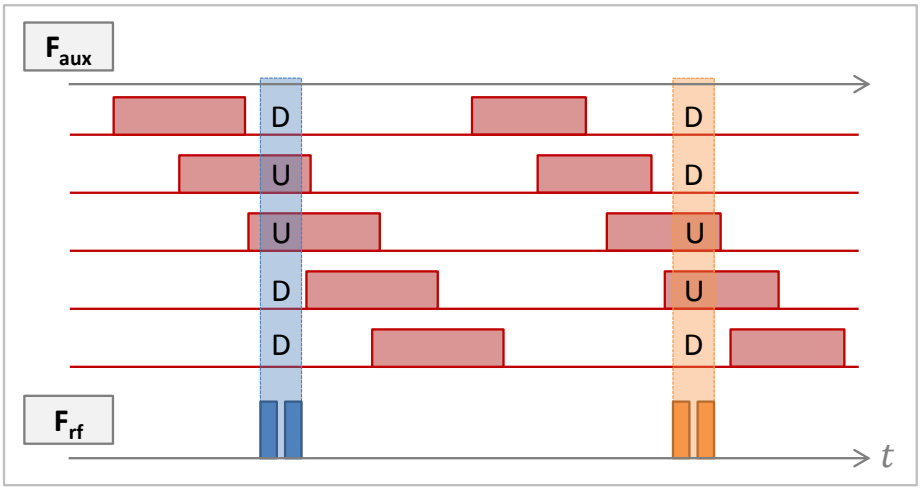

Figure 4.11: The electric field pulses are moved through the two pairs of radio-frequency pulses, σ^+ (blue) and σ^- polarized (orange). Depending on the trigger time of the AWG generating the electric field pulses, we pass through the following regimes: DD: first radio-frequency pulse pair in F_{down}, second pair in F_{down} (first line), UD: first pair in F_{up}, second pair in F_{down} (second line), UU (third line), DU (fourth line) and back to DD (fifth line).

- The second radio-frequency pulse pair happens during the second electric field pulse, while the first radio-frequency pulse happens still during the first electric field pulse (UU). The probability P'_q decreases proportional to $\Delta\Phi^- = \alpha^-\Delta F$ and the two phase shifts, $\Delta\Phi^-$ and $\Delta\Phi^+$ cancel each other between 13.0 μs and 13.3 μs. The fact that the probability P'_q is exactly the same as in the DD-regime, shows that the phase sensitivities α^+ and α^- are very well adjusted.

- The first radio-frequency pulse pair does no longer happen during the first electric field pulse, while the second radio-frequency pulse pair still happens during the second electric field pulse (DU). The probability P'_q decreases proportionally to $\Delta\Phi^- = \alpha^-\Delta F$ between 13.4 μs and 13.8 μs.

- The second radio-frequency pulse pair does no longer happen during the second electric field pulse (DD) and the probability P'_q returns to its initial value of the first regime at the inflection point from 14.0 μs onwards.

To explain the transitory regimes we numerically simulate $\Delta\Phi^+$ and $\Delta\Phi^-$. We take into account the fitted Rabi frequencies, radio-frequency pulse duration and the interrogation times for the σ^+ and the σ^- pulse pairs. However, in the simulation we do not take into account the 100 ns edge time of the electric field pulses, but use an infinitely steep slope. The only free parameter to fit the numerical simulation to the experimental data is the contrast $C \approx 63\%$. The measured data and the simulation are in good agreement. We see that the rise time of the experimental signal is in the order of ~100 ns, which sets already a lower bound on the cut-off frequency. However, this measurement is limited by the edge time of the electric field pulses. To go beyond, we need to look at the response of the AC-electrometer to an electric field pulses with sharper edges. Unfortunately, we observe that with shorter edge times we excite a resonance of the electric circuit that drive the electrode C1.

4.3.2.b Time and frequency response of the electric circuit

In the previous section, we apply electric field pulses with edge times of 100 ns making it difficult to distinguish the contributions to the rise time of $\Delta\Phi$ due to the bandwidth of the AC-electrometer and due to the edge time of the electric field pulses.

However, when applying an electric field waveform with a shorter edge time, we observe on the oscilloscope oscillations with a frequency of about 8 MHz. Fig. 4.12 presents the voltage on the electrode C1 as recorded on the oscilloscope when we apply an electric field pulse of 1 μs duration with different edge times. For the shortest possible edge time of 5 ns, we see very strong oscillations. For an edge time of 70 ns the oscillations are still visible, and for 100 ns edge time they start to vanish.

Fig. 4.13a shows the Fourier transform $\tilde{h}(\nu)$ of the oscilloscope signal of the 5 ns edge time pulse, as well as the Fourier transform $\tilde{f}(\nu)$ of a perfect square pulse of 1 μs pulse duration. We observe the characteristic shape of the Fourier transform of the square pulse, the normalized sinc function, with vanishing frequency components at multiples

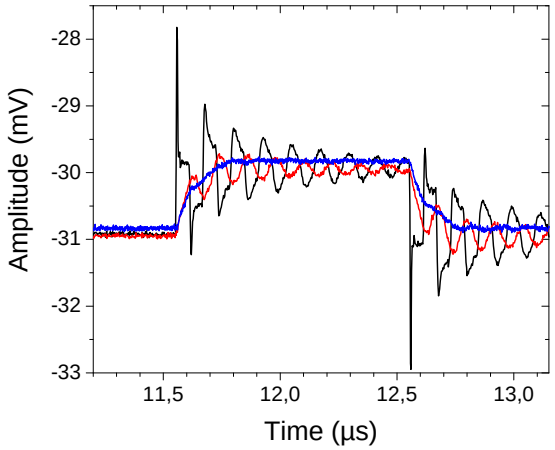

Figure 4.12: The response of the experiment to different electric field steps of 1 µs pulse duration with different edge times of 5 ns (black), 70 ns (red) and 100 ns (blue). The trigger signal is sent at 11.5 µs.

of 1 MHz, being the inverse of the electric field pulse duration. The Fourier transform $\tilde{h}(\nu)$ also vanishes every 1 MHz, but we see that there are additional resonances. We observe a clear resonance at about $\nu_{\text{res}} \approx 8$ MHz as well as several resonances at higher frequencies around ~25 MHz, ~43 MHz, ~60 MHz etc. In order to extract the frequency response of the system, we can simply divide the Fourier transform of the output, $\tilde{h}(\nu)$, by the Fourier transform of the input, $\tilde{f}(\nu)$. The result is shown in Fig. 4.13b.[4]

To confirm this measurement, we use the auxiliary AWG to apply sine-shaped waveforms of different frequencies and record the response of the plane electrode C1 with the oscilloscope (see Fig. 3.8 for the electric circuit). Fig. 4.13b shows the amplitude of the signal on the oscilloscope normalized by the amplitude of the signal generated by the AWG (divided by the factor $5.1 \cdot 10^{-4}$ that takes into account the voltage divider created by the 100 kΩ resistor at the output of the AWG, described in Sec. 3.2.4). We recover the ratio of the Fourier transform and again see a resonance in the response of the experiment at around $\nu_{\text{res}} \approx 8$ MHz.

4.3.2.c Frequency response of the AC-electrometer

We record the response of the electrometer to a sinusoidal variation of the electric field. This allows us to compensate for the resonance of the plane electrode driving circuit in order to get the response of the AC-electrometer.

Instead of a time response of the AC-electrometer to a sudden change of the electric field, discussed at the beginning of this section, we now investigate the response to a sine-shaped variation of the electric field. This allows us to measure directly the response in the frequency domain.

[4] In Fig. 4.13b, we removed all points for which the Fourier transform of the input, $\tilde{f}(\nu)$, lies below a certain threshold (in our case $1 \cdot 10^{-6}$) since they correspond to points for which we effectively divide a very small number by zero.

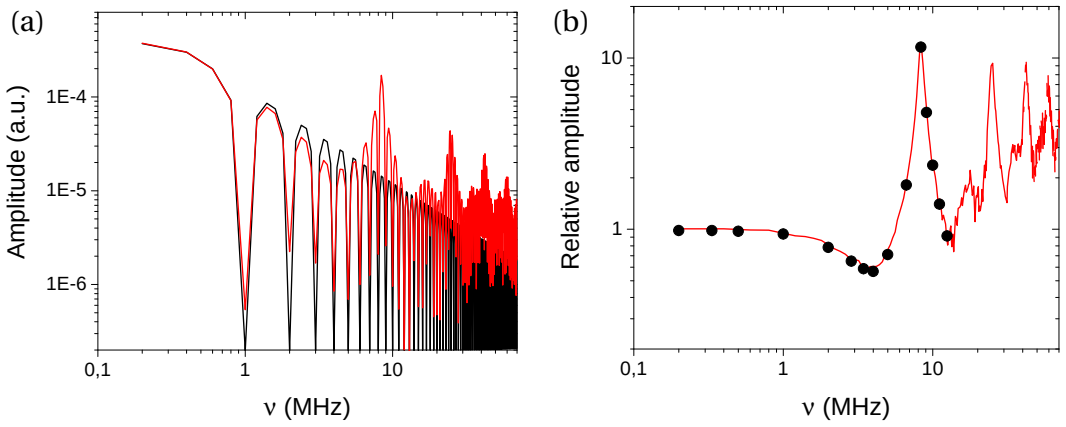

Figure 4.13: (a) Fourier transform $\tilde{f}$ of a perfect 1 µs square signal (black) and $\tilde{h}$ of the oscilloscope trace for the pulse with 5 ns edge time (see Fig. 4.12 for time response) (red). (b) The frequency response is calculated from $\tilde{h}/\tilde{f}$ (red). It is compared to a direct recording of the response of the electric circuit at different fixed frequencies (black).

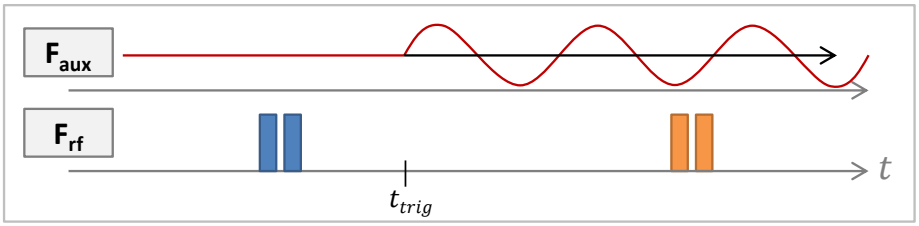

Figure 4.14: The experimental sequence to measure the bandwidth of the AC-electrometer. A sine-shaped waveform is moved through the second radio-frequency pulse pair at $t^- = t^+ + 9$ µs while the first radio-frequency pulse pair at $t^+ = 13.4$ µs is at a constant electric field. This allows us to measure the response of the σ^- polarized radio-frequency pulse pair in the frequency domain.

In order to measure the frequency response of the AC-electrometer and to deduce its cut-off frequency, we now use a sequence sketched in Fig. 4.14. We apply a flat electric field at time t^+, when the first (σ^+ polarized) radio-frequency pulse pair is applied, followed by several oscillations of the electric field at a given frequency ν, triggered by an independent digital pulse at time t_{trig}. By scanning the time of the trigger pulse with respect to the time t^-, we vary the phase of the sinusoidal oscillation sampled by the second (σ^- polarized) radio-frequency pulse pair.

First, we record Ramsey fringes with both radio-frequency pulse pairs applied, but without a modulation in the electric field, in order to set the phase of the interferometer at the point of maximum slope, see Fig. 4.15a. At this point, the variation of the probability P'_q is directly proportional to the phase $\Delta\Phi^-$. Fig. 4.15b presents two signals of the recorded probability P'_q as a function of the time of t_{trig} for two different frequencies ν of the applied electric field oscillations. For each value of ν we fit the contrast of the oscillations, $\delta P(\nu)$, shown in Fig. 4.16a as a function of the frequency ν.

The amplitude of Fig. 4.15b is the product of the response of the electrometer at a given frequency, $G(\nu)$, and the amplitude of the electric field $\delta F(\nu)$ that we apply. This

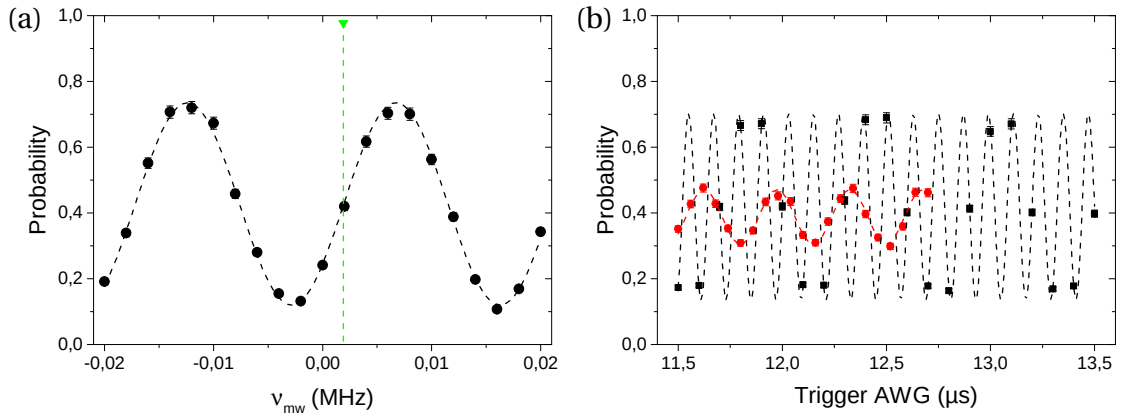

Figure 4.15: (a) Ramsey fringes (plotted as the P'_q to find the atom in the $|49c\rangle$ state) in the electric field F_0 ($\delta F = 0$). The relative microwave phase is chosen to be at the point of maximum slope (green dashed line). (b) The probability P'_q is measured for different sine-periods, here 0.12 µs (8.33 MHz, black) and 0.35 µs (2.86 MHz, red), as a function of the trigger time of the AWG. The 8.33 MHz signal is at the limit of the sampling rate that we can achieve with our experiment control hardware, forcing us to measure the oscillations stroboscopically. The amplitude of the sine-wave generated by the AWG is $V_{out} = 1.02$ mV.

leads to a frequency response

$$G(\nu) = \frac{\delta P(\nu)}{\delta F(\nu)}.$$

The amplitude $\delta F(\nu)$ is calculated using the frequency response of the electric circuit driving the electrode C1, which is measured in the previous section (see Fig. 4.13b). For low frequencies ν, we expect that the frequency response follows $G(\nu) \approx G_0$, where $G_0 = C/(2\alpha)$ as introduced in the previous section.

Fig 4.16b shows the normalized frequency response $G(\nu)/G_0$ of the AC-electrometer as a function of the frequency of the electric field waveform. The frequency response of the AC-electrometer is in good agreement with the numerical simulation of the experiment, corresponding to a cut-off frequency of ~5 MHz.

4.3.3 Charge correlation measurement

Up to here, we have considered the linear response of the electrometer, by setting the phase of the interferometer at a point of maximum slope. In this section, we show that by setting the phase of the interferometer at a point of minimum slope [4, 180], we can access the correlation function of the electric field. This could be interesting for example to observe the dynamics of a charge in a quantum dot [181–183].

We consider an electron placed at ~95 μm from the Rydberg atom. It creates an electric field of $\Delta F \approx 160$ mV/m at the position of the atom. This corresponds to the electric field difference that leads to a shift in the accumulated quantum phase of $\alpha \Delta F = \pi$, shown in Fig. 4.17a. If the electron is not present, the electric field seen by the atom is F_{down}. If

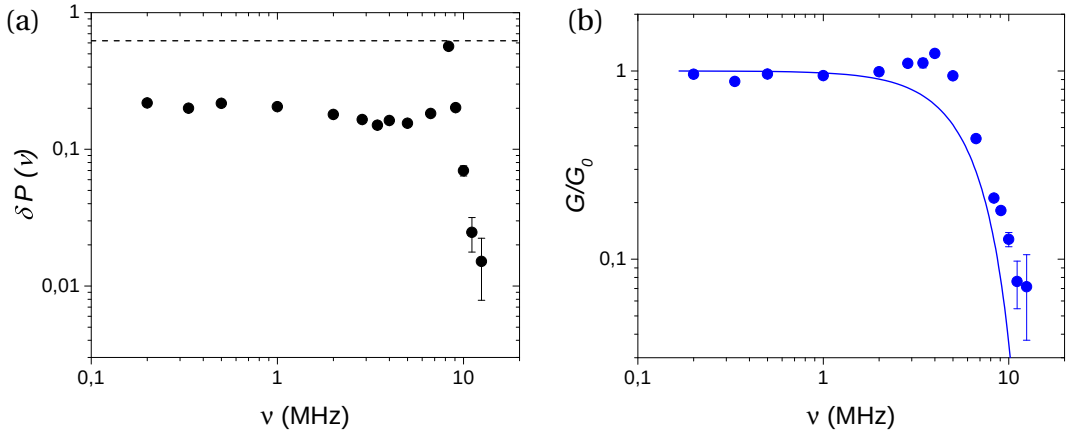

Figure 4.16: (a) The contrast $\delta P(\nu)$ of the Ramsey fringes as a function of the frequency of the applied sine-signal. The dashed line corresponds to the contrast of the Ramsey fringes in Fig. 4.15a. The amplitude of the sine-wave generated by the AWG is $V_{out} = 1.02$ mV. (b) The frequency response of the AC-electrometer $G(\nu)/G_0$ (blue points). Theblue line corresponds to the frequency response of the σ^- polarized radio-frequency pulse pair simulated numerically.

the electron is present, the electric field is $F_{\text{up}} = F_{\text{down}} + \Delta F$. Measuring the average value of the electric field only gives the probability of the presence of the electron. To access the dynamics [134, 135], we need to measure the correlation function $\langle \Sigma_{t+} \Sigma_{t-} \rangle$ where $\Sigma_t = \pm 1$ depending whether the electron is present or not at t.

Fig. 4.17b presents the result of an experiment which simulates the measurement of the correlation of a presence of a charge. The sequence is similar to the one presented in Sec. 4.3.2.a, with the important difference that this time the phase of the interferometer is set to a point of minimum slope of the probability P'_q to find the atom in the $|49c\rangle$ state for a constant electric field. We then scan the double electric field pulse, consisting in two electric field pulses of 1 μs duration, starting time separated by 8.5 μs and amplitude of $\Delta F \approx 160$ mV/m, across the two radio-frequency pulse pairs by changing the time t_{trig} of the digital pulse that triggers the electric field pulses (similar to Fig. 4.9).

If we compare Fig. 4.10 to Fig. 4.17, we see that here, the probability P'_q to find the atom in the $|49c\rangle$ state is the same whether the interference fringes are shifted by $+\alpha\Delta F$ (corresponding to the electric field pulse occurring during the first radio-frequency pulse pair and not during the second, UD) or by $-\alpha\Delta F$ (corresponding to the electric field pulse occurring during the second radio-frequency pulse pair and not during the first, DU). Therefore, there are only two possible outcomes of the interferometer: either the probability P'_q is low (DD and UU) or high (DU and UD). If the variation of the electric field is created by the presence or absence of a charge, the probability P'_q is directly related to $\Sigma_t^+ \Sigma_t^-$. In the case where $\alpha\Delta F = \pi$, the atom exits the interferometer mostly in the $|49c\rangle$ state if $\Sigma_{t+}\Sigma_{t-} = +1$ and mostly in the $|51c\rangle$ state if $\Sigma_{t+}\Sigma_{t-} = -1$. This allows us to measure the correlation function of the presence of the charge at times t^+ and t^- with a very high signal to noise ratio.

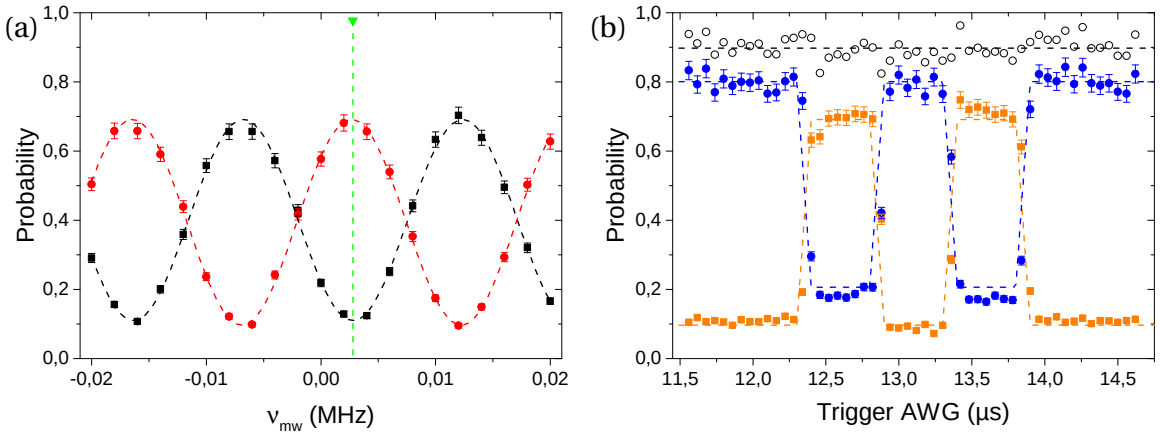

Figure 4.17: (a) Ramsey fringes for DD (both radio-frequency pairs in F_{down}) (black) and UD (first radio-frequency pair in F_{up}, second in F_{down}) (red) with $\Delta F = 160$ mV/m matching exactly a π phase shift. The relative microwave frequency is chosen to be in one of the extrema of the fringes (green). (b) The probability to detect the atom in the $|51c\rangle$ state (blue) and in the $|49c\rangle$ state (orange), together with the sum (hollow black) and the predicted behaviour (dashed). The measured probabilities do not add up to 100% but only to 90%. This is mainly due to the reduced probability to return to the $|51c\rangle$ state after the two σ^+ and the two σ^- radio-frequency pulse pairs (see Figs. 4.4 and 4.6).

4.4 Noise correlation function measurement

So far we have used our electrometer to detect deterministic electric field signals synchronized with the experiment. However, if we want to demonstrate that the atom can be used as an electrometer to characterize other condensed matter devices, we need to be able to measure phenomena that are not synchronous with the experiment.

In this section, we show how it is possible to use our experiment to measure the time correlation of the electric field in order to characterize the electric field noise, or detect asynchronous deterministic variations of the electric field.

4.4.1 Theory of noise measurement

The probability to return to the initial $|51c\rangle$ state is given by Eq. 4.1 as

$$P_q = P_q(\varphi_{\mathrm{rf}}^+, \varphi_{\mathrm{rf}}^-, \varphi_{\mathrm{mw}}) = \frac{1}{2} + \frac{C_0}{2}\cos(\alpha F(t^+) - \alpha F(t^-) - \varphi_{\mathrm{mw}}),$$

where $F(t^\pm)$ is the electric field when the $\sigma^\pm$ polarized radio-frequency pulse pairs are applied at time $t^\pm$. We assume that the phase sensitivities are equal for both radio-frequency pulse pairs, $\alpha^+ = -\alpha^- = \alpha$ and where C_0 is the intrinsic contrast of the Ramsey fringes. If there is electric field noise $\delta F(t)$ and the electric field is $F(t) = F_0 + \delta F(t)$ with

$\langle \delta F(t) \rangle = 0$, then the observed probability is the average

$$\begin{aligned} P_q &= \left\langle \frac{1}{2} + \frac{C_0}{2} \cos(\alpha F(t^+) + \alpha F(t^-) - \varphi_{\mathrm{mw}}) \right\rangle \\ &= \frac{1}{2} + \frac{C_0}{2} \left\langle \Re\left(e^{i(\alpha(\delta F(t^+) - \delta F(t^-))} e^{-i\varphi_{\mathrm{mw}}} \right) \right\rangle \\ &= \frac{1}{2} + \frac{C_0}{2} \Re\left(\left\langle e^{i(\alpha(\delta F(t^+) - \delta F(t^-))} \right\rangle e^{-i\varphi_{\mathrm{mw}}} \right). \end{aligned}$$

We define

$$\left\langle e^{i(\alpha(\delta F(t^+) - \delta F(t^-))} \right\rangle = C_r e^{i\Phi_C},$$

introducing the phase Φ_C and the contrast reduction C_r of the Ramsey fringes. The probability to return to the circular state is now given by

$$P_q = \frac{1}{2} + \frac{C_0 C_r}{2} \cos(\Phi_C - \varphi_{\mathrm{mw}}),$$

where

$$C_r = \left| \left\langle e^{i(\alpha(\delta F(t^+) - \delta F(t^-))} \right\rangle \right| = \left| \left\langle e^{i\delta\Phi} \right\rangle \right|, \tag{4.3}$$

which depends on the difference in the electric field fluctuations at times t^+ and t^- leading to a phase noise $\delta\Phi = \alpha(\delta F(t^+) - \delta F(t^-))$.

4.4.1.a Taylor expansion of a stationary random noise

If the differential phase variations are small, $\delta\Phi \ll 1$, the contrast reduction can be expanded to second order in $\delta\Phi$ as

$$C_r \approx \left| 1 + i \langle \delta\Phi \rangle - \frac{1}{2} \langle \delta\Phi^2 \rangle \right|,$$

where the term $i\langle\delta\Phi\rangle$ vanishes since $\langle \delta F \rangle = 0$ making $\langle \delta\Phi \rangle = \langle \alpha(\delta F(t^+) - \delta F(t^-)) \rangle = 0$ and the above expression becomes

$$\begin{aligned} C_r &\approx 1 - \frac{1}{2}\alpha^2 \left\langle \left(\delta F(t^+) - \delta F(t^-) \right)^2 \right\rangle \\ &= 1 - \frac{1}{2}\alpha^2 \left(\left\langle \delta F(t^+)^2 \right\rangle + \left\langle \delta F(t^-)^2 \right\rangle - 2 \left\langle \delta F(t^+) \delta F(t^-) \right\rangle \right), \end{aligned} \tag{4.4}$$

where $\langle \delta F(t^+)^2 \rangle$ and $\langle \delta F(t^-)^2 \rangle$ take into account the noise at times t^+ and t^- and where $\langle \delta F(t^+) \delta F(t^-) \rangle$ accounts for the correlations of the noise between times t^+ and t^-. Expansions to higher order can be found in Appendix C.

Since the electric field fluctuations are stationary, the mean noise measured at two different times are the same, $\langle \delta F(t^+)^2 \rangle = \langle \delta F(t^-)^2 \rangle$, and the contrast in terms of electric

field fluctuations becomes

$$C_r \approx 1 - \alpha^2 \left(\left\langle \delta F(t^+)^2 \right\rangle - \left\langle \delta F(t^+) \delta F(t^-) \right\rangle \right).$$

In the case of uncorrelated electric field fluctuations at t^+ and t^-, the correlation term can be separated, $\langle \delta F(t^+) \delta F(t^-) \rangle = \langle \delta F(t^+) \rangle \langle \delta F(t^-) \rangle = 0$, and vanishes, leading to

$$C_r \approx 1 - \alpha^2 \langle \delta F(t^+)^2 \rangle. \tag{4.5}$$

4.4.1.b Stationary uncorrelated Gaussian random noise

In most cases, the noise distribution is Gaussian. It is then possible to calculate the exact expression of the contrast reduction C_r. The probability density for the electric field fluctuation $\delta F(t)$ is given by

$$S[\delta F(t) = \delta F] = \frac{1}{\sigma_F \sqrt{2\pi}} e^{-\frac{\delta F(t)^2}{2\sigma_F^2}},$$

which is the Gaussian probability density with average value $\langle \delta F \rangle = 0$ and standard deviation σ_F. The probability densities for $\delta F(t^+)$ and $\delta F(t^-)$ have the same standard deviation since the electric field fluctuations are assumed to be stationary.

The contrast reduction of the Ramsey fringes (Eq. 4.3) is now found by integrating over the electric field fluctuations,

$$\begin{aligned} C_r &= \left| \left\langle e^{i\alpha(\delta F(t^+) - \delta F(t^-))} \right\rangle \right| \\ &= \left| \int \int e^{i\alpha(\delta F(t^+) - \delta F(t^-))} S[\delta F(t^+) = \delta F^+, \delta F(t^-) = \delta F^-] d(\delta F^+) d(\delta F^-) \right|. \end{aligned} \tag{4.6}$$

Since we assume uncorrelated noise or a delay between the times t^+ and t^- larger than the correlation time t_{corr}, we can separated the Gaussian distribution

$$S[\delta F(t^+) = \delta F^+, \delta F(t^-) = \delta F^-] = S[\delta F(t^+) = \delta F^+] \; S[\delta F(t^-) = \delta F^-]$$

and we can treat the two integrals independently. We use

$$\int e^{i\alpha\delta F(t)} \frac{1}{\sigma_F \sqrt{2\pi}} \exp(-\frac{\delta F^2}{2\sigma_F^2}) d(\delta F) = e^{-\frac{1}{2}\alpha^2\sigma_F^2}$$

and find

$$C_r = e^{-\alpha^2 \sigma_F^2}. \tag{4.7}$$

4.4.1.c Stationary correlated Gaussian random noise

The calculation can be generalized to the case where the noise is correlated, but the probability density $S[\delta F(t^+) - \delta F(t^-)]$ of the difference between the noise at t^+ and t^- remains Gaussian. This means it is still possible to calculate the integral in Eq. 4.6. We find

$$C_r = e^{-\frac{1}{2}\alpha^2\langle(\delta F(t^+)-\delta F(t^-))^2\rangle} = e^{-\alpha^2\left(\langle\delta F(t^+)^2\rangle-\langle\delta F(t^+)\delta F(t^-)\rangle\right)}.$$

4.4.2 Noise measurement

To demonstrate that the contrast of the fringes can give access to the correlation function of the electric field noise, we have recorded Ramsey fringes in the presence of a well known artificial noise. We measure the contrast of the Ramsey fringes as a function of the standard deviation σ_F of artificially applied electric field fluctuations. The experimental sequence is sketched in Fig. 4.18. As before we have a first radio-frequency pulse pair at time t^+ which is σ^+ polarized and a second at $t^- = t^+ + 9\ \mu$s which is σ^- polarized.

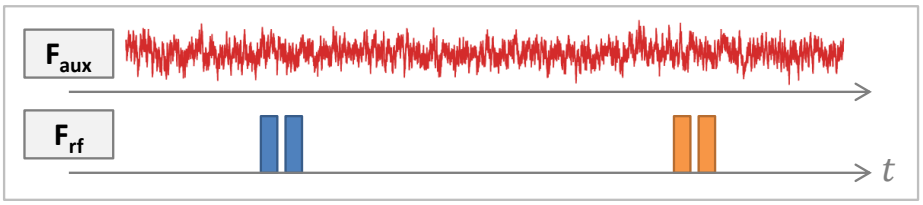

Figure 4.18: The experimental sequence to measure the contrast of the Ramsey fringes with double radio-frequency pulse pair (blue and orange) as a function of the standard deviation of the applied electric field fluctuations (red).

4.4.2.a Characteristics of the artificial electric field noise

We programme a sequence of artificial noise applied by the auxiliary AWG that is connected to the plane electrodes through the 100 kΩ resistor (see Fig. 3.8). The sequence is a waveform of $2^{17} = 131072$ points that is run at a 100 MSample/s rate, corresponding to a total duration of ~1.3 ms. The waveform is run continuously in a loop. Since the sequence is much longer than the duration of the experimental sequence of 311 μs and its duration is not a multiple of the latter, the radio-frequency pulse pairs will happen at random times during the noise sequence as we repeat the experiment, and will eventually explore the full noise sequence.

To create the sequence, we first generate 2^{17} values $y_0(i)$ randomly chosen with a Gaussian distribution. We then apply a numerical low-pass filter with a time constant of $t_{\text{corr}} = 1.5\ \mu$s to generate the sequence $y(i)$ with

$$y(i) = \sum_{j=0}^{131071} e^{-j/150} y_0(i-j)$$

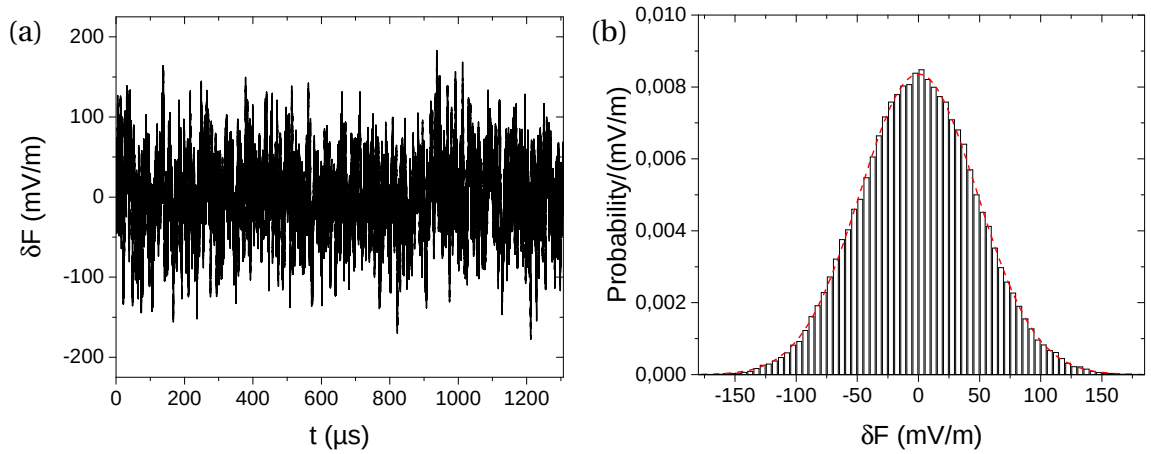

Figure 4.19: (a) Noise sequence with a numerical low-pass filter with time constant of 1.5 μs. (b) Histogram of the probability to find an electric field fluctuation value δF (histogram) with Gaussian fit (red) yielding a variance of $\sigma_F = 47.787$ mV/m.

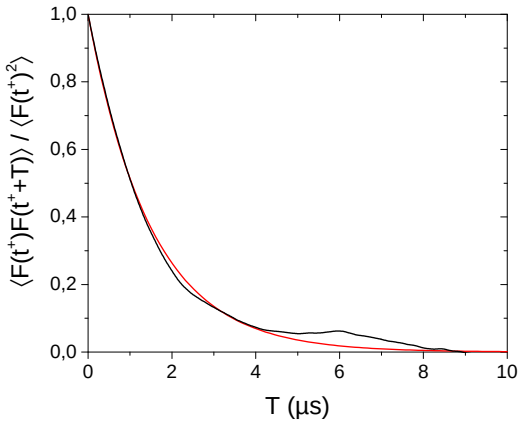

Figure 4.20: The correlation function calculated for the generated electric field noise with $t_{corr} = 1.5$ μs as a function of the delay T (black) follows the theoretical behaviour $e^{-T/t_{corr}}$ (red). The difference is due to the finite length of the noise sequence.

taking $y_0(i) = y_0(i + 131072)$ when $i < 0$ since the sequence is played in a loop. This transforms the initial Gaussian white noise into a signal with an exponentially decaying correlation. We then convert this signal into a 16-bit digital waveform by scaling the sequence so that the largest value $|y(i)|$ is 2^{15}. After loading the waveform in the AWG memory, we can choose the amplitude with which the AWG runs the sequence.

The electric field noise sequence for the maximum amplitude of the AWG is shown in Fig. 4.19a as a function of time. Fig. 4.19b shows the probability to find a certain value of the electric field fluctuation δF. The Gaussian fit yields a standard deviation of $\sigma_F = 47.8$ mV/m.

Fig. 4.20 presents the autocorrelation function $G_F(T) = \langle F(t^+)F(t^+ + T)\rangle / \langle F(t^+)^2\rangle$ as a function of the delay T. For short delay $T \approx 0$, the correlation function $G_F(0) = 1$. It decreases for increasing delay with a time constant $t_{\mathrm{corr}} = 1.5$ μs. The correlation function calculated for the actual noise follows the theoretical value $e^{-t/t_{\mathrm{corr}}}$. The difference is due

to the finite length of the noise sequence.

We create a second artificial noise sequence with a correlation time constant of $t_{\mathrm{corr}} = 0.5\ \mu$s with the same techniques as described here.

Finally, we create a sequence which simulates white noise. To this end, we generate 2^{17} random values and average them on a sliding window with a length corresponding to 200 ns. This means that the sequence has no correlations for $T > 200$ ns. However, this averaging filters out frequency components above 5 MHz to assure that there is no electric field noise component at a frequency of the resonance of the cryostat at ~8 MHz, discussed in Sec. 4.3.2.

4.4.2.b Measurement of the artificial electric field noise

We record the Ramsey fringes for the noise with $t_{\mathrm{corr}} = 1.5\ \mu$s applied with different amplitudes, corresponding to different values of σ_F. The radio-frequency pulses are applied at t^+ and t^- such that $T = t^- - t^+ = 9\ \mu$s. At this delay, no correlation is observed in Fig. 4.20.

Fig. 4.21 shows the Ramsey fringes for different amplitudes of the applied artificial noise. The fitted contrast is presented in Fig. 4.22a as a function of the standard deviation σ_F of the noise. For small values of σ_F the contrast is high and follows the second-order approximation $C \propto 1 - \alpha^2\sigma_F^2$ (Eq. 4.5). As σ_F increases the second order approximation is not valid any more and the contrast follows $C \propto \exp(-\alpha^2\sigma_F^2)$ (Eq. 4.7).

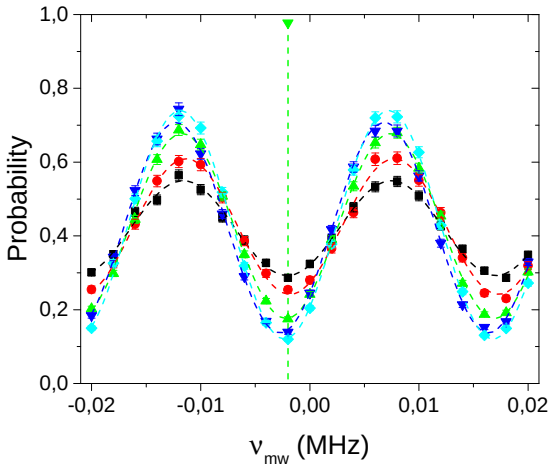

Figure 4.21: Ramsey fringes with radio-frequency pulse with delay $T = 9\ \mu$s for different standard deviations σ_F of the applied electric field noise: $\sigma_F = 47.8$ mV/m (black), 36.1 mV/m (red), 24.1 mV/m (green), 12.0 mV/m (blue), 0 mV/m (cyan).

Since $\langle \delta F \rangle = 0$, the phase of the fringes does not move. It is therefore as well possible to deduce the standard deviation of the noise σ_F by fixing the phase of the interferometer at a point at minimum slope. Fig. 4.22b shows the recorded probability P_q for different values of σ_F.

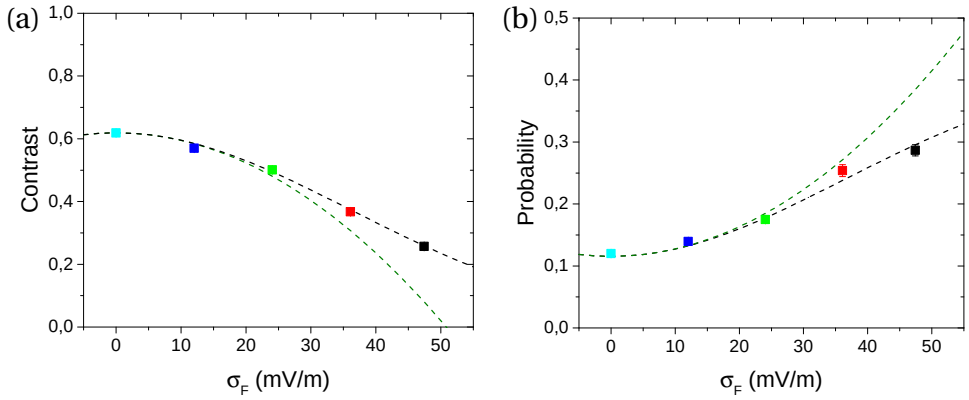

Figure 4.22: (a) Contrast of the Ramsey fringes of Fig. 4.21 (same colours) as a function of the amplitude of the applied artificial noise, corresponding to the standard deviation σ_F. The second order approximation $C = C_0(1-\alpha^2\sigma_F^2)$ holds for small σ_F (green dashed). For larger σ_F we have to use $C = C_0\exp(-\alpha^2\sigma_F^2)$ (black dashed). C_0 is the contrast without applied noise. (b) The probability at the fixed microwave frequency at a minimum of Ramsey fringes (indicated as green dashed line in Fig. 4.21) as a function of σ_F.

4.4.3 Measure the correlation of noise

The correlation function of the applied electric field noise is accessible by changing the delay T between the radio-frequency pulse pairs. However, we have to ensure that the phase sensitivity α^- of the pair of radio-frequency pulses which we move stays constant to achieve the best result. This is not trivial as the atoms fly at about 250 m/s through the experimental set-up meaning that the distance between the atom and the electrodes that create the radio-frequency field changes. We need to assure that the polarization is optimized at each position and that the amplitude of the radio-frequency field seen by the atoms is constant.

4.4.3.a Calibration of time varying radio-frequency pulses

The second radio-frequency pulse pair is applied at different times from $t^- = 11.4\ \mu$s to 22.4 μs after the initial laser pulse at 0 μs. A range of 11 μs corresponds to a distance of 2.8 mm at the speed of the atom. This length is not negligible with respect to the distance from the center of the experimental zone to the ring electrodes of 25 mm. Therefore, the polarization of the σ^- polarized radio-frequency field is optimized for each time t^-. This is done by varying the phase of the signal applied on electrode E4, while the phase of the signal applied on electrode E3 is fixed, in order to find the relative phase that optimizes the σ^- polarization, for each time t^- corresponding to each position of the atom. The optimum phase of the signal applied on electrode E4 as a function of the time t^- is shown in Fig. 4.23.

The amplitude of the radio-frequency field seen by the atoms increases as they move towards the electrodes. We therefore need to reduce the amplitude of the radio-frequency drive to keep the Rabi frequency Ω_{rf}^- at a constant value while varying t^-. To that end, we

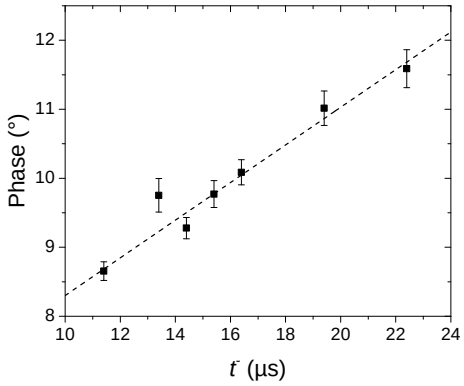

Figure 4.23: Variation of the phase of the radio-frequency signal applied on electrode E4 that optimizes the σ^- polarized radio-frequency field as a function of the time t^-. The dashed line is the linear fit.

first record a resonant Rabi oscillation in the $n = 51$ manifold: we measure the probability $P(51c)$ to find the atom in the $|51c\rangle$ state as a function of the duration t^-_{rf} of a σ^- polarized radio-frequency pulse for the correct Rabi frequency Ω^-_{rf}, shown in Fig. 4.24a. We observe that the atom returns to the $|51c\rangle$ state after a radio-frequency pulse duration of $t^-_{\mathrm{rf,ref}} =$ 237 ns.

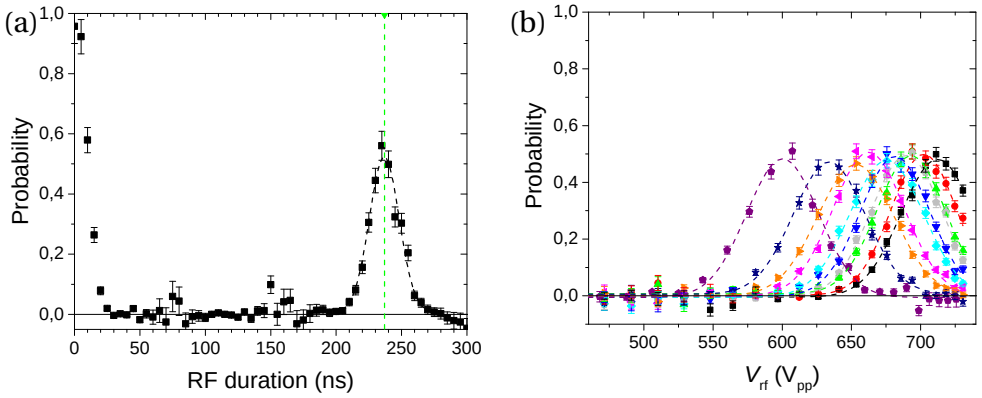

Figure 4.24: (a) Resonant Rabi oscillation in the $n = 51$ manifold for a σ^- polarized radio-frequency field. The probability is plotted as a function of the radio-frequency duration. The maximum return is fitted (black dashed) and the maximum is indicated at 237 ns (green dashed). (b) The probability to return to the initial $|51c\rangle$ state after a σ^- polarized radio-frequency pulse of duration $t^-_{rf} = 237$ ns at different times $t^- = 11.4$ µs (black), 12.4 µs (red), 13.4 µs (green), 13.8 µs (grey), 14.4 µs (blue), 15.4 µs (cyan), 16.4 µs (pink), 17.4 µs (orange), 19.4 µs (navy), 22.4 µs (violet).

For each value of t^-, we record the probability to return to the $|51c\rangle$ state after a pulse of duration $t_{\mathrm{rf,ref}}$ as a function of the amplitude of the radio-frequency signal sent to electrodes E3 and E4. This amplitude is measured on the oscilloscope which monitors the radio-frequency signal reflected back from the cryostat (see Fig. 2.11 for the radio-frequency circuit). The result of this experiment is shown in Fig. 4.24b. For each time t^-, we observe a peak in the probability $P(51c)$ as a function of the radio-frequency signal amplitude. The maximum for each time t^- occurs when the amplitude of the

radio-frequency drive is such that the atom sees a radio-frequency field with correct Rabi frequency Ω_{rf}^{-}. We observe that when t^- is larger, we need to apply a radio-frequency signal with smaller amplitude on the electrodes to get the same Rabi frequency since the atoms are closer to the field-creating electrodes.

Finally, we verified that the Ramsey fringes for the σ^- polarized radio-frequency pulses have the same phase sensitivity over time t^-. Fig. 4.25 shows the phase sensitivity α^- as a function of the time t^-. The results are constant within 3% and all very close to the value of the phase sensitivity α^+ averaged over several days.

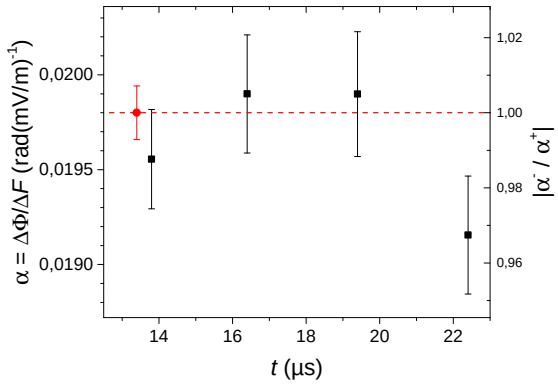

Figure 4.25: The phase sensitivity α^- (black) plotted as a function of the moment when the σ^- radio-frequency pulse pair is applied compared to the phase sensitivity α^+ (red) at $t^+ = 13.4$ μs averaged over several days.

4.4.3.b Measure the correlation of a random Gaussian noise

We now move on to measure the correlation function of the noise we artificially apply. The experimental sequence is sketched in Fig. 4.26. The σ^+ polarized pair of radio-frequency pulses happen at 13.4 μs after the laser pulse. The σ^- polarized pair of radio-frequency pulses is applied for various $t^- > t^+$ but also for two values of $t^- < t^+$. For each value of t^- we record Ramsey fringes and fit their contrast.

The results are shown in Fig. 4.27. The contrast of the Ramsey fringes is plotted as a function of the delay between the two pairs of radio-frequency pulses $T = t^- - t^+$. In the

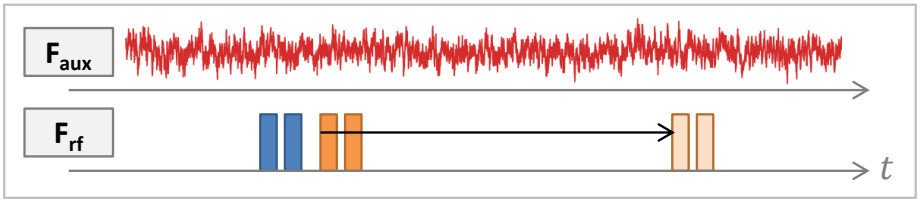

Figure 4.26: The experimental sequence to measure the contrast of the Ramsey fringes with double radio-frequency pulse pair (blue and orange) in the presence of applied electric field fluctuations (red) as a function of the delay between the σ^+ (blue) and the σ^- (orange) polarized pulse pair.

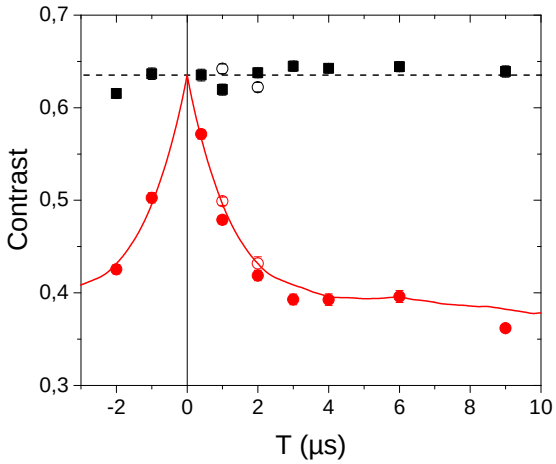

Figure 4.27: The contrast of the Ramsey fringes as a function of the delay between the two radio-frequency pulse pairs for no applied electric field fluctuations (black) and applied electric field fluctuations with $t_{corr} = 1.5$ µs (red) for $t^+ = 13.4$ µs (full dots) and $t^+ = 15.4$ µs (hollow dots). The calculated contrast from the applied noise (red line) is normalized by the mean contrast without electric field fluctuations (dashed line).

case where no artificial electric field noise is applied the contrast is constant around an average value of $C_0 = (63.5 \pm 0.3)\%$. When the artificial electric field noise with correlation time constant $t_{\mathrm{corr}} = 1.5$ µs is applied, the contrast depends on the delay T between the two radio-frequency pulse pairs. Here, we set the amplitude of the AWG in order to generate a noise with standard deviation $\sigma_F = 36.4$ mV/m. For very short delays T the contrast is high, since the noise at times t^+ and t^- is highly correlated. For increasing delay T the contrast decreases as the correlation of the artificial noise decreases. Since the correlation function is symmetric around $T = 0$ µs, the contrast for values with $t^- < t^+$ behave the same way as for $t^- > t^+$.

To exclude any systematic effects associated to t^-, we repeated the measurement for $t'^+ = t^+ + 2$ µs $= 15.4$ µs and two values of t^-. We see in Fig. 4.27 that the behaviour of the contrast does not depend on the absolute value of t^+, but that the signal we measure does only depend on the delay between the radio-frequency pulse pairs. The measured contrast fits extremely well with the value of the simulation calculated from the noise and the intrinsic contrast C_0 deduced from the measurement without applied noise.

Fig. 4.28 presents, in addition to the curves presented in Fig. 4.27, the contrast of the Ramsey fringes in the presence of the noise with correlation time constant $t_{\mathrm{corr}} = 0.5$ µs as a function of the delay T between the two radio-frequency pulse pairs. Since the correlation time constant is shorter, the contrast decreases faster than in the case of $t_{\mathrm{corr}} = 1.5$ µs. We also record the contrast for our artificial white noise with $t_{\mathrm{step}} = 200$ ns. Here, we see that the contrast we measure experimentally is systematically higher than the one expected from our numerical model. This is probably due to the high frequency components close to ~5 MHz of the noise which are not well seen by the interferometer.

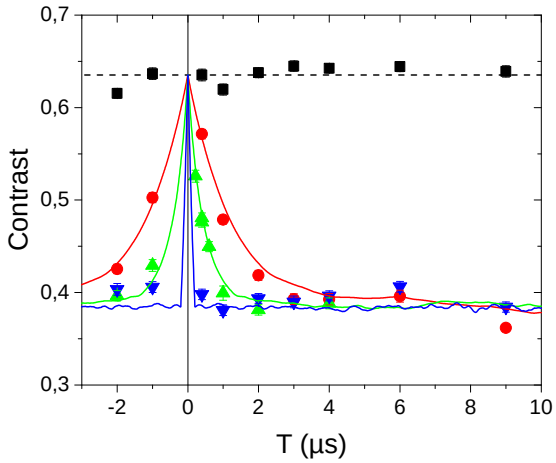

Figure 4.28: The contrast of the Ramsey fringes as a function of the distance between the two radio-frequency pulse pairs for no applied electric field fluctuations (black) and applied electric field fluctuations with $t_{corr} = 1.5$ µs (red), $t_{corr} = 0.5$ µs (green) and $t_{step} = 0.2$ µs (blue) together with the corresponding calculated expected contrast.

4.4.3.c Detection of a hidden deterministic signal

The AC-electrometer can also be used to detect an underlying asynchronous signal by measuring the correlation that this signal induces. To demonstrate this, we apply a sinusoidal electric field without sending a trigger signal to the AWG that generates the signal. Since the signal is not synchronized with the experimental sequence, measuring it with a single radio-frequency pulse pair means that we would only see a global contrast reduction. However, our correlation measurement method allows us to observe the hidden sine-signal of the noise.

Fig. 4.29 presents the contrast of the Ramsey fringes when we apply a sine-signal with $T_{\text{sine}} = 4.45$ µs period and standard deviation $\sigma_F = 12.94$ mV/m. In Fig. 4.22, presented above, we see that with this chosen variance we can safely use the second-order approximation of the contrast in the presence of an electric field fluctuation (Eq. 4.4),

$$C \approx C_0 \left(1 - \frac{1}{2}\alpha^2 \langle (\delta F(t^+) - \delta F(t^-))^2 \rangle\right),$$

where C_0 is the intrinsic contrast without artificial electric field noise. When the delay T between the radio-frequency pulse pairs equal a multiple integer of the period of the sine-signal, $T = nT_{\text{sine}}$, the electric field at t^+ and $t^- = t^+ + nT_{\text{sine}}$ are the same, so $\langle \delta F(t^+) \rangle = \langle \delta F(t^- + nT_{\text{sine}}) \rangle$, and the contrast is maximum with $C = C_0$. This includes $T = t^- - t^+ = 0$ µs, for which the contrast is maximum for any correlated electric field fluctuation. For a delay T of half-integer multiple of the sine signal, $T = \left(n + \frac{1}{2}\right) T_{\text{sine}}$, the electric field at t^+ and $t^- = t^+ + \left(n + \frac{1}{2}\right) T_{\text{sine}}$ have opposite signs, $\langle \delta F(t^+) \rangle = -\left\langle \delta F\left(t^+ + \left(n + \frac{1}{2}\right) T_{\text{sine}}\right) \right\rangle$, and the contrast is minimum with $C = C_0(1 - 2\alpha^2 \langle \delta F(t)^2 \rangle) = C_0(1 - 2\alpha^2 \sigma_F^2)$.

The experimental results are shown together with the expected contrast (see Fig. 4.29). The expected contrast is calculated with $C = C_0\left(1 - \alpha^2 \sigma_F^2 (1 - \cos(2\pi T / T_{\text{sine}})\right)$, where

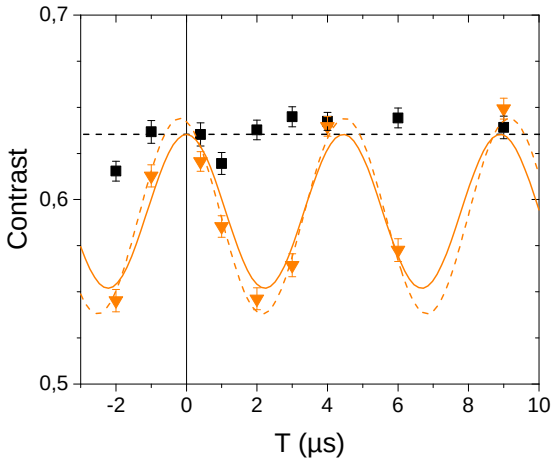

Figure 4.29: The contrast of the Ramsey fringes as a function of the distance between the two radio-frequency pulse pairs for a non-triggered sine-signal with 4.45 µs period (orange). The expected behaviour of the contrast (orange line) corresponds qualitatively to the fitted sine (dashed orange). The contrast for no applied electric field fluctuations (black) is shown for comparison.

$C_0(1-\alpha^2\sigma_F^2)$ is the mean value around which the reduced contrast oscillates. When we fit the recorded sine-signal, we find a period of $T_{\text{sine}} = (4.67 \pm 0.10)$ μs and a standard deviation of $\sigma_F = (14.48 \pm 0.59)$ mV/m. These values do not correspond exactly to the expected values, $T_{\text{sine}} = 4.45$ μs and $\sigma_F = 12.94$ mV/m, but show that we are able to clearly resolve the sinusoidal period of the applied noise within 5% and its standard deviation within 12%.

The AC-electrometer can resolve electric field fluctuation with a bandwidth up to ~5 MHz limited by the duration of the single radio-frequency pulse pairs. After the proof of principle in the last section, we now investigate the correlation time constant of the intrinsic electric field fluctuations of the experiment. However, the contrast for no applied electric field noise in Fig. 4.27 stays at a constant value when scanning the delay T between the two pairs of radio-frequency pulses. In the next section we describe how it is nevertheless possible to characterize the intrinsic noise of the experiment.

4.5 Characterization of the noise in the experiment

To measure the intrinsic noise of the experiment, we need to increase the sensitivity of the electrometer. This can be achieved by increasing the delay τ between the radio-frequency pulses of both pulse pairs, since the phase sensitivity scales with the latter. Unfortunately, as we increase the delay τ, the contrast of the Ramsey fringes becomes more sensitive to the inhomogeneity of the driving radio-frequency field. We were afraid [112] that the inhomogeneity of the radio-frequency field created by only two electrodes would not allow us to observe fringes with a good enough contrast at a longer interrogation time. This is why we decided to characterize the intrinsic noise using a sequence derived

from the echo-measurement presented in Sec. 3.4.[5] Since this sequence only involves σ^+ polarized radio-frequency fields, this allows us to generate each pulse using four electrodes. To increase the sensitivity we increase the interrogation time of both σ^+ radio-frequency pulse pairs to $\tau_{51} = \tau_{49} = 400$ ns leading to increased phase sensitivities of $\alpha_{51} \approx -\alpha_{49} \approx 0.113$ rad/(mV/m).

The experimental sequence is sketched in Fig. 4.30. Both pairs of radio-frequency pulses are σ^+ polarized and generated by four electrodes. All radio-frequency pulses have the same frequency $\omega_{\mathrm{rf}} = 2\pi \cdot 230$ MHz. The first radio-frequency pulse pair is resonant with the lowest diagonal in the $n = 51$ manifold. The static electric field is then ramped up so that the radio-frequency field is resonant with the lowest diagonal in the $n = 49$ manifold.

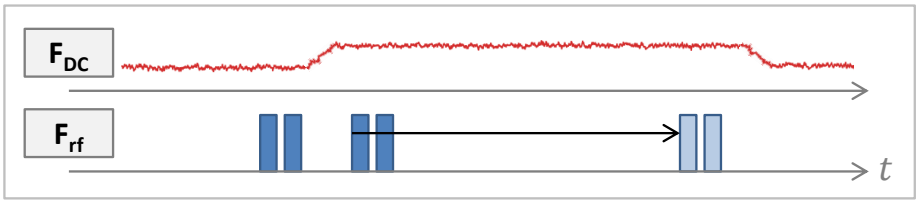

Figure 4.30: The experimental sequence to measure the contrast of the Ramsey fringes with double σ^+ polarized radio-frequency pulse pair (blue) to obtain the intrinsic electric field noise of the experiment. The intrinsic noise of the experiment is indicated as an electric field fluctuation on the applied DC electric field.

However, since there is an electric field step of finite duration between the two radio-frequency pulse pairs at t_{51}^+ and t_{49}^+ we cannot bring the pulses as close together as shown in the previous part of this chapter. This limits the ability to measure the correlation function for short delays.

Fig. 4.31a presents the contrast of the Ramsey fringes with the two radio-frequency pulse pairs as a function of the delay $T = t_{49}^+ - t_{51}^+$ for two different values of $t_{51}^+ = 13.4$ μs and $t_{51}^+ = 15.4$ μs. We see a first decrease in contrast which is the same for both values of t_{51}^+. The second decrease in contrast, however, differs for the two curves. In fact, if we plot the contrast as a function of the time of the second radio-frequency pulse pair t_{49}^+ instead of the delay T, shown in Fig. 4.31b, we see that the second contrast reduction actually happens at the same time $t_{49}^+ > 19$ μs. Fig. 4.31b also presents the contrast of the Ramsey fringes when only the second pair of radio-frequency pulses is applied as a function of t_{49}^+. We also observe a decrease of this contrast for $t_{49}^+ > 19$ μs. We thus believe that the second decrease in contrast in Fig. 4.31a is not due to a variation in the correlation function of the intrinsic noise, but rather due to an additional noise or imperfection occurring at times $t > 19$ μs. This contrast reduction could be due, for example, to a degradation of the polarization of the radio-frequency field. It could also be caused by the fact that the electric field gradient is less compensated as the atom moves away from the center of the electrode structure.

To find the correlation time constant t_{corr} of the intrinsic electric field noise of the

[5] In the case of two electrodes, the observed contrast is smaller than in the case of four electrodes, but might have been enough to observe the intrinsic noise of the experiment.

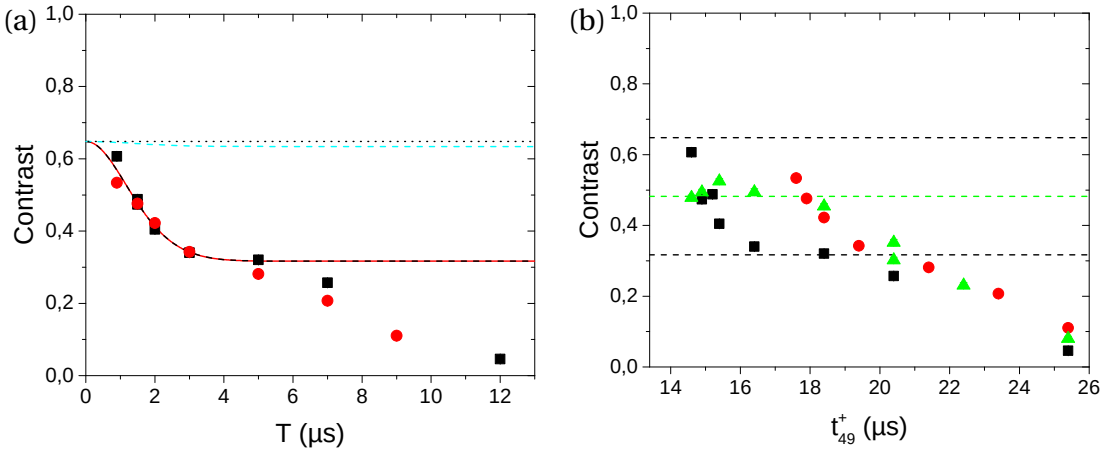

Figure 4.31: (a) Contrast of the double σ^+ radio-frequency Ramsey fringes as a function of the delay $T = t^+_{49} - t^+_{51}$ between the two radio-frequency pulse pairs for $t^+_{51} = 13.4$ µs (black) and $t^+_{51} = 15.4$ µs (red). The contrast for short delays T can be fitted by the model of a Gaussian noise with standard deviation $\sigma_F = 7.48$ mV/m (red/black line). The same noise model with the same σ_F but with the phase sensitivity $\alpha = 0.0198$ rad/(mV/m) for $\tau = 0$ ns shows that the contrast (cyan dashed) stays close to the initial contrast at $T = 0$ (black dashed). (b) Contrast of the double σ^+ radio-frequency Ramsey fringes as a function of the delay t^+_{49} for $t^+_{51} = 13.4$ µs (black) and $t^+_{51} = 15.4$ µs (red). The contrast is reduced from about $t \approx 6$ µs onwards indicated by the contrast of the single σ^+ fringes at t^+_{49} (green) which detaches from its expected value halfway between upper and lower bound of the fit in (a).

experiment, we fit the contrast $C(T)$ with the following function

$$C(T) \approx C_0 \exp\left(-\alpha^2 \sigma_F^2 \left(1 - e^{-T^2/t_{\text{corr}}^2}\right)\right),$$

assuming a Gaussian noise with a Gaussian correlation function, and excluding points that correspond to $t^+_{49} > 19$ µs. We find that the intrinsic noise has a correlation time constant of $t_{\text{corr}} = (2.01 \pm 0.26)$ µs and a standard deviation of $\sigma_F = (7.48 \pm 0.36)$ mV/m.

The value of σ_F is significantly smaller than $\sigma_F = 12.01$ mV/m, obtained from the contrast reduction of the microwave fringes in Sec. 3.3.4. The reason may be the different time scales in the noise correlation function. It is possible that there is a noise component whose correlation time constant is so short that it cannot be measured with this experiment. Or, on the contrary, that there are electric field fluctuations with timescales much longer than 10 µs which lead to a decrease of the contrast of the fringes of a single radio-frequency pulse pair, but are cancelled out by the echo measurement.

4.6 Discussion

The rich structure of the Rydberg atom allows us not only to measure very small electric field changes but also the time correlation of the electric field. Using a combination of

σ^+ and σ^- polarized radio-frequency field pulses, we are able to perform Ramsey fringes whose phase is sensitive to the difference in the electric field amplitude at times t^+ and t^-. This makes it possible to create an AC-electrometer able to measure time variations of the electric field while at the same time cancelling the contribution of DC fluctuations of the electric field.

If we set the phase of the interferometer at the maximum or minimum of the Ramsey fringes, we can obtain a non-linear response which allows us to access the time correlation of the electric field. This could be used for example to measure the correlation function of the presence of a single charge in a mesoscopic device.

We also presented how we can use the contrast of the interference to deduce information about the time correlation of the electric field noise seen by the atom and demonstrated this technique by characterizing an artificial electric field noise.

Finally, we used a similar method to characterize the correlation time of the noise in our experiment and found a time constant of $\sim$2 μs. This correlation time constant of 2 μs is very promising for Rydberg quantum engineering experiments. Preparing complex quantum states of the Rydberg atom often requires to transiently prepare a superposition of states with very different polarizabilities whose relative phase is very sensitive to the electric field noise. The relatively long correlation time of electric field fluctuations makes it possible to compensate the accumulated phase shift by echo-π pulses which reverses the decoherence process and eventually cancels it. This method is extensively used in the next chapter.

Chapter 5

Quantum-enabled magnetometry

The superposition of two opposite circular Rydberg states is highly sensitive to variations of the magnetic field, since the difference in the magnetic quantum number is in the order of $\Delta m \sim 100$. At the same time, this quantum state is almost insensitive to electric field fluctuations making it an ideal magnetic sensor.

The preparation of this large quantum state is complex, since we have to cross the region of the Rydberg manifold with $|m| < 3$, where the energy difference between the m-ladder states in the presence of the static electric field is highly irregular.

In this chapter we describe the preparation scheme of this large superposition (Sec. 5.1) which consists of two steps: the crossing of the low-m region and the fast circularization of the low-m state. We then show the sensitivity to magnetic field variations of the superposition state (Sec. 5.2).

5.1 Preparation of the opposite circular superposition

5.1.1 General preparation scheme

The aim is to prepare a superposition between the two circular states $|+52c\rangle$ and $|-52c\rangle$, states with opposite maximum magnetic quantum numbers. These states correspond to the levels at the outermost tips of the manifold (see Fig. 1.11).

In order to prepare this superposition, we choose to prepare a superposition of opposite $m = +2$ and $m = -2$ states of the lowest σ^+ and σ^- spin ladders, respectively, from which the circularization can be achieved by a fast Rabi π pulse [176]. We decide to prepare the positive circular state in the $n = 52$ manifold and the negative circular state in the $n = 50$ manifold. By choosing two different manifolds, the σ^+ polarized radio-frequency field, resonant in the $n = 52$ manifold, and the σ^- polarized radio-frequency field, resonant in the $n = 50$ manifold, have different frequencies. Therefore, the σ^-

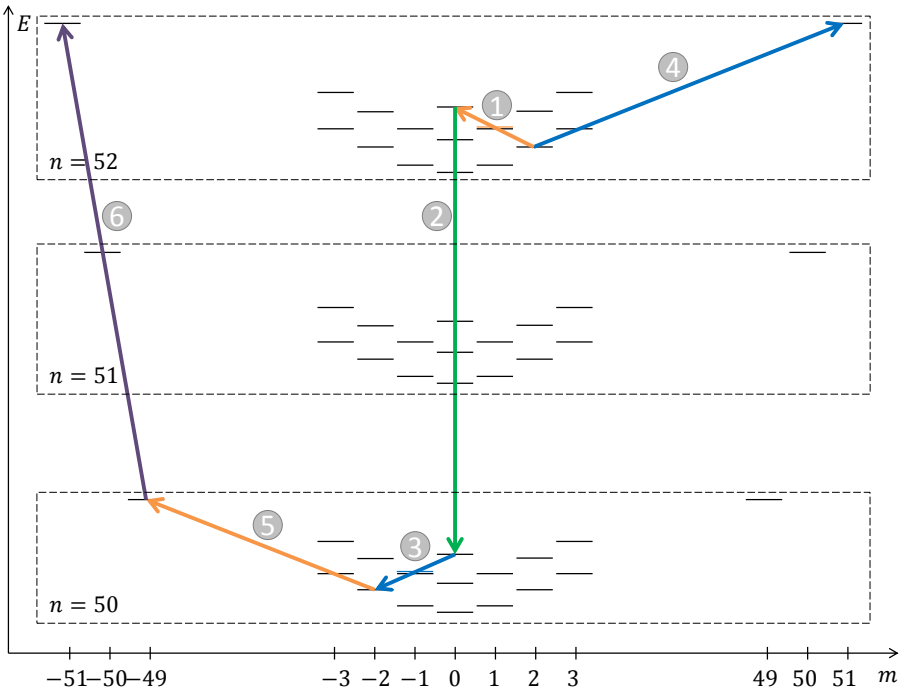

Figure 5.1: The involved levels and transitions in order to prepare a superposition of the opposite circular states $|+52c\rangle$ *and* $|-50c\rangle$ *are: (1) radio-frequency* $\pi/2$ *pulse from* $|52,+2\rangle$ *to* $|52,0''\rangle$*, (2) two-photon microwave* π *pulse from* $|52,0''\rangle$ *to* $|50,0''\rangle$*, (3) radio-frequency* π *pulse from* $|50,0''\rangle$ *to* $|50,-2\rangle$*, (4) Rabi* π *pulse from* $|52,+2\rangle$ *to* $|+52c\rangle$*, (5) Rabi* π *pulse from* $|50,-2\rangle$ *to* $|-50c\rangle$*. (6) By applying an additional microwave pulse resonant with the* $|-50c\rangle - |-52c\rangle$ *transition, the atom can finally be excited in a superposition of opposite circular states of the same manifold.*

polarized radio-frequency field used to prepare the $|-50c\rangle$ state, does not affect the part of the wave-function in the $n = 52$ manifold.

The preparation of a superposition between the $|52,+2\rangle$ and the $|50,-2\rangle$ states is not trivial since the low lying m states have very different polarizabilities. The decoherence of a superposition of states with different Stark shifts is very sensitive to fluctuations of the electric field. The solution is therefore either to stay as much as possible in levels with similar Stark shifts or to reach the final superposition of opposite circular states as fast as possible. Once in the circular states, which are not shifted by the electric field in first order, the superposition is almost insensitive to electric field fluctuations.

Radio-frequency pulses, with their large Rabi frequency, allow very fast transfers between the low-m states. This is why we use mostly radio-frequency pulses and only one microwave pulse to get from the $|52,+2\rangle$ to the $|50,-2\rangle$ state. Fig. 5.1 shows a sketched level structure together with the involved microwave and radio-frequency transitions. The transitions are labelled with a number corresponding to the order with which the pulses are applied. The atom is initially in the state $|52,+2\rangle$. A first two-photon radio-frequency $\pi/2$ pulse brings half of the population into the $|52,0''\rangle$ state (1).[1] The $|52,0''\rangle$

[1] In this chapter "prime" and "second" refer to the different levels of a vertical m-ladder: the lowest level of the m-ladder is denoted as $|n,m\rangle$, the second lowest as $|n,m'\rangle$, the third lowest as $|n,m''\rangle$, etc.

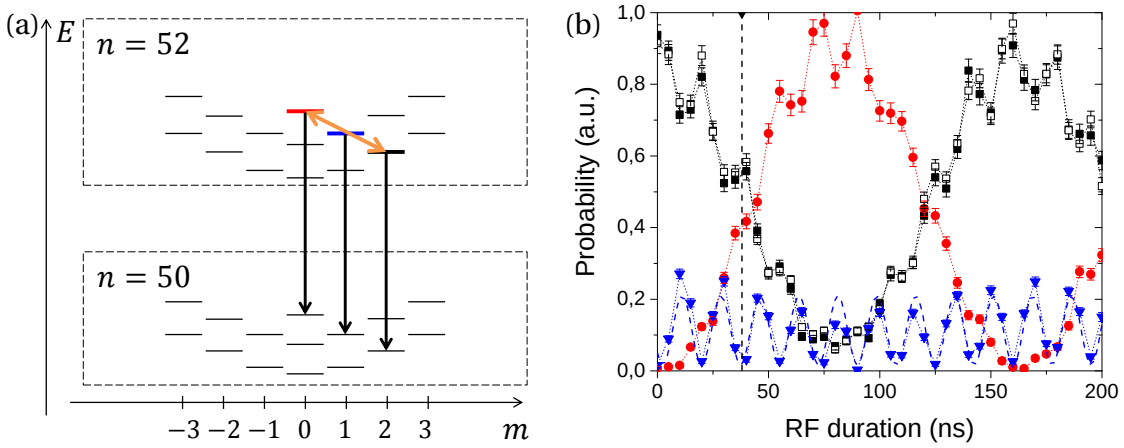

Figure 5.2: (a) The levels $|52,+2\rangle$ *(black, thick),* $|52,+1'\rangle$ *(blue) and* $|52,0''\rangle$ *(red) are involved in the first radio-frequency pulse. The applied radio-frequency field (orange) is polarized* σ^-*. Each population is read out using microwave probe pulses that transfer the states into another manifold (black arrows). (b) The probability to find the atom in* $|52,+2\rangle$ *(black),* $|52,+1'\rangle$ *(blue) and* $|52,0''\rangle$ *(red) as a function of the radio-frequency duration. The duration of the* $\pi/2$ *pulse of 38 ns is chosen by keeping in mind that the population of the intermediate level should be zero after the radio-frequency pulse. The dotted lines connect the experimental data points to guide the eye, the dashed blue line is a sine-fit of the off-resonant oscillation in the population of the* $|52,+1'\rangle$ *state.*

state is then transferred by a two-photon microwave π pulse into the $|50,0''\rangle$ state in the $n = 50$ manifold (2). A two-photon radio-frequency π pulse brings the population into the $|50,-2\rangle$ state (3). At this point, the superposition of opposite $m = \pm 2$ states is reached. In the next steps both parts of the wave-function are transferred from the $m = \pm 2$ states to the respective circular states, $|+52c\rangle$ and $|-50c\rangle$, (4) and (5). To finally reach a superposition of opposite circular states in the same manifold, another microwave π pulse is applied to transfer the population from the $|-50c\rangle$ to the $|-52c\rangle$ state (6). In the following, the steps involving radio-frequency pulses are discussed in detail.

Since the radio-frequency field has to be optimized at a given frequency, all σ^+ polarized radio-frequency pulses are at a frequency of 230 MHz, and all σ^- polarized radio-frequency pulses at 221.64 MHz. We tune the atom to be on resonance with the respective radio-frequency field by changing the amplitude of the electric field that maintains the quantization axis.

5.1.2 Preparation of the low-m superposition

The first radio-frequency pulse (1), polarized σ^-, drives the two-photon transition from the initial $|52,+2\rangle$ state to the $|52,0''\rangle$ state. Fig. 5.2 shows the probability to find the atom in the states $|52,+2\rangle$, $|52,0''\rangle$, and the intermediate $|52,+1'\rangle$ state as a function of the radio-frequency pulse duration. The applied radio-frequency field is polarized σ^- with a frequency of $\omega^- = 2\pi \cdot 221.64$ MHz. The electric field is set to $F_1 = 138$ V/m and precisely fine tuned to maximizes the transfer into the $|52,0''\rangle$ state. At this electric field,

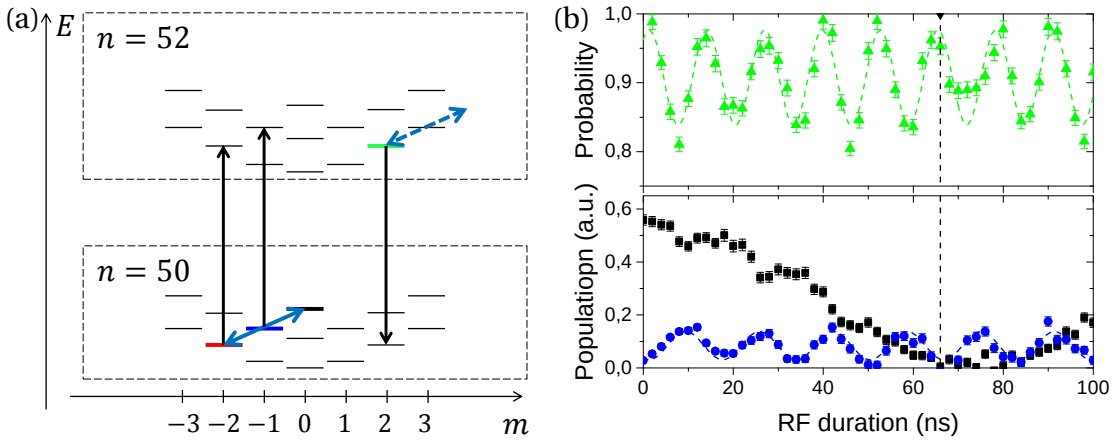

Figure 5.3: (a) The levels $|50,0''\rangle$ *(black, thick),* $|50,-1'\rangle$ *(blue) and* $|50,-2\rangle$ *(red) are involved in the second radio-frequency pulse. The applied radio-frequency field (blue) is polarized* σ^+*. The population in the* $|52,+2\rangle$ *state (green) undergoes off-resonant Rabi oscillations. The population is read out by microwave probe pulses to another manifold (black arrows). (b) The probability of an atom to remain in the* $|52,+2\rangle$ *state (top) and the population of the states* $|50,0''\rangle$ *(black) and* $|50,-1'\rangle$ *(blue) as a function of the radio-frequency duration (bottom). For technical reasons the value of the black and the blue signal cannot be properly normalized. The curves shown are only proportional to the actual population. This explains why the first point of the black curve is at ~0.6.*

the intermediate state, $|52,+1'\rangle$ is detuned from the two-photon transition frequency of the $|52,+2\rangle$ to $|52,0''\rangle$ state. However, the detuning is not completely negligible with respect to the Rabi frequency, and we observe the off-resonant Rabi oscillations of the population in the intermediate state as a function of the applied radio-frequency duration shown in Fig. 5.2b. We choose for the $\pi/2$ pulse a duration that corresponds to an integer number of periods of the $|52,+1'\rangle$ Rabi oscillation, to ensure that the population of the intermediate level is zero after the radio-frequency pulse.

The electric field is changed and the microwave pulse (2) transfers the population of the $|52,0''\rangle$ to the $|50,0''\rangle$ state by a two-photon π pulse with an efficiency in the order of 80%.

The electric field is then changed again, this time to $F_3 = 150$ V/m so that the σ^+ polarized radio-frequency field (3) with frequency $\omega = 2\pi \cdot 230$ MHz becomes close to resonant to the two-photon transition from $|50,0''\rangle$ to $|50,-2\rangle$. Fig. 5.3 shows the populations of the initial $|50,0''\rangle$ and the intermediate $|50,-1'\rangle$ state as a function of the radio-frequency pulse duration. We observe the transient population in the $|50,-1'\rangle$ state. Here again, we need to choose a duration of the pulse that is an integer number of the off-resonant Rabi oscillations. In addition, we see that the σ^+ polarized field (at 230 MHz) is also affecting the part of the wave-function that is left in the $|52,+2\rangle$ state, depicted in Fig. 5.3a. At an electric field of 150 V/m, the frequency ω_{at} of all the transitions $m = 2 \rightarrow 3 \rightarrow ...$ in the $n = 52$ manifold is in the order of 150 MHz. The 80 MHz detuning is not large enough compared to the coupling due to the radio-frequency field to protect the part of the wave-function in the $n = 52$ manifold, and the radio-frequency field also drives off-resonant oscillations that take the population out of the $|52,+2\rangle$ level. We thus have

to adapt the radio-frequency power to find a duration of the radio-frequency pulse that corresponds to both an integer number of oscillations of the blue and the green signal in Fig. 5.3b, near the duration of the π pulse of the $|50,0''\rangle \rightarrow |50,-2\rangle$ transition.

5.1.3 Circularization to opposite circular states

5.1.3.a Circularization via multiple Rabi pulses

We first restrict the description to the circularization in the $n = 52$ manifold with a σ^+ polarized radio-frequency field. The circularization with a resonant Rabi π pulse has the advantage to be very fast. However, due to the non-hydrogen-like behaviour of the $m = 0$ and $m = 1$ states of the lowest diagonal, we know that the states with $m = 2$, $m = 3$ up to the circular state behave like an angular momentum on a truncated generalized Bloch sphere, for which the two lowest levels are missing. Therefore, a Rabi pulse applied when the atom is in the Dicke state $m = 2$ state never transfers the $m = 2$ state into the circular states with 100% probability. In fact, due to the large amplitude of the radio-frequency field, the $m = 1$ state is slightly populated during the evolution. We know from chapter 3 (see Sec. 3.3.1) that we cannot transfer the circular state into a single Dicke state with 100% efficiency, even for the largest applied radio-frequency field power. The atom is always in a coherent superposition involving different m states (see Fig. 3.12c). If it is not possible to transfer the circular state into the $m = 2$ state, the time reversal symmetry imposes that it is not possible to transfer the $m = 2$ state into the circular state. However, we can use the time reversal symmetry to optimize the transfer to the circular state.

We label $|\psi_a\rangle$ the state we obtain after applying a radio-frequency pulse of duration t_{rf} on the atom initially in the circular state. If we were able to prepare the conjugate state $|\psi_a\rangle^*$, we could transfer $|\psi_a\rangle^*$ into the circular state with 100% probability.

To improve the efficiency of the preparation of the circular state, we use a sequence of two radio-frequency pulses separated by a waiting time t_{delay} to transfer the atom from the $m = 2$ to the circular state. The idea of the method is illustrated in Fig. 5.4. Fig. 5.4a presents the population of the state $|\psi_a\rangle$ for $t_{\text{rf}} = 98$ ns and $\Omega_{\text{rf}} = 2\pi \cdot 4.5$ MHz. We compare it to the state $|\psi_b\rangle$ of the atom initially in the $m = 2$ state, on which is applied a 3 ns radio-frequency pulse (see Fig. 5.4b). We see that the distribution of probability is qualitatively similar at least for $m = 1$ and $m = 2$. However, we observe a difference in phase between the components of states $|\psi_a\rangle^*$ (prepared from the circular state) and $|\psi_b\rangle$ (black and blue vectors in Fig. 5.4c). The phase of the components with $m \geq 2$ of $|\psi_b\rangle$ evolve in the rotating frame, since their transition frequencies are very close to the one of the radio-frequency. However, the phase of the $m = 1$ level, whose transition frequency is detuned from the radio-frequency by ~50 MHz (see Sec. 1.2.3), evolves very fast. It is therefore possible to improve the overlap between the state of the atom and $|\psi_a\rangle^*$ by tuning the delay t_{delay} (red and blue vectors in Fig. 5.4c).

By optimizing the duration of the first pulse and the duration of the waiting time, it is possible to gain up to nearly 10% in the transfer probability, reaching a transfer of about 80% for $|+52c\rangle$ and $|-50c\rangle$.

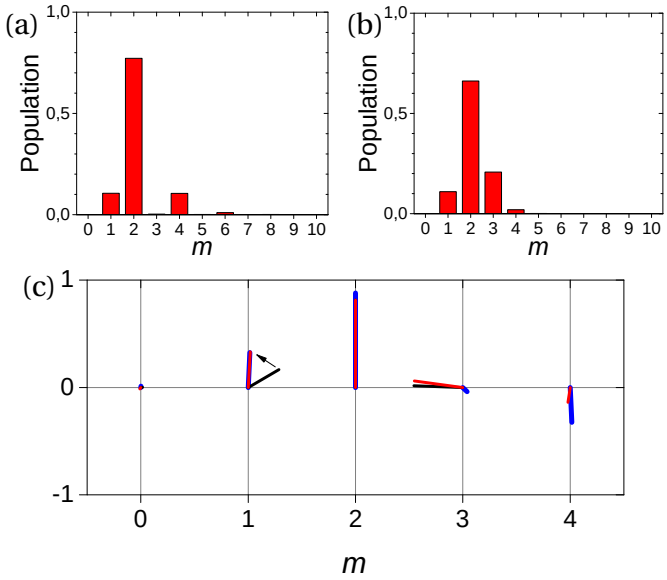

Figure 5.4: (a) The population of the m-levels of the state $|\psi_a\rangle$ prepared from the circular state $|+52c\rangle$ by a radio-frequency pulse with $\Omega_{rf} = 2\pi \cdot 4.5$ MHz and duration $t_{rf} = 98$ ns. (b) The population of the m-levels of the state $|\psi_b\rangle$ prepared from the $m = 2$ state by a radio-frequency pulse duration $t_{rf} = 3$ ns (and same Ω_{rf}). (c) The vector describing the probability amplitude in the complex plane for each m-level: the conjugate $|\psi_a\rangle^*$ of the state $|\psi_a\rangle$ prepared from the circular state (blue), the state $|\psi_b\rangle$ prepared from the $m = 2$ state after 0 ns (black) and the same state after 3 ns waiting time (red). The population of the $|\psi_b\rangle$ in the $m = 1$ levels accumulates a phase with respect to the $m = 2$ state which brings the state $|\psi_b\rangle$ closer to $|\psi_a\rangle^*$ (the red and blue vector for $m = 1$ and $m = 2$ now overlap).

Fig. 5.5 shows the probability to find the atom in the circular state $|52c\rangle$ as a function of the total duration of the σ^+ polarized radio-frequency pulse. We find that when a single radio-frequency pulse is applied, the atom is transferred into the $|+52c\rangle$ state with a maximum probability of ~74%. In the case of a multiple radio-frequency pulse, we find that for a first short radio-frequency pulse of 3 ns, a waiting time of 3 ns and a second radio-frequency pulse of 98 ns, the maximum probability is now 79%.

Fig. 5.6 shows the combination of all radio-frequency and microwave pulses needed in order to prepare the superposition of opposite circular states $|+52c\rangle$ and $|-50c\rangle$.

5.1.3.b Circular to circular transition via radio-frequency dressing

In a last step, the part of the wave-function in the $|-50c\rangle$ state has to be transferred to the $|-52c\rangle$ state (see step (6) in Fig. 5.1) by a two-photon microwave π pulse. However, since the transition frequencies between $|-50c\rangle \rightarrow |-52c\rangle$ and $|+52c\rangle \rightarrow |+50c\rangle$ are the same, and since we are not able to control the polarization of the microwave field, the two-photon microwave pulse would also transfer a part of the population of the $|+52c\rangle$ state. In order to avoid this, we carefully shift the transition frequencies with respect to each other, as depicted in Fig. 5.7. We use the σ^+ polarized radio-frequency field to

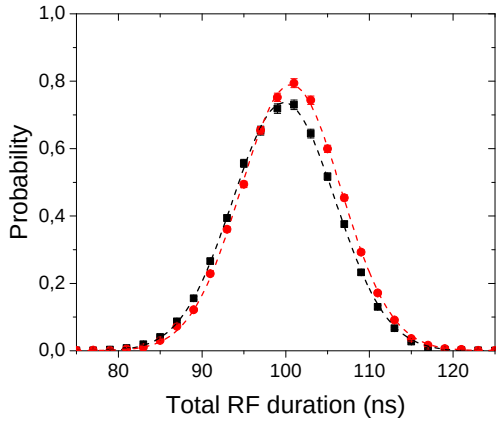

Figure 5.5: The probability to find the atom in the circular state by applying a single radio-frequency pulse (black) and by applying a first, preparatory, radio-frequency pulse of 3 ns, wait for 3 ns and second long pulse, which then transfers the low-m state to the circular state (red).

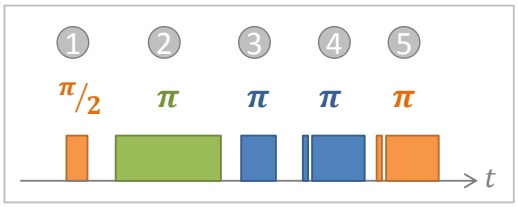

Figure 5.6: The combination of all pulses needed in order to prepare the superposition of the opposite circular states $|+52c\rangle$ *and* $|-50c\rangle$*. The numbers correspond to the ones in Fig. 5.1: (1) radio-frequency* $\pi/2$ *pulse from* $|52,+2\rangle$ *to* $|52,0''\rangle$*, (2) microwave* π *pulse from* $|52,0''\rangle$ *from* $|50,0''\rangle$*, (3) radio-frequency* π *pulse from* $|50,0''\rangle$ *to* $|50,-2\rangle$*, (4) multiple Rabi* π *pulse from* $|50,-2\rangle$ *to* $|-50c\rangle$*, (5) multiple Rabi* π *pulse from* $|52,+2\rangle$ *to* $|+52c\rangle$*.*

induce a different *AC-Stark shift* [184] on the two transitions.

To this end, we increase the electric field to detune the frequency of the σ^+ polarized radio-frequency field from the transitions $|+52c\rangle - |+52e1\rangle$ and $|-52c\rangle - |-52e1'\rangle$ by δ ~+5 MHz. In the presence of the σ^+ polarized radio-frequency field, the $|-52c\rangle$ is shifted to lower energies, whereas the $|+52c\rangle$ state is shifted to higher energies by $\sim 51\Omega_{\mathrm{rf}}^2/(4\delta^2)$. At the same time, the transitions $|+50c\rangle - |+50e1\rangle$ and $|-50c\rangle - |-50e1'\rangle$ are detuned by δ ~-5 MHz with respect to the radio-frequency field, leading to a shift to a higher energy of the $|-50c\rangle$ and to lower energy of the $|+50c\rangle$ state. As a result, the transition frequencies between $|-50c\rangle \rightarrow |-52c\rangle$ and $|+52c\rangle \rightarrow |+50c\rangle$ are shifted with respect to each other, allowing us to selectively transfer the $|-50c\rangle$ state to the $|-52c\rangle$ state.

To ensure that the circular states connect to the states shifted by the radio-frequency field, we adiabatically ramp up in 300 ns the σ^+ polarized radio-frequency field, sketched in step (6) in Fig. 5.7. We then apply the two-photon microwave π pulse, resonant with the shifted $|-50c\rangle \rightarrow |-52c\rangle$ transition, before adiabatically ramping down the radio-frequency field.

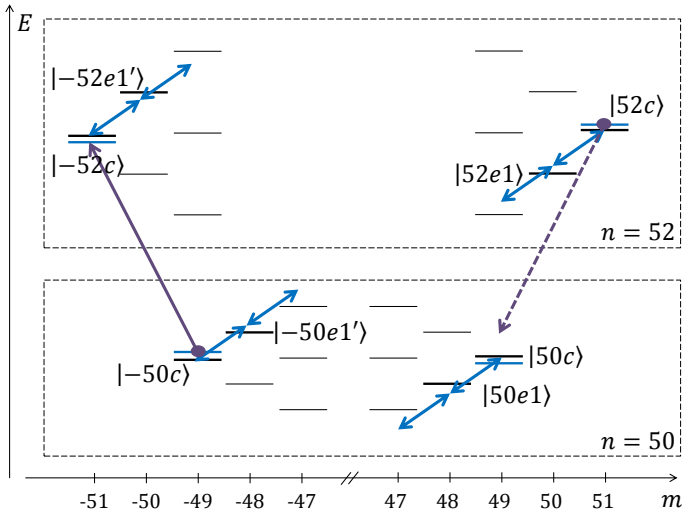

Figure 5.7: The involved levels and transitions for the last step in the preparation process (see step (6) in Fig. 5.1) for the superposition of the states $|+52c\rangle$ and $|-52c\rangle$. The radio-frequency dressing field (blue) is detuned by ~+5 MHz in the $n = 52$ manifold and by ~-5 MHz in the $n = 50$ manifold. This leads to a shift in the circular levels (resulting levels in blue) big enough to be resolved by the microwave pulse (violet). We are then able to drive the $|-50c\rangle \rightarrow |-52c\rangle$ transition (violet full line) and not the $|+52c\rangle \rightarrow |+50c\rangle$ transition (violet dashed line).

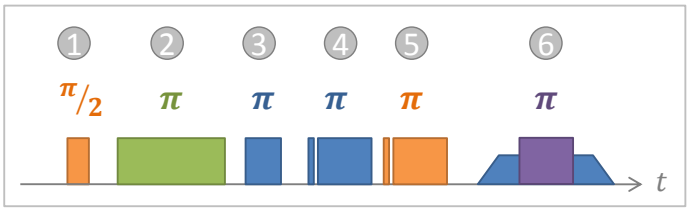

Figure 5.8: The combination of all pulses needed in order to prepare the superposition of the opposite circular states $|+52c\rangle$ and $|-52c\rangle$. The numbers correspond to the ones in Fig. 5.1: (1) to (5) are the same as in Fig. 5.6, (6) microwave π pulse in the presence of a dressing radio-frequency field (ramped up and down adiabatically) from $|-50c\rangle$ to $|-52c\rangle$.

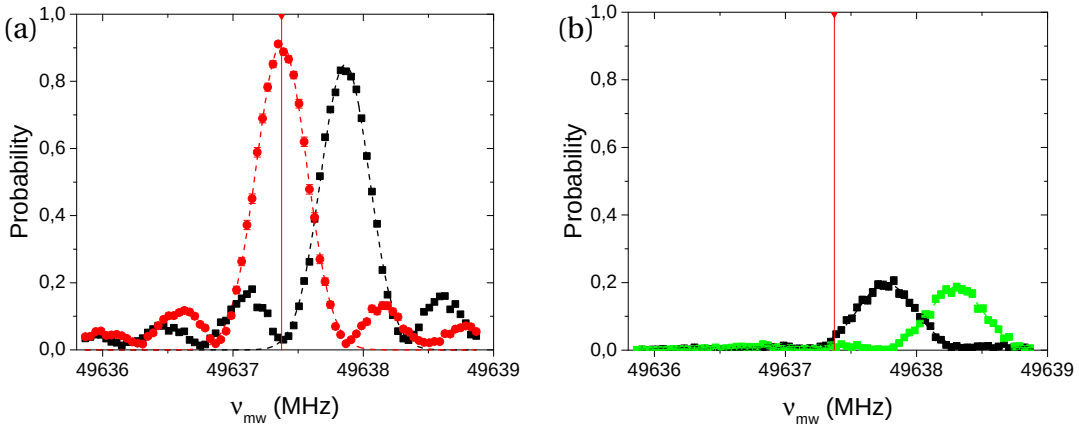

Figure 5.9: (a) Microwave spectroscopy of the $|-50c\rangle \rightarrow |-52c\rangle$ *transition with radio-frequency dressing (red) and without (black). (b) Microwave spectroscopy in the same conditions of the* $|+52c\rangle \rightarrow |+50c\rangle$ *transition with radio-frequency dressing (green) and without (black). The Gaussian-fitted (dashed lines) transition frequency of* $|-50c\rangle \rightarrow |-52c\rangle$ *transition with radio-frequency dressing is indicated as a red vertical line in both figures. The transfer presented is shown as a function of the driving microwave frequency, which is two-times smaller than the* $|52c\rangle - |50c\rangle$ *transition frequency since we drive a two-photon transition.*

Fig. 5.9a shows the microwave spectroscopy of the transition $|-50c\rangle \rightarrow |-52c\rangle$ with radio-frequency dressing, in comparison we also show the same spectroscopy without applied radio-frequency field. The radio-frequency dressing ($\Omega_{\mathrm{rf}} = 2\pi \cdot 0.38$ MHz) shifts the transition frequency by ~980 kHz towards smaller frequencies. Fig. 5.9b shows the microwave spectroscopy of the transition $|+52c\rangle \rightarrow |+50c\rangle$, with and without radio-frequency dressing. Here, the radio-frequency dressing shifts the transition frequency to higher frequencies, by ~1060 kHz. Fig. 5.9a and Fig. 5.9b are recorded in the same conditions (microwave power and pulse duration). We observe that the transition probability is smaller in Fig. 5.9b than in Fig. 5.9a. This is due to the standing wave structure of the microwave modes in the experimental zone. At the moment of the microwave pulse, the microwave field has a much larger σ^+ than σ^- component. We also see that, in the presence of the radio-frequency dressing, the probability to transfer the $|+52c\rangle$ to the $|+50c\rangle$ state is almost zero at the frequency of the dressed $|-50c\rangle \rightarrow |-52c\rangle$ transition (see red vertical line in Fig. 5.9b).

We conclude that we transfer the population of the $|-50c\rangle$ state with a probability over 90% into the $|-52c\rangle$ state, while leaving the $|+52c\rangle$ state unaffected.

5.1.4 The superposition of opposite circular states

To have an idea about the coherence of the superposition we need to vary the phase of the interferometer. The complete sequence in Fig. 5.10a amounts to a complex Ramsey interferometer with two branches. The first $\pi/2$ pulse separates the wave-function in two parts which each follow a different branch of the interferometer. The part of the

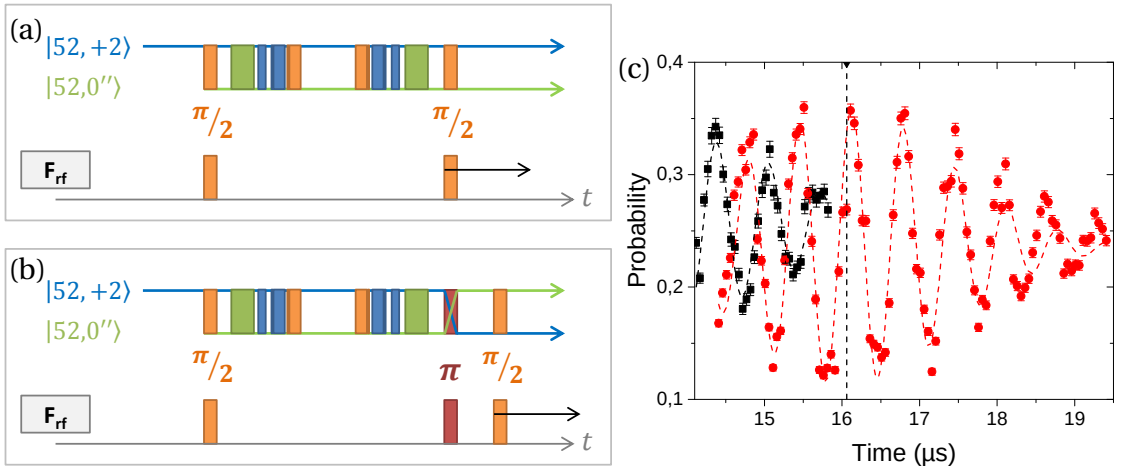

Figure 5.10: (a) The atom, initially in the $|52,+2\rangle$ *state (blue), is prepared in a superposition of the* $|52,+2\rangle$ *and the* $|52,0''\rangle$ *state (green) by a first* $\pi/2$ *pulse (blue). The superposition then undergoes several steps to the superposition of opposite circular states and back. The second* $\pi/2$ *pulse (orange) is scanned over time. (b) In the same sequence as in (a) we add a* π *pulse (red) at* $t = 14.32$ *μs which exchanges the population between the* $|52,+2\rangle$ *and the* $|52,0''\rangle$ *state. The second* $\pi/2$ *pulse is scanned over time. (c) The Ramsey fringes of (a) without echo pulse (black) and (b) with echo pulse (red) as a function of the timing of the second* $\pi/2$ *pulse. In the echo sequence, the maximum contrast is reached 1.65 μs after the echo* π *pulse (vertical dashed line).*

wave-function in $|52,+2\rangle$ is transferred to the circular state $|+52c\rangle$ and back. The part of the wave-function in $|52,0''\rangle$ goes into the circular $|-52c\rangle$ state through the states $|50,0''\rangle$, $|50,-2\rangle$, and $|-50c\rangle$ and back. Finally, the last $\pi/2$ pulse recombines the two parts of the wave-function. The outcome of the interferometer depends on the relative phase accumulated by each branch.

5.1.4.a Application of echo-techniques

At first, to observe the interference fringes, we choose to vary the time at which we apply the final $\pi/2$ pulse. This induces an additional delay, shown in Fig. 5.10a. Because of the small detuning between the $|52,+2\rangle$ and the $|52,0''\rangle$ transition frequency and the radio-frequency, the relative phase between the two branches evolves during this additional delay. This leads to oscillations in the probability to detect the atom in the $|52,+2\rangle$ state, the contrast of which measures the coherence of the superposition.

The black curve in Fig. 5.10c presents the result of this experiment. We clearly see that the contrast decays very fast on a time scale of 1.64 μs. This is due to the electric field noise to which the superposition of $|52,+2\rangle$ and $|52,0''\rangle$ is very sensitive and which induces a dispersion of the relative phase. However, we find in Sec. 4.5 that this noise has a correlation time of $t_{\mathrm{corr}} = 2.01$ μs. Therefore, it is possible to compensate for a part of the amplitude reduction by using an echo π pulse [123], shown in Fig. 5.10b. Instead of immediately applying a $\pi/2$ pulse, we insert a π pulse which exchanges the

population between the $|52,+2\rangle$ and the $|52,0''\rangle$ state. This π pulse inverts the roles of the two branches. The relative phase of the quantum superposition has now the opposite sensitivity to the electric field reducing the global sensitivity of the superposition to the electric field noise: the phase accumulated by the superposition between the π and the $\pi/2$ pulse partially cancels the phase induced by the noise before the π pulse.

The red curve in Fig. 5.10c presents the result of the experiment in which we apply a π pulse and we vary the time of the $\pi/2$ pulse. We observe that the contrast first increases as we increase the delay between the two pulses. The maximum occurs at a delay consistent with the correlation time of the noise that we measured before. For a delay larger than 2 μs the noise seen by the atom is uncorrelated to the noise the atom has seen before the π pulse and the contrast decrease again.

We also add an echo pulse to the first $\pi/2$ pulse at the beginning of the sequence. The echo of the first $\pi/2$ pulse compensates the noise at the beginning of the sequence, while the echo of the second $\pi/2$ pulse compensates the noise at the end of the sequence. After optimization we find that the best contrast is obtained for the same ~400 ns delay between the $\pi/2$ pulse and the π pulse at the beginning and at the end of the sequence.

5.1.4.b Direct detection of the opposite circular states

The state of the atom is read out by ionization (see Sec. 2.2.3). In Fig. 5.11, the red signal is the ionization signal of the superposition of $|+52c\rangle + |-52c\rangle$. The peak at −45V corresponds to the ionization threshold of the $n = 52$ circular states. The blue signal corresponds to the ionization signal of the state $|+52c\rangle + |-50c\rangle$ obtained just before the (6) pulse. The difference in height at the ionization threshold of the $|\pm 52c\rangle$ state (at −45V) between the red peak and the blue peak directly gives the number of atoms in the $|-52c\rangle$ state. Finally, the grey signal is obtained after we have transferred the population of the $|-50c\rangle$ into the $|-49c\rangle$ state, and the $|+52c\rangle$ into the $|+50c\rangle$ state. The residual population at the ionization threshold of −45V corresponds to atoms in the blue and red signal which are neither in the $|+52c\rangle$ nor in the $|-52c\rangle$ state, but ionize at the same threshold. The difference between the blue and the grey signal thus gives us the population of the $|+52c\rangle$ state in the superposition.

We find 0.40 atoms/curve in the $|-52c\rangle$ state and 0.53 atoms/curve in the $|+52c\rangle$. The superposition is a bit unbalanced with 43% in the $|-52c\rangle$ and 57% in the $|+52c\rangle$ state. In these curve we prepare on average 1.54 atomes/curve. The efficiency to prepare the superposition, defined as the number of atoms in the $|+52c\rangle$ and $|-52c\rangle$ levels divided by the total number of atoms, is therefore ~60%.

5.1.4.c Coherence of the opposite circular states

We now scan the relative phase between the two parts of the wave-function by varying the microwave frequency of the two-photon microwave π pulses which drive the $|52,0''\rangle$

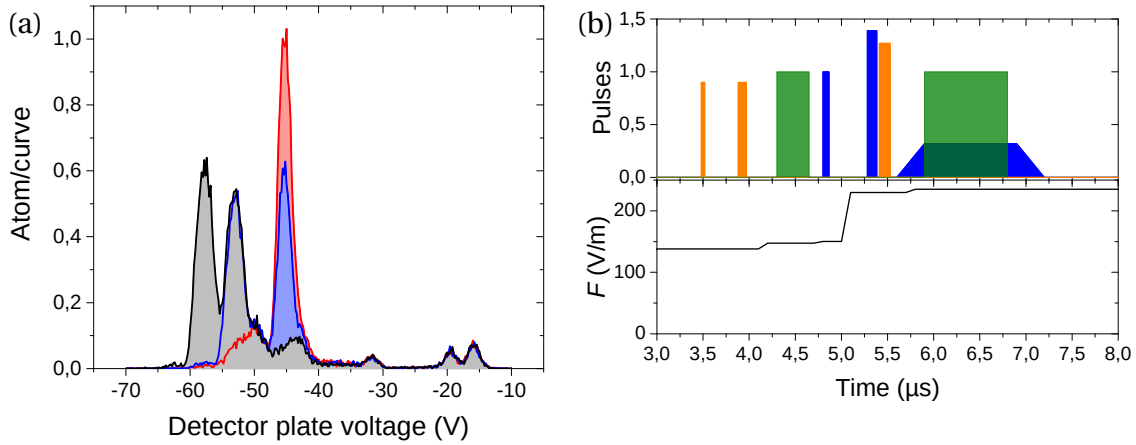

Figure 5.11: (a) Ionization signal of different superpositions of opposite circular states: $|+52c\rangle$ and $|-52c\rangle$ (red), $|+52c\rangle$ and $|-50c\rangle$ (blue), and $|+50c\rangle$ and $|-49c\rangle$ (black). For the latter, the population of the $|-50c\rangle$ state is transferred into the $|-49c\rangle$ state and the population of the $|+52c\rangle$ into the $|+50c\rangle$ state. The small peaks on the right side of the ionization signal corresponds to the residual population in the low-m levels of the $n = 52$ and $n = 50$ manifold. (b) The timing of the pulses: radio-frequency σ^- (orange), radio-frequency σ^+ (blue), microwave (green), electric field (black).

to $|50,0''\rangle$ transition with [179]

$$|52,0''\rangle \rightarrow e^{i\phi_{\mathrm{mw}}}|50,0''\rangle \quad \text{and} \quad |50,0''\rangle \rightarrow e^{-i\phi_{\mathrm{mw}}}|52,0''\rangle,$$

where the accumulated phase $\phi_{\mathrm{mw}} = 2\pi\nu_{\mathrm{mw}}\Delta t$ depends on the delay Δt, fixed to about 20.5 μs, between the microwave pulses and on the relative frequency ν_{mw}.

Fig. 5.12 shows the Ramsey fringes as a function of the relative microwave frequency ν_{mw}. The visibility, a measure of coherence of the branches of an interferometer, is given by,

$$s = \frac{P_{\mathrm{max}} - P_{\mathrm{min}}}{P_{\mathrm{max}} + P_{\mathrm{min}}},$$

where P_{max} and P_{min} are the maximum and minimum, respectively, of the measured probability of the interference signal. From the Ramsey fringes in Fig. 5.12, we find a visibility of $s = (50 \pm 1)\%$, which shows the high degree of coherence of the superposition and sets a lower bound of the fidelity of the preparation of the superposition of the opposite circular states.

5.1.4.d Sensitivity to electric field fluctuations

To study the sensitivity of the superposition to the electric field, we vary an electric field square pulse through the sequence, shown in Fig. 5.13, similar to the bandwidth assessment of the correlation experience (Sec. 4.3.2.a). We alternate a realization where the electric field pulse is applied from time t_{trig} and a realization without the electric field pulse. Because of the electric field step, the superposition accumulates a difference in

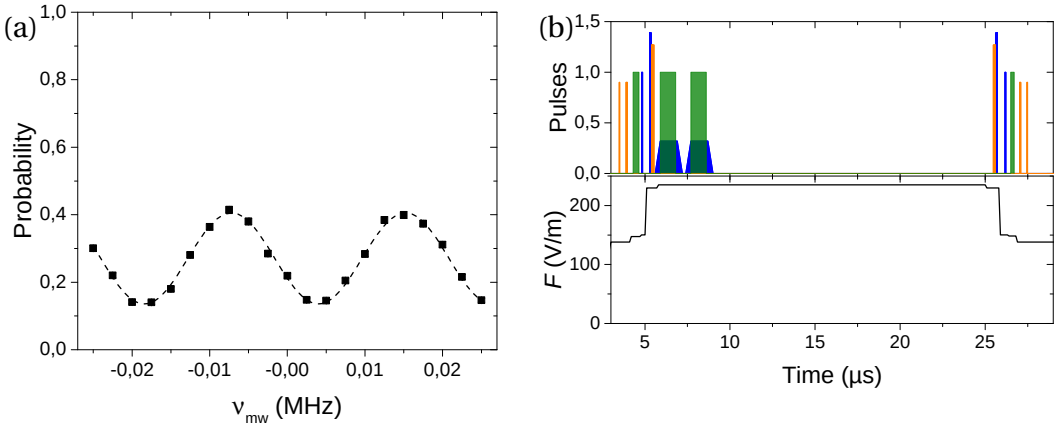

Figure 5.12: (a) The microwave Ramsey fringes of the superposition of $|+52c\rangle$ *and* $|-52c\rangle$ *as a function of the relative microwave frequency* ν_{mw}*. The fringes are recorded with a delay of* $\tau_2 = 19.942$ *μs between the circularization pulses. The state is in a superposition of* $|+52c\rangle$ *and* $|-52c\rangle$ *at* $t = 7.3$ *μs. The contrast of the signal, that oscillates around* $P_0 = (27.0 \pm 0.2)\,\%$*, is* $C = (27.0 \pm 0.6)\,\%$*. (b) The timing of the pulses: radio-frequency* σ^- *(orange), radio-frequency* σ^+ *(blue), microwave (green), electric field (black).*

phase $\Delta\Phi$ between the two realizations (with and without the electric field step) depending on the integral of the differential Stark shift between the two branches from the time t_{trig} to the end of the sequence.

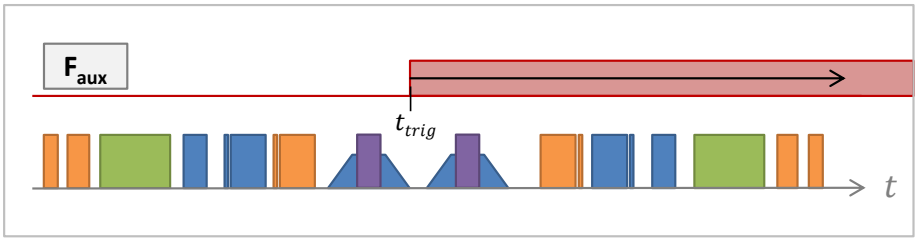

Figure 5.13: The experimental sequence to measure the sensitivity of the superposition to the electric field.

The difference in phase $\Delta\Phi$ can be measured in the linear regime of the microwave Ramsey fringes. We fix the microwave frequency at the point of maximum slope as indicated in Fig. 5.14 and measure the probability to detect the atom in the $|52,+2\rangle$ state with and without the electric field step. The difference in probability $\Delta P \approx \frac{C}{2}\Delta\Phi$ is in first order proportional to the difference in phase $\Delta\Phi$. Fig. 5.15a presents the value of ΔP as a function of the time t_{trig} of the pulse which triggers the electric field step.

The sensitivity of the relative phase Φ to the electric field varies as a function of time, as we transfer the atom from one state to the other. Fig. 5.16a presents the sensitivity to the electric field for each branch of the superposition, obtained by calculating for each time t the variation of the Stark energy of the state of the atom induced by a variation of the electric field. The bottom part, Fig. 5.16b, shows the corresponding sequence of the microwave and radio-frequency pulses. The differential Stark shift between the two components of the superposition, the difference between the red and the black curve in

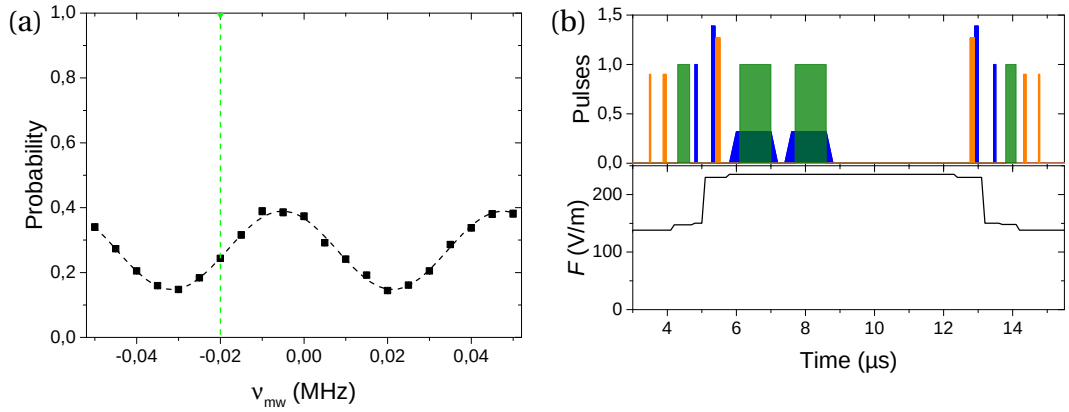

Figure 5.14: (a) The microwave Ramsey fringes as a function of the relative microwave frequency ν_{mw}. The position of the point of maximum slope is marked by the green vertical line. (b) The timing of the pulses: radio-frequency σ^- (orange), radio-frequency σ^+ (blue), microwave (green), electric field (black).

Fig. 5.16a, is most pronounced for low-m states. As soon as the state of the atom reaches the superposition of circular states, the differential Stark shift is reduced to zero in first order.

The very interesting feature of our method of preparation is that the sensitivity to the electric field of the superposition between $t = 3.83$ μs and $t = 5.28$ μs, when the atom is in the low-m state, is compensated by the sensitivity of the superposition to the electric field when the $|52,+2\rangle$ state has been transferred into the $|+52c\rangle$ state, but the other part of the wave-function is still in a low-m state of the $n = 50$ manifold (Fig. 5.16). As a result, the phase accumulated between $t = 3.83$ μs and $t = 5.28$ μs in Fig. 5.15 is cancelled by the phase accumulated between $t = 5.28$ μs and $t = 5.53$ μs, making the state globally less sensitive to fluctuations of the electric field. This is the reason why we chose to transfer $|52,+2\rangle \rightarrow |+52c\rangle$ before transferring $|50,-2\rangle \rightarrow |-50c\rangle$. The same effect occurs around $t \approx 14$ μs. The fact that the compensation is not perfect is corrected by the spin echo before and after the sequence.[2] The measured value of $\Delta\Phi$ is in good agreement with the simulation (solid line Fig. 5.15a) from the calculated energy (see Fig. 5.16a).

5.1.4.e Superposition of opposite circular states in different manifolds

The states $|+52c\rangle$ and $|-52c\rangle$ have exactly the same Stark shifts to all orders, making them completely insensitive to electric field variations. However, from Fig. 5.15 we can also see that the superposition of $|+52c\rangle$ and $|-50c\rangle$ is already very insensitive to the electric field.

Fig. 5.17 shows the Ramsey interference fringes of the sequence where the state of the

[2] The duration of the time interval between $t = 3.83$ μs and $t = 5.28$ μs is not negligible with respect to the correlation time. As a result, random phase accumulated by the atom at the beginning of this time interval cannot be completely compensated by the phase accumulated between $t = 5.28$ μs and $t = 5.53$ μs. The echo pulse very likely helps to compensate for the noise seen by the atom at the beginning of the interval between $t = 3.83$ μs and $t = 5.28$ μs.

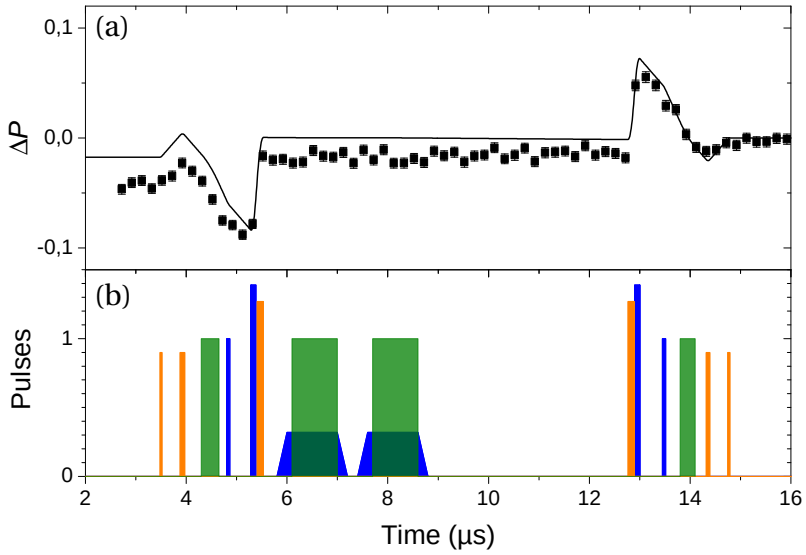

Figure 5.15: (a)The probability to detect the atom in the $|52,+2\rangle$ *state with and without the applied electric field pulse are measured as a function of the trigger time* t_{trig} *of the electric field step and are subtracted, leading to the relative probability* ΔP*. (b) The timing of the pulses: radio-frequency* σ^- *(orange), radio-frequency* σ^+ *(blue), microwave (green).*

atom is in the superposition of $|+52c\rangle$ and $|-50c\rangle$ for $\tau_2 = 19.942\ \mu$s. We find a visibility of $s = (66.8 \pm 0.6)\%$, which is higher than the visibility of the sequence where the state passes through the superposition of $|+52c\rangle$ and $|-52c\rangle$. It seems that the microwave pulse which transfers the state to and from the $|-52c\rangle$ state leads to a reduced contrast of ~4.5%. However, using the $|-50c\rangle$ instead of the $|-52c\rangle$ state reduces the difference in magnetic quantum number from $\Delta m = 102$ to $\Delta m = 100$, corresponding to ~2%. Additionally, we find that we cannot increase the delay between the two pulses which brings the $|-50c\rangle$ in the $|-52c\rangle$ and back, due to the standing wave structure of the microwave field. Overall, we choose to use the superposition of $|+52c\rangle$ and $|-50c\rangle$ to perform the magnetometry measurement.

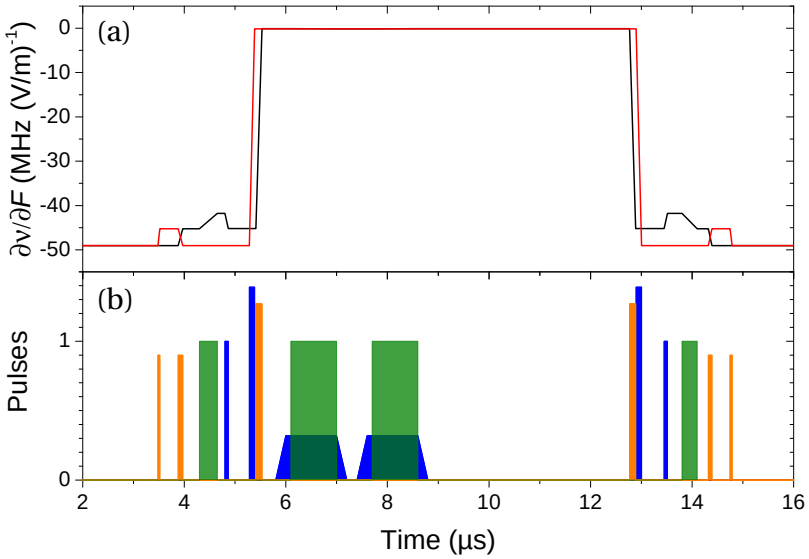

Figure 5.16: (a) Stark shift of the two components of the superposition. For low-m states, the Stark shift is significant, whereas for circular states, the relative Stark shift is almost zero. (b) The timing of the pulses: radio-frequency σ^- (orange), radio-frequency σ^+ (blue), microwave (green).

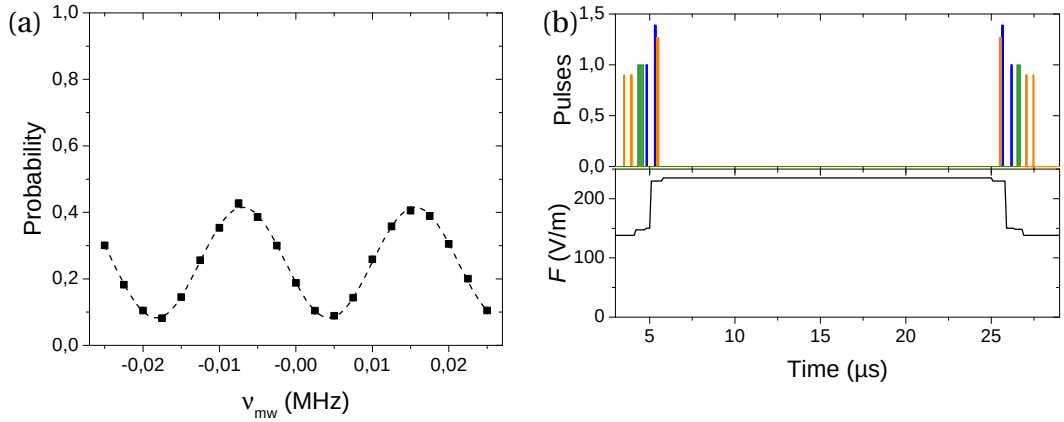

Figure 5.17: (a) The microwave Ramsey fringes of the superposition of $|+52c\rangle$ and $|-50c\rangle$ as a function of the relative microwave frequency ν_{mw}. The state is in the superposition of $|+52c\rangle$ and $|-50c\rangle$ for $\tau_2 = 19.942$ µs. The contrast of the signal, that oscillates around $P_0 = (24.9 \pm 0.1)\,\%$, is $C = (33.2 \pm 0.3)\,\%$. (b) The timing of the pulses: radio-frequency σ^- (orange), radio-frequency σ^+ (blue), microwave (green), electric field (black).

5.2 Magnetic field measurement

5.2.1 The magnetic field coils

To characterizes the influence of the magnetic field on the opposite circular states superposition we need to be able to apply a magnetic field. We therefore installed superconducting coils around the experimental zone, shown in Fig. 5.18. The coil consists in a superconducting wire with 254 μm bare diameter and is installed on the upper and lower edge of the two sapphire plates which hold the capacitor plates of the experimental zone. We can see on the picture in Fig. 5.18b, that the material was maximally removed in the copper plane electrodes to reduce eddy currents which would counteract the switching of the magnetic field. The radius of the coil is ~9 cm and the distance between the upper and the lower loops is ~8.5 cm. We use the same superconducting wire for all four turns.

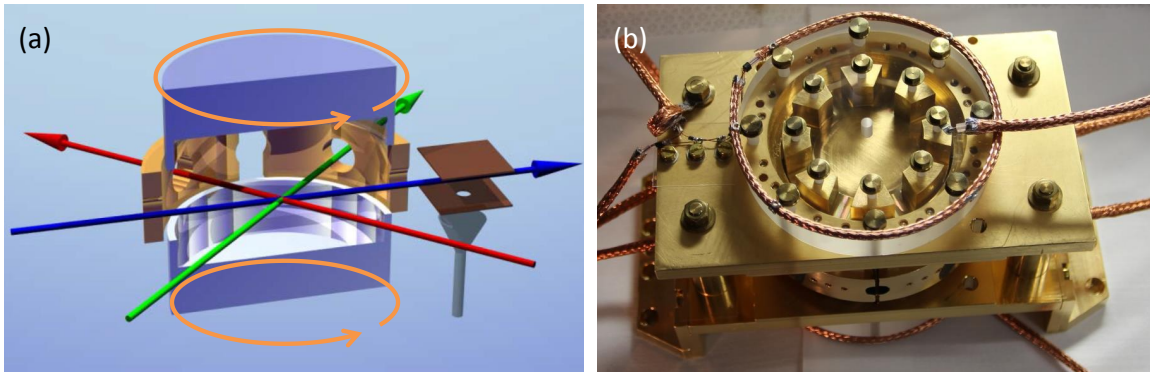

Figure 5.18: (a) The magnetic field coil (orange) in the sketch of the experiment. (b) Picture of the electrode structure of the experimental zone. The magnetic field coils are wrapped around the far edges of the sapphire plates.

The magnetic field created by a current I in the two coils of radius R and n loops separated by a distance D is calculated by the Biot-Savart law along the coil axis z as

$$B(z) = \frac{1}{2}\mu_0 nIR^2 \left[\left(R^2 + \left(z - \frac{D}{2} \right)^2 \right)^{-\frac{3}{2}} + \left(R^2 + \left(z - \frac{D}{2} \right)^2 \right)^{-\frac{3}{2}} \right],$$

where μ_0 is the permeability constant. Since this does not correspond to a Helmholtz configuration we do not have a flat maximum halfway between the two double-loops but rather a local minimum in the center of the experimental zone, with a magnetic field of $B = 215$ μG for an applied current of $I = 1$ mA, as shown in Fig. 5.19.

However, the size of the atomic packet defined by the intersection of the two laser beams of about 0.5 mm^3 is very small in comparison to the dimension of the local minimum and the magnetic field can therefore be assumed homogeneous at the relevant length scale.

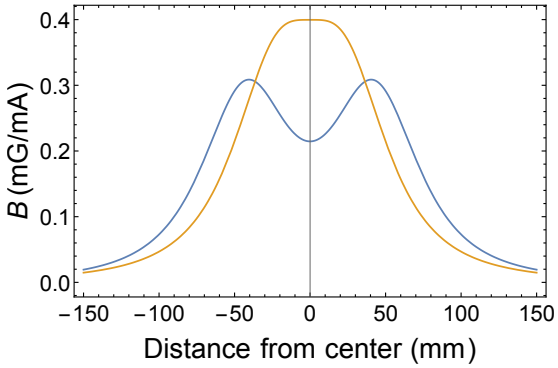

Figure 5.19: The magnetic field as a function of the distance from the center of the experimental zone along the axis of the magnetic field coils for the ideal Helmholtz setting (yellow) and the real setting (blue).

5.2.2 Calibration of the magnetic field

We calibrate the magnetic field by using the superposition of the two circular states $|+52c\rangle$ and $|+50c\rangle$. The phase of the Ramsey fringes of this superposition is shifted by the applied magnetic field. Fig. 5.20 shows the absolute phase of these Ramsey fringes as a function of the magnetic field we apply. We find a conversion factor between the applied current and the magnetic field of $\Delta B/\Delta I = (203 \pm 7)\ \mu$G/mA.

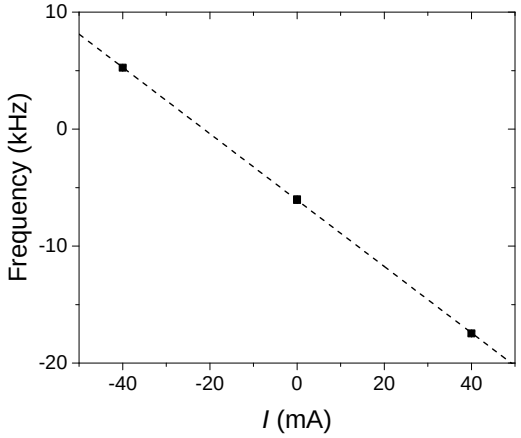

Figure 5.20: Calibration curve of the magnetic field by employing the superposition of the two circular states $|+52c\rangle$ and $|+50c\rangle$. The frequency shift of the Ramsey fringes is shown as a function of the applied current through the magnetic field coils.

5.2.3 Measurement of the magnetic field

5.2.3.a Sensitivity of the magnetometer

The sensitivity of the quantum superposition of the two opposite circular state $|+52c\rangle$ and $|-50c\rangle$ can be assessed by recording Ramsey fringes, described in Sec. 5.1.4, for different

amplitudes of the applied magnetic field. The sensitivity of a single-shot measurement is given by

$$\sigma_B^{(1)} = \sigma_P \left(\frac{\partial P}{\partial B}\right)^{-1} = \sigma_P \left(\frac{\partial P}{\partial \Phi}\right)^{-1} \left(\frac{\partial \Phi}{\partial B}\right)^{-1}, \tag{5.1}$$

where $\sigma_P = 1/2$ is the standard deviation of an atomic state detection[3], where the term $(\partial P/\partial\Phi) = C/2$ takes into account the contrast of the Ramsey fringes and where $(\partial\Phi/\partial B)$ is the accumulated quantum phase as a function of the magnetic field.

Fig. 5.21a shows the probability of detecting the atom in the $|52,+2\rangle$ state after the full Ramsey sequence during which the atom is in a superposition of the two opposite circular states for $\tau_1 = 7.237$ μs. Fig. 5.21b shows Ramsey fringes of a sequence where the atom in the state of opposite circular levels, for a significantly longer time $\tau_2 = 19.942$ μs.

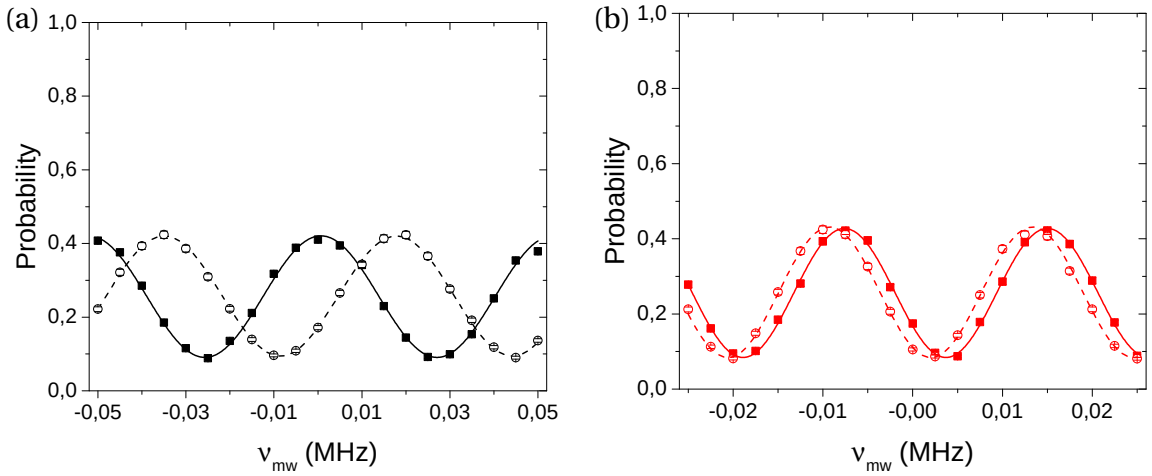

Figure 5.21: (a) Probability of detecting the atom in the $|52,+2\rangle$ state after the full Ramsey sequence, where the atom is in a superposition of the two opposite circular states for $\tau = 7.237$ μs, is shown as a function of the microwave frequency ν_{mw} for $B = 0$ μG (full) and $B = -324$ μG (hollow) together with the respective sine-fit. (b) Same as (a): Here, the atom is in a superposition of the opposite circular states for $\tau = 19.942$ μs for $B = 0$ μG (full) and $B = -324$ μG (hollow), shown together with the respective sine-fit. Note that the interference fringes are shifted by almost 2π with respect to each other.

The curves in Fig. 5.21 are fitted by a sine function to deduce their contrast C and their phase Φ for different values of the magnetic field B. Fig. 5.22 presents the phase as a function of the applied magnetic field. We see that the slope is much steeper for a longer interrogation time τ. In principle, the slope follows

$$\frac{\Delta\Phi}{\Delta B} = \frac{2\pi\mu_B \tau \Delta m}{h}.$$

When we compare the fitted slope with the expected value, we find that the difference in the magnetic quantum number m, the only free parameter, does not match exactly the expected $\Delta m = 100$. For the interrogation times of τ_1 and τ_2, we find $\Delta m = 106.8 \pm 4.7$

[3] We neglect the fact that the fringes oscillate around $P \approx 0.25$ and therefore $\sqrt{P(1-P)} \approx \sqrt{3}/4 < 1/2$.

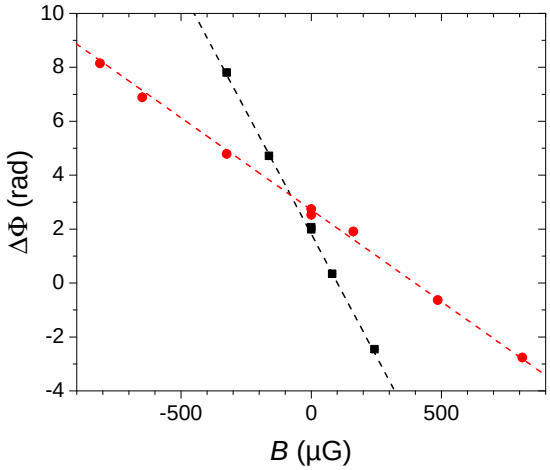

Figure 5.22: The accumulated quantum phase as a function of the applied magnetic field for a superposition of opposite circular states for a time $\tau = 7.237$ μs (red) and $\tau = 19.942$ μs (black).

and $\Delta m = 103.5 \pm 4.8$ respectively. This is probably due to the magnetic field dependent phase accumulated by the superposition while it is in the low-m states at the beginning and at the send of the sequence. However, when we take the difference in slope (of the red an black line in Fig. 5.22), this corresponds to the relative phase accumulated by the superposition during a time $\tau = 19.942 - 7.237 = 12.705$ μs. In this case we find a difference in magnetic quantum number

$$\Delta m_{cc} = 101.6 \pm 6.5. \tag{5.2}$$

The sensitivity of our method is calculated as (Eq. 5.1)

$$\sigma_B^{(1)} = \frac{1}{2}\left(\frac{C}{2}\right)^{-1}\left(\frac{\Delta\Phi}{\Delta B}\right)^{-1} = \frac{1}{C}\left(\frac{\Delta\Phi}{\Delta B}\right)^{-1} \tag{5.3}$$

where $(\Delta\Phi/\Delta B)$ is fitted from the slopes in Fig. 5.22 and the contrast C from the Ramsey fringes in Fig. 5.21. We find a contrast of C=(32.7 ± 0.7)% for τ_1 and C=(34.3 ± 0.2)% for τ_2.

For an interrogation time of $\tau_1 = 7.237$ μs, we find a single-atom sensitivity of

$$\sigma_B^{(1)} = (450 \pm 20)\ \mu\text{G}.$$

For an interrogation time of $\tau_2 = 19.942$ μs, we find

$$\sigma_B^{(1)} = (161 \pm 8)\ \mu\text{G}.$$

Again, the repetition rate f_{rep} of the experiment is limited by the time of flight of the atom (~300 μs). The best integrated sensitivity (for $\tau_2 = 19.942$ μs) we can get is therefore

$$\sigma_{B,\text{int}} = \sigma_B^{(1)}\sqrt{2/f_{\text{rep}}} = (4.0 \pm 0.2)\ \mu\text{G}/\sqrt{\text{Hz}} = (400 \pm 20)\ \text{pT}/\sqrt{\text{Hz}}.$$

5.2.3.b Comparison to standard quantum limit and Heisenberg limit

Finally, we compare the sensitivity of the single-atom magnetometer to the standard quantum limit and the Heisenberg limit. In a simple picture, we consider the atom is described by two angular momenta $\hat{\boldsymbol{J}}_1$ of $n = 52$ and $\hat{\boldsymbol{J}}_2$ of $n = 50$. We therefore expect classical strategies to have a sensitivity proportional to $1/\sqrt{2} \times 1/\sqrt{2J} = 1/\sqrt{4J}$. The standard quantum limit is then given by

$$\sigma^{(1)}_{SQL} = \sigma_\Phi \left(\frac{\partial\Phi}{\partial B}\right)^{-1} = \sigma_\Phi \left(\frac{\partial\Phi}{\partial\omega_B}\right)^{-1} \left(\frac{\partial\omega_B}{\partial B}\right)^{-1} = \frac{1}{\sqrt{4J}} \frac{1}{\tau} \left(\frac{\partial\omega_B}{\partial B}\right)^{-1}, \tag{5.4}$$

where $(\partial\omega_B/\partial B) = \mu_B/\hbar = 2\pi \cdot 1.4$ MHz/G (Eq. 1.14). The Heisenberg limit corresponds to the best possible strategy, which is in this case a superposition of maximum difference in the magnetic quantum number $\Delta m = 100$. It therefore scales like $1/(4J)$ and is given by

$$\sigma^{(1)}_{HL} = \frac{1}{4J} \frac{1}{\tau} \left(\frac{\partial\omega_B}{\partial B}\right)^{-1}. \tag{5.5}$$

As in chapter 3, we calculate the sensitivity during the interrogation time τ. We therefore calculate (Eq. 5.3)

$$\sigma^{(1)}_{B,\tau} = \frac{1}{C} \frac{\Delta B}{\Delta\Phi - \Delta\Phi_0},$$

where $\Delta\Phi_0$ is the phase accumulated during the preparation and recombination part. We find

$$\frac{\Delta\Phi - \Delta\Phi_0}{\Delta B} = 2\pi \frac{\mu_B}{h} \Delta m_{cc} \tau,$$

where Δm_{cc} is the fitted difference in the magnetic quantum number of the superposition (Eq. 5.2).

For $\tau_2 = 19.942$ μs we find

$$\sigma^{(1)}_B = (164 \pm 11)\ \mu\text{G},$$

which is ~3.5-times below the standard quantum limit at τ_2 ns, $\sigma^{(1)}_{SQL} = 570$ μG, corresponding to -10.8 dB. The sensitivity is at the same time ~2.9-times above the Heisenberg limit, $\sigma^{(1)}_{HL} = 57$ μG.

5.3 Discussion

In this chapter we show that we are able to prepare a quantum superposition of the two opposite circular states $|+52c\rangle$ and $|-52c\rangle$ using a complex sequence of radio-frequency and microwave pulses. The efficiency of preparation is 60%. The balance between the two

levels $|+52c\rangle$ and $|-52c\rangle$ is 57%/43%. We demonstrate the coherence of the superposition by recombining the two branches of the interferometer and observe a visibility of 50%.

The preparation process is highly sensitive to electric field fluctuations since the involved levels, with low magnetic quantum number m, have a large Stark shift. It is possible to reduce the sensitivity to the electric field noise in the preparation process by carefully choosing the sequence of the pulses, so that the differential polarizability of the two branches is zero in average. Additionally, we add spin-echo sequences at the beginning and at the end of the sequence to further reduce the effect of the electric field noise. Once the atom is in a superposition of circular levels, it is much less sensitive to electric field fluctuations and can remain for a long time in the quantum superposition.

The superposition is very sensitive to the magnetic field and can be used as a magnetometer. In fact, we choose to measure the sensitivity of the superposition of the circular states $|+52c\rangle$ and $|-50c\rangle$ for two different interrogation times $\tau = 7.2$ μs and $\tau = 19.9$ μs. We observe a sensitivity of 161 μG corresponding to an integrated sensitivity of 4 $\mu\text{G}/\sqrt{\text{Hz}} = 400$ $\text{pT}/\sqrt{\text{Hz}}$, which is already comparable to the sensitivity of the best single spin nitrogen vacancy centres which reach a sensitivity of ~1 $\text{nT}/\sqrt{\text{Hz}}$ [50].

We observe a reduced contrast due to the preparation and recombination efficiency, but no additional contrast reduction due to the decoherence between $\tau = 7.2$ μs and $\tau = 19.9$ μs, as long as we work at night [4]. The sensitivity could therefore be further improved by increasing the interrogation time, limited in our experiment by the time of flight of the atom. Our method has a sensitivity of −10.8 dB beyond the standard quantum limit, mainly limited by the preparation efficiency. By improving the transfer into the circular, we hope to reach the fundamental Heisenberg limit.

[4] The magnetic field noise is reduced at night during the hours, that seems to correspond to the break of operation of the Paris public transport.

Conclusions

In this manuscript, we showed that the state of the hydrogen atom inside the Rydberg manifold can be described by two angular momenta related to the symmetry of the Coulomb problem. This picture provides a very simple representation to describe the coupling of the atom to a radio-frequency field, and is an insightful approach to understand the dynamics of the atom driven by a classical electromagnetic field. In a second step, we have studied the case of the rubidium Rydberg states, where, due to the size of the ionic core, the symmetry of the hydrogen-atom model is broken. We have seen, however, that this only affects the states with low magnetic quantum number, and that as long as the evolution is restricted to states with $m \geq 3$, the dynamics can still be described by the model of the two angular momenta.

In the second chapter, we described our experimental set-up, especially the electrode structure that allows us to generate the radio-frequency field with controllable polarization that we use to manipulate the state of the Rydberg atom inside a given manifold. We described the procedure we use to optimize the polarization which enables us to create a well defined σ^+ polarization. We discussed that due to the very large coupling of the Rydberg atom to the static electric field, the inhomogeneous Stark broadening is the main source of decoherence in our experiment. We then described how we can optimize the electric field homogeneity inside the electrode structure.

We presented a method to measure very small electric field variations with a precision below the standard quantum limit, close to the Heisenberg limit, using Schrödinger cat states. This method measures the quantum phase accumulated by a large angular momentum evolving on the generalized Bloch sphere. It requires to prepare the atom in a Schrödinger cat state. The wave-function of this state corresponds to a valence electron of the Rydberg atom that is in two different classical trajectories at the same time. These two trajectories have very different polarizabilities, leading to the high sensitivity of the quantum superposition to the electric field. Our method is transposable [70] to other experiments that manipulate large angular momenta or ensembles of two-level systems.

Our single-atom electrometer measures an electric field variation of 30 mV/m in 200 ns. The experimental repetition rate is limited by the duration of the time of flight necessary for the atom to reach the detector. The integrated sensitivity is therefore 0.76 mV/m/$\sqrt{\text{Hz}}$ corresponding to the possible detection, in 1 s, of a single charge located at a 1.4 mm distance from the atom. This number could be improved by detecting the atom inside the

electrode structure, which would reduce the repetition rate down to a few microseconds, leading to an improvement of factor ten of the integrated sensitivity. Nevertheless, the current achieved sensitivity of our electrometer is already several orders of magnitude better with respect to nitrogen-vacancy centres (20 kV/m/$\sqrt{\text{Hz}}$ [185], later improved by nearly two orders of magnitude [54]) or quantum dots (5 V/m/$\sqrt{\text{Hz}}$ [107]).

The comparison with solid state electrometers is less straightforward, as the figure of merit of those devices is usually expressed in term of charge sensitivity. The best mechanical resonator [109, 110] or single electron transistor [64, 66] have sensitivities in the $10^{-6}e/\sqrt{\text{Hz}}$ range. For a typical distance in the micrometer range, this corresponds to a sensitivity of 1 mV/m/$\sqrt{\text{Hz}}$. Even the sensor described in [124], with its unprecedented charge sensitivity of $2 \cdot 10^{-8}e/\sqrt{\text{Hz}}$, has also a sensitivity of 1 mV/m/$\sqrt{\text{Hz}}$ once expressed in term of electric field. Our Rydberg atom is therefore the electrometer with the best sensitivity to the electric field and could have practical applications at a quantum sensor.

If we want to use the electrometer for mesoscopic physics applications, we need to find a way to measure the electric field faster without being limited by the repetition rate of the experiment. To this end, we developed a correlation measurement using the richness of the Rydberg manifold. By modulating the polarizability of the components of the Schrödinger cat state, the electrometer measures the difference in amplitude of the electric field between two times, with a sensitivity of 80 mV/m, which corresponds to the electric field created by a single charge at a distance of 140 μm. Using the non-linear response of the interferometer, we have presented a proof of principle experiment where we showed that we could use this feature to measure the time correlation of the electric field. This experiment opens the way to interesting applications, like the characterization of the dynamics of charge in a quantum dot. Measuring temporal current fluctuations in conductors are intensely investigated, as it provides insight into the relevant transport mechanism [134]. The bandwidth of our device, with a time resolution of 200 ns, is already faster than the typical time scales observed in the experiments that have measured the full counting statistic of the electron so far (between 0.5 us and 1 ms [142–148]).

In the final part of this thesis, we demonstrated the ability to manipulate the atomic state across the region affected by the ionic core of the rubidium Rydberg atom. This leads, in particular, to the generation of the quantum superposition of two opposite circular states, $|-52c\rangle$ and $|+52c\rangle$. We measured the preparation efficiency and the coherence of this superposition. Moreover, we demonstrated a very high sensitivity of this state to the magnetic field, -11 dB below the standard quantum limit, essentially limited by the preparation efficiency. With the repetition rate of the experimental sequence, this corresponds to an integrated sensitivity of 400 pT/$\sqrt{\text{Hz}}$. The sensitivity of magnetometers depends very much on the size of the device. The sensitivity we obtain is better than that of single nitrogen-vacancy centres (4 nT/$\sqrt{\text{Hz}}$ [50] or 7 nT/$\sqrt{\text{Hz}}$ [186]) or magnetic resonance force microscopes (2.3 nT/$\sqrt{\text{Hz}}$ [187]). Only magnetometers with $10-100$ μm^3 volume, like superconducting quantum interference devices (SQUID) [188] or Bose-Einstein condensates [33, 34] manage to reach sensitivities on the order of $10-100$ pT/$\sqrt{\text{Hz}}$ [68]. Most notably, the phase measurement proves that we have a sensor with a magnetic moment of 100 μ_B. This is nearly two orders of magnitude larger than the best present microscopic probes, the nitrogen-vacancy centres (with ~2 μ_B of magnetic moment). This improves

the sensitivity by a factor of 50 for a given interrogation time, opening a way to very fast measurements of the magnetic field.

Perspectives

The quest to find a charge electrometer with very low sensitivity, while at the same time providing a high bandwidth and ideally being able to be operated without temperature restrictions, has lead to remarkable progresses in the last three decades [141]. In this context, our electrometer has several advantages. First of all, it is composed of a single atom, making it very non-invasive. It does not have to be integrated onto the device. The atom can be trapped [113–116, 189] and moved, allowing our sensor to perform spatially resolved measurements of the electric fields at different positions above a surface. Another advantage is that our experiment works at a temperature of 4 K, much less demanding than the ~100 mK required to operate a single electron transistor.

In our proof-of-principle experiment, we showed that we can detect in 200 ns the electric field created by a single charge at a ~100 μm distance, leading to a sensitivity of $4\cdot10^{-4}e/\sqrt{\text{Hz}}$. Even though charge sensors can reach sensitivities in the $10^{-6}e/\sqrt{\text{Hz}}$ range, many devices get this level of sensitivity for a much lower bandwidth [65, 146]. This is why the development of new electrometers is still a very active topic of research [124, 138–141]. Nevertheless, our electrometer used as a charge sensor is not yet at the state of the art. The limiting factor is the duration of the applied radio-frequency pulses, due the intrinsic structure of the Rydberg manifold. The duration of the pulses are constrained to be on the order of $1/\delta$, which limits the duration of the shortest measurement time. An idea could be to use states with low magnetic quantum number subject to the quantum defect, in order to use as the reference state a level which is more detuned from the radio-frequency field. This would allow to apply more powerful, shorter radio-frequency pulses, potentially leading to a higher bandwidth and lower charge sensitivity.

The Rydberg atom magnetometer is also a promising quantum sensor. The results presented here show that it is possible to create sequences that allow to generate superpositions of states with $m > 0$ and $m < 0$. By using an echo-like sequence, and choosing wisely the order of the pulses, we can ensure that the average differential Stark shift between the two parts of the wave-function average to zero on the time scale that corresponds to the correlation function of the noise (2 microseconds in our case). This makes the relative phase of the superposition much less sensitive to the electric field noise.

The sensitivity of our magnetometer is limited by two factors: the low transfer efficiency of the pulses, mainly due to the anharmonic structure of the energy levels of the rubidium atom, and the limited interrogation time. To improve the preparation process, we plan to implement a more complex protocol that should allow us to reach a much higher transfer between the low-m states and the circular states. To this end, we have a collaboration with the group of Christiane Koch at the University of Kassel who has developed a quantum control algorithm to optimize such kind of problems [190]. The second limitation is the interrogation time in the experiment. We do not see any contrast reduction as we increase the interrogation time from 7 to 20 μs, which seems to suggest that

the coherence time of the superposition of the states $|+52c\rangle$ and $|-50c\rangle$ is much larger than 10 microseconds. As the sensitivity of the measurement is inversely proportional to the interrogation time (as long as it remains small compared to the coherence time), it should be possible to achieve much better sensitivity by increasing the delay between preparation and recombination. Bose-Einstein condensate or nitrogen vacancy center experiments use interrogation times in the milliseconds range. This would correspond for us to a two order of magnitude gain in sensitivity. However, this requires to work with slower or even trapped atoms.

Appendix A

The quantum defect constant

Quantum numbers	Quantum defect constant δ_{n,l_j}
l=0	$\delta_{n,l_j} = 3.131145 + 0.195/(n-3.131145)^2$
l=1, j=1/2	$\delta_{n,l_j} = 2.65486 + 0.280/(n-2.65486)^2$
l=1, j=3/2	$\delta_{n,l_j} = 2.64165 + 0.318/(n-2.64165)^2$
l=2, j=3/2	$\delta_{n,l_j} = 1.34807 - 0.603/(n-1.34807)^2$
l=2, j=5/2	$\delta_{n,l_j} = 1.34642 - 0.545/(n-1.34642)^2$
l=3, j=5/2	$\delta_{n,l_j} = 0.0165192 - 0.085/(n-0.0165192)^2$
l=3, j=7/2	$\delta_{n,l_j} = 0.0165437 - 0.086/(n-0.0165437)^2$
l=4	$\delta_{n,l_j} = 0.004$
l=5	$\delta_{n,l_j} = 0.001$
l=6	$\delta_{n,l_j} = 0.0006$
l=7	$\delta_{n,l_j} = 0.0003$

Table A.1: Second order quantum defects for Rubidium-85. For l>2 the fine structure is neglected. The values from l=0 to l=3 are experimental values. The values for $l = 0$, $l = 1$ and $l = 2$ are taken from Meschede [170], $l = 3$ from Jianing Han et al. [171], $l = 4,5,6,7$ from Paulo Nussenzveig [172].

Appendix B

Off-resonant Rabi oscillations - geometrical derivation

B.1 Off-resonant Rabi oscillation - single RF pulse

We derive geometrically the analytic expression of $|\langle j_1, j_1|\boldsymbol{J}_1(t_{\mathrm{rf}})\rangle|^2$ used in Fig. 2.12 in Sec. 2.3.2. The initial state $|\boldsymbol{J}_1(t_{\mathrm{rf}}=0)\rangle = |j_1, j_1\rangle$ is represented as the vector $\boldsymbol{J}_1(t_{\mathrm{rf}}=0)$ pointing along the z-direction to the north pole of the Bloch sphere. The vector $\boldsymbol{J}_1(t_{\mathrm{rf}})$ evolves on the Bloch sphere and returns periodically to the north pole. The probability to return to the north pole is given by the overlap of the two spin coherent states $|\boldsymbol{J}_1(t_{\mathrm{rf}}=0)\rangle = |j_1, j_1\rangle$ and $|\boldsymbol{J}_1(t_{\mathrm{rf}})\rangle$ given by [80] (Eq. 1.34) as

$$P_1(t_{\mathrm{rf}}) = |\langle J_1(0)|J_1(t_{\mathrm{rf}})\rangle|^2 = \cos^{4j}\left(\frac{\Theta_1(t_{\mathrm{rf}})}{2}\right) = \left(\frac{1}{2}+\frac{1}{2}\cos(\Theta_1(t_{\mathrm{rf}}))\right)^{2j},$$

where $\Theta_1(t_{\mathrm{rf}})$ is the angle between the vectors $\boldsymbol{J}_1(0)$ and $\boldsymbol{J}_1(t_{\mathrm{rf}})$ and $j = (n-1)/2 = 49/2$. The angle $\Theta_1(t_{\mathrm{rf}})$ is derived geometrically from Fig. B.1. The expression for $\cos(\Theta_1)$ can be found be expressing $\boldsymbol{J}_1(0)$ and $\boldsymbol{J}_1(t)$ in the new coordinates (x', y', z'), see Fig. B.1a, as $\boldsymbol{J}_1(0) = [-\sin(\theta_1'), 0, \cos(\theta_1')]$ and $\boldsymbol{J}_1(t) = [-\sin(\theta_1')\cos(\tilde{\Omega}_+ t), -\sin(\theta_1')\sin(\tilde{\Omega}_+ t), \cos(\theta_1')]$. The scalar product of the two then directly yields

$$\cos(\Theta) = \boldsymbol{J}_1(0)\cdot\boldsymbol{J}_1(t) = \cos^2(\theta_1') + \sin^2(\theta_1')\cos(\tilde{\Omega}_+ t), \tag{B.1}$$

where $\theta_1' = \mathrm{Atan}(\Omega_+/\delta_+)$ defines the angle of the Rabi vector $\boldsymbol{\Omega}_+ = (\Omega_+, 0, \delta_+)$ with length $\tilde{\Omega_\pm} = (\Omega_\pm^2 + \delta_\pm^2)^{1/2}$.

Similarly, we find $P_2(t_{\mathrm{rf}}) = |\langle J_2(0)|J_2(t_{\mathrm{rf}})\rangle|^2$. Using Eq. 2.2, the probability to find the atom in the circular states is

$$P_{|50c\rangle}(t_{\mathrm{rf}}) = P_1(t_{\mathrm{rf}})P_2(t_{\mathrm{rf}}) = \left(\frac{1}{2}+\frac{1}{2}\cos(\Theta_1(t_{\mathrm{rf}}))\right)^{2j}\left(\frac{1}{2}+\frac{1}{2}\cos(\Theta_2(t_{\mathrm{rf}}))\right)^{2j} \tag{B.2}$$

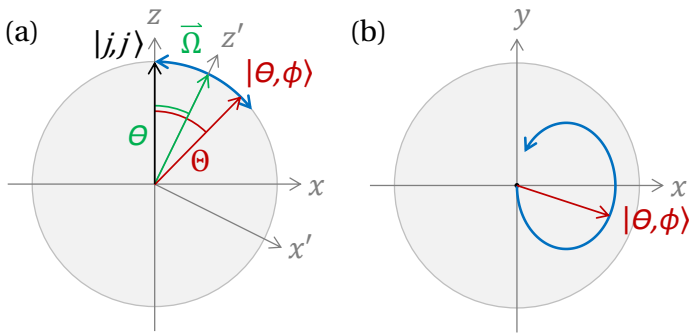

Figure B.1: (a) Front view and (b) top view of the Bloch sphere is shown for the geometrical derivation of the angle Θ *(red) between the initial state* $|j,j\rangle$ *(black) at the north pole of the Bloch sphere. The spin coherent state* $|\theta,\phi\rangle$ *(red) rotates around the Rabi vector* $\mathbf{\Omega} = (\Omega, 0, \delta)$ *(green).*

with

$$\cos(\Theta_1) = \cos^2(\theta_1') + \sin^2(\theta_1')\cos(\tilde{\Omega}_+ t)$$

and

$$\cos(\Theta_2) = \cos^2(\theta_2') + \sin^2(\theta_2')\cos(\tilde{\Omega}_- t),$$

where $\theta_2' = \mathrm{Atan}(\Omega_-/\delta_-)$, and $j = (n-1)/2 = 49/2$.

B.2 Ramsey-like off-resonant Rabi oscillations

In Fig. 2.14 in Sec. 2.3.2 is shown the analytically calculated probability to find the atom in the $|50c\rangle$ state after the sequence with the two short RF pulses as a function of the waiting time t_{delay}. The probability $P_{|50c\rangle}(t_{\mathrm{delay}})$ can be written as

$$P_{|50c\rangle}(t_{\mathrm{delay}}) = P_1(t_{\mathrm{delay}})P_2(t_{\mathrm{delay}}), \tag{B.3}$$

where $P_i(t_{\mathrm{delay}})$ corresponds to the overlap between the spin coherent state $|\boldsymbol{J}_i(t_{\mathrm{delay}})\rangle$ and $|j_i, j_i\rangle$,

$$P_i(t_{\mathrm{rf}}, t_{\mathrm{delay}}) = \left(\frac{1}{2} + \frac{1}{2}\cos(\Xi_i)\right)^{2j}, \tag{B.4}$$

where Ξ_i is the angle between $\boldsymbol{J}_i$ and the vertical z-axis. This angle can be derived geometrically (see Fig. B.2). The overlap $|\langle j,j|\theta_1,\phi_1\rangle|^2$ for $\boldsymbol{J}_1$ can be expressed with

$$|\langle j,j|\theta_1,\phi\rangle|^2 = |\langle j,j|R_{\mathrm{rf2}}R_{\mathrm{delay}}R_{\mathrm{rf1}}|j,j\rangle|^2$$

as a sequence of rotations, where

$$R_{\mathrm{delay}}R_{\mathrm{rf1}}|j,j\rangle = R_{\mathrm{delay}}|\Theta_1,\Phi_1\rangle = |\Theta_1,\Phi_1 + \delta^+ t_{\mathrm{delay}}\rangle$$

and $R_{\mathrm{rf2}}\,|j,j\rangle = |\Theta_1, -\Phi_1\rangle$. We can therefore write

$$\langle j,j|\,R_{\mathrm{rf2}}R_{\mathrm{delay}}R_{\mathrm{rf1}}\,|j,j\rangle = \langle\Theta_1,-\Phi_1|\Theta,\Phi_1+\delta^+ t_{\mathrm{delay}}\rangle\,.$$

The relative angle Ξ between $|\Theta,0\rangle$ and $|\Theta,2\Phi_1+\delta^+ t_{\mathrm{delay}}\rangle$ follows geometrically by again using two vectors on the Bloch sphere, this time in terms of Θ_1 and Φ_1. The angles Θ_1 and Φ_1 are found geometrically form Fig. B.2. After the first RF pulse the angular momentum $\boldsymbol{J}_1$ points at the direction with coordinates Θ_1 and Φ_1 (depicted in Fig. B.2) which depend on the RF duration t_{rf}. During the waiting time the angular momentum $\boldsymbol{J}_1$ rotates around the vertical axis and accumulates an azimuthal angle $\delta_+ t_{\mathrm{delay}}$ at a latitude defined by the polar angle Θ_1. Due to the precession along this latitude, the spin coherent state returns for the first time in the circular state after rotation of an angle $2\Phi_1$. The two vectors are

$$\boldsymbol{J}_1(0) = [\sin(\Theta),0,\cos(\Theta)]$$

for the initial state and

$$\boldsymbol{J}_1(t) = [\sin(\Theta_1)\cos(2\Phi_1+\delta^+ t_{\mathrm{delay}}),-\sin(\Theta_1)\sin(2\Phi_1+\delta^+ t_{\mathrm{delay}}),\cos(\Theta_1)]$$

for the spin coherent state. The scalar product of the two vectors directly yields

$$\cos(\Xi_1) = (1-\cos^2(\Theta_1))\cos(2\Phi_1+\delta_+ t_{\mathrm{delay}})+\cos^2(\Theta_1), \tag{B.5}$$

with (Eq. B.1)

$$\cos(\Theta_1) = \cos^2(\theta_1')+\sin^2(\theta_1')\cos(\tilde{\Omega}_+ t_{\mathrm{rf}})$$

and

$$\Phi_1 = \mathrm{Atan}\left(-\frac{\cot(\Omega_+ t_{\mathrm{rf}}/2)}{\cos(\theta_1')}\right),$$

where θ_1', $\tilde{\Omega}_+$ and Ω_+ have been introduced before.

In order to have an even more precise control of the $\sigma-$ component of the RF field, we also measure the probability $P_{|50e1'\rangle}(t_{\mathrm{rf}},t_{\mathrm{delay}})$ to return to the $|50e'1\rangle = |j_1,j_1\rangle\otimes|j_2,j_2-1\rangle$ state, which is given as

$$P_{|50e1'\rangle}(t_{\mathrm{delay}}) = |\,\langle j_1,j_1|J_1(t_{\mathrm{rf}},t_{\mathrm{delay}})\rangle\,|^2\cdot|\,\langle j_2,j_2-1|J_2(t_{\mathrm{rf}},t_{\mathrm{delay}})\rangle\,|^2,$$

where the first term $P_1(t_{\mathrm{delay}}) = |\,\langle j_1,j_1|J_1(t_{\mathrm{rf}})\rangle\,|^2$ is given by Eq. B.4. The second term is found with [80] as

$$\begin{aligned}P_{2,e1'}(t_{\mathrm{delay}}) &= |\,\langle j_2,j_2-1|J_2(t_{\mathrm{delay}})\rangle\,|^2\\ &= 2j_2\left(\frac{1}{2}-\frac{1}{2}\cos(\Xi_2)\right)\left(\frac{1}{2}+\frac{1}{2}\cos(\Xi_2)\right)^{n-2}\end{aligned}$$

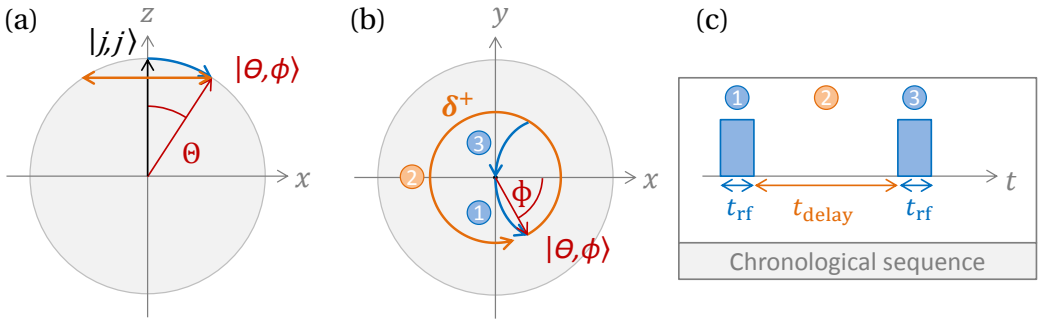

Figure B.2: (a) Front view and (b) top view of the Bloch sphere is shown for the geometrical derivation of the overlap between the initial state $|j,j\rangle$ (black) at the north pole of the Bloch sphere and the SCS $|\theta,\phi\rangle$ (red), expressed in terms of Θ (red on left graph) and Φ (red on center graph). The spin coherent state $|\theta,\phi\rangle$ is rotated with a first RF pulse (1) from the initial state at the north pole to a certain latitude (orange), where it precesses with δ_+ around the z-axis (2) until a second RF pulse is applied (3) to rotate it back to the north pole. The angle $\Phi \approx \pi/2$ is exaggerated in this picture. (c) The experimental sequence.

with $j_2 = 49/2$ and $\cos(\Xi_2)$ given by Eq. B.5. The general expression is found as

$$P_{2,e1'}(t_{\text{delay}}) = |\langle j_2, m_2 | J_2(t_{\text{rf}}, t_{\text{delay}})\rangle|^2 = \begin{pmatrix} 2j_2 \\ j_2+m_2 \end{pmatrix} \left(\frac{1}{2} - \frac{1}{2}\cos(\Xi_2)\right)^{j_2-m_2} \left(\frac{1}{2} + \frac{1}{2}\cos(\Xi_2)\right)^{j_2+m_2}.$$

B.3 Resonant Rabi oscillation - single RF pulse

In the case of a Rabi oscillation driven by a purely $\sigma+$ polarized RF field resonant in the $n = 51$ manifold, the detuning of the $\sigma+$ component becomes $\delta_+ = \omega_{\text{rf}} - \omega_{\text{at}} \approx 0$ and the Rabi frequency of the $\sigma-$ component becomes $\Omega_- \approx 0$. Thus, Eq. B.2 reduces to

$$P_{|51c\rangle}(t) = \left(\frac{1}{2} + \frac{1}{2}\cos(\Omega_+ t)\right)^{2j} = \cos^{4j}\left(\frac{\Omega_+ t}{2}\right), \tag{B.6}$$

with $j = (n-1)/2 = 50/2$, giving rise to the expected evolution of a resonant Rabi oscillation along the $n_1 = 0$ ladder. The period to return to the initial $|51c\rangle$ state is given by $2/\Omega_+$.

Appendix C

Electric field noise - higher order contrast reduction

The contrast reduction due to electric field noise (Eq. 4.3 in the main text),

$$C_r = \left|\left\langle e^{i(\alpha(\delta F(t^+)-\delta F(t^-))}\right\rangle\right| = \left|\left\langle e^{i\delta\Phi}\right\rangle\right|,$$

is expanded to second order in Sec. 4.4.1.a (see Eq. 4.4). If we take into account terms up to the fourth order, the above expression becomes[1]

$$C_r \approx 1 - \frac{1}{2}\langle\delta\Phi^2\rangle + \frac{1}{24}\langle\delta\Phi^4\rangle,$$

which can be simplified in the case of a time-independent random noise with no correlation between the electric field fluctuations at times t^+ and t^- to

$$C_r \approx 1 - \alpha^2\langle\delta F(t^+)^2\rangle + \frac{1}{12}\alpha^4\left(\langle\delta F(t^+)^4\rangle + \langle\delta F(t^+)^2\rangle^2\right).$$

In this step we use

$$\begin{aligned}\langle\delta\Phi^4\rangle =& \alpha^4\big(\langle\delta F(t^+)^4\rangle + \langle\delta F(t^-)^4\rangle - 4\langle\delta F(t^+)^3\delta F(t^-)\rangle \\ &+ 2\langle\delta F(t^+)^2\delta F(t^-)^2\rangle - 4\langle\delta F(t^+)\delta F(t^-)^3\rangle\big).\end{aligned}$$

In the case of uncorrelated noise the mean values of $\langle\delta F(t^+)^3\delta F(t^-)\rangle$ and $\langle\delta F(t^+)\delta F(t^-)^3\rangle$ can each be evaluated separated and will vanish since $\langle\delta F(t^+)\rangle = \langle\delta F(t^-)\rangle = 0$. Since the noise is time-independent, $\langle\delta F(t^+)^4\rangle = \langle\delta F(t^-)^4\rangle$ and $\langle\delta F(t^+)^2\rangle = \langle\delta F(t^-)^2\rangle$.

[1] The contrast becomes in fourth order $C_r \approx |1 - \frac{\langle\delta\Phi^2\rangle}{2} + \frac{\langle\delta\Phi^4\rangle}{24} + i(\langle\delta\Phi\rangle - \frac{\langle\delta\Phi^3\rangle}{6})| = \sqrt{1 - \langle\delta\Phi^2\rangle + \frac{\langle\delta\Phi^2\rangle^2}{4} + \frac{\langle\delta\Phi^4\rangle}{12} + \ldots} \approx 1 - \frac{\langle\delta\Phi^2\rangle}{2} + \frac{\langle\delta\Phi^4\rangle}{24} + \ldots$ where we neglected orders higher than four in each step.

Appendix D

Calibration of the magnetic field using a dark state

The magnetic field is calibrated by the relative Zeeman shift in a superposition of two low-m states. We choose the superposition of the $|51,+1\rangle$ and $|51,-1\rangle$ states which is impervious to electric field fluctuations since both levels are subject to the same Stark shift. This states can be prepared by via a microwave dark state.

D.1 Preparation of the microwave dark state

The atom is initially in the $|52,+2\rangle$ state. A resonant microwave field between the $|0\rangle = |50,0\rangle$ and the $|51,+1\rangle$ states is at the same time resonant with the $|50,0\rangle$ to $|51,-1\rangle$ transition, shown in the left panel in Fig. D.1. This Λ-level structure results in a dark and a bright state, $|-\rangle$ and $|+\rangle$ respectively. The new levels $|-\rangle$ and $|+\rangle$ are linear superpositions of $|51,+1\rangle$ and $|51,-1\rangle$ with $|-\rangle = \frac{1}{\sqrt{2}}(|51,+1\rangle - |51,-1\rangle)$ and $|+\rangle = \frac{1}{\sqrt{2}}(|51,+1\rangle + |51,-1\rangle)$. The dark state $|-\rangle$ is not coupled to $|0\rangle$, however the bright state $|+\rangle$ is coupled to the state $|0\rangle$ by a coupling strength $\sqrt{2}\Omega_{\mathrm{mw}}$, where Ω_{mw} is the coupling strength induced by the microwave for both transitions $|0\rangle \leftrightarrow |51,-1\rangle$ and $|0\rangle \leftrightarrow |51,+1\rangle$, shown in the central panel in Fig. D.1.

In the presence of the resonant microwave field between $|+\rangle$ and $|0\rangle$, the dressed states are $\frac{1}{\sqrt{2}}(|0\rangle + |+\rangle$ and $\frac{1}{\sqrt{2}}(|0\rangle - |+\rangle$ while the dark states remains unaffected by the dressing microwave field, shown in the right panel in Fig. D.1.

Fig. D.2 shows a spectroscopy of the microwave frequency of the transition between the $|52,+2\rangle$ and $|51,\pm1\rangle$ states in the presence of a dressing microwave between $|50,0\rangle$ and $|51,\pm1\rangle$. The central peak corresponds to the microwave field resonant to the transition to the dark state $|-\rangle$. The two side peaks correspond to the two dressed state of the bright state and the $|0\rangle$ state and are separated by $\sqrt{2}\Omega_{\mathrm{mw}} \approx 2\pi\cdot 3.3$ MHz. Therefore we see a population transfer from the $n = 52$ manifold to the $n = 51$ manifold at all three peaks,

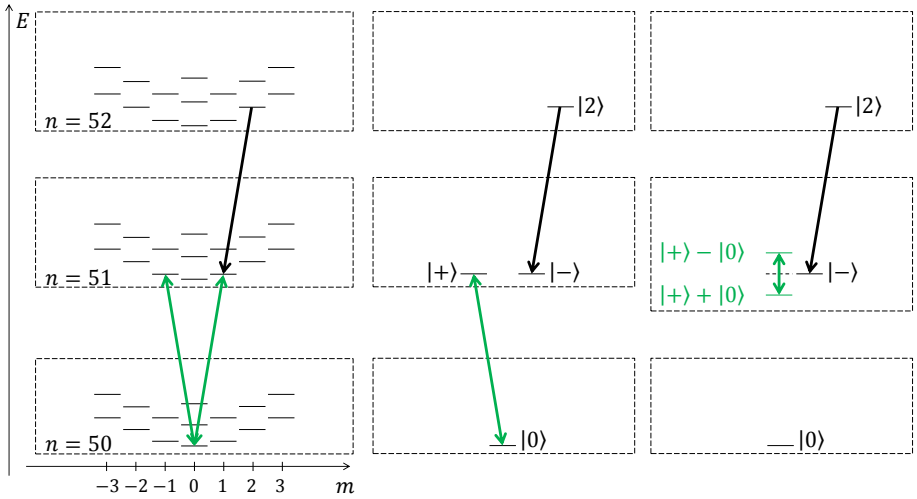

Figure D.1: The levels involved in the preparation of the dark state $|-\rangle$*, superposition of* $|51,+1\rangle$ *and* $|51,-1\rangle$*. The* Λ*-system is made up of* $|51,+1\rangle$*,* $|51,-1\rangle$*, and* $|50,0\rangle$ *(left panel). After a change of basis (center panel) it is possible to excite only the dark state* $|-\rangle$ *since the bright state* $|+\rangle$ *and the* $|0\rangle$ *state form dressed states split by the Rabi frequency* $\sqrt{2}\Omega$ *(right panel).*

but only a transfer in the $n = 50$ manifold for the two side peaks.

While the dressing microwave is applied we can easily distinguish between the dark state and the bright state. Moreover, it is possible to transfer the atom from the initial $|52,+2\rangle$ state to the dark state $|-\rangle$, being a coherent superposition of the states $|51,+1\rangle$ and $|51,-1\rangle$, by a microwave π pulse.

D.2 Calibration of the magnetic field using the dark state

In the presence a magnetic field, the superposition $|-\rangle$ becomes $\frac{1}{\sqrt{2}}(|51,+1\rangle - e^{i\Phi}|51,-1\rangle)$, where the phase $\Phi = \omega_B t$ depends on the applied magnetic field. For $\Phi = \pi$, the superposition becomes $\frac{1}{\sqrt{2}}(|51,+1\rangle - e^{i\Phi}|51,-1\rangle) = \frac{1}{2}(|51,+1\rangle + |51,-1\rangle) = |+\rangle$. The state is then coupled again to the $|50,0\rangle - |51,\pm1\rangle$ microwave and a microwave π pulse between the bright state $|+\rangle$ and the state $|50,0\rangle$ allows to read out the probability to find the atom in the $|+\rangle$ state.

Fig. D.3 shows the probability to find the atom in the bright state $|+\rangle$ and as a function of the applied current through the superconducting magnetic field coils. A full period of the Ramsey fringes of 2π is recorded for $\Delta I = (99 \pm 2)$ mA allowing to calibrate the magnetic field. The relative shift of the levels $|51,+1\rangle$ and $|51,-1\rangle$ of the superposition due to the Zeeman effect (see Sec. 1.1.3) leads to an accumulated phase of

$$\Phi = 2\pi\Delta\nu_B t$$

where $\Delta\nu_B = \Delta m \mu_B B/h$ (Eq. 1.14) is the relative Zeeman shift and t the delay of the two

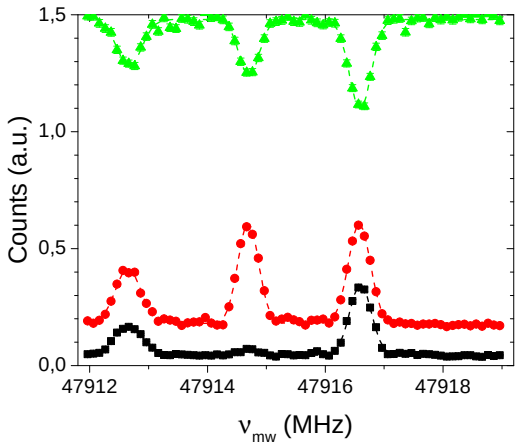

Figure D.2: Spectroscopy of the dark state (center peak) and the dressed states of the bright state (side peaks). There is a population transfer from the $n = 52$ (black) to the $n = 51$ manifold (red) for all three peaks, however, only the in the dressed states the population is transferred in the $n = 50$ manifold (green). From left to right, the peaks correspond to $\frac{1}{\sqrt{2}}(|0\rangle + |+\rangle, |-\rangle$ and $\frac{1}{\sqrt{2}}(|0\rangle - |+\rangle$. The corresponding levels are shown in the right panel of Fig. D.1.

Ramsey pulses. The superposition accumulates an additional phase of 2π for a change in the magnetic field which can be written as

$$\Delta B = \frac{\Delta \nu}{\Delta m \mu_B / h}.$$

where $\Delta \nu = 1/t$. The Ramsey pulses are separated by $t = (19.85 \pm 1)$ μs leading to a change in magnetic field of $\Delta B = (18.0 \pm 0.9)$ mG. This leads to a conversion factor between the applied current and the magnetic field seen by the atom of $\Delta B / \Delta I = (181 \pm 9)$ μG/mA, smaller than the theoretical value of $\Delta B / \Delta I = 215$ μG/mA in Sec. 5.2.1.

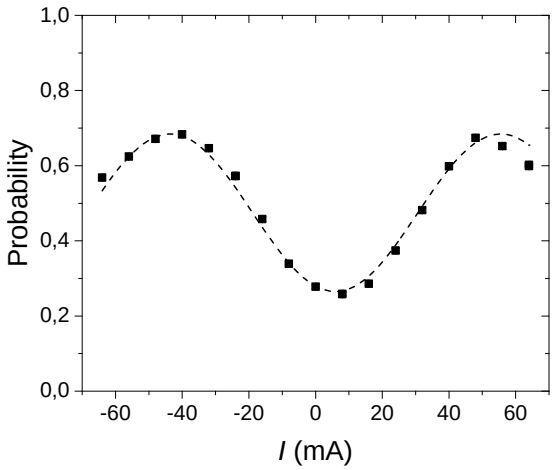

Figure D.3: Calibration curve of the magnetic field. The probability to find the atom in the $|+\rangle$ *state is shown as a function of the applied current through the magnetic field coils. The atom is prepared in the dark state* $|-\rangle$ *superposition of* $|51,+1\rangle$ *and* $|51,-1\rangle$*. The phase of the superposition varies as a function of the amplitude of the applied magnetic field, leading to oscillations in the probability to find the atom in the bright state* $|+\rangle$*.*

Bibliography

[1] D. Deutsch. Quantum theory, the church-turing principle and the universal quantum computer. *Proceedings of the Royal Society of London A: Mathematical, Physical and Engineering Sciences* **400**, 97–117 (1985).

[2] D. DiVincenzo. The physical implementation of quantum computation. *Fortschritte der Physik* **48** (2000).

[3] N. Gisin, G. Ribordy, W. Tittel & H. Zbinden. Quantum cryptography. *Rev. Mod. Phys.* **74**, 145–195 (2002).

[4] C. L. Degen, F. Reinhard & P. Cappellaro. Quantum sensing. *Rev. Mod. Phys.* **89**, 035002 (2017).

[5] C. M. Caves. Quantum-mechanical noise in an interferometer. *Phys. Rev. D* **23**, 1693–1708 (1981).

[6] R. E. Slusher, L. W. Hollberg, B. Yurke, J. C. Mertz & J. F. Valley. Observation of squeezed states generated by four-wave mixing in an optical cavity. *Phys. Rev. Lett.* **55**, 2409–2412 (1985).

[7] A gravitational wave observatory operating beyond the quantum shot-noise limit. *Nat Phys* **7**, 962–965 (2011).

[8] Aasi J. *et al.* Enhanced sensitivity of the LIGO gravitational wave detector by using squeezed states of light. *Nat Photon* **7**, 613–619 (2013).

[9] S. Lloyd. Enhanced sensitivity of photodetection via quantum illumination. *Science* **321**, 1463–1465 (2008).

[10] S.-H. Tan, B. I. Erkmen, V. Giovannetti, S. Guha, S. Lloyd, L. Maccone, S. Pirandola & J. H. Shapiro. Quantum illumination with gaussian states. *Phys. Rev. Lett.* **101**, 253601 (2008).

[11] M. A. Taylor, J. Janousek, V. Daria, J. Knittel, B. Hage, BachorHans-A. & W. P. Bowen. Biological measurement beyond the quantum limit. *Nat Photon* **7**, 229–233 (2013).

[12] O. Schwartz, J. M. Levitt, R. Tenne, S. Itzhakov, Z. Deutsch & D. Oron. Superresolution microscopy with quantum emitters. *Nano Letters* **13**, 5832–5836 (2013). PMID: 24195698.

[13] A. D. O'Connell, M. Hofheinz, M. Ansmann, R. C. Bialczak, M. Lenander, E. Lucero, M. Neeley, D. Sank, H. Wang, M. Weides, J. Wenner, J. M. Martinis & A. N. Cleland. Quantum ground state and single-phonon control of a mechanical resonator. *Nature* **464**, 697–703 (2010).

[14] M. Aspelmeyer, T. J. Kippenberg & F. Marquardt. Cavity optomechanics. *Rev. Mod. Phys.* **86**, 1391–1452 (2014).

[15] Moser J., Guttinger J., Eichler A., Esplandiu M. J., Liu D. E., Dykman M. I. & Bachtold A. Ultrasensitive force detection with a nanotube mechanical resonator. *Nat Nano* **8**, 493–496 (2013).

[16] F. G. Cervantes, L. Kumanchik, J. Pratt & J. M. Taylor. High sensitivity optomechanical reference accelerometer over 10 khz. *Applied Physics Letters* **104**, 221111 (2014).

[17] Chaste J., Eichler A., Moser J., Ceballos G., Rurali R. & Bachtold A. A nanomechanical mass sensor with yoctogram resolution. *Nat Nano* **7**, 301–304 (2012).

[18] S. Forstner, E. Sheridan, J. Knittel, C. L. Humphreys, G. A. Brawley, H. Rubinsztein-Dunlop & W. P. Bowen. Ultrasensitive optomechanical magnetometry. *Advanced Materials* **26**, 6348–6353 (2014).

[19] D. Rugar, R. Budakian, H. J. Mamin & B. W. Chui. Single spin detection by magnetic resonance force microscopy. *Nature* **430**, 329–332 (2004).

[20] T. Bagci, A. Simonsen, S. Schmid, L. G. Villanueva, E. Zeuthen, J. Appel, J. M. Taylor, A. Sorensen, K. Usami, A. Schliesser & E. S. Polzik. Optical detection of radio waves through a nanomechanical transducer. *Nature* **507**, 81–85 (2014).

[21] D. Budker & M. Romalis. Optical magnetometry. *Nat Phys* **3**, 227–234 (2007).

[22] I. K. Kominis, T. W. Kornack, J. C. Allred & M. V. Romalis. A subfemtotesla multichannel atomic magnetometer. *Nature* **422**, 596–599 (2003).

[23] H. B. Dang, A. C. Maloof & M. V. Romalis. Ultrahigh sensitivity magnetic field and magnetization measurements with an atomic magnetometer. *Applied Physics Letters* **97**, 151110 (2010).

[24] M. Livanov, A. Kozlov, A. Korinevskii, V. Markin & S. Sinel'nikova. Recording of human magnetic fields. *Doklady Akademii nauk SSSR* **238**, 253—256 (1978).

[25] G. Bison, N. Castagna, A. Hofer, P. Knowles, J.-L. Schenker, M. Kasprzak, H. Saudan & A. Weis. A room temperature 19-channel magnetic field mapping device for cardiac signals. *Applied Physics Letters* **95**, 173701 (2009).

[26] K. Jensen, R. Budvytyte, R. A. Thomas, T. Wang, A. M. Fuchs, M. V. Balabas, G. Vasilakis, L. D. Mosgaard, H. C. Stærkind, J. H. Müller, T. Heimburg, S.-P. Olesen & E. S. Polzik. Non-invasive detection of animal nerve impulses with an atomic magnetometer operating near quantum limited sensitivity. *Scientific reports* **6**, 29638 (2016).

[27] H. Xia, A. B.-A. Baranga, D. Hoffman & M. V. Romalis. Magnetoencephalography with an atomic magnetometer. *Applied Physics Letters* **89**, 211104 (2006).

[28] A. D. Ludlow, M. M. Boyd, J. Ye, E. Peik & P. O. Schmidt. Optical atomic clocks. *Rev. Mod. Phys.* **87**, 637–701 (2015).

[29] M. Kasevich & S. Chu. Measurement of the gravitational acceleration of an atom with a light-pulse atom interferometer. *Applied Physics B* **54**, 321–332 (1992).

[30] A. Peters, K. Y. Chung & S. Chu. Measurement of gravitational acceleration by dropping atoms. *Nature* **400**, 849–852 (1999).

[31] T. L. Gustavson, P. Bouyer & M. A. Kasevich. Precision rotation measurements with an atom interferometer gyroscope. *Phys. Rev. Lett.* **78**, 2046–2049 (1997).

[32] T. L. Gustavson, A. Landragin & M. A. Kasevich. Rotation sensing with a dual atom-interferometer sagnac gyroscope. *Classical and Quantum Gravity* **17**, 2385 (2000).

[33] M. Vengalattore, J. M. Higbie, S. R. Leslie, J. Guzman, L. E. Sadler & D. M. Stamper-Kurn. High-resolution magnetometry with a spinor bose-einstein condensate. *Phys. Rev. Lett.* **98**, 200801 (2007).

[34] C. F. Ockeloen, R. Schmied, M. F. Riedel & P. Treutlein. Quantum metrology with a scanning probe atom interferometer. *Phys. Rev. Lett.* **111**, 143001 (2013).

[35] R. Maiwald, D. Leibfried, J. Britton, J. C. Bergquist, G. Leuchs & D. J. Wineland. Stylus ion trap for enhanced access and sensing. *Nat Phys* **5**, 551–554 (2009).

[36] M. Brownnutt, M. Kumph, P. Rabl & R. Blatt. Ion-trap measurements of electric-field noise near surfaces. *Rev. Mod. Phys.* **87**, 1419–1482 (2015).

[37] I. Baumgart, J.-M. Cai, A. Retzker, M. B. Plenio & C. Wunderlich. Ultrasensitive magnetometer using a single atom. *Phys. Rev. Lett.* **116**, 240801 (2016).

[38] T. Ruster, H. Kaufmann, M. A. Luda, V. Kaushal, C. T. Schmiegelow, F. Schmidt-Kaler & U. G. Poschinger. Entanglement-based dc magnetometry with separated ions. *arXiv preprint arXiv:1704.01793* (2017).

[39] N. Huntemann, C. Sanner, B. Lipphardt, C. Tamm & E. Peik. Single-ion atomic clock with 3×10^{-18} systematic uncertainty. *Phys. Rev. Lett.* **116**, 063001 (2016).

[40] P. P. Herrmann, J. Hoffnagle, N. Schlumpf, V. L. Telegdi & A. Weis. Stark spectroscopy of forbidden two-photon transitions: a sensitive probe for the quantitative measurement of small electric fields. *Journal of Physics B: Atomic and Molecular Physics* **19**, 1271 (1986).

[41] A. Osterwalder & F. Merkt. Using high Rydberg states as electric field sensors. *Physical review letters* **82**, 1831 (1999).

[42] Kübler H., Shaffer J. P., Baluktsian T., Low R. & Pfau T. Coherent excitation of Rydberg atoms in micrometre-sized atomic vapour cells. *Nat Photon* **4**, 112–116 (2010).

[43] J. A. Sedlacek, A. Schwettmann, H. Kubler, R. Low, T. Pfau & J. P. Shaffer. Microwave electrometry with Rydberg atoms in a vapour cell using bright atomic resonances. *Nat Phys* **8**, 819–824 (2012).

[44] H. Fan, S. Kumar, J. Sedlacek, H. Kübler, S. Karimkashi & J. P. Shaffer. Atom based rf electric field sensing. *Journal of Physics B: Atomic, Molecular and Optical Physics* **48**, 202001 (2015).

[45] S. Gleyzes, S. Kuhr, C. Guerlin, J. Bernu, S. Deleglise, U. Busk Hoff, M. Brune, J.-M. Raimond & S. Haroche. Quantum jumps of light recording the birth and death of a photon in a cavity. *Nature* **446**, 297–300 (2007).

[46] G. Nogues, A. Rauschenbeutel, S. Osnaghi, M. Brune, J. M. Raimond & S. Haroche. Seeing a single photon without destroying it. *Nature* **400**, 239–242 (1999).

[47] S. Haroche. Nobel lecture: Controlling photons in a box and exploring the quantum to classical boundary. *Rev. Mod. Phys.* **85**, 1083–1102 (2013).

[48] G. S. Waters & P. D. Francis. A nuclear magnetometer. *Journal of Scientific Instruments* **35**, 88 (1958).

[49] J. E. Lenz. A review of magnetic sensors. *Proceedings of the IEEE* **78**, 973–989 (1990).

[50] G. Balasubramanian, P. Neumann, D. Twitchen, M. Markham, R. Kolesov, N. Mizuochi, J. Isoya, J. Achard, J. Beck, J. Tissler, V. Jacques, P. R. Hemmer, F. Jelezko & J. Wrachtrup. Ultralong spin coherence time in isotopically engineered diamond. *Nat Mater* **8**, 383–387 (2009).

[51] T. Wolf, P. Neumann, K. Nakamura, H. Sumiya, T. Ohshima, J. Isoya & J. Wrachtrup. Subpicotesla diamond magnetometry. *Phys. Rev. X* **5**, 041001 (2015).

[52] J. M. Taylor, P. Cappellaro, L. Childress, L. Jiang, D. Budker, P. R. Hemmer, A. Yacoby, R. Walsworth & M. D. Lukin. High-sensitivity diamond magnetometer with nanoscale resolution. *Nat Phys* **4**, 810–816 (2008).

[53] C. Arnold, V. Loo, A. Lemaître, I. Sagnes, O. Krebs, P. Voisin, P. Senellart & L. Lanco. Cavity-Enhanced Real-Time Monitoring of Single-Charge Jumps at the Microsecond Time Scale. *Physical Review X* **4** (2014).

[54] F. Dolde, M. W. Doherty, J. Michl, I. Jakobi, B. Naydenov, S. Pezzagna, J. Meijer, P. Neumann, F. Jelezko, N. B. Manson & J. Wrachtrup. Nanoscale Detection of a Single Fundamental Charge in Ambient Conditions Using the NV – Center in Diamond. *Physical Review Letters* **112** (2014).

[55] R. L. Fagaly. Superconducting quantum interference device instruments and applications. *Review of Scientific Instruments* **77**, 101101 (2006).

[56] R. C. Jaklevic, J. Lambe, J. E. Mercereau & A. H. Silver. Macroscopic quantum interference in superconductors. *Phys. Rev.* **140**, A1628–A1637 (1965).

[57] Y. Nakamura, Y. A. Pashkin & J. S. Tsai. Coherent control of macroscopic quantum states in a single-Cooper-pair box. *Nature* **398**, 786–788 (1999).

[58] D. Vion, A. Aassime, A. Cottet, P. Joyez, H. Pothier, C. Urbina, D. Esteve & M. H. Devoret. Manipulating the quantum state of an electrical circuit. *Science* **296**, 886–889 (2002).

[59] J. M. Martinis, S. Nam, J. Aumentado & C. Urbina. Rabi oscillations in a large josephson-junction qubit. *Phys. Rev. Lett.* **89**, 117901 (2002).

[60] A. Wallraff, D. I. Schuster, A. Blais, L. Frunzio, R.-S. Huang, J. Majer, S. Kumar, S. M. Girvin & R. J. Schoelkopf. Strong coupling of a single photon to a superconducting qubit using circuit quantum electrodynamics. *Nature* **431**, 162–167 (2004).

[61] J. Clarke & F. K. Wilhelm. Superconducting quantum bits. *Nature* **453**, 1031–1042 (2008).

[62] M. Bal, C. Deng, J.-L. Orgiazzi, F. Ong & A. Lupascu. Ultrasensitive magnetic field detection using a single artificial atom. *Nature Communications* **3**, 1324 (2012).

[63] M. A. Kastner. The single-electron transistor. *Rev. Mod. Phys.* **64**, 849–858 (1992).

[64] M. J. Yoo, T. A. Fulton, H. F. Hess, R. L. Willet, L. N. Dunkleberger, R. J. Chichester, L. N. Pfeiffer & K. W. West. Scanning Single-Electron Transistor Microscopy: Imaging Individual Charges. *Science* **276**, 579–582 (1997).

[65] R. J. Schoelkopf, P. Wahlgren, A. A. Kozhevnikov, P. Delsing & D. E. Prober. The radio-frequency single-electron transistor (rf-set): A fast and ultrasensitive electrometer. *Science* **280**, 1238–1242 (1998).

[66] M. H. Devoret & R. J. Schoelkopf. Amplifying quantum signals with the single-electron transistor. *Nature* **406**, 1039–1046 (2000).

[67] W. Wasilewski, K. Jensen, H. Krauter, J. J. Renema, M. V. Balabas & E. S. Polzik. Quantum noise limited and entanglement-assisted magnetometry. *Phys. Rev. Lett.* **104**, 133601 (2010).

[68] W. Muessel, H. Strobel, D. Linnemann, D. Hume & M. Oberthaler. Scalable Spin Squeezing for Quantum-Enhanced Magnetometry with Bose-Einstein Condensates. *Physical Review Letters* **113** (2014).

[69] O. Hosten, N. J. Engelsen, R. Krishnakumar & M. A. Kasevich. Measurement noise 100 times lower than the quantum-projection limit using entangled atoms. *Nature* **529**, 505–508 (2016).

[70] T. Tanaka, P. Knott, Y. Matsuzaki, S. Dooley, H. Yamaguchi, W. J. Munro & S. Saito. Proposed Robust Entanglement-Based Magnetic Field Sensor Beyond the Standard Quantum Limit. *Physical Review Letters* **115** (2015).

[71] D. Leibfried, M. D. Barrett, T. Schaetz, J. Britton, J. Chiaverini, W. M. Itano, J. Jost, C. Langer & D. J. Wineland. Toward Heisenberg-Limited Spectroscopy with Multiparticle Entangled States. *Science* **304**, 1476–1478 (2004).

[72] T. Nagata, R. Okamoto, J. L. O'Brien, K. Sasaki & S. Takeuchi. Beating the Standard Quantum Limit with Four-Entangles Photons. *Science* **316**, 723–726 (2007).

[73] J. A. Jones, S. D. Karlen, J. Fitzsimons, A. Ardavan, S. C. Benjamin, G. A. D. Briggs & J. J. Morton. Magnetic field sensing beyond the standard quantum limit using 10-spin NOON states. *Science* **324**, 1166–1168 (2009).

[74] H.-Y. Lo, D. Kienzler, L. de Clercq, M. Marinelli, V. Negnevitsky, B. C. Keitch & J. P. Home. Spin–motion entanglement and state diagnosis with squeezed oscillator wavepackets. *Nature* **521**, 336–339 (2015).

[75] E. E. Wollman, C. U. Lei, A. J. Weinstein, J. Suh, A. Kronwald, F. Marquardt, A. A. Clerk & K. C. Schwab. Quantum sqeezing of motion in a mechanical resonator. *Science* **349**, 952–955 (2015).

[76] W. Heisenberg. Über den anschaulichen Inhalt der quantentheoretischen Kinematik und Mechanik. *Zeitschrift fur Physik* **43**, 172–198 (1927).

[77] C. M. Caves, K. S. Thorne, R. W. Drever, V. D. Sandberg & M. Zimmermann. On the measurement of a weak classical force coupled to a quantum-mechanical oscillator. I. Issues of principle. *Reviews of Modern Physics* **52**, 341 (1980).

[78] V. B. Braginskii & Y. I. Vorontsov. Quantum-mechanical limitations in macroscopic experiments and modern experimental technique. *Soviet Physics Uspekhi* **17**, 644 (1975).

[79] V. Giovannetti, S. Lloyd & L. Maccone. Quantum-Enhanced Measurments: Beating the Standard Quantum Limit. *Science* **305**, 1330–1336 (2004).

[80] F. T. Arecchi, E. Courtens, R. Gilmore & H. Thomas. Atomic coherent states in quantum optics. *Physical Review A* **6**, 2211 (1972).

[81] M. Kitagawa & M. Ueda. Squeezed spin states. *Physical Review A* **47**, 5138 (1993).

[82] M. J. Holland & K. Burnett. Interferometric detection of optical phase shifts at the heisenberg limit. *Phys. Rev. Lett.* **71**, 1355–1358 (1993).

[83] V. Giovannetti, S. Lloyd & L. Maccone. Advances in quantum metrology. *Nature Photonics* **5**, 222–229 (2011).

[84] S. L. Braunstein, C. M. Caves & G. Milburn. Generalized Uncertainty Relations: Theory, Examples, and Lorentz Invariance. *Annals of Physics* **247**, 135–173 (1996).

[85] R. A. Fisher. On the mathematical foundations of theoretical statistics. *Philosophical Transactions of the Royal Society of London A: Mathematical, Physical and Engineering Sciences* **222**, 309–368 (1922).

[86] H. Cramér. *Mathematical Methods of Statistics. Princeton landmarks in mathematics and physics* (Princeton University Press, 1946).

[87] C. R. Rao. *Linear Statistical Inference and its Applications* (John Wiley & Sons, Inc., 1973).

[88] C. W. Helstrom. Quantum detection and estimation theory. *Journal of Statistical Physics* **1**, 231–252 (1969).

[89] A. S. Holevo. *Probabilistic and Statistical Aspects of Quantum Theory* (North-Holland Publishing Company, Amsterdam, 1982).

[90] S. L. Braunstein & C. M. Caves. Statistical distance and the geometry of quantum states. *Phys. Rev. Lett.* **72**, 3439–3443 (1994).

[91] M. G. A. Paris. Quantum estimation for quantum technology. *International Journal of Quantum Information* **07**, 125–137 (2009).

[92] D. J. Wineland, J. J. Bollinger, W. M. Itano, F. L. Moore & D. J. Heinzen. Spin squeezing and reduced quantum noise in spectroscopy. *Phys. Rev. A* **46**, R6797–R6800 (1992).

[93] J. Esteve, C. Gross, A. Weller, S. Giovanazzi & M. K. Oberthaler. Squeezing and entanglement in a Bose-Einstein condensate. *Nature* **455**, 1216–1219 (2008).

[94] T. Fernholz, H. Krauter, K. Jensen, J. F. Sherson, A. S. Sørensen & E. S. Polzik. Spin squeezing of atomic ensembles via nuclear-electronic spin entanglement. *Phys. Rev. Lett.* **101**, 073601 (2008).

[95] M. F. Riedel, P. Böhi, Y. Li, T. W. Hänsch, A. Sinatra & P. Treutlein. Atom-chip-based generation of entanglement for quantum metrology. *Nature* **464**, 1170–1173 (2010).

[96] J. Appel, P. J. Windpassinger, D. Oblak, U. B. Hoff, N. Kjaergaard & E. S. Polzik. Mesoscopic atomic entanglement for precision measurements beyond the standard quantum limit. *Proceedings of the National Academy of Sciences* **106**, 10960–10965 (2009).

[97] I. D. Leroux, M. H. Schleier-Smith & V. Vuletić. Implementation of cavity squeezing of a collective atomic spin. *Phys. Rev. Lett.* **104**, 073602 (2010).

[98] A. Louchet-Chauvet, J. Appel, J. J. Renema, D. Oblak, N. Kjaergaard & E. S. Polzik. Entanglement-assisted atomic clock beyond the projection noise limit. *New Journal of Physics* **12**, 065032 (2010).

[99] M. H. Schleier-Smith, I. D. Leroux & V. Vuletić. States of an ensemble of two-level atoms with reduced quantum uncertainty. *Phys. Rev. Lett.* **104**, 073604 (2010).

[100] R. J. Sewell, M. Koschorreck, M. Napolitano, B. Dubost, N. Behbood & M. W. Mitchell. Magnetic sensitivity beyond the projection noise limit by spin squeezing. *Phys. Rev. Lett.* **109**, 253605 (2012).

[101] Bohnet, J. G., Cox, K. C., Norcia, M. A., Weiner, J. M., Chen, Z. & Thompson, J. K. Reduced spin measurement back-action for a phase sensitivity ten times beyond the standard quantum limit. *Nat Photon* **8**, 731–736 (2014).

[102] K. C. Cox, G. P. Greve, J. M. Weiner & J. K. Thompson. Deterministic squeezed states with collective measurements and feedback. *Phys. Rev. Lett.* **116**, 093602 (2016).

[103] S. Massar & E. S. Polzik. Generating a Superposition of Spin States in an Atomic Ensemble. *Physical Review Letters* **91** (2003).

[104] H. W. Lau, Z. Dutton, T. Wang & C. Simon. Proposal for the Creation and Optical Detection of Spin Cat States in Bose-Einstein Condensates. *Physical Review Letters* **113** (2014).

[105] T. Monz, P. Schindler, J. T. Barreiro, M. Chwalla, D. Nigg, W. A. Coish, M. Harlander, W. Hänsel, M. Hennrich & R. Blatt. 14-Qubit Entanglement: Creation and Coherence. *Physical Review Letters* **106** (2011).

[106] A. Signoles, A. Facon, D. Grosso, I. Dotsenko, S. Haroche, J.-M. Raimond, M. Brune & S. Gleyzes. Confined quantum zeno dynamics of a watched atomic arrow. *Nature Physics* **10**, 715–719 (2014).

[107] A. N. Vamivakas, Y. Zhao, S. Fält, A. Badolato, J. M. Taylor & M. Atatüre. Nanoscale Optical Electrometer. *Physical Review Letters* **107** (2011).

[108] J. Houel, A. V. Kuhlmann, L. Greuter, F. Xue, M. Poggio, B. D. Gerardot, P. A. Dalgarno, A. Badolato, P. M. Petroff, A. Ludwig, D. Reuter, A. D. Wieck & R. J. Warburton. Probing Single-Charge Fluctuations at a GaAs / AlAs Interface Using Laser Spectroscopy on a Nearby InGaAs Quantum Dot. *Physical Review Letters* **108** (2012).

[109] A. N. Cleland & M. L. Roukes. A nanometre-scale mechanical electrometer. *Nature* **392**, 160–162 (1998).

[110] J. S. Bunch, A. M. van der Zande, S. S. Verbridge, I. W. Frank, D. M. Tanenbaum, J. M. Parpia, H. G. Craighead & P. L. McEuen. Electromechanical resonators from graphene sheets. *Science* **315**, 490–493 (2007).

[111] A. Facon, E.-K. Dietsche, D. Grosso, S. Haroche, J.-M. Raimond, M. Brune & S. Gleyzes. A sensitive electrometer based on a Rydberg atom in a Schrödinger-cat state. *Nature* **535**, 262–265 (2016).

[112] A. Facon. *Chats de Schrödinger d'un atome de Rydberg pour la métrologie quantique*. Ph.D. thesis, Université Pierre et Marie Curie - Paris VI, Paris (2015).

[113] P. Hyafil, J. Mozley, A. Perrin, J. Tailleur, G. Nogues, M. Brune, J. M. Raimond & S. Haroche. Coherence-preserving trap architecture for long-term control of giant ryberg atoms. *Phys. Rev. Lett.* **93**, 103001 (2004).

[114] S. K. Dutta, J. R. Guest, D. Feldbaum, A. Walz-Flannigan & G. Raithel. Ponderomotive optical lattice for rydberg atoms. *Phys. Rev. Lett.* **85**, 5551–5554 (2000).

[115] D. A. Anderson, A. Schwarzkopf, R. E. Sapiro & G. Raithel. Production and trapping of cold circular rydberg atoms. *Phys. Rev. A* **88**, 031401 (2013).

[116] A. Sarlette, Z. Leghtas, M. Brune, J. M. Raimond & P. Rouchon. Stabilization of nonclassical states of one- and two-mode radiation fields by reservoir engineering. *Phys. Rev. A* **86**, 012114 (2012).

[117] C. H. Hsu & R. S. Muller. Micromechanical electrostatic voltmeter. In *Solid-State Sensors and Actuators, 1991. Digest of Technical Papers, TRANSDUCERS '91., 1991 International Conference on*, 659–662 (1991).

[118] Measuring isolated surface charge with a noncontacting voltmeter. *Journal of Electrostatics* **35**, 203 – 213 (1995). Selected papers from the special technical session.

[119] M. N. Horenstein & P. R. Stone. A micro-aperture electrostatic field mill based on mems technology. *Journal of Electrostatics* **51**, 515 – 521 (2001). Electrostatics 2001: 9th International Conference on Electrostatics.

[120] D. Taylor. Measuring techniques for electrostatics. *Journal of Electrostatics* **51**, 502 – 508 (2001). Electrostatics 2001: 9th International Conference on Electrostatics.

[121] B. Bahreyni, G. Wijeweera, C. Shafai & A. Rajapakse. Analysis and design of a micromachined electric-field sensor. *Journal of Microelectromechanical Systems* **17**, 31–36 (2008).

[122] S. Lina, L. Xinxing, Q. Hua & G. Xiaofeng. A sensitive charge scanning probe based on silicon single electron transistor. *Journal of Semiconductors* **37**, 044008 (2016).

[123] E. L. Hahn. Spin echoes. *Phys. Rev.* **80**, 580–594 (1950).

[124] O. E. Dial, M. D. Shulman, S. P. Harvey, H. Bluhm, V. Umansky & A. Yacoby. Charge noise spectroscopy using coherent exchange oscillations in a singlet-triplet qubit. *Phys. Rev. Lett.* **110**, 146804 (2013).

[125] C. P. Slichter. *Principles of Magnetic Resonance* (Springer-Verlag, 1996).

[126] L. Viola & S. Lloyd. Dynamical suppression of decoherence in two-state quantum systems. *Phys. Rev. A* **58**, 2733–2744 (1998).

[127] H. Y. Carr & E. M. Purcell. Effects of diffusion on free precession in nuclear magnetic resonance experiments. *Phys. Rev.* **94**, 630–638 (1954).

[128] K. Khodjasteh & D. A. Lidar. Fault-tolerant quantum dynamical decoupling. *Phys. Rev. Lett.* **95**, 180501 (2005).

[129] P. Szańkowski, M. Trippenbach & L. Cywiński. Spectroscopy of cross correlations of environmental noises with two qubits. *Phys. Rev. A* **94**, 012109 (2016).

[130] M. J. Biercuk, H. Uys, A. P. VanDevender, N. Shiga, W. M. Itano & J. J. Bollinger. Optimized dynamical decoupling in a model quantum memory. *Nature* **458**, 996–1000 (2009).

[131] S. Kotler, N. Akerman, Y. Glickman, A. Keselman & R. Ozeri. Single-ion quantum lock-in amplifier. *Nature* **473**, 61–65 (2011).

[132] J. Bylander, S. Gustavsson, F. Yan, F. Yoshihara, K. Harrabi, G. Fitch, D. G. Cory, Y. Nakamura, J.-S. Tsai & W. D. Oliver. Noise spectroscopy through dynamical decoupling with a superconducting flux qubit. *Nat Phys* **7**, 565–570 (2011).

[133] J. Medford, L. Cywiński, C. Barthel, C. M. Marcus, M. P. Hanson & A. C. Gossard. Scaling of dynamical decoupling for spin qubits. *Phys. Rev. Lett.* **108**, 086802 (2012).

[134] Y. Blanter & M. Büttiker. Shot noise in mesoscopic conductors. *Physics Reports* **336**, 1–166 (2000).

[135] A. Cottet, W. Belzig & C. Bruder. Positive cross-correlations due to dynamical channel blockade in a three-terminal quantum dot. *Physical Review B* **70** (2004).

[136] W. Belzig. Full counting statistics of super-poissonian shot noise in multilevel quantum dots. *Phys. Rev. B* **71**, 161301 (2005).

[137] S. Gustavsson, R. Leturcq, B. Simovič, R. Schleser, P. Studerus, T. Ihn, K. Ensslin, D. C. Driscoll & A. C. Gossard. Counting statistics and super-Poissonian noise in a quantum dot: Time-resolved measurements of electron transport. *Physical Review B* **74** (2006).

[138] T. M. Buehler, D. J. Reilly, R. P. Starrett, N. A. Court, A. R. Hamilton, A. S. Dzurak & R. G. Clark. Development and operation of the twin radio frequency single electron transistor for cross-correlated charge detection. *Journal of Applied Physics* **96**, 4508–4513 (2004).

[139] D. J. Reilly, C. M. Marcus, M. P. Hanson & A. C. Gossard. Fast single-charge sensing with a rf quantum point contact. *Applied Physics Letters* **91**, 162101 (2007).

[140] K. Nishiguchi, H. Yamaguchi, A. Fujiwara, H. S. J. van der Zant & G. A. Steele. Wide-bandwidth charge sensitivity with a radio-frequency field-effect transistor. *Applied Physics Letters* **103**, 143102 (2013).

[141] J. Jalil, Y. Zhu, C. Ekanayake & Y. Ruan. Sensing of single electrons using micro and nano technologies: a review. *Nanotechnology* **28**, 142002 (2017).

[142] W. Lu, Z. Ji, L. Pfeiffer, K. W. West & A. J. Rimberg. Real-time detection of electron tunnelling in a quantum dot. *Nature* **423**, 422–425 (2003).

[143] T. Fujisawa, T. Hayashi, Y. Hirayama, H. D. Cheong & Y. H. Jeong. Electron counting of single-electron tunneling current. *Applied Physics Letters* **84**, 2343–2345 (2004).

[144] J. Bylander, T. Duty & P. Delsing. Current measurement by real-time counting of single electrons. *Nature* **434**, 361–364 (2005).

[145] T. Fujisawa, T. Hayashi, R. Tomita & Y. Hirayama. Bidirectional counting of single electrons. *Science* **312**, 1634–1636 (2006).

[146] S. Gustavsson, R. Leturcq, B. Simovič, R. Schleser, T. Ihn, P. Studerus, K. Ensslin, D. C. Driscoll & A. C. Gossard. Counting statistics of single electron transport in a quantum dot. *Phys. Rev. Lett.* **96**, 076605 (2006).

[147] I. T. Vink, T. Nooitgedagt, R. N. Schouten, L. M. K. Vandersypen & W. Wegscheider. Cryogenic amplifier for fast real-time detection of single-electron tunneling. *Applied Physics Letters* **91**, 123512 (2007).

[148] T. Choi, T. Ihn, S. Schön & K. Ensslin. Counting statistics in an inas nanowire quantum dot with a vertically coupled charge detector. *Applied Physics Letters* **100**, 072110 (2012).

[149] L. Viola, E. Knill & S. Lloyd. Dynamical decoupling of open quantum systems. *Phys. Rev. Lett.* **82**, 2417–2421 (1999).

[150] A. G. Kofman & G. Kurizki. Universal dynamical control of quantum mechanical decay: Modulation of the coupling to the continuum. *Phys. Rev. Lett.* **87**, 270405 (2001).

[151] T. F. Gallagher. *Rydberg Atoms* (Cambridge Univeristy Press, 1994).

[152] N. Bohr. On the constitution of atoms and molecules. *Philisophical Magazine and Journal of Science* **26**, 13–33 (1913).

[153] E. Schrödinger. Quantisierung als Eigenwertproblem. *Annalen der Physik* **4**, 489–527 (1926).

[154] A. Signoles. *Manipulations cohérents d'états de Rydberg elliptiques par dynamique Zénon quantique*. Ph.D. thesis, Université Pierre et Marie Curie - Paris VI, Paris (2014).

[155] P. S. Epstein. Zur Theorie des Starkeffektes. *Annalen der Physik* **355**, 489–520 (1916).

[156] K. Schwarzschild. *Sitzungsberichte der Preussischen Akademie der Wissenschaften (Berlin)* **548** (1916).

[157] H. J. Silverstone. Perturbation theory of the stark effect in hydrogen to arbitrarily high order. *Physical Review A* **18**, 1853 (1978).

[158] M. Englefield. *Group theory and the Coulomb Problem* (Wiley-Interscience, 1972).

[159] M. L. Zimmerman, M. G. Littman, M. M. Kash & D. Kleppner. Stark structure of the rydberg states of alkali-metal atoms. *Physical Review A* **20**, 2251 (1979).

[160] H. A. Bethe & E. E. Salpeter. *Quantum Mechanics of One- and Two-Electron Atoms* (Academic Press, New York and Springer Verlag, Berlin, 1957).

[161] W. Pauli Jr. Über das Wasserstoffspektrum vom Standpunkt der neuen Quantenmechanik. *Zeitschrift für Physik* **36**, 336–363 (1926).

[162] E. Lieb. The classical limit of quantum spin systems. *Commmun. Math. Phys.* **31**, 327–340 (1973).

[163] C. Chandler, L. Cohen, C. Lee, M. Scully & K. Wodkiewicz. Quasi-probability distribution for spin-1/2 particles. *Found.Phys.* **22** (1992).

[164] G. Ramachandran, A. Usha Devi, P. Devi & S. Sirsi. Quasi-probability distributions for arbitrary spin-j particles. *Found.Phys.* **26** (1996).

[165] G. Agarwal. State reconstruction for a collection of two-level systems. *Physical Review A* **57**, 671 (1998).

[166] G. S. Agarwal. Relation between atomic coherent-state representation, state multipoles, and generalized phase-space distributions. *Phys. Rev. A* **24**, 2889–2896 (1981).

[167] J.-C. Gay, D. Delande & A. Bommier. Atomic quantum states with maximum localization on classical elliptical orbits. *Physical Review A* **39**, 6587–6590 (1989).

[168] P. Bellomo & C. R. Stroud Jr. Classical evolution of quantum elliptic states. *Physical Review A* **59**, 2139 (1999).

[169] K. Mogensen, J. Day, T. Ehrenreich, E. H. Pedersen & K. Taulbjerg. Coherent elliptic states in lithium. *Physical Review A* **51**, 4038 (1995).

[170] D. Meschede. Centimeter-wave spectroscopy of highly excited rubidium atoms. *JOSA B* **4**, 413–419 (1987).

[171] J. Han, Y. Jamil, D. V. L. Norum, P. J. Tanner & T. F. Gallagher. Rb nf quantum defects from millimeter-wave spectroscopy of cold rb85 rydberg atoms. *Phys. Rev. A* **74**, 054502 (2006).

[172] P. Nussenzveig. *Measurements of fields at the single photon level by atom interferometry*. Ph.D. thesis, Université Pierre et Marie Curie - Paris VI, Paris (1994).

[173] E.-K. Dietsche. *Preparation of circular Rydberg atoms in a superconducting cavity*. Master's thesis, Diplomarbeit, Technische Universität München (2012).

[174] B. V. Numerov. A method of extrapolation of perturbations. *Monthly Notices of the Royal Astronomical Society* **54** (1924).

[175] J. Neukammer, H. Rinneberg, K. Vietzke, A. König, H. Hieronymus, M. Kohl, H.-J. Grabka & G. Wunner. Spectroscopy of Rydberg atoms at n 500: Observation of quasi-Landau resonances in low magnetic fields. *Physical review letters* **59**, 2947 (1987).

[176] A. Signoles, E. K. Dietsche, A. Facon, D. Grosso, S. Haroche, J. M. Raimond, M. Brune & S. Gleyzes. Coherent transfer between low-angular-momentum and circular rydberg states. *Phys. Rev. Lett.* **118**, 253603 (2017).

[177] M. G. Littman, M. M. Kash & D. Kleppner. Field-ionization processes in excited atoms. *Physical Review Letters* **41**, 103 (1978).

[178] W. M. Itano, J. C. Bergquist, J. J. Bollinger, J. M. Gilligan, D. J. Heinzen, F. L. Moore, M. G. Raizen & D. J. Wineland. Quantum projection noise: Population fluctuations in two-level systems. *Phys. Rev. A* **47**, 3554–3570 (1993).

[179] J. M. Raimond & S. Haroche. *Exploring the quantum* (Oxford Graduate Texts, 2006).

[180] C. A. Meriles, L. Jiang, G. Goldstein, J. S. Hodges, J. Maze, M. D. Lukin & P. Cappellaro. Imaging mesoscopic nuclear spin noise with a diamond magnetometer. *The Journal of Chemical Physics* **133**, 124105 (2010).

[181] Y. Zhang, L. DiCarlo, D. T. McClure, M. Yamamoto, S. Tarucha, C. M. Marcus, M. P. Hanson & A. C. Gossard. Noise Correlations in a Coulomb-Blockaded Quantum Dot. *Physical Review Letters* **99** (2007).

[182] G. Gotz, G. A. Steele, W.-J. Vos & L. P. Kouwenhoven. Real time electron tunneling and pulse spectroscopy in carbon nanotube quantum dots. *Nano Letters* **8**, 4039–4042 (2008).

[183] M. J. Biercuk, D. J. Reilly, T. M. Buehler, V. C. Chan, J. M. Chow, R. G. Clark & C. M. Marcus. Charge sensing in carbon-nanotube quantum dots on microsecond timescales. *Phys. Rev. B* **73**, 201402 (2006).

[184] S. H. Autler & C. H. Townes. Stark effect in rapidly varying fields. *Phys. Rev.* **100**, 703–722 (1955).

[185] F. Dolde, H. Fedder, M. W. Doherty, T. Nobauer, F. Rempp, G. Balasubramanian, T. Wolf, F. Reinhard, L. C. L. Hollenberg, F. Jelezko & J. Wrachtrup. Electric-field sensing using single diamond spins. *Nat Phys* **7**, 459–463 (2011).

[186] L. M. Pham, N. Bar-Gill, C. Belthangady, D. Le Sage, P. Cappellaro, M. D. Lukin, A. Yacoby & R. L. Walsworth. Enhanced solid-state multispin metrology using dynamical decoupling. *Phys. Rev. B* **86**, 045214 (2012).

[187] H. J. Mamin, T. H. Oosterkamp, M. Poggio, C. L. Degen, C. T. Rettner & D. Rugar. Isotope-selective detection and imaging of organic nanolayers. *Nano Letters* **9**, 3020–3024 (2009).

[188] J. R. Kirtley, M. B. Ketchen, K. G. Stawiasz, J. Z. Sun, W. J. Gallagher, S. H. Blanton & S. J. Wind. High-resolution scanning squid microscope. *Applied Physics Letters* **66**, 1138–1140 (1995).

[189] T. L. Nguyen, J.-M. Raimond, C. Sayrin, R. Cortinas, T. Cantat-Moltrecht, F. Assemat, I. Dotsenko, S. Gleyzes, S. Haroche, G. Roux, T. Jolicoeur & M. Brune. Towards quantum simulation with circular rydberg atoms (2017).

[190] J. P. Palao, D. M. Reich & C. P. Koch. Steering the optimization pathway in the control landscape using constraints. *Phys. Rev. A* **88**, 053409 (2013).